Unshrouded Turbine Blade Tip Heat Transfer and Film Cooling

Brian M. T. Tang

Balliol College

Oxford University

This thesis is submitted in partial fulfilment
of the requirements for the degree of

Doctor of Philosophy

Trinity Term 2011

Unshrouded Turbine Blade Tip Heat Transfer and Film Cooling

Brian M. T. Tang
Balliol College, Oxford University

Supervised by Dr David Gillespie

This thesis is submitted in partial fulfilment of the requirements for the degree of
Doctor of Philosophy
Trinity Term 2011

Abstract

This thesis presents a joint computational and experimental investigation into the heat transfer to unshrouded turbine blade tips suitable for use in high bypass ratio, large civil aviation turbofan engines. Both the heat transfer to the blade tip and the over-tip leakage flow over the blade tip are characterised, as each has a profound influence on overall engine efficiency.

The study is divided into two sections; in the first, computational simulations of a very large scale, low speed linear cascade with a flat blade tip were conducted. These simulations were validated against experimental data collected by Palafox (2006). A thorough assessment of turbulence models and minimum meshing requirements was performed. The standard k-ω and standard k-ϵ turbulence models significantly overpredicted the turbulence levels within the tip gap. The other models were very similar in performance; the SST k-ω and realisable k-ϵ models were found to be the most suitable for the flow environment.

The second section documents the development and testing of a novel hybrid blade tip design, the *squealet* tip, which seeks to combine the known benefits of winglet and double squealer tips. The development of the external geometry was performed primarily through engine-representative CFD simulations at a range of tip gaps from 0.45% to 1.34% blade chord. The squealet tip was found to have a similar aerodynamic sensitivity to tip clearance as a baseline double squealer tip, with a tip gap efficiency exchange rate of 2.03, although this was 18% greater than the alternative winglet tip. The squealet tip displayed higher predicted stage efficiency than the winglet tip over the majority of the range of tip clearances investigated, however. The overall heat load was reduced by 14% compared with the winglet tip but increased by 28% over the double squealer tip, primarily due to the change in wetted surface area. The predicted local heat transfer coefficients were similar across all geometries. A realistic internal cooling plenum and an array of blade tip cooling holes were subsequently added to the squealet tip geometry and the cooling configuration refined by the selective sealing of cooling holes. Film cooling performance was largely assessed by the predicted

adiabatic wall temperature distributions. A viable cooling scheme which reduced the cooling air requirement by 38% was achieved, compared to the initial case which had all cooling holes open. This was associated with just a 7% increase in blade tip heat flux and no penalty in peak temperature on the blade tip. Film cooling air ejected from holes on the blade suction side was swept away from the blade tip region, making the squealet rim at the crown of the blade particularly challenging to cool. It was demonstrated that this region could be cooled effectively by ballistic cooling from holes located on the blade tip cavity floor, although this was expensive in terms of the mass flow rate of cooling air required.

The computational results were reinforced with experimental data collected in a transonic linear cascade. Downstream aerodynamic loss measurements were taken for a linearised version of the squealet tip design without cooling at nominal tip gaps of 0.45%, 0.89% and 1.34% blade chord, which was compared to similar data taken by O'Dowd (2010) for flat and winglet tips. The squealet was seen to have a similar aerodynamic loss to the flat tip and a reduced loss compared with the winglet tip. Full surface heat transfer measurements were taken for the uncooled squealet tip, at tip gaps of 0.89% and 1.34% blade chord, and for two configurations of the cooled squealet tip, at a tip clearance of 0.89% blade chord. The qualitative similarity between the measured heat transfer distributions and the those predicted by the engine-representative CFD simulations was good. A CFD simulation of the uncooled linear cascade environment at the 1.34% blade chord tip clearance was performed using a single blade with translationally periodic boundary conditions. The predicted size of the over-tip leakage vortex was smaller than had been measured, resulting in a large underprediction in the magnitude of the downstream area-averaged aerodynamic loss. The magnitudes of the predicted blade tip Nusselt number distribution were similar to those produced by the engine-representative CFD simulations and lower than that measured experimentally. Differences in the shape of the Nusselt number distribution were observed in the vicinity of regions of separated and reattaching flow, but other salient features were replicated in the computational data.

The squealet tip has been shown to be a promising, viable unshrouded blade tip design with an aerodynamic performance similar to the double squealer tip but is more amenable to film cooling. It is significantly lighter than a winglet tip and incurs a reduced thermal load. The squealet tip design can now be developed into a blade tip geometry for use in real engines to provide an alternative to shrouded turbine blades and current unshrouded blade tip designs. A commercial CFD solver, Fluent 6.3, was shown to capture blade tip heat transfer and over-tip leakage flow sufficiently well to be a useful design guide. However, the sensitivity of the flow structure (and hence, heat transfer) in the forward part of the blade tip cavity suggests that physical testing cannot be eliminated from the design process entirely.

Dedication

To everyone who has helped me along the way—
You know who you are

Truth is much too complicated to allow anything but approximations

—*John von Neumann*

Acknowledgements

First and foremost, I would like to thank my supervisor, David Gillespie. Without his seemingly limitless patience and infinite wisdom, I am absolutely certain that I would never have made it all the way through to the end! Thank you, David, for guiding me through the difficult times, for your expert technical help, but most of all, thank you for continuing to believe in me when I'd lost that faith in myself.

I must thank Rolls-Royce plc. for their support, both financial and technical. Their funding made this project possible. I would specifically like to thank Brian Cheong, Ed Romero, Dougal Jackson and Ed Dane for their ongoing help and support. My thanks must also go to the Engineering and Physical Sciences Research Council (EPSRC) who provided additional financial support.

I don't believe that Peter Ireland realises quite how much of an impact he has had on me. Thank you, Peter, for getting me interested in research in the first place. If it hadn't been for you, I would never have ended up in this mess!

I am extremely grateful to the HSLC team, Devin O'Dowd, Qiang Zhang and Li He, who so graciously accommodated me on their rig and helped me complete the experimental portion of my work, never asking for anything in return. Thank you for all of your patience and your help. Thanks must also go to Dave Mountain, Trev Godfrey, Gerald Walker and the other technicians, and Paul Cox, Bill Godfrey and the rest of the maintenance team at the lab.

To all of my colleagues at the Osney lab, both past and present, thank you for your companionship. Whether you were there only for a few months or for longer than me(!), you are the people who made these years at the lab such an enjoyable and interesting experience. Thank you for your friendship, advice, banter, sympathy, jokes, help, questions and solidarity. Some of you I've already mentioned; others that I'd like to mention explicitly are Aleen, Alex, Andrew Neely, Andy Fawcett, Bharat, Chris, Helen, Inés, Ioanna, James Aubry, James Batstone, Jiby, Josh, J.T., Kenny, Laura, Matt McGilvray, Noel, Paul Beard, Rex, Rod, Salva and Tom. I wish you (and the lab!) all the best for the future.

A huge thank you goes to all of my friends. You are far too many to mention individually here, but I hope that you all realise how much you have helped me. All of those cups of tea, hugs, much-needed pints, emails, phone calls and letters—those are the things that have helped me stay sane. Thank you for helping me through the dark days and being there to celebrate the good times with me too.

Last, but certainly by no means least, thank you to my amazing family. For supporting and encouraging me, through the bad times as well as the good—Mum, Dad, Andrew and Wai, thank you for sticking by me!

Contents

Chapter 0

Preliminary

Figures 1.4, 1.5, 1.6, 1.7, 1.8, 1.9a, 2.1, 2.2, 2.3, 2.4, 2.5, 2.6, 2.7, 2.8, 2.9, 2.10, 2.11, 2.12, 2.14, 2.15, 2.16, 2.17, 2.18, 2.19, 2.20, 2.21 and 2.23 have been removed from this edition due to copyright restrictions.

0.1 List of figures

0.2 List of tables

0.3 Nomenclature

c	Specific heat capacity	$[\mathrm{J\,kg^{-1}\,K^{-1}}]$
c_{ax}	Axial chord	
Cp_0	Pressure loss coefficient $= \frac{P_{0\mathrm{i}}-P_0}{\left(\frac{1}{2}\rho u^2\right)}$	$[-]$
g	Tip gap	$[\mathrm{m}]$
h	Heat transfer coefficient	$[\mathrm{W\,m^{-2}\,K^{-1}}]$
h	Specific enthalpy	$[\mathrm{J\,kg^{-1}}]$
H	Blade span	$[\mathrm{m}]$
k	Turbulent kinetic energy	$[\mathrm{J\,kg^{-1}}]$
k	Thermal conductivity	$[\mathrm{W\,m^{-1}\,K^{-1}}]$
l	Characteristic length	$[\mathrm{m}]$
$\dot{m}$	Mass flow rate	$[\mathrm{kg\,s^{-1}}]$
M	Mach number	$[-]$
Nu	Nusselt number $= \frac{hl}{k}$	$[-]$
p	Pressure	$[\mathrm{Pa}]$
Pr	Prandtl number $= \mu c_{\mathrm{p}}/k$	$[-]$
q	Heat flux	$[\mathrm{W\,m^{-2}}]$
R	Specific gas constant	$[\mathrm{J\,kg^{-1}\,K^{-1}}]$
Re	Reynolds number $= \frac{\rho u l}{\mu}$	$[-]$
s	Entropy	$[\mathrm{J\,K^{-1}}]$
t	Time	$[\mathrm{s}]$
T	Temperature	$[\mathrm{K}]$
u	Flow velocity	$[\mathrm{m\,s^{-1}}]$
u^*	Friction velocity $= \sqrt{\tau_{\mathrm{w}}/\rho}$	$[\mathrm{m\,s^{-1}}]$
U	Blade speed	$[\mathrm{m\,s^{-1}}]$
w	Specific work	$[\mathrm{J\,kg^{-1}}]$
x	Axial coordinate	$[\mathrm{m}]$
y	Distance to wall	$[\mathrm{m}]$
y^+	Non-dimensional measure of wall distance $= \frac{\rho y u^*}{\mu}$	$[-]$

Greek

α	Thermal diffusivity $= \frac{k}{\rho c}$	$[\mathrm{m^2\,s^{-1}}]$
γ	Ratio of specific heats	$[-]$

ϵ	Turbulent kinetic energy dissipation rate	$[\mathrm{J\,kg^{-1}\,s^{-1}}]$
ζ	Kinetic energy loss coefficient	$[-]$
η	Efficiency	$[-]$
μ	Dynamic viscosity	$[\mathrm{Pa\,s}]$
ρ	Density	$[\mathrm{kg\,m^{-3}}]$
τ_w	Wall shear stress	$[\mathrm{Pa}]$
ψ	Stage loading coefficient $= \frac{\Delta h_0}{U^2}$	$[-]$
ω	Specific turbulent kinetic energy dissipation rate	$[\mathrm{s^{-1}}]$

Subscript

0	Total quantity
abs	Absolute frame of reference
ad	Adiabatic
ct	Constant temperature
i	Initial
i	Rotor inlet
N	NGV
NGVin	NGV inlet
o	Rotor outlet
R	Rotor blade row
rel	Relative frame of reference
s	Ideal isentropic process
St	Turbine stage
SS	Static-to-static
t	Turbulent
TS	Total-to-static
w	Wall

Abbreviations

ANTLE	Advanced Near-Term Low Emissions	
CAD	Computer Aided Design	
CFD	Computational Fluid Dynamics	
EFE	Environmentally Friendly Engine	
FEA	Finite Element Analysis	
GUI	Graphical User Interface	
HSLC	High Speed Linear Cascade	
HP	High Pressure	
IP	Intermediate Pressure	
IR	Infra-Red	
LE	Leading Edge	
NGV	Nozzle Guide Vane	
NHFR	Net Heat Flux Reduction $= \frac{q_\text{without cooling} - q_\text{with cooling}}{q_\text{without cooling}}$	$[-]$
OPR	Overall Pressure Ratio	$[-]$
ORF	Oxford Rotor Facility	

PID	Proportional–Integral–Derivative	
PS	Pressure Side	
RAM	Random Access Memory	
RANS	Reynolds Averaged Navier Stokes	
RNG	Renormalisation Group Theory	
RSM	Reynolds Stress Model	
SFC	Specific Fuel Consumption	$[\mathrm{kg\,s^{-1}\,N^{-1}}]$
SFP	Secondary Flow Plane	
SIMPLE	Semi-Implicit Method for Pressure-Linked Equations	
SLA	Stereolithography	
SS	Suction Side	
SST	Shear Stress Transport	
TE	Trailing Edge	
TET	Turbine Entry Temperature	[K]
TUI	Text User Interface	
ZnSe	Zinc-Selenide	

Chapter 1

Introduction

The invention of the gas turbine engine is a relatively recent one, with the first patent for a jet engine to power an aircraft granted to Guillaume (1922). It was not, however, until the late-1930s that genuinely successful jet engines were developed by the parallel efforts of Sir Frank Whittle in Britain and Hans von Ohain in Germany. Although Whittle (1931) successfully patented his ideas first, the first jet-powered flight was by a He-178 aeroplane on 27 August 1939, which was powered by the HeS-3 engine designed by Ohain. The first flight of a Whittle design followed two years later on 15 May 1941, when a Gloster E.28/39 took to the air powered by a Power Jets W.1 turbojet. The increased thrust produced by the jet engine compared to piston engines, combined with its superior power-to-weight ratio, allowed aircraft to become heavier and fly higher and faster, ensuring its rapid development and subsequent adoption in production aeroplanes towards the end of the Second World War. By 1952, the de Havilland Ghost turbojet engine was powering the first civil jet-powered airliner, the de Havilland Comet.

In the decades since, air travel and air freight has expanded to become a large, global industry, powered almost entirely by gas turbine engines. As the industry has grown in scale and importance, there has been a push towards increasing efficiency, both for environmental and economic reasons. Turbofan and turboprop engines have entirely supplanted their turbojet alternatives in civil aviation, providing a sizeable increase in fuel efficiency and reduction in noise due to their increased propulsive

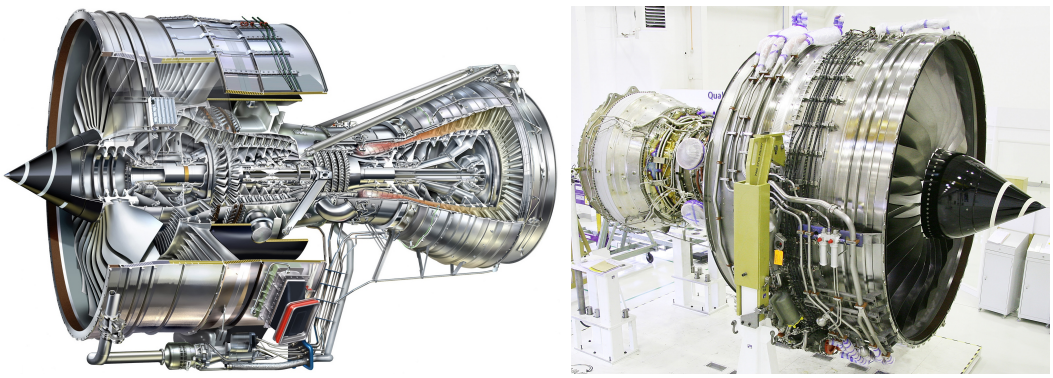

(a) Cutaway diagram (b) Production engine

Figure 1.1: Rolls-Royce Trent 900 engine
(Images courtesy of Rolls-Royce plc.)

efficiency. In 1972, Rolls-Royce plc. produced the first three spool turbofan engine to enter service, the RB-211, which allowed the fan to spin at a slower speed than the intermediate pressure compressor, realising further efficiency benefits. This three shaft architecture has been developed into the Trent family of engines, most recently the Trent XWB (due to enter service in 2013), with each engine building on the knowledge and understanding gained from the previous designs.

Improvements made to one engine therefore have a wider impact than just to the engine to which the modifications are applied; design changes continue to be felt in the subsequent generations, potentially decades later. Moreover, industrial power-generation and marine power gas turbines are frequently derived directly from aero-engine designs by the removal of the fan and the fitting of a power take-off shaft in its place. The Rolls-Royce MT30 marine gas turbine, for instance, is derived from the Trent 800 that powers the Boeing 777, retaining 80% commonality with its aero-engine parent; this is illustrated in figure 1.2. Thus, changes made to the core of an engine will be carried across to many subsequent derivative engines, whether industrial, marine or aero.

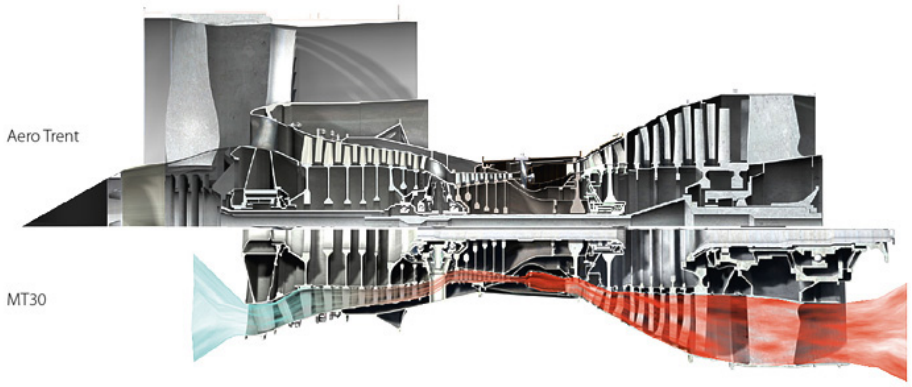

Figure 1.2: Comparison of the Trent 800 aero-engine to the MT30 marine gas turbine (Image courtesy of Rolls-Royce plc.)

1.1 Joule cycle

The ideal thermodynamic cycle for a gas turbine is the Joule (or Brayton) cycle, shown on a $T{\sim}s$ diagram in figure 1.3. Air is drawn in at atmospheric pressure, p_1, and compressed isentropically to p_{2s}. Isobaric combustion then heats the air to T_3 before it is expanded isentropically through the turbines to p_{4s}, extracting work to drive the compressors. The exhaust gases are then expanded isentropically to p_{5s}, either through a nozzle to accelerate them into a jet to provide thrust, or through a further set of turbines to extract more work to power the fan. The efficiency of the cycle is therefore given by the net work output divided by the input heat; i.e.

$$\eta_{\text{cycle}} = \frac{(h_3 - h_{5s}) - (h_{2s} - h_1)}{h_3 - h_{2s}} \tag{1.1}$$

Since the compression process 1–2s and the expansion process 3–4s–5s are isentropic, and that $p_1 = p_{5s}$ and $p_{2s} = p_3$, assuming ideal gas behaviour (constant c_p), the efficiency becomes

$$\eta_{\text{cycle}} = 1 - \left(\frac{p_{2s}}{p_1}\right)^{\frac{1-\gamma}{\gamma}} \tag{1.2}$$

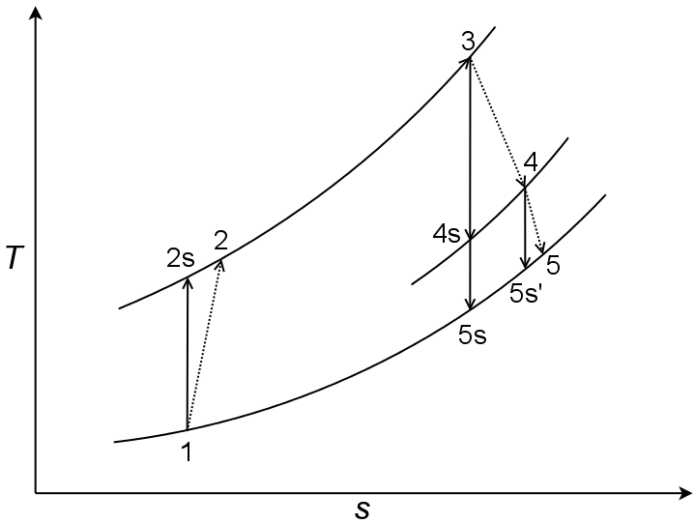

Figure 1.3: Joule cycle

In the case of the ideal, perfectly loss-less cycle, the overall cycle efficiency is dependent only on $\frac{p_{2s}}{p_1}$, the *Overall Pressure Ratio* (OPR). The specific work is given by

$$\begin{aligned} w &= (h_3 - h_{5s}) - (h_{2s} - h_1) \\ &= c_p \left[T_3 \left(1 - \left(\frac{p_{2s}}{p_1} \right)^{\frac{\gamma-1}{\gamma}} \right) - T_1 \left(\left(\frac{p_{2s}}{p_1} \right)^{\frac{1-\gamma}{\gamma}} - 1 \right) \right] \end{aligned} \tag{1.3}$$

The specific work (and hence, specific thrust) is also dependent on OPR, but is additionally increased by increasing T_3, the *Turbine Entry Temperature* (TET). The expressions in equations 1.2 and 1.3 are derived for the ideal Joule cycle, in which the compression and expansion are performed isentropically. In reality, there are losses in the compressors, turbines and nozzle, which are represented by the processes 1–2 and 3–4–5 in figure 1.3. There is also likely to be some pressure drop through the combustor (Saravanamuttoo et al., 2009), so $p_3 < p_2$ (not shown). When these losses and non-ideal gas behaviour are taken into account, the cycle efficiency also becomes dependent on TET. This is illustrated in figure 1.4, where net thrust specific fuel consumption, which directly reflects overall efficiency, and specific thrust are shown plotted against TET.

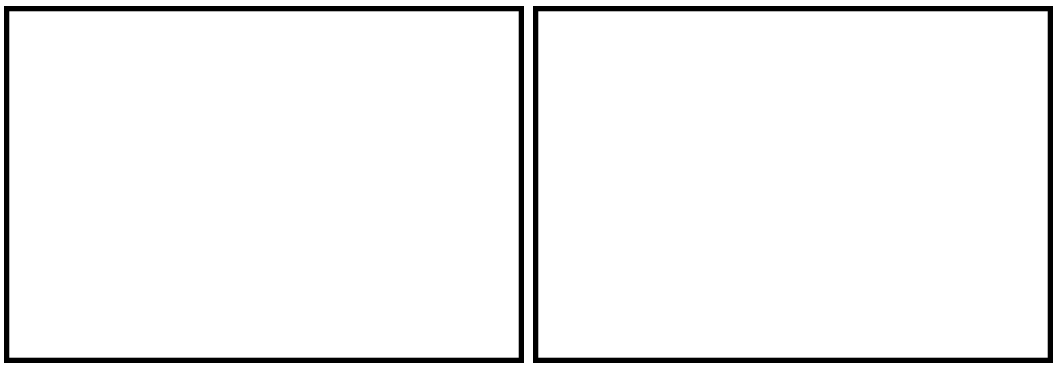

(a) SFC (b) Specific thrust

Figure 1.4: Effect of TET on SFC and specific thrust
(Reproduced from Rolls-Royce plc. (2005))

Evidently, increasing TET can reduce SFC, which is one of the most important performance criteria for civil aero-engines. With rising fuel costs, SFC has a huge impact on the cost of running an engine; it has been estimated that an extra 1% in SFC can cost as much as US$150,000 per year for a single four-engined aircraft (Rolls-Royce plc., 2005). The impact of SFC is not solely economic either—a reduction in fuel burn translates directly into a reduction in CO_2 emissions, which is becoming increasingly important as environmental concerns gain prominence. There has been a steady trend in increasing TET and decreasing SFC over the last few decades, as can be seen in figure 1.5.

It is, however, possible that the SFC benefit derived from TET increases will level off in the near future. Although a higher TET can reduce CO_2 emissions, it also increases NO_x emissions, so the environmental benefit is not clear-cut. The economic consideration is not simple either—the cost of nickel and the exotic metals needed to make the superalloys needed for the turbine blades to withstand extremely high temperatures has risen steeply in recent years. If these already expensive materials continue to increase in price, it may eventually work out to be better economically to make some sacrifice in SFC and accept higher total fuel costs so that TET can be reduced and turbine vanes and blades can be made from cheaper materials. It is not

(a) SFC

(b) TET

Figure 1.5: Historical trends in SFC and TET
(Reproduced from Rolls-Royce plc. (2005))

even clear that raising TET further will continue to yield reductions in SFC; Horlock et al. (2001) performed cycle analyses that included the efficiency penalty incurred by the increased cooling air requirements needed to run at higher TET and concluded that the benefit of continuing to increase TET was marginal.

Regardless of whether or not TET continues to increase in the future, it has already reached extremely high levels. The F135 turbofan engine for example, a military rather than a civil aero-engine, runs with a TET of 1980°C (Langston, 2007). In this era of extremely high combustor exit temperatures, the subject of turbine cooling and the efficient use of the expensive (in terms of impact on cycle efficiency) cooling air are more critical than ever before.

1.2 High pressure turbine over-tip leakage flow

The high pressure turbine stage sits immediately downstream of the combustor, bathed in the hottest flow of the engine outside of the combustor itself. While HP turbine blades in modern, large civil aviation turbofan engines are made of nickel superalloys which can survive peak temperatures as high as 1200°C (Pollock and Tin, 2006) without excessive oxidation or softening, the mainstream flow from the combustor is typically several hundred degrees hotter; the TET for the newest, large civil aero-engines can be in excess of 1800°C. This gap is bridged by the combination of thermal barrier coatings and film-cooling air, which is bled out of cooling holes on the aerofoil surfaces, removing heat through internal cooling schemes and forming a protective film of cooler air over the surface of the component.

In modern engines, HP turbine blade tips can travel at speeds as high as $500\,\mathrm{ms}^{-1}$, so there is necessarily a small gap between them and the stationary casing that surrounds the rotor. This gap is typically of the order of 1%–3% blade span (Harvey, 2004) and varies between different phases of flight (e.g. during take-off, cruise or landing) but cannot ever be entirely eliminated (Hennecke, 1984). Regulating this tip gap is not a trivial task. Both the rotor assembly and the stator casing expand and contract as they heat and cool at different rates, while the rotor parts also elongate with rotor speed, due to the centrifugal stresses. Moreover, there will be some degree of non-circularity in both sets of parts, plus some installation eccentricity (where the axes of the rotor and casing do not exactly coincide) to contend with, which will make the tip gap vary around the circumference. Small axial displacements of the rotor assembly will affect the tip clearance if the outer annulus line over the tip is haded. While both active and passive tip clearance control systems are used to minimise the tip gap throughout the flight cycle and the engine lifetime, it is always a difficult exercise, and one in which the avoidance of tip rubs (where the blade tip collides with the casing) must take priority over closing the tip gap to the smallest possible size. The variation in rotor, casing and tip clearance size during a typical flight cycle

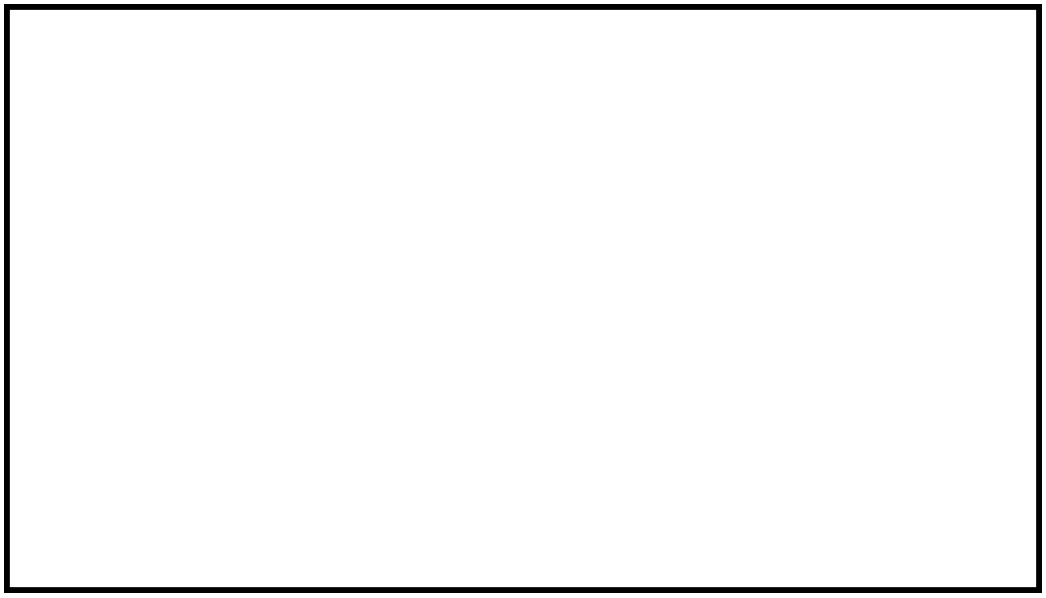

Figure 1.6: Variation in tip gap during a typical flight cycle
(Reproduced from Halila et al. (1982))

is shown in figure 1.6, both with and without the use of *Active Clearance Control* (ACC).

The pressure difference between the pressure side and suction side of the turbine blade drives an over-tip leakage flow through the tip gap. This flow is not turned by the blade, so very little work is extracted from it; in fact, the tip may act as a compressor, with work done on the fluid in this region (Thorpe et al., 2007). Due to the mismatch in flow angle with the mainstream passage flow, the over-tip leakage flow wraps into a vortex as it emerges on the suction side, causing a significant loss in total pressure. This is evidently detrimental to turbine stage efficiency—it has been estimated that over-tip leakage flow could account for as much as one-third of overall turbine stage losses (Boyle et al., 1984)—and so the over-tip leakage has a direct and significant impact on overall SFC.

Aside from the implications on efficiency, the over-tip leakage flow has a serious impact on heat transfer to the blade tip. The over-tip leakage flow is characterised by a strong acceleration into the pressure side of the blade, resulting in high speed flow

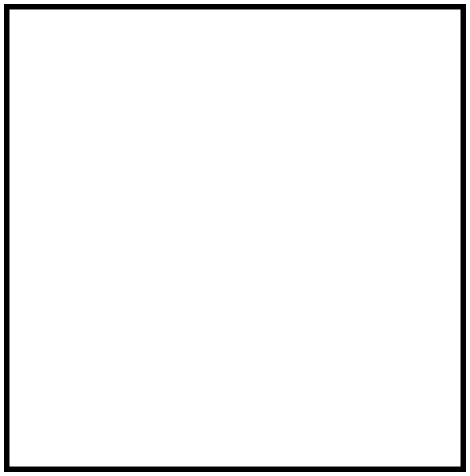

Figure 1.7: Near-tip secondary flow structure
(Reproduced from Harvey and Ramsden (2001))

and thin boundary layers within the tip gap (Kwak and Han, 2003a). The sink-like behaviour of the pressure side of the tip gap draws flow up the pressure side of the blade, bringing very hot air from smaller radii up to the tip region and surrounding the blade tip on three sides with extremely high temperature fluid (Mayle and Metzger, 1982). As a result, the blade tips are subjected to very high thermal loading and are prone to failure by oxidation and burn-out. Temperature gradients across the blade tip can also induce thermal stresses, leading to cracking. An example of a damaged unshrouded blade tip removed from service is shown in figure 1.8. Thermal control at the blade tip is therefore critical to ensure sufficient blade life is achieved and has made turbine blade tip cooling a priority for gas turbine manufacturers.

1.3 Motivation for the present study

There are two broad approaches for the control of turbine blade over-tip leakage flow control. The first is to have a shrouded blade tip, which has been the approach that Rolls-Royce has historically taken with all of its large[1] civil turbofan aero-engines. With a shrouded blade, a platform is attached to the blade tip that extends circumferentially

[1]Engines rated at $\gtrsim$ 35000 lb (156 kN) maximum thrust.

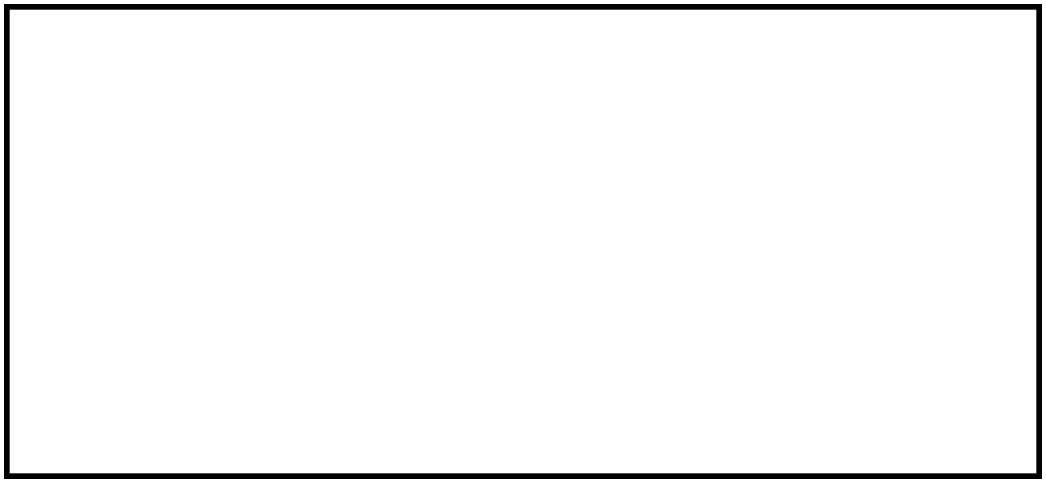

Figure 1.8: Damaged unshrouded blade removed from service
(Reproduced from Bunker (2004))

in both directions, as seen in figure 1.9a. These blade tip shrouds extend all the way to the shrouds of the adjacent blades, to form a contiguous ring at the outer extremity of the rotor blade set, effectively preventing pressure side-to-suction side over-tip leakage flow. Knife-edged fins and fences on the outer surface of the shroud act as labyrinth seals against the stationary casing to minimise over-shroud leakage flow in the axial direction. Blade tip shrouds provide a number of benefits. They not only provide excellent sealing of over-tip leakage flow, but can do so over a wide range of tip gaps. As the outer annulus line is formed by the shroud inner surface, but the sealing against the leakage flow is performed by the fins and fences on the shroud outer surface, the outer annulus at the rotor blade may be haded without fear of axial displacements of the rotor assembly affecting the tip gap. Hading the turbine annulus in this way can help reduce the overall length of the engine, as a smaller change in radius is required in the interduct between the HP rotor exit and the IP NGV inlet.

However, blade tip shrouds carry a number of disadvantages as well. They are relatively heavy, as they extend far from the aerofoil. Since this extra mass is carried at the outermost radius of the rotor, it increases the centrifugal stress on the rest of the blade, the disc, which connects the turbine blade set to the shaft, and the

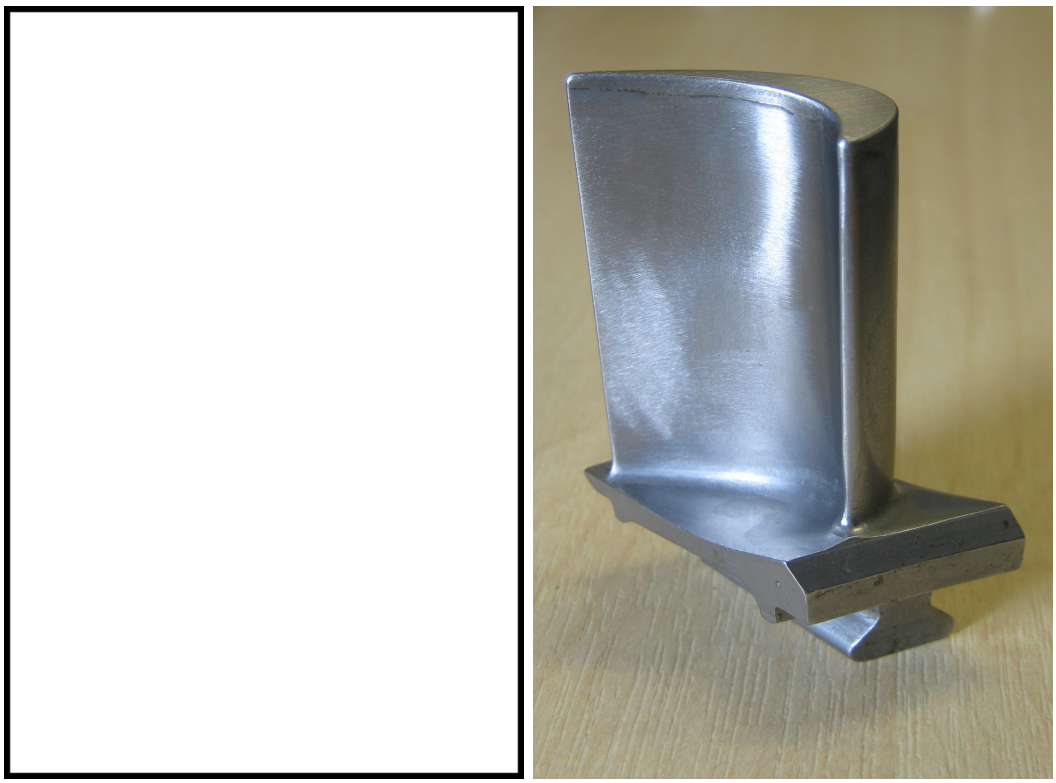

(a) Shrouded blade tip
(Reproduced from Rolls-Royce plc. (2005))

(b) Unshrouded blade tip

Figure 1.9: Comparison of a shrouded to an unshrouded turbine blade tip

fir tree, which attaches the turbine blades to the disc—all of which must then be made stronger to support this extra load, resulting in an increase in weight of those components as well. The circumferential extent of each shroud is structurally limited, so their use could also increase the overall blade count. Increases in blade number add to the production and maintenance cost of the blade set and can also increase the overall weight of the engine. Blade tip shrouds have a very large cooling air requirement as their wetted area is large, which is detrimental to overall efficiency. Recent years have seen a trend towards higher rotor speeds to decrease blade loading, which improves turbine efficiency (Saravanamuttoo et al., 2009). As rotor speeds and TET have increased, blade tip shrouds become increasingly vulnerable to "shroud curl", where the corners of the shroud curl outwards under load and rub against the

casing, and are increasingly seen as a less attractive option as a way of controlling over-tip leakage for the HP turbine blade.

The alternative is to have an unshrouded blade. Without a shroud, there is a direct leakage path between the pressure side and suction side of each aerofoil, so over-tip leakage flow is much larger for unshrouded blades than for shrouded ones. Because of the reduced sealing capability, unshrouded blade tips are less aerodynamically efficient at typical tip gaps that can currently be maintained in real engines. However, the efficiency penalty incurred by the increase in over-tip leakage mass flow rate is partly offset by the reduction in weight and cooling requirements. The major disadvantage of unshrouded blade tips is that they are much more sensitive to changes in tip gap than shrouded blade tips are, so their performance will decrease over the lifetime of the engine as material is lost from the blade tip by erosion, corrosion and through tip rubs. Heat transfer to the over-tip casing is also higher with unshrouded blades, so a more aggressive cooling design is required for the casing liner.

1.4 Aims and objectives of the present study

The study presented in this thesis focuses on the unshrouded blade tip. In the UK, there is limited experience in the design of unshrouded blade tips in aero-engines; for example, within Rolls-Royce these have been used only for a few military and small civil aero-engines. If rotor speeds and TET continue to increase, unshrouded blade tips will inevitably become a necessity and this study seeks to develop their understanding and design.

The current research is divided into two separate, but related, pieces of work. The first is a computational study that investigates the methodology requirements for the high-fidelity simulation of over-tip leakage flow and heat transfer in a low speed, incompressible flow environment. The main objective of this part of the study is to assess the capability of the commercial solver FLUENT 6.3 and its various turbulence

models to predict the flow around and heat transfer to a representative model of an HP turbine blade with a flat tip. By doing this, the simulation of other low speed experimental studies will be aided, allowing reliable CFD simulations to be performed to supplement the experimental programme and thus to enhance the understanding of the flow fields and mechanisms in ways not possible experimentally.

The second part of the study is much larger and concerns the development of a new, hybrid unshrouded blade tip design that can realise the benefits of two separate existing designs. This section has both computational and experimental threads that seek to introduce the new tip concept, demonstrate its potential and develop it into a viable candidate for subsequent development towards implementation in a real engine. The aim is not to produce a finished, engine-ready blade tip design, but rather to deliver a concept ready for an engine programme to develop into a finished design. Both heat transfer and aerodynamic performance are extremely important in the design of any component in the main gas path of an engine, but these two strands are extremely difficult to couple and develop simultaneously. The focus of this study is therefore chosen primarily to be heat transfer, but aerodynamics cannot be disregarded entirely. The new blade tip should therefore exhibit enhanced thermal performance (e.g. through a reduced cooling air requirement) and acceptable aerodynamic performance (i.e. comparable to currently available alternative unshrouded blade tip designs).

1.5 Dimensional analysis for aero-thermal scaling

In order to achieve similarity between a model, whether experimental or numerical, and the conditions found in a real engine, the governing non-dimensional parameters must be identified and matched. The present study concerns both the aerodynamic performance of a turbine blade row and the heat transfer into the turbine blade tips. Assuming geometric similarity between the model and the real engine, the aerodynamics of the turbine blade row are primarily governed by 13 variables, to

γ	Ratio of specific heats	$[-]$
η	Efficiency	$[-]$
μ	Dynamic viscosity	$[\mathrm{ML^{-1}T^{-1}}]$
ρ	Density	$[\mathrm{ML^{-3}}]$
c_p	Specific heat capacity at constant pressure	$[\mathrm{L^2T^{-2}\Theta^{-1}}]$
h	Heat transfer coefficient	$[\mathrm{MT^{-3}\Theta^{-1}}]$
k	Thermal conductivity	$[\mathrm{MLT^{-3}\Theta^{-1}}]$
l	Characteristic length	$[\mathrm{L}]$
$\dot{m}$	Mass flow rate	$[\mathrm{MT^{-1}}]$
N	Rotor speed	$[\mathrm{T^{-1}}]$
p_o	Exit static pressure	$[\mathrm{ML^{-1}T^{-2}}]$
p_0i	Inlet total pressure	$[\mathrm{ML^{-1}T^{-2}}]$
R	Specific gas constant	$[\mathrm{L^2T^{-2}\Theta^{-1}}]$
ΔT_0	Total temperature drop	$[\Theta]$
T_0i	Inlet total temperature	$[\Theta]$
T	Gas temperature	$[\Theta]$
T_w	Wall temperature	$[\Theta]$
u	Flow velocity	$[\mathrm{LT^{-1}}]$

Table 1.1: Main governing variables for turbine aero-thermal performance

which a further 5 are added when heat transfer is investigated. These 18 variables are listed in table 1.1.

Incorporating the equations

$$c_\mathrm{p} = \frac{\gamma}{\gamma - 1} R \tag{1.4}$$

and

$$\dot{m} = \rho u l^2 \tag{1.5}$$

there remain 16 independent variables in four dimensions. Applying the Π theorem (Buckingham, 1914), these variables may be reduced to 12 dimensionless groups which, if matched, ensure similarity between the model and the real engine environment is achieved. Selecting appropriate non-repeating variables and arranging them into the common forms of the dimensionless groups, the following relationship is obtained.

$$\eta, \frac{\dot{m}\sqrt{RT_\mathrm{0i}}}{p_\mathrm{0i} l^2}, \frac{\Delta T_0}{T_\mathrm{0i}} \frac{hl}{k}, = f\left(\gamma, \frac{c_\mathrm{p}\mu}{k}, \frac{\rho u l}{\mu}, \frac{u}{\sqrt{\gamma RT}}, \frac{p_\mathrm{0i}}{p_\mathrm{o}}, \frac{Nl}{\sqrt{RT_\mathrm{0i}}}, \frac{T}{T_\mathrm{w}}, \frac{u^2}{c_\mathrm{p}\left(T - T_\mathrm{w}\right)}\right) \tag{1.6}$$

Correct aerothermal scaling will therefore be achieved if the dimensionless groups on the right hand side of equation 1.6 are matched. The first two, γ and Prandtl number, are approximately matched if air is used as the test gas, although a small correction for the dependence on temperature may need to be applied in the case of γ. Full aerodynamic similarity requires that Reynolds number, Mach number, pressure ratio and specific speed are matched between the engine environment and the model. For similarity in heat transfer, gas-to-wall temperature ratio and Eckert number must additionally be matched or corrected for. Empirical correlations for the effect of gas-to-wall temperature ratio have been suggested by several previous studies, which allow discrepancies in gas-to-wall temperature ratio to be accounted for; the available correlations are summarised in Abu Talib (2003). Incorporating the ideal gas law, Eckert number may be written as

$$\mathrm{Ec} = \frac{u^2}{c_\mathrm{p}\left(T - T_\mathrm{w}\right)} = (\gamma - 1)\left(\frac{T}{T - T_\mathrm{w}}\right)\mathrm{M}^2 \tag{1.7}$$

reducing it to a function of γ, Mach number and gas-to-wall temperature. Hence, providing that γ and Mach number are matched, these correlations also simultaneously correct for discrepancies in Eckert number.

1.6 Outline of thesis

Chapter 2 contains a literature review, giving a relatively brief overview of the research into turbine blade over-tip leakage flow and heat transfer that has been published in the open literature. It would be impossible to produce an exhaustive review of all studies in this subject, and this is not intended to be a comprehensive survey; rather it seeks to highlight salient pieces of research that together form a representative view of the overall field. Chapter 3 presents the low speed portion of the study. It is an exercise in CFD validation, performed using data from Palafox (2006) taken from a large scale linear cascade run at a tip gap of 1.5% blade chord. The flow in

this linear cascade, and hence in the CFD simulations presented in this chapter, is at sufficiently low speed to be considered incompressible. The use of wall functions is tested and six turbulence models are assessed. Chapter 4 introduces the new, hybrid blade tip concept, the squealet tip. Its aerodynamic and thermal performance is assessed by the use of engine-representative CFD simulations at a range of tip gaps from 0.45% to 1.34% blade chord and compared against double squealer and winglet tip geometries. These simulations are performed using realistic pressure and temperature boundary conditions at real engine scale, so the flow regime is transonic and compressible. Chapter 5 continues the development of the squealet tip concept by the addition of film cooling. Further high speed, compressible CFD simulations are performed, this time focusing on a single tip gap of 0.89% blade chord. Several design variants are considered on the basis of the results of the simulations using the author's engineering judgement to refine the cooling configuration. Chapter 6 describes the experimental portion of the study, where the squealet tip is tested in the High Speed Linear Cascade, a 1.9× scale blowdown facility. Aerodynamic measurements with an uncooled version of the squealet tip are taken to measure the aerodynamic loss of the tip geometry at tip gaps of 0.45%, 0.89% and 1.34% blade chord. Heat transfer coefficient distributions over the uncooled blade tip are inferred from temperature measurements using IR thermography at tip gaps of 0.89% and 1.34% blade chord. Heat transfer coefficient and adiabatic wall temperature distributions are also reported for two cooling configurations of the film-cooled blade tip. Finally, chapter 7 provides a summary of the entire body of work and lists suggestions for the continuation of the study.

The research described in chapter 3 has been published as Tang et al. (2010). The squealet tip concept developed in chapters 4, 5 and 6 has been patented by Rolls-Royce plc. as Cheong and Diamond (2010).

Chapter 2

Literature Review

The study of over-tip leakage flow and the associated heat transfer dates back to the mid-1950s with the studies of Rains (1954) and Allen and Kofskey (1955). Since that time, the field has grown to become an extremely important and widely studied subject. There are already several excellent literature reviews on the topic available; this chapter is intended to highlight pieces of research that are particularly relevant to the present study and to help contextualise it. Readers seeking to build a more complete catalogue of the published research in the field are directed also to consult the literature surveys of Sunden and Xie (2010), O'Dowd (2010), Palafox (2006) and Bunker (2001).

2.1 Experimental studies using simple models

The early flow study of Rains (1954) used a simple, 2D model that was intended to be representative of the tip section rather than an actual aerofoil section to study the flow structure in the tip gap. The use of such idealised models allows for well-conditioned experimental setups that permit fine, independent control of variables. Moreover, their simplicity makes instrumentation easier and can improve the spatial resolution of the collected data; thus, simple 2D approaches have continued to be taken in the subsequent decades by some researchers, for example, Wadia and Booth (1982), Chyu et al. (1989) and Sjolander and Cao (1995). Although these extremely idealised

experimental rigs are still occasionally used today, most recently by Krishnababu et al. (2009), they have largely been superceded by linear cascades, annular cascades and rotating rigs, which are significantly more realistic and thus better suited to replicate the complex, 3D flow found in the near-tip region. Studies performed in idealised rigs will therefore largely be disregarded in this brief overview of the open literature.

2.2 Flat tips

The simplest and most widely studied unshrouded blade tip geometry is the flat blade tip. It is not, however, generally considered a viable option for modern aero-engine turbine blades because of its poor performance, both aerodynamically and thermally, relative to alternative designs. Nevertheless, there has been a lot of research done using flat tip geometries and it remains a popular baseline case against which alternatives can be compared.

Early studies, such as those of Moore and Tilton (1988), Yaras et al. (1989) and Heyes et al. (1992) focused on developing models for the aerodynamic loss caused by over-tip leakage flow, primarily using data collected in low speed linear cascades. While these studies gradually developed the picture of over-tip leakage flow structure, it was not until the computational study of Ameri and Steinthorsson (1995) that the full flow structure around the near-tip region became clear. They performed CFD simulations on the space shuttle main engine HP fuel side turbine blade, running them at a tip clearance of 2% blade span. Their flow visualisation, shown in figure 2.1a, shows the formation of a separation bubble over the pressure side edge of the blade tip and the subsequent reattachment of the over-tip leakage flow on to the blade tip surface. The over-tip leakage flow then forms a vortex on the suction side of the blade as it interacts with the mainstream passage flow. The predicted mid-gap velocity vectors in figure 2.1b show the direction of the over-tip leakage flow. It is predominantly parallel to the camber line in the forward part of the blade and almost perpendicular

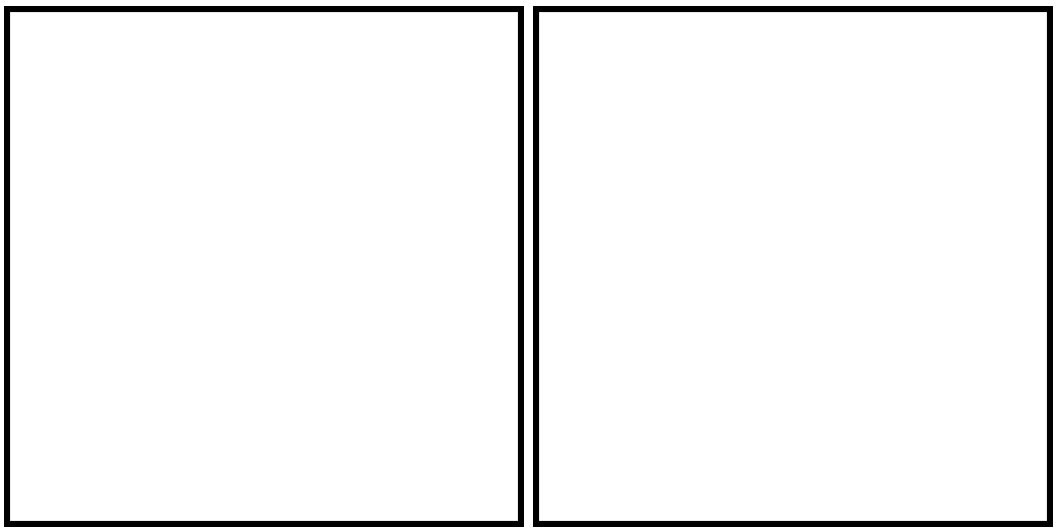

(a) Pathlines (b) Mid-gap velocity vectors

Figure 2.1: Over-tip leakage flow structure for a flat blade tip
(Reproduced from Ameri and Steinthorsson (1995))

to the camber line in the aft portion. More recent investigations have continued to fill in extra detail, but the general picture of over-tip leakage flow structure remains unchanged.

An aspect of turbine blade tip aerodynamics of particular interest is the variation of stage efficiency with increasing tip gap. This is especially important not only because the tip clearance varies between different stages of a flight cycle, but because it generally increases over the lifetime of an engine as material is eroded from the blade tip and casing liner. The sensitivity of the blade tip geometry to tip clearance size is normally quoted as the tip gap efficiency exchange rate, which is defined as

$$\text{Tip gap efficiency exchange rate} = \frac{\Delta\eta_{\text{St}}}{\frac{\Delta g}{H}} \tag{2.1}$$

By considering the entropy generated by the over-tip leakage flow mixing with the mainstream flow on the suction side, Denton (1993) concluded that typical unshrouded turbine blades would give tip gap efficiency exchange rates in the range 2.0–3.0, with higher values for rotors with larger stage loading coefficient, ψ. Measurements taken

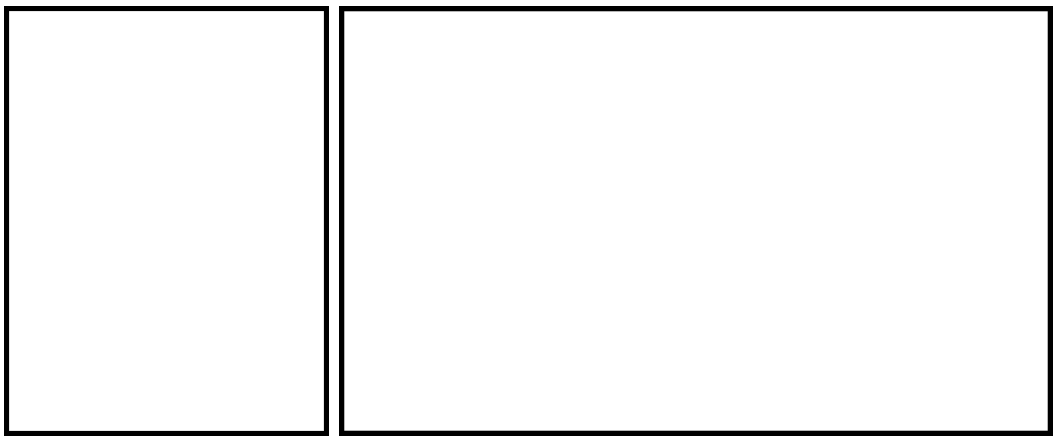

(a) Reproduced from Hourmouziadis and Albrecht (1987)

(b) Reproduced from Harvey (2004)

Figure 2.2: Tip gap efficiency exchange rates from various studies

from a wide variety of studies have shown that unshrouded turbine blades typically have tip gap efficiency exchange rates close to 2.0, as can be seen in the two summaries shown in figure 2.2. The desensitisation of the blade tip to reduce the tip gap efficiency exchange rate, whilst also maintaining an acceptable turbine stage efficiency, is a key target of the design process and this parameter is an important metric of blade tip aerodynamic performance.

2.2.1 Low speed[1] heat transfer

The full surface heat transfer coefficient distribution on a flat blade tip in a low speed environment was first measured by Bunker et al. (2000) in a two passage linear cascade. This study was shortly followed by Azad et al. (2000b) and Teng et al. (2001), who used a transient liquid crystal technique in a 3× scale, four passage linear cascade

[1]The term "low speed" is inherently subjective. In this context, it is implicitly defined to include any flow regimes that cannot capture shock waves and their associated effects on aerodynamics and heat-transfer; i.e. regimes that are subsonic rather than transonic. There are therefore experimental rigs that operate in compressible flow regimes but are still included in the "low speed" category, such as the linear cascade of Azad et al. (2000b), which has an exit Mach number of 0.59, or the *Axial Flow Turbine Research Facility* (AFTRF) used in Dey and Camci (2001), which has an exit Mach number of 0.24.

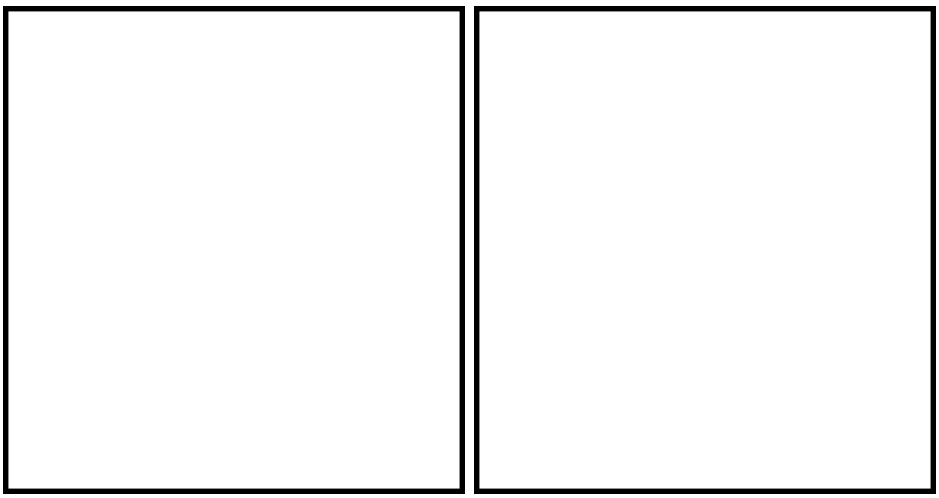

(a) Flat tip (Reproduced from Azad et al. (2000b))

(b) Double squealer tip (Reproduced from Azad et al. (2000a))

Figure 2.3: Heat transfer coefficient distributions on flat and double squealer tips (NB: Scales are different)

also to measure flat tip heat transfer coefficient distributions. Their results, shown in figure 2.3a, show a large area of low heat transfer in the forward part of the blade, dubbed the "sweet spot" by Bunker et al. (2000), with much higher heat transfer coefficients further towards the trailing edge. As tip clearance is increased, the heat transfer coefficients in the sweet spot are seen to decrease still further and the high heat transfer coefficients are elevated. Numerical simulations of these experiments by Ameri and Bunker (2000) and Yang et al. (2002a) showed that the separation of the over-tip leakage flow over the sharp pressure side edge and the associated reattachment on to the blade tip surface was a major contributing factor to the very high heat transfer coefficients seen close to the pressure side edge. The footprint of the separation bubble is not itself visible in the experimental data as the separation bubble is short; however, the extremely large scale of the linear cascade used in the study of Palafox (2006) and Palafox et al. (2012), which had a blade chord of 1 m, enabled an unprecedented spatial resolution of the data and the line of peak heat transfer can clearly be seen to be separated from the pressure side edge.

The heat transfer distribution to a flat blade tip at low speed has been measured experimentally and simulated numerically many times, with each result exhibiting the same key features observed in the first studies of Bunker and Bailey (2000) and Azad et al. (2000b). However, the recent studies of Wheeler et al. (2011a), O'Dowd (2010) and Zhang et al. (2011b) have uncovered fundamental discrepancies in the thermal behaviour of a flat tip at subsonic and transonic speeds, which cast doubt on the findings of these studies run at low speed. These differences are discussed in detail in section 2.6.

2.2.2 Control of over-tip leakage flow and heat transfer

Some attempts have been made to improve the performance of flat blade tips. One technique that has been applied several times by various researchers is that of leaning the blade tip in the circumferential direction to reduce near-tip aerodynamic loading and hence curtail the pressure difference that drives the over-tip leakage flow. Kingcombe and Steeden (1991) performed a computational design study and subsequently evaluated the resultant design in a cold flow, rotating turbine rig. The blade tip was leant by 47° away from the blade pressure side to minimise the pressure difference across the tip. The near-tip efficiency was significantly improved by the new design, but no overall improvement in turbine efficiency was measured, as this improvement was offset by worse performance closer to the hub. Staubach et al. (1996), as reported in Harvey (2004), also tested turbine blades with leant tips. The best geometry gave a 40% reduction in tip gap efficiency exchange rate, showing significant desensitisation of the blade tip to changes in tip clearance. It should be noted, however, that although blade tip lean has been shown to be an effective way of off-loading the tip region aerodynamically, it poses significant problems from a mechanical perspective.

Dey and Camci (2000), Rao and Camci (2004a), Rao and Camci (2004b) and Rao and Camci (2004c) investigated the possibility of improving sealing in the tip clearance by injecting air from a series of trenched cooling holes in the blade tip

surface. Using a rotating turbine rig at tip clearances of 0.72% and 1.4% blade span, they demonstrated that the pressure loss associated with the over-tip leakage vortex could be substantially reduced by the application of cooling air.

Behr et al. (2007) and Mischo et al. (2007) considered a similar idea, but with cooling air delivered through discrete holes located in the stationary over-tip casing rather than the rotating blade tip. Through a joint computational and experimental programme using a rotating turbine rig, a 0.55% increase in stage efficiency was achieved. The over-tip leakage mass flow rate was reduced by approximately 11% by the use of casing ejection and the size of both the over-tip leakage and the passage vortices were reduced. As the cooling air was introduced from a stationary component, the flow over the blade tip was inherently unsteady and a fluctuation in over-tip leakage mass flow rate with a magnitude of 1.4% was predicted.

Van Ness et al. (2006) and Van Ness et al. (2008) made a novel attempt at reducing heat transfer to flat blade tips. Instead of trying to minimise the over-tip leakage mass flow rate, they chose to eliminate the separation bubble at the pressure side edge, thereby also suppressing the associated reattachment. By using a plasma actuator embedded in the blade tip, shown in figure 2.4, the flow over the blade tip was intentionally accelerated to produce a wall jet over the blade tip surface. This both prevented the formation of the separation bubble on the blade tip and pushed the over-tip leakage vortex further into the passage away from the blade. The aerodynamic loss was also reduced, with a decrease in strength of the over-tip leakage vortex.

2.3 Double squealer tips

Squealer tips are flat blade tips with one or more thin rims that extend radially outwards from the flat surface, with the sealing of over-tip leakage flow performed between the squealer rim and the over-tip casing. They are lighter than flat blade tips and have the additional benefit that the risk of catastrophic failure in the event

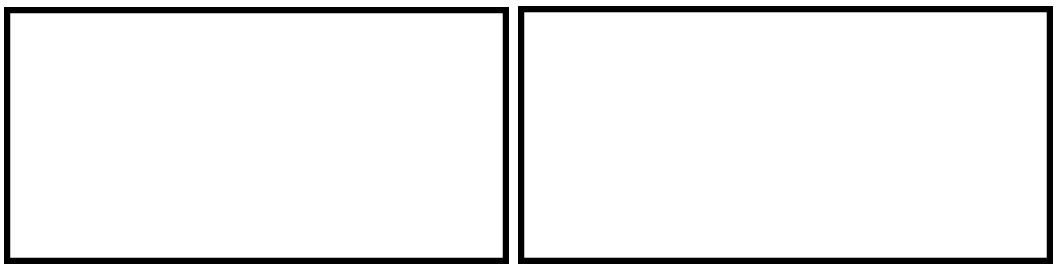

(a) Schematic of plasma actuator (b) Plasma actuator mounted in test blade

Figure 2.4: Plasma actuator active flow control device
(Reproduced from Van Ness et al. (2008))

of a tip rub is reduced. A wide range of different squealer tip variants have been tested; figure 2.5 provides some idea of the breadth of the spectrum of squealer tip geometries that have been tried by various researchers. However, one consistent theme that pervades the research into squealer tips is the general conclusion that the double squealer tip geometry provides the best overall aero-thermal performance. In the interests of brevity and relevance, only research into double squealer tip designs will be discussed in this section. For the interested reader, studies that have considered alternative squealer tip designs include Bunker and Bailey (2000), Ameri (2001), Acharya et al. (2003), Camci et al. (2003), Kwak et al. (2003), Saxena and Ekkad (2004), Saxena et al. (2004), Nasir (2004), Nasir et al. (2004b), Newton (2005), Newton et al. (2006), Palafox (2006), Yang et al. (2006), Kavurmacioglu et al. (2007a), Kavurmacioglu et al. (2007b), Krishnababu et al. (2007b), Krishnababu et al. (2007a), Hofer and Arts (2009), El-Ghandour et al. (2010b) and Palafox et al. (2012).

Research into double squealer tips has generally focused on heat transfer characteristics, with only a few studies specifically examining aerodynamic properties. Ameri et al. (1998) conducted computational simulations of double squealer tips with cavity depths of 2% and 3% blade axial chord at a tip gap of 1% blade axial chord, comparing the results to simulations run with a flat blade tip. The over-tip leakage mass flow rate was found to be reduced by 10% and 14% for the 2% and 3% squealer tips, respectively, caused by an increase in blockage in the over-tip region due to the

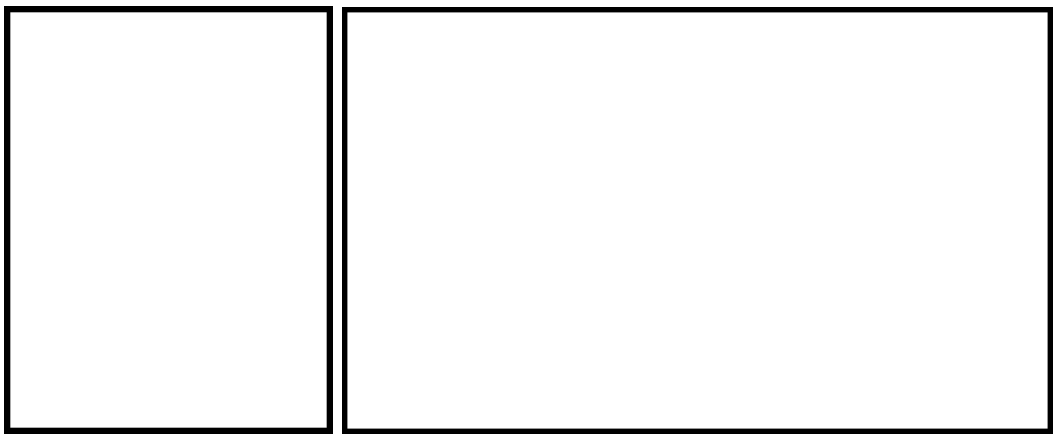

(a) Reproduced from Bunker and Bailey (2000)

(b) Reproduced from Kwak et al. (2003)

(c) Reproduced from Saxena et al. (2004)

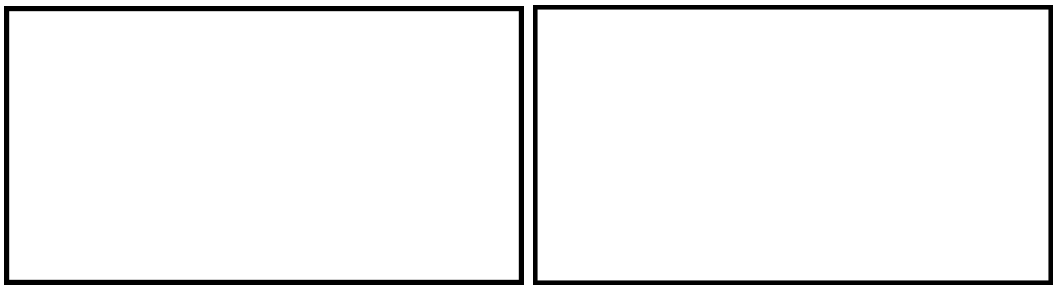

(d) Reproduced from Nasir et al. (2004b)

(e) Reproduced from El-Ghandour et al. (2010b)

Figure 2.5: Examples of squealer tip variants investigated in the open literature

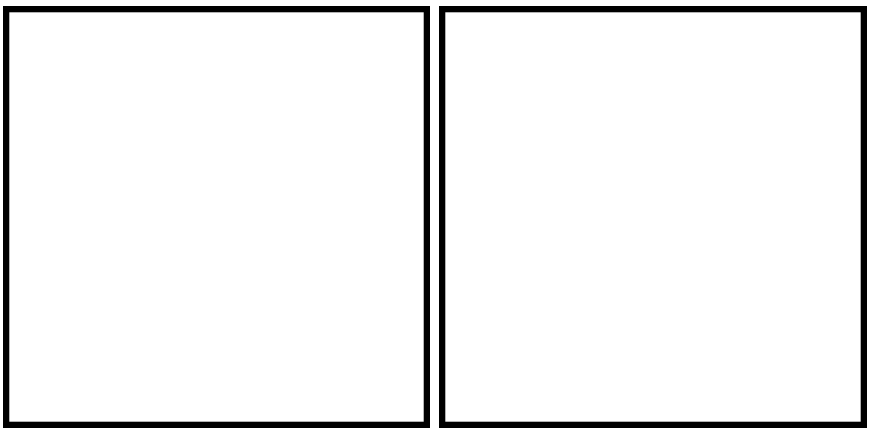

(a) Flat tip (b) Double squealer tip

Figure 2.6: Mid-gap over-tip leakage flow velocity
(Reproduced from Yang et al. (2002b))
(NB: Scales are different)

vortex structure set up within the cavity. Separation vortices were formed against the inner squealer rim along both the pressure and suction sides, the latter being driven by the separation of flow entering from near the leading edge. However, despite the reduction in over-tip leakage flow, the predicted row efficiency for both double squealer tip cases increased from 91.3% to just 91.4%.

Yang et al. (2002b) simulated the experimental setup of Azad et al. (2000a), testing a double squealer tip with a cavity depth of 3.77% blade span at tip gaps of 1%, 1.5% and 2.5% blade span. A significant reduction in over-tip leakage flow velocity was seen with the double squealer tip compared to a flat tip geometry, shown for the 1.5% blade span tip gap in figure 2.6, with flow velocities in the mid-chord region reduced by a factor of 1.5–2. Over-tip leakage mass flow rate was also reduced, particularly at the smaller tip clearances, and the over-tip leakage vortex was found to be substantially weakened by the double squealer tip. The reduction in over-tip leakage flow velocity was also observed by Newton (2005), who conducted experimental tests using a linear cascade that were supported by computational simulations.

The recent study of Wheeler et al. (2011b) used computational simulations of a transonic linear cascade to compare the aerodynamic performance of a double squealer tip with a cavity depth of 9% blade chord against a flat tip. The tip clearance was held constant at 3% blade chord. The double squealer tip was found to reduce aerodynamic losses by approximately 10% due to a reduction in over-tip leakage mass flow rate of 15%–20%.

The experimental study of Azad et al. (2000a) measured heat transfer coefficients on a double squealer tip with a cavity depth of 3.77% blade span in a linear cascade at three tip gaps of 1%, 1.5% and 2.5% blade span. Comparing their measurements to the equivalent cases for a flat tip reported in Azad et al. (2000b), significantly lower heat transfer coefficients were seen over the majority of the cavity floor than in the equivalent location on a flat blade tip. Both sets of data are shown in figure 2.3. A hot spot was observed in the centre of the cavity, starting close to the leading edge, which increased in size with tip gap; this is caused by the impingement of over-tip leakage flow. Very high heat transfer coefficients were measured on the squealer rims themselves.

Since this study, heat transfer to double squealer tips have been measured experimentally and simulated numerically several times by various researchers, for instance Acharya et al. (2003) and Mischo et al. (2008). These various studies have largely produced similar maps of heat transfer coefficient and drawn similar conclusions to those of Azad et al. (2000a). Some differences have been noted for different blade and cavity geometries, however. The oil dot flow visualisation performed by Key and Arts (2006) shown in figure 2.7b implies a single, wide vortex occupies the majority of the blade tip cavity, matching the computational flow visualisation of Yang et al. (2002b). However, the oil dot flow visualisation performed by Papa et al. (2003), shown later in figure 2.11a, suggests that an additional recirculation is trapped close to the squealer rim on the pressure side and forward section of the suction side. This matches the flow structure found by Mischo et al. (2008), also shown later in figure 2.9a. The

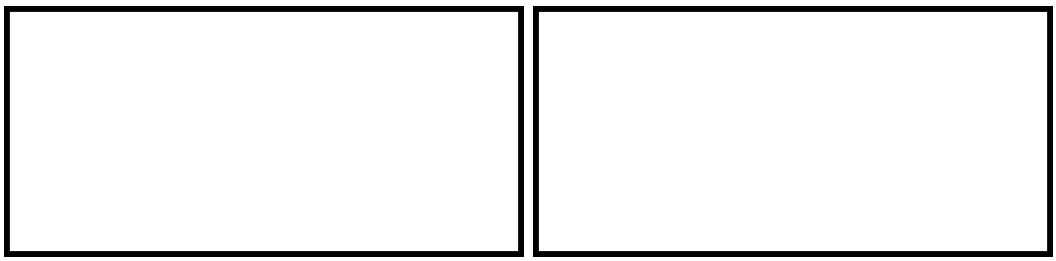

(a) Flat tip (b) Double squealer tip

Figure 2.7: Oil dot tip flow visualisation
(Reproduced from Key and Arts (2006))

heat transfer coefficient distributions for the two cavity vortex structures are similar, however.

Bunker and Bailey (2001) examined the effect of cavity depth on heat transfer. Maintaining the tip clearance constant at 2% span, double squealer tips with cavity depths of 1%, 1.75%, 2.5% and 3% blade span were tested in a linear cascade. Only heat transfer to the cavity floor was measured. It was found that increasing cavity depth reduced heat transfer coefficient for the entire range of values studied. Examining the average Nusselt number at different axial chord locations for all of the cavity depths, the authors also noted a nearly linear trend between cavity floor Nusselt number and the depth-to-width ratio of the cavity, with deeper cavities producing lower heat transfer. Park et al. (2010) tested a double squealer blade at a tip clearance of 2% axial chord in a linear cascade using the mass transfer analogy with a napthalene sublimation technique. They too observed a significant drop in heat/mass transfer on the cavity floor as the cavity depth was increased from 3% to 9% axial chord. However, as cavity depth was increased, the heat/mass transfer to the squealer rims increased significantly, a problem exacerbated by the increase in the rim surface area. This increase in thermal load to the squealer rims ultimately limits the maximum depth of a blade tip cavity.

2.3.1 Double squealer tip variants

Bunker and Bailey (2001) examined the effect of blade tip geometry degradation on the performance of a double squealer tip. Using a two-passage linear cascade at a tip clearance of 2.03 mm (2% blade span), they tested a convential double squealer tip with a cavity depth of 2.54 mm (1.25× tip gap), measuring the heat transfer to the tip with a thin-foil heater and thermochromic liquid crystals. Having identified plausible regions of oxidation damage, part of the pressure side rim (the extent of which can be seen in figure 2.8a) was then reduced in height to 1.02 mm to simulate such damage to the blade tip; a section of the suction side rim was also subsequently reduced to the same height. The heat transfer coefficients to the cavity floor were actually reduced by the partial loss of the pressure side rim. This was believed to be due to the elimination of flow separation and reattachment near the pressure side edge, while the sealing of the tip gap was still adequately performed by the suction side rim alone. However, simultaneously reducing the rim height on both sides provided a low loss flow path for the over-tip leakage flow, resulting in significantly increased heat transfer. The large augmentation in heat transfer coefficient continued aft of the region of material loss, indicating that the change in flow structure continued to affect the cavity downstream.

El-Ghandour et al. (2010a) tested half-width cavity tips numerically, with the cavity running either from the pressure side squealer rim to the camber line (with a flat tip between the camber line and the suction side), or with the cavity between the camber line and the suction side. Both half-width cavity tip geometries increased both over-tip leakage mass flow rate and aerodynamic loss significantly compared with a conventional double squealer tip, but still performed better than a flat tip.

Prakash et al. (2006) and Cherry et al. (2004) conducted a numerical study to investigate improvements to a double squealer tip by making small changes to the pressure side rim. Recessing the rim slightly to introduce a tip shelf, they created a small recirculation beside the outer pressure side rim surface that would trap any

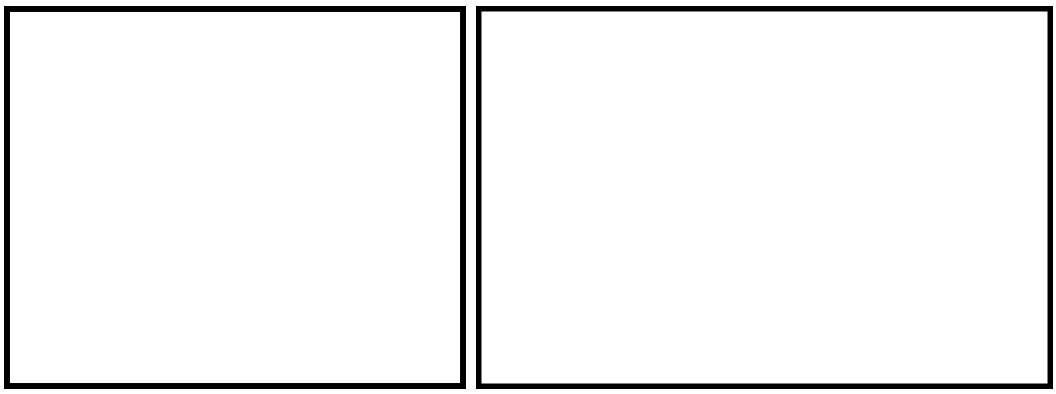

(a) Regions of squealer rim reduction (b) Averaged heat transfer coefficients

Figure 2.8: Effect of squealer rim damage on heat transfer
(Reproduced from Bunker and Bailey (2001))

cooling air bled out in that region. In doing so, the pressure gradient across the tip was increased slightly (due to the decreased width between the squealer rims), resulting in an increase in over-tip leakage mass flow rate and a decrease in efficiency. By inclining the recessed rim towards the incoming over-tip leakage flow, the pressure gradient was restored while the separation over the rim itself was enhanced, resulting in a net reduction in over-tip leakage mass flow rate and an improvement in row efficiency of 0.1%–0.2% compared to the baseline case. The important recirculation in front of the rim was unaffected by the inclination of the rim.

Mischo et al. (2008) and Mischo et al. (2009) sought to eliminate the hot spot in the forward part of a double squealer tip caused by over-tip leakage flow impinging on to the cavity floor. Through numerical simulations of a baseline double squealer geometry, the authors identified several key structures present in the cavity flow that left their imprint upon the heat transfer profile within the cavity, shown in figure 2.9a. By reprofiling the cavity shape, the cavity flow structure was dramatically changed, eliminating some of the recirculations and controlling blade tip heat transfer very effectively; a reduction of 7% in heat load was seen for the reprofiled double squealer tip compared with the baseline double squealer tip. A small reduction in over-tip leakage mass flow rate was also seen. Experimental validation of the CFD predictions

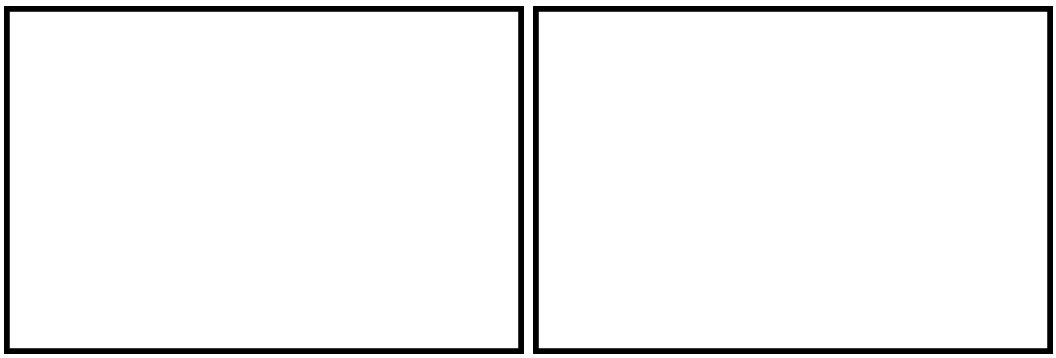

(a) Baseline double squealer tip (b) Reprofiled double squealer tip

Figure 2.9: Flow structure and Nusselt number for a reprofiled double squealer tip (Reproduced from Mischo et al. (2008))

was successfully performed using a rotating turbine experimental rig and revealed an improvement of 0.3% in aerodynamic efficiency compared with a baseline flat tip.

2.3.2 Film cooling

With the good overall performance and actual in-service use of double squealer tips, a number of studies have examined the application of film cooling to this blade tip geometry. Kwak and Han (2003b) measured heat transfer coefficient and film cooling effectiveness for a film-cooled double squealer tip in a linear cascade at tip gaps of 1%, 1.5% and 2.5% blade span. Coolant ejection was from holes along the camber line on the cavity floor, from holes exiting on the near-tip pressure side and from both sets of holes simultaneously. The same configuration was tested in the same experimental rig, albeit with slightly fewer cooling holes, by Ahn et al. (2005) using a pressure-sensitive paint technique instead of thermochromic liquid crystals. Both studies found that increasing blowing ratio from 0.5 to 2.0 increased film cooling effectiveness but also increased heat transfer coefficients. The cooling air ejected from the camber line was drawn towards the pressure side, resulting in an accumulation of coolant and hence better cooling of the half of the cavity closer to the pressure side than the half closer to the suction side. Adiabatic cooling effectiveness over the

blade tip was generally low, however, with values no higher than 0.3 anywhere on the tip surface even at the highest blowing ratio. These experiments were subsequently simulated computationally by Yang et al. (2004).

Mhetras et al. (2005) continued the study of Ahn et al. (2005) by angling the camber line holes towards the inner pressure side rim surface. This placed the exit of the cooling holes much closer to the pressure side rim than previously. The holes ejecting from the pressure side were also replaced with laid-back, fan shaped holes. The study was aided by complementary CFD simulations. Unsurprisingly, relatively high cooling effectiveness was seen on the inner surface of the pressure side squealer rim, although this still remained below 0.3. Little spreading of coolant was observed on the outer pressure side rim, where peaks in effectiveness of nearly 0.5 were seen downstream of cooling holes with troughs of 0.15 in between. Mhetras et al. (2008) used a very similar arrangement, but this time inclining the camber line holes along the camber line towards the trailing edge instead of towards the pressure side. A second set of similarly inclined holes was added between the camber line and the suction side wall of the cavity. The squealer tip was also cut back, removing the pressure side rim near the trailing edge to open the cavity at the rear. A marginally increased cooling effectiveness was observed on the cavity floor, particularly towards the trailing edge. Wang et al. (2010) tested another cut back double squealer tip with film cooling ejection from camber line holes on the cavity floor and from the near-tip pressure surface. Velocity measurements made using PIV in a linear cascade together with flow visualisation from CFD simulations showed that the cooling flow could affect the sealing characteristics of the squealer tip.

Nasir et al. (2007) used transient infra-red thermography to measure film cooling effectiveness and heat transfer coefficients for double squealer tips at a tip gap of 1.0% blade span in a linear cascade. Cooling air was ejected from holes along the camber line on the cavity floor and on the pressure surface. Again, film effectiveness was seen to increase as blowing ratio was increased from 1.0 to 2.0, but decreased when blowing

ratio was increased to 3.0. An earlier study using the same facility by Nasir et al. (2004a) examined a similar geometry, but at a tip clearance of 0.5% blade span. A cooling effectiveness of zero (or nearly zero) was recorded at all points in the blade cavity at all three blowing ratios, which was attributed to a much higher local blowing ratio than the nominal values due to the low flow velocities within the cavity. Similar geometries were investigated computationally by Acharya et al. (2002) and Acharya et al. (2010).

Park et al. (2010) used a napthalene sublimation technique and applied the mass transfer analogy to investigate double squealer tips with film cooling. Heat/mass transfer measurements were taken on the cavity floor and the inner surfaces of the squealer rims. The blowing ratio was 1.5 and the tip gap was 1% blade axial chord. Three cooling configurations were examined; one with cooling holes ejecting along the camber line, one with the cooling holes offset towards the pressure side and one with the cooling holes offset towards the suction side. Enhanced heat/mass transfer coefficients were observed in the vicinity of the cooling hole exits. Very low film cooling effectiveness was seen within the cavity, with localised peak values of approximately 0.3 for the case with camber line ejection. Film cooling effectiveness was generally below 0.1.

The computational study of Yang et al. (2009) had film cooling from holes located on the cavity floor along the camber line, along the line of flow reattachment and along a line between the pressure surface and the reattachment line, with each line of holes simulated separately. At a blowing ratio of 1.0, much higher film cooling effectiveness was predicted than in other studies, with peak values of over 0.6 recorded. The best film coverage was provided by the cooling configuration of holes along the reattachment line, with most of the cooling air caught by the recirculation in the pressure side of the cavity and drawn back towards the pressure side rim. Cooling air for the configuration of holes closer to the pressure side was trapped in the same region and likewise showed good cooling effectiveness locally, especially on the inner

surface of the pressure side rim. The line of reattachment, being a line of diverging flow on the cavity floor, pushed cooling air in opposite directions, so almost no cooling effectiveness was seen on the suction side half of the cavity in those two configurations. Ejecting cooling air over the pressure side edge rather than the tip had a relatively small impact on cooling effectiveness within the cavity, although values of 0.3 were seen in places. This is in contrast to the findings of Ahn et al. (2005) who found that pressure side film cooling ejection alone had virtually no impact on cavity cooling.

Uniquely, Hofer et al. (2009) conducted aerodynamic measurements with a film-cooled double squealer tip blade in a transonic linear cascade environment. Cooling air was ejected from holes on the near-tip pressure side as well as along the camber line of the blade tip. The experimental campaign was supported by CFD simulations validated with the rig data. The use of cooling air was found to increase the over-tip flow resistance, but had only a marginal impact on overall aerodynamic loss, slightly decreasing loss at the lower exit isentropic Mach number of 0.8 but slightly increasing loss at the higher exit isentropic Mach number of 1.1.

Krishnababu et al. (2010) performed a computational study on a double squealer tip blade for an industrial gas turbine in rotating, engine-realistic conditions. However, the blade used is very thin and has a low turning angle, and the cooling holes span the entire width of the cavity, so this study is not very applicable to modern, high work, high turning blades that are typically found in large, modern turbofan engines. Zhou and Hodson (2009) and Zhou and Hodson (2011) present an aerodynamic study of a film-cooled double squealer blade, with both CFD simulations and experimental data from a low speed linear cascade. The blade profile is also very thin and has a turning angle of just 43°, so its usefulness in the context of HP turbine blades for civil aero-engines is extremely limited.

Gao et al. (2007) investigated the effect of inlet flow angle using the same experimental setup as Ahn et al. (2005), with the same cooling configuration as Mhetras et al. (2008), including the cut back squealer rim. Tests were conducted at incidence

angles of $-5°$, $0°$and $+5°$, with blowing ratios of 0.5, 1.0, 1.5 and 2.0. At all blowing ratios, it was found that changing the incidence angle altered the jet direction from each cooling hole slightly, distorting the map of cooling effectiveness. However, the overall levels of cooling effectiveness were largely unaltered.

Recognising the difficulty in assessing the performance of cooling designs for turbine blade tips, Vogel et al. (2009) attempted to develop a model for predicting overall metal effectiveness in film cooled blade tips. They performed CFD simulations and conjugate heat transfer analyses of a turbine blade with a double squealer tip and internal cooling geometry. Cooling holes were located in a line on the cavity floor and also on the near-tip pressure surface. These computational simulations were performed at tip clearances of 1.4%, 2.2% and 4.1% blade span. Through their simulations, the authors concluded that a reduction in tip gap of 1% resulted in a reduction in blade tip heat transfer of approximately 15% and a 1.5% reduction in blade tip temperature.

2.4 Winglet tips

Another concept for sealing over-tip leakage flow is that of the winglet. Winglets are small blade tip extensions in the circumferential direction that are designed to reduce the pressure gradient across the blade tip, either by off-loading the blade tip or merely by extending the distance over which the pressure drop occurs. Yaras and Sjolander (1991) investigated the possibility of using winglets to reduce the aerodynamic losses caused by over-tip leakage flow. In a low speed linear cascade, they tested a pressure side winglet tip, a suction side winglet tip and a double sided winglet tip against a flat blade tip at two tip gaps of 2.4% and 3.7% blade chord, with downstream aerodynamic loss measurements conducted by the traverse of a seven-hole probe. All three winglet tips were found to reduce the over-tip leakage loss by approximately 10%, with the double sided winglet giving the largest reduction and the pressure side winglet the smallest. The suction side winglet appeared to act by reducing the driving

pressure difference across the tip, whereas the pressure side winglet increased the size of separation bubble over the edge, thereby reducing the effective throat size (the area of the vena contracta produced by the flow separation).

Dey and Camci (2001) tested a pressure side winglet tip and two suction side winglet tips against a baseline flat tip in a rotating rig at a tip gap of 1.14% blade span. Aerodynamic pressure loss measurements conducted at 30% blade chord downstream of the rotor exit showed that both of the suction side winglet tips displaced the over-tip leakage vortex further away from the blade, an observation that had also been made by Yaras and Sjolander (1991), but did not affect the entrance of fluid into the tip gap. The suction side winglets were therefore not found to be effective at desensitising the blade tip and did not reduce either the over-tip leakage mass flow rate or the aerodynamic pressure loss caused by over-tip leakage flow. The pressure side winglet, by contrast, showed a significant reduction in the strength of the over-tip leakage vortex. This was attributed to increased viscous losses at the entrance to the tip gap reducing the over-tip leakage mass flow rate.

Shavalikul and Camci (2008) continued the work of Dey and Camci (2001) numerically, focusing on the pressure side winglet. Four different winglet tips were tested against a baseline flat tip (pictured in figure 2.10) in a linear cascade geometry with a moving endwall. All four winglet tips showed a marked improvement over the baseline case, with the best case (the "modified bump no. 2" tip) reducing over-tip leakage mass flow rate by 11.6% and aerodynamic over-tip leakage loss of 10%. The over-tip leakage vortex was seen to reduce in both size and strength as the over-tip leakage mass flow rate was reduced.

Kusterer et al. (2007) added small pressure side winglets to the second and third stage blades of an industrial gas turbine. Through computational simulations, they predicted a reduction of 7.2% and 3.2% in over-tip leakage mass flow rate for the second and third stage blades, respectively, and a small overall increase in polytropic

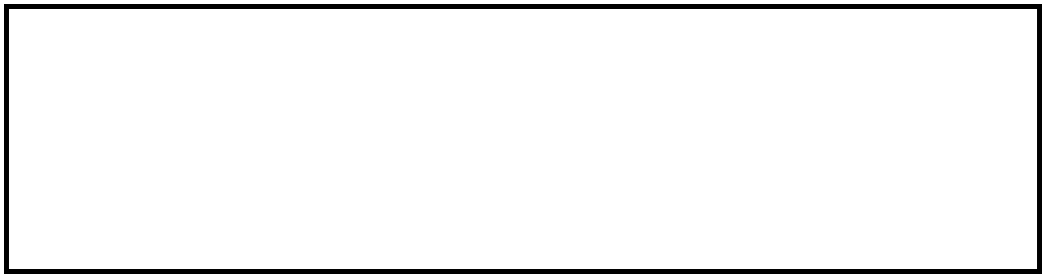

Figure 2.10: Winglet tip geometries tested by Shavalikul and Camci (2008) (Reproduced from Shavalikul and Camci (2008))

efficiency. The aerofoil shape is, however, very different to that of aero-engine HP turbine blades, being much thinner and with a much lower turning angle.

2.4.1 Winglet-squealer tips

An obvious development that could be made from winglet and squealer tips is to combine the two in some way. Saha et al. (2003) and Saha et al. (2006) examined two such hybrid tips; one with a pressure side extension attached to a double squealer rim and one with a pressure side winglet and a suction side squealer rim. These were tested numerically at a tip clearance of 1% blade span against a flat tip, a pressure side winglet tip, a double squealer tip and a suction side squealer tip. Comparing the pressure side winglet tip with the flat tip, similar aerodynamic observations were made to the previous studies, with a predicted 12% reduction in aerodynamic loss in the case of the winglet. There was also a small reduction in over-tip leakage flow velocity, particularly in the 30% to 70% blade chord region. This was evident in the predicted blade tip heat transfer coefficient distributions, which were noticably reduced in this region. The overall average heat transfer coefficient was reduced by 7%, while local reductions of as much as 30% were seen at some locations.

By contrast, the benefits realised by the addition of pressure side winglets to squealer tips were found to be small. The inclusion of an extension on the pressure side rim of the double squealer tip made no difference to the blade tip heat transfer

coefficient magnitudes. The over-tip leakage vortex was very slightly weakened with the winglet, but remained unchanged in size, producing a modest 5% reduction in pressure loss compared to the standard double squealer tip. In the case of the suction side squealer tip, the addition of a pressure side winglet once again caused no significant change in either heat transfer, with a reduction of just 1.4% in average heat transfer coefficient, or aerodynamic performance, with a 2.5% reduction in loss.

The combination of a suction side squealer rim and a pressure side winglet was also tested by Papa et al. (2003), who compared it to a baseline double squealer tip. This was performed experimentally in a linear cascade using the mass transfer analogy with a napthalene sublimation technique. Measurements were taken at tip clearances of 0.6%, 1.1%, 2.0% and 3.6% blade chord. With the double squealer tip, the peak heat/mass transfer occurred near the leading edge in the forward part of the cavity, whereas the winglet-squealer tip exhibited a patch of low heat/mass transfer in this region. The winglet-squealer tip also showed two stripes of very high heat/mass transfer at each tip gap, located in the trailing edge region at the largest tip gap but moving forwards with decreasing tip gap. Mass transfer coefficients for the double squealer tip were found to be consistently greater than for the winglet-squealer tip, although they were comparable at the smallest tip gap.

An oil dot flow visualisation technique was used with both blade tip geometries at the 3.6% blade chord tip gap, shown in figure 2.11. The flow visualisation revealed very different flow structures over the blade tip. For the double squealer tip, there is a line of impingement in the forward part of the cavity (line 2) with a large vortex formed below it that occupies the majority of the cavity. With the winglet-squealer tip, there is a very large region in the leading edge with virtually no dot movement, suggesting low flow velocities in this region. Two lines of flow impingement are evident (lines 4 and 5), whose formation is attributed to the discontinuity of the winglet on the pressure side which does not start smoothly at the leading edge.

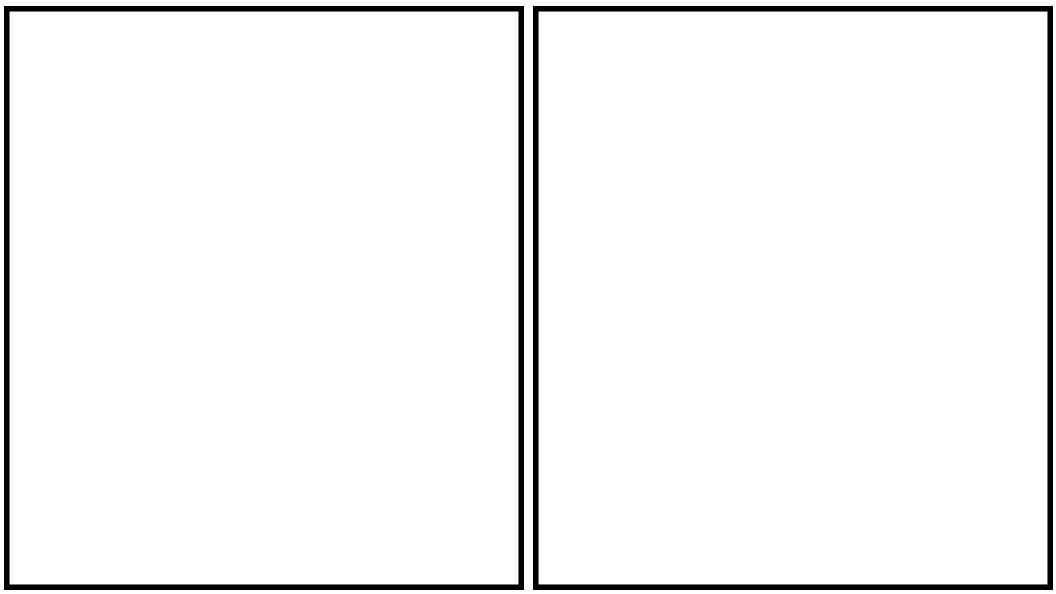

(a) Double squealer tip (b) Winglet-squealer tip

Figure 2.11: Oil dot tip flow visualisation
(Reproduced from Papa et al. (2003))

Schabowski and Hodson (2007) took a slightly different approach to combining winglet and squealer tips. Instead of attaching winglet-like extensions to squealer rims, they attached squealer rims to winglets, thereby forming a tip that more closely resembled a wide double squealer tip, although with a gutter open at both the leading and trailing edges. The authors tested two winglet-squealer hybrid tips against a pure winglet, a double squealer tip, a suction side squealer tip and a flat tip in a low speed linear cascade. Supporting CFD simulations of the experimental cascade were also performed. The winglet-squealer hybrid with thin squealer-like rims produced the best aerodynamic performance, with both a reduced overall loss and an improved tip gap efficiency exchange rate (by 22% compared with the flat tip). Three major loss reduction techniques were identified; the use of winglets to decrease the driving pressure difference across the tip gap, the use of two rims to split the total loading into two parts, effectively doubling the number of blade tips, and the use of sufficiently thin squealer rims to avoid flow reattachment on the rims themselves.

The study was continued by Schabowski et al. (2010) numerically, using a combination of CFD and FEA simulations to perform an optimisation on the winglet-squealer tip design, focusing solely on suction side extensions. 12 optimisation parameters were used, controlling the height of both squealer rims, the length of the frontal opening to the cavity and the remaining ten determining the size and shape of the winglet. The objective function used was a combination of maximising aerodynamic efficiency and minimising the maximum radial deflection of the winglet tip under centrifugal load. The optimised winglet design significantly reduced the driving pressure difference across the tip gap, with a large extension by the crown of the blade that tapered back down towards the rear of the blade. The front of the cavity was closed. A 27% reduction in over-tip leakage mass flow rate was achieved compared with the baseline flat tip, with a reduction in flow under-turning in the near-tip region as well. The tip gap efficiency exchange rate was decreased by 37% relative to the flat tip. Two further variants of the optimised winglet tip were tested; one with the pressure side squealer rim inclined by 30° in a similar way to the inclined squealer tip of Prakash et al. (2006) and the other with a portion of the squealer rim removed from the suction side near the leading edge to open the front of the cavity. The inclined squealer rim was found to produce a small improvement in aerodynamic performance, but the open cavity caused a marginal decrease in efficiency.

2.4.2 Developed winglets

The winglet studies discussed so far have all used very idealised blade tip extensions. A few pieces of research have been performed with more realistic winglet geometries which are more representative of turbine blade tips that could endure the high stresses and temperatures found in the harsh environment of a real engine. Harvey and Ramsden (2001) presented a computational test of a winglet tip designed for the MT2 aerofoil, using a flat blade tip for comparison. Rather than having the very thin squealer rims of Schabowski and Hodson (2007), the sections either side of the

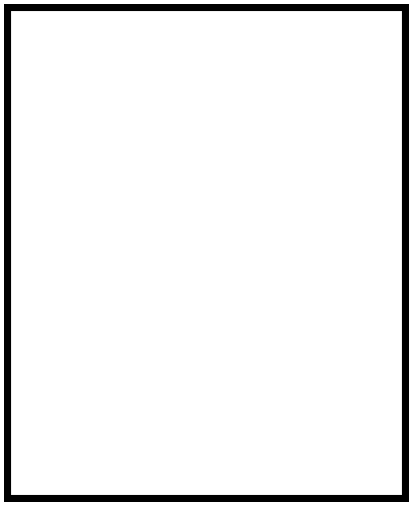

Figure 2.12: ANTLE winglet tip size comparison
(Reproduced from Harvey and Ramsden (2001))

gutter are almost aerofoil shaped. The gutter itself is open at the leading edge and trailing edge, allowing relatively cool air from near the casing to flow over the blade tip. The reduction in size compared with a typical turbine shroud is shown in figure 2.12, although the authors do caution that the extent of the suction side trailing edge may not be mechanically feasible and a cut back version might be needed. The winglet tip improved the stage efficiency for the turbine by 1.2% and also reduced the tip-gap efficiency exchange rate by 31%, from 1.85 to 1.28. The winglet tip was found to perform more of its sealing over the pressure side, with more of the pressure drop across the pressure side winglet than the suction side winglet. Much of the over-tip leakage flow that entered the tip gap rolled into a vortex between the two halves and remained confined in the gutter, exiting the tip region at the trailing edge. Some of the over-tip leakage flow did continue over the suction side and join the over-tip leakage vortex, however. Capturing over-tip leakage flow in the gutter allowed this flow to be turned, and near-tip under-turning was significantly reduced by the winglet.

Following the impressive performance of that early study, Harvey et al. (2006) presented a similar design for the ANTLE technology demonstrator engine. Initial CFD simulations suggested that the winglet tip design would improve tip gap efficiency

exchange rate by just 7% over the flat tip, despite also showing a significant degree of unloading in the tip region. However, experimental testing in a cold-flow rotating turbine rig showed that the ANTLE winglet tip actually performed as well as a shrouded turbine blade tip with two fins, achieving a 45% reduction in exchange rate. Despite this vast improvement over a flat tip, the winglet tip still fell far short of typical in-service shrouded blade tips (with two fins and two fences), with almost double the exchange rate and a 1% deficit in stage efficiency at a typical real tip clearance.

For the successor to ANTLE, EFE, another winglet design was produced. This was tested both experimentally and computationally by O'Dowd (2010) and O'Dowd et al. (2011b). Aerodynamic loss measurements were taken by the downstream traverse of a three-hole probe and a single-hole probe and heat transfer measurements by a transient infra-red thermographic technique in the transonic *High Speed Linear Cascade* (HSLC) facility at the Osney Thermofluids Laboratory, Oxford University. Supporting CFD simulations of the cascade using the Rolls-Royce HYDRA solver were also performed to enable a more thorough investigation of the flowfield. The uncooled winglet tip showed a marginally increased level of aerodynamic loss compared to the baseline flat tip at both the 0.9% and 1.3% blade chord tip gaps, although the mixed-out aerodynamic loss for the winglet tip decreased with the addition of film cooling flow. High Nusselt number distributions were recorded over the blade tip surface, as shown in figure 2.13, with a 35% increase in area-averaged Nusselt number for the uncooled winglet tip compared with the baseline flat tip case. This figure rose to 41% with the addition of film cooling. Moreover, the wetted surface area of the winglet tip is 2.4 times larger than the flat tip, so the uncooled winglet received an overall thermal load 3.2 times greater.

The same winglet tip was tested by Zhou et al. (2011a) in a low speed linear cascade with supporting low speed CFD. This study noted that the film-cooled winglet tip suffers a higher heat load than the uncooled flat tip, agreeing with the study of

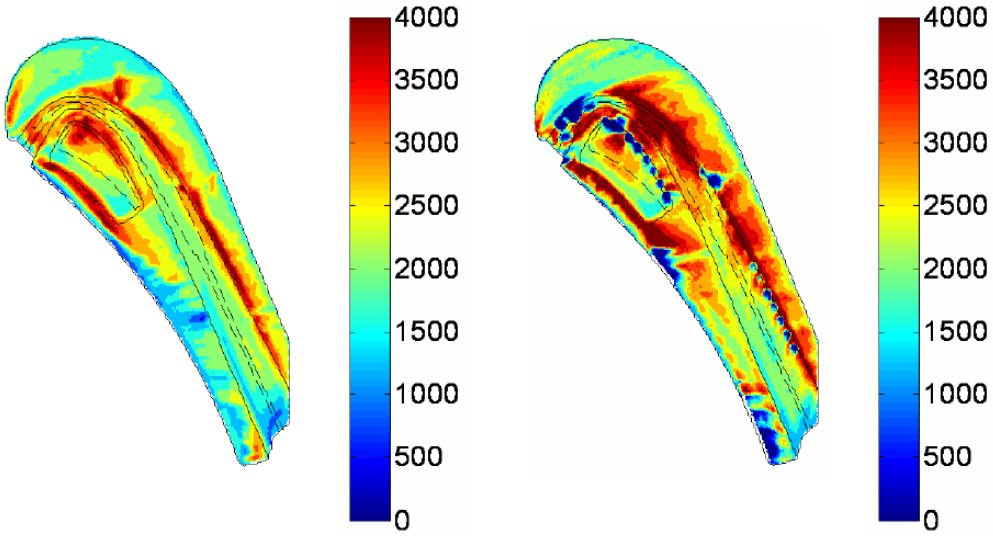

(a) No film cooling (b) With film cooling

Figure 2.13: Winglet tip Nusselt number distributions
(Reproduced from O'Dowd (2010))

O'Dowd (2010). However, Zhou et al. (2011a) showed a 6% increase in over-tip leakage aerodynamic loss with the addition of coolant, contradicting the findings of the earlier study. It should be noted that this study is performed at low speed, whereas the study of O'Dowd (2010) was transonic and hence much more representative of a real engine environment; the differences between low speed and high speed experiments are very significant and are discussed in more detail in section 2.6.

2.5 Effects of relative endwall motion and rotation

As so much of the research into over-tip leakage flow is performed in cascade environments, it is important that the inherent limitations of such data are understood. Both linear and annular cascades typically have two major simplifications; that there is no relative motion between the blade tip and the over-tip casing and that the experiments are performed in a stationary frame of reference, which will therefore omit the effects of centrifugal and Coriolis accelerations.

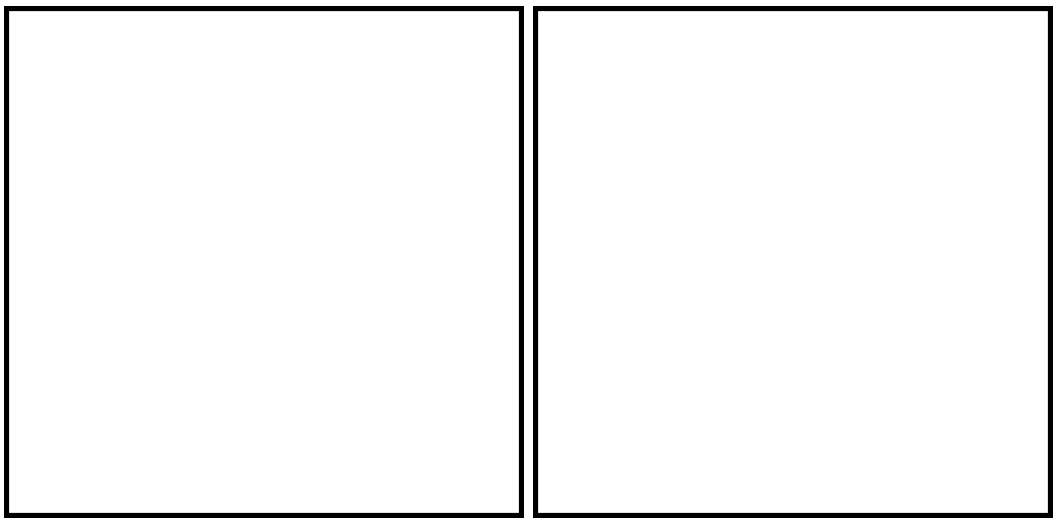

Figure 2.14: Over-tip leakage flow model with relative endwall motion (Reproduced from Mayle and Metzger (1982))

The first study to investigate the effect of relative blade-to-casing movement was also the first to investigate blade tip heat transfer. Mayle and Metzger (1982) used an idealised, 2D model of a flat blade tip that incorporated a rotating disc that was used to represent the endwall (figure 2.14). A concave test surface represented the "flat" blade tip, in order to maintain a constant tip gap to the disc. Using a foil resistance heater on the test surface and measuring the gas and surface temperatures by way of thermocouples, the average Nusselt number to the test surface was measured. It was found that the Nusselt number was invariant with disc rotational speed, and hence the authors concluded that the heat transfer to the blade tip was unaffected by the relative endwall motion.

Graham (1986) used a moving rubber belt to represent the endwall in a water analogy linear cascade run at a Reynolds number of 1×10^5 based on blade chord. As the belt speed was increased, the over-tip leakage flow velocities were reduced and it was found that at small tip clearances of 0.6% and 1.2% blade chord, it was possible to prevent the over-tip leakage entirely by increasing the belt speed to the engine-equivalent speed or higher. The strength of the over-tip leakage vortex was

also reduced by increasing the endwall speed, disappearing entirely at sufficiently high belt speeds.

Yaras and Sjolander (1991), Yaras and Sjolander (1992a) and Yaras et al. (1992) also used a motorised rubber belt to represent the endwall in a low speed linear cascade run at a Reynolds number of 1.4×10^5 based on blade chord. Running the cascade at a large tip clearance of 3.8% blade chord, the large scale of the rig (with a blade chord of 250 mm) allowed them to insert a three-hole probe into the tip gap itself to measure the velocity profile of the over-tip leakage flow over 80% of the tip gap. They sought to identify the physical mechanism through which relative endwall motion reduced the over-tip leakage mass flow rate, having identified two broad possibilites: shear-dominated and pressure-dominated (illustrated schematically in figure 2.15). It was found that the separation bubble length was reduced with increasing belt speed and, in line with the findings of other studies, total over-tip leakage mass flow rate was reduced by 50% with the belt travelling at engine-equivalent speed. Engine-equivalent speed is the belt speed that allows the real engine flow coefficient (the ratio of flow axial velocity to blade velocity) to be matched. The shear layer caused by the endwall motion was found to be thin, almost entirely confined within the 20% of the tip gap closest to the belt for which no data could be taken due to the probe thickness. The authors therefore concluded that the decrease in mass flux was primarily effected by a pressure mechanism rather than through shear. It is, however, noteworthy that this study was performed at a very large tip clearance (the design tip gap is stated as 2% blade chord, which is already large by modern standards) and the importance of shear can reasonably be expected to increase as tip clearances are narrowed, increasing the mean velocity gradient within the tip gap.

Tallman and Lakshminarayana (2001b) performed a CFD study on another low speed linear cascade, using the experimental data of Bindon and Morphis (1992) to validate the simulation predictions. With a much smaller tip gap than Yaras and Sjolander (1992a), at 1.0% blade chord, a significant change in flow angle was seen

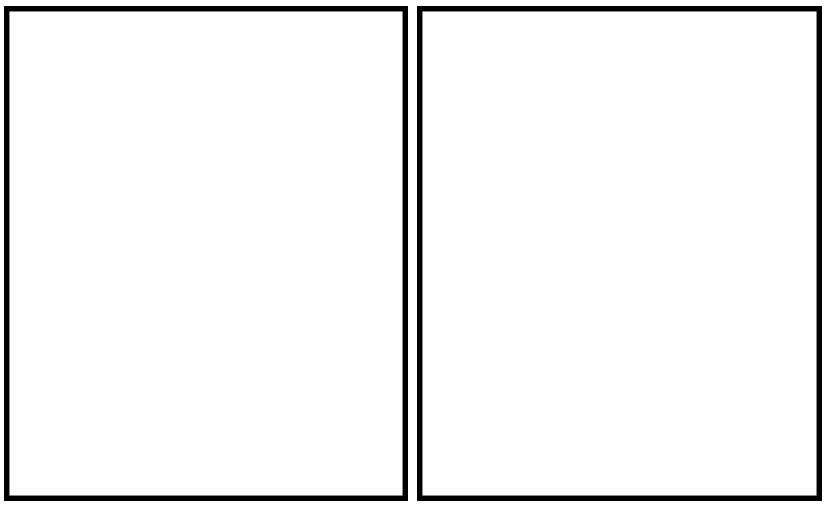

(a) Shear-dominated (b) Pressure-dominated

Figure 2.15: Possible interaction mechanisms for relative endwall motion (Reproduced from Yaras and Sjolander (1992a))

mid-gap, indicative of a greater influence of shear than had been observed in the older study. This study also observed a reduction of 31% in over-tip leakage mass flow rate and a large reduction in the size of the over-tip leakage vortex. A shift in the over-tip leakage mass flow rate distribution was measured, with a greater proportion occurring towards the aft of the blade.

Srinivasan and Goldstein (2003) returned to the question of the effect of endwall motion on blade tip heat transfer. Using a linear cascade with a neoprene belt, the authors applied the mass transfer analogy by a napthalene sublimation technique at tip clearances of 0.6%, 0.86%, 1.72%, 3.45% and 6.9% blade chord. At the smallest tip clearance, small but measurable reductions of up to 9% in local heat/mass transfer were seen at certain locations on the tip surface near mid-chord. This appears to contradict the finding of Mayle and Metzger (1982), but the reduction observed was both small and localised. The local reduction in heat/mass transfer disappeared at the 0.86% tip gap and no differences in the mass transfer distributions due to endwall motion were observed at any of the larger tip gaps.

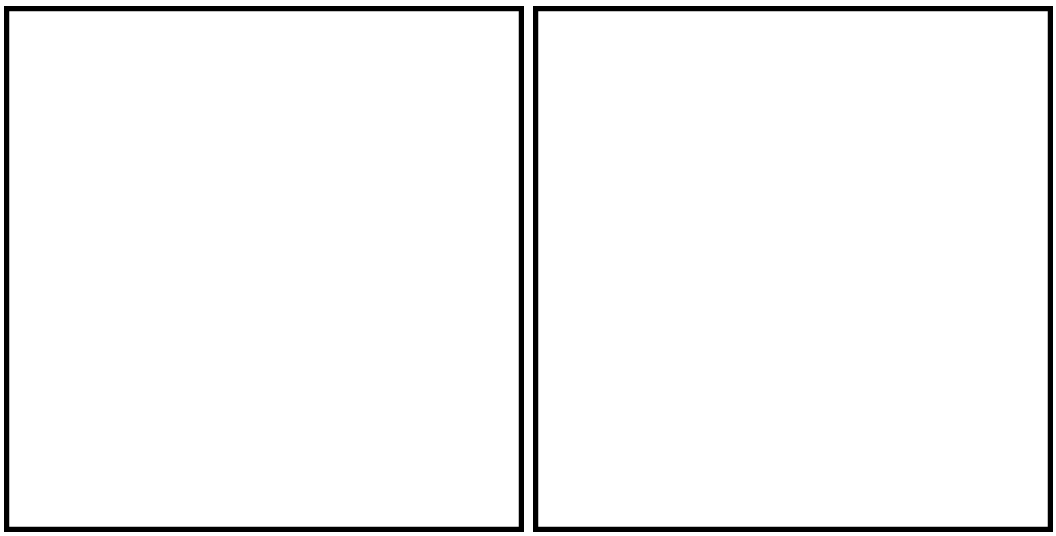

(a) Stationary endwall (b) Moving endwall

Figure 2.16: Effect of endwall motion on secondary flow
(Reproduced from Palafox et al. (2008))

A very large scale, low speed linear cascade was used by Palafox (2006), Palafox et al. (2008) and Palafox et al. (2012), run at tip clearances of 1%, 1.5% and 3% blade chord. A *Particle Image Velocimetry* (PIV) system allowed mean flow fields to be measured directly and heat transfer measurements were also taken by infra-red thermography. A reduction in height of the separation bubble (along with the commensurate reduction in length) was observed with the introduction of relative endwall motion, along with a reduction in over-tip leakage flow speed in the forward part of the blade that did not occur towards the trailing edge, mirroring the change in mass flow rate distribution observed by Tallman and Lakshminarayana (2001b). The average blade tip Nusselt number was also reduced by up to 13%. On the suction side of the tip gap, the over-tip leakage vortex and passage vortex were shifted closer to the blade suction side and a weak scraping vortex was also formed that was not present without relative endwall motion. These can be seen in figure 2.16. The formation of a scraping vortex had previously also been observed in the rotating turbine rig of Xiao et al. (2001) and McCarter et al. (2001).

The study of Krishnababu et al. (2007a) investigated the heat transfer to the blade tip by way of a numerical simulation of another low speed linear cascade. The tip clearance was constant at 1.6% blade chord, but three blade tip geometries were tested; a flat tip, a double squealer tip and a suction side squealer tip. In all three cases, the blade tip heat transfer was reduced with relative endwall motion, although the difference was found to be marginal for the suction side squealer tip. An increase in near-tip heat transfer was also noted, due to the over-tip leakage vortex being pressed up against the blade suction side surface.

O'Dowd et al. (2010) applied CFD simulations to test the effect of a moving endwall for a flat tip in a transonic linear cascade environment. A small reduction in aerodynamic loss was seen over the entire range of tip clearances tested (0.5%, 1.0% and 1.5% blade span). The over-tip leakage vortex was once again seen to be pushed towards the blade suction side and slightly reduced in size by the relative endwall movement, with these effects becoming more significant at smaller tip clearances. O'Dowd et al. (2011b) also tested the EFE winglet design in a similar way and noted a reduction in Nusselt number in the forward part of the blade tip when run with a moving endwall.

Fewer studies have focused on the effects of blade rotation than have investigated relative endwall motion. The early study of Dring and Joslyn (1981) conducted measurements in the blade-relative frame of a low speed rotating rig. Using an ammonia-Ozalid flow visualisation technique, they showed that the spanwise flow around the rotor blade (in particular, the strong radial migration towards the blade tip on the blade pressure surface) was significantly affected by rotation. Comparison of flow visualisations run at two tip gaps (shown in figure 2.17) showed that while over-tip leakage flow did affect the spanwise flow in the near-tip region, its influence did not extend far enough towards the hub to be the primary driving force. Yamamoto et al. (1994b) also conducted downstream pressure measurements in the rotating frame of a low speed rotating rig. They noted that the over-tip leakage vortex is confined to

Figure 2.17: Effect of tip gap on blade pressure surface flow migration (Reproduced from Dring and Joslyn (1981))

the region close to the near-tip casing by the interaction with the passage vortex and centrifugal forces when rotation is present.

Yang et al. (2006) examined the effect of rotation on heat transfer to flat tips and double squealer tips computationally. This study was performed at a single tip clearance of 1.5% blade span. Only a minor effect was found on blade tip heat transfer, although significant increases in heat transfer coefficient were seen on the over-tip casing with rotation. Zhang et al. (2009) presented a numerical study investigating the effect of rotation on a low speed, scaled up blade with film cooling. They considered three tip configurations; a flat tip with cooling holes ejecting directly from the tip surface, a flat tip with cooling holes ejecting into a trench and a double squealer tip with cooling holes ejecting from the cavity floor. In all three cases, the cooling effectiveness was seen to decrease with increasing rotational speed and heat transfer coefficients were augmented. Zhou et al. (2011b) performed a numerical study that examined the effect of endwall motion on the film-cooled EFE winglet. They observed

an increase in cooling effectiveness of 9% with relative endwall motion, together with a reduction in Nusselt number, the opposite of the trends seen by Zhang et al. (2009).

The only study to have attempted to separate out the effects of relative endwall motion and rotation is that of Yang et al. (2010). Simulations were performed with three sets of boundary conditions: (1) a rotating blade domain with stationary endwall (engine-representative case with both relative endwall motion and rotation), (2) a stationary blade domain and a rotating endwall (relative endwall motion but no rotation) and (3) a stationary blade domain and endwall (no relative endwall motion or rotation). These were conducted for a blade with a flat tip and a blade with a double squealer tip at a tip clearance of 1% blade span. The aerodynamic observations made for the case of the flat tip were similar to those seen in other studies: that relative endwall movement reduced over-tip leakage flow and biased the leakage distribution towards the aft portion of the blade tip. In the case of the double squealer tip, there was a slight change in the vortex structure seen within the cavity caused by the endwall motion. Rotation had no great effect on the tip gap flow field for either geometry. As can be seen in figure 2.18, the heat transfer coefficients over the blade tip surfaces were generally increased by the addition of relative endwall movement (change from Case 3 to Case 2), and slightly decreased by rotation (change from Case 2 to Case 1).

2.6 Low speed and high speed flows

One subject that has only gained attention recently is the difference in over-tip leakage flow between high speed, transonic flow conditions and that produced in low speed experimental rigs. As early as 1989, Moore et al. (1989) recognised the potential for the over-tip leakage flow to be supersonic and applied a hydraulic analogy between free surface flow and 2D compressible flow. The authors used a water table with an idealised tip gap to visualise the possible shock structures that could be formed in the tip gap region. At higher simulated Mach numbers, a complex shock structure formed,

(a) Case 1—Blade domain rotating, endwall stationary

(b) Case 2—Blade domain stationary, endwall rotating

(c) Case 3—Blade domain stationary, endwall stationary

Figure 2.18: Effect of rotation and endwall motion on heat transfer coefficient (Reproduced from Yang et al. (2010))

with oblique shocks interacting with multiple reflections, shown in figure 2.19. The hydraulic analogy was further developed by Moore and Elward (1993), who recognised that the shock-boundary layer interaction could cause a local enhancement of heat transfer.

However, the issue of compressibility effects and shock wave formation was largely forgotten, with almost all research being conducted in low speed environments. While there have been some high speed experimental rigs, such as that used by Key and Arts (2006), Hofer and Arts (2009) and Hofer et al. (2009), these have been the minority and the distinction between subsonic near-tip flow and transonic near-tip flow was not drawn until the study of Wheeler et al. (2011a). In this study, the HYDRA CFD code was used to simulate the transonic, one and a half stage *Oxford Rotor Facility* (ORF), which has a rotor exit relative Mach number of 0.98. The simulations were successfully validated against blade tip heat flux data from the ORF for the fully turbulent region

Figure 2.19: Water table shock structures in a simulated tip gap (Reproduced from Moore et al. (1989))

over the aft of the blade tip. Simulations were then performed with three blade profiles designed to give the same loading distribution and Reynolds number at exit Mach numbers of 0.96, 0.67 and 0.1. Both the blade and the over-tip casing were stationary in these simulations, so the simulations are representative of an annular cascade. All three cases were run with both the Spalart-Allmaras and the k-ϵ turbulence models, using wall functions in both cases. A large increase of 60% in blade tip heat flux was observed when decreasing the exit Mach number from 0.96 to 0.1. Even more significantly, there was an observed reversal of the heat flux distribution: at low Mach number, there was the familiar low heat transfer "sweet spot" at the front of the blade and very high heat fluxes further towards the trailing edge; the opposite trends were observed at high Mach numbers, with very low heat fluxes recorded in the thin trailing edge region, as can be seen in figure 2.20. This discrepancy was attributed to an increase in turbulent viscosity at low Mach number, with approximately double the turbulent viscosity ratio predicted in the lowest Mach number case compared to the highest Mach number case. At high Mach number, a striping was seen in the Nusselt number distributions with the stripes running approximately chordwise, caused by an oblique shock wave reflecting between the blade tip and casing surfaces. This caused the boundary layer to thicken and thin as it impinged on the blade tip and hence caused flow to decelerate and accelerate. A new model of leakage flow over a flat tip

Figure 2.20: Effect of Mach number on flat blade tip heat flux
(Reproduced from Wheeler et al. (2011a))

was therefore proposed to explain the flow structure seen in a transonic environment, shown in figure 2.21.

Interestingly, the same blade tip heat flux data from the ORF that were used to validate the study of Wheeler et al. (2011a) were presented in Thorpe et al. (2005), but the changes in the heat transfer distribution due to transonic effects were not noticed. Indeed, the authors of the earlier study noted that the time-mean heat flux data, recorded by thin-film heat flux gauges on the blade tip camber line, were broadly consistent with low speed cascade data from other studies. From the simulations of the later study, it is now understood that the slight depression in heat flux measured in the forward part of the blade was not due to the "sweet spot" of heat transfer that is present in low speed environments, but rather due to the over-tip flow in the region being transitional rather than fully turbulent. The experimental data towards the rear of the blade falls into line with that predicted by Wheeler et al. (2011a) and is consistent with the transonic over-tip flow presented there.

Figure 2.21: Supersonic over-tip leakage flow structure
(Reproduced from Wheeler et al. (2011a))

The study published in Zhang et al. (2011a), O'Dowd (2010), Zhang et al. (2011b) and O'Dowd et al. (2010) provided the first direct experimental verification of this critical effect. Experimental heat transfer data were collected in the HSLC transonic linear cascade. By reducing the inlet total pressure to the test section, the HSLC could be run at a much lower Mach number than the design condition, albeit also with a reduced Reynolds number. Heat transfer measurements with a flat blade tip were taken at two conditions, one at low speed (with an exit Mach number of 0.27 and an exit Reynolds number of 0.35×10^6), and one at high speed (with an exit Mach number of 1.02 and an exit Reynolds number of 1.27×10^6). In order to allow a direct comparison between the data, the low speed Nusselt number data were scaled to match the Reynolds number of the high speed case using the Nusselt number correlation for a flat plate with a laminar boundary layer:

$$\mathrm{Nu}_x = 0.332\,\mathrm{Re}_x^{1/2}\,\mathrm{Pr}^{1/3} \tag{2.2}$$

The same qualitative reversal in the heat transfer distribution observed in Wheeler et al. (2011a) is clearly seen in the results from O'Dowd (2010), shown as Nusselt

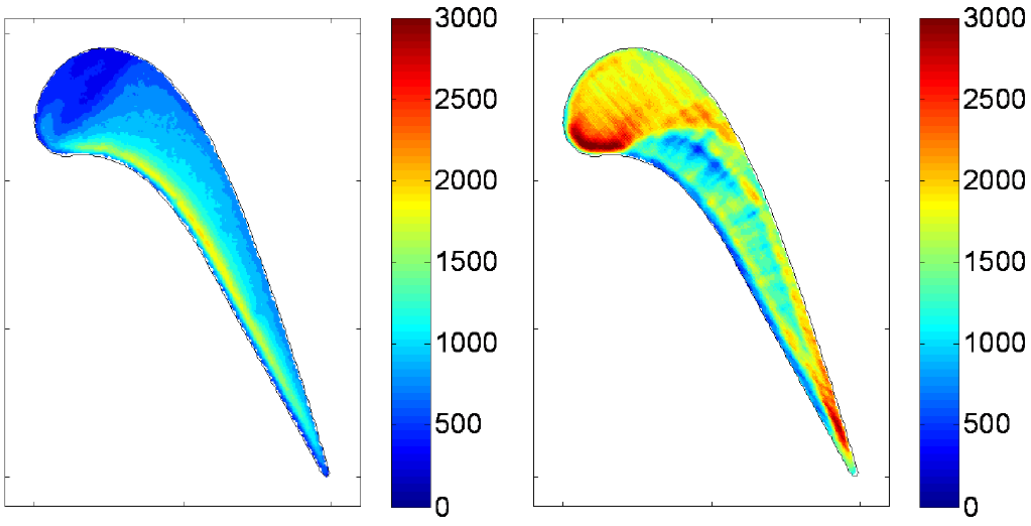

(a) M = 0.27, Re = 0.35×10^6
(Data scaled to account for difference in Re)

(b) M = 1.02, Re = 1.27×10^6

Figure 2.22: Effect of Mach number on flat blade tip Nusselt number (Reproduced from O'Dowd (2010))

number in figure 2.22. The characteristic striping is also clearly evident in the high Mach number experimental data. A numerical study was performed to support the experimental program, which was validated extremely well by the experimental heat flux data from the HSLC. The cause of the chordwise striping in heat flux was confirmed to be the shock structure that formed in the tip gap, as can be seen in figure 2.23.

Supersonic over-tip leakage flow was predicted by the numerical simulations over approximately half of the blade tip in both the flat tip and winglet tip cases. The flow is therefore choked in this region, suggesting that the common approach of attempting to minimise the over-tip leakage mass flow rate by minimising the over-tip pressure gradient when designing over-tip leakage control strategies is flawed. This finding casts the general assumption of over-tip leakage flow being primarily controlled by the driving pressure difference into doubt. The implications of high speed over-tip flow have further been addressed and developed by Wheeler et al. (2011b) and Zhang and He (2011), which seek to improve the understanding of the aerodynamic losses

Figure 2.23: Heat flux striping with virtual Schlieren
(Reproduced from Zhang et al. (2011b))

linked to transonic over-tip leakage flow. Shyam and Ameri (2011) presented an early computational attempt at optimisation of a flat blade tip with supersonic over-tip leakage flow to minimise heat transfer by contouring the blade tip. Their best geometry gave a 2.8% improvement in aerodynamic loss relative to a baseline flat tip geometry, while simultaneously reducing average blade tip heat flux by 37.3%. This geometry, however, included a bypass hole joining the blade tip surface to the blade pressure side that would likely not be usable in a real engine, due to the heat transfer to the inside of the hole. The same geometry without the bypass hole reduced the average blade tip heat flux by 39.4% relative to the baseline, but increased aerodynamic loss by 2.9%.

2.7 Chapter summary

In this chapter, an overview of the previous research into unshrouded blade tip heat transfer and aerodynamics that has been published in the open literature has been presented, with a focus on work that is particularly relevant to the present study.

From this survey, it is clear that although much research into the field has already been performed, there are still some significant areas that are, relatively speaking, poorly understood. The complexity of the flow field around unshrouded blade tips, combined with the difficulty of taking measurements in the rotating frame of reference and in transonic flow regimes, has meant that much of the research conducted to date has been performed in simplified environments. Recent studies have shown that this approach is becoming increasingly difficult to defend and that the significance of high speed compressibility effects and the effects of rotation is such that they cannot easily be ignored. The importance of high veracity computational simulations to support experimental programmes is also clearly visible in the literature; such simulations allow for a much more detailed understanding of the underlying physics by providing flow visualisation and full surface data that may not be possible to measure experimentally. However, in order to maximise the usefulness of the simulations, computational methods require careful validation against appropriate experimental data to ensure that the numerical predictions can be trusted.

Another conclusion that must be drawn from the review presented in this chapter is that while flat tip and double squealer tip geometries have been studied widely and thoroughly, the same cannot be said of the promising new blade tip geometry of the winglet tip. There is no generally agreed consensus on the effectiveness of winglet tips from either an aerodynamic or a thermal point of view and precious little understanding of how best to combine winglet and squealer tips. It is on this point that the majority of the present study focuses and a novel design approach to create a hybrid winglet-squealer tip is introduced. The new design is tested and refined using 3D, engine-representative CFD simulations that are capable of capturing flow features that are not seen and cannot be reproduced in low speed cascade environments. These numerical predictions are supported by experimental measurements taken in a transonic linear cascade where full surface heat transfer data and detailed downstream aerodynamic loss maps are measured in a fully compressible flow regime.

Chapter 3

Large Scale, Low Speed CFD Simulations

3.1 Introduction

This chapter covers CFD validation work carried out using results from an experimental study performed by Palafox (2006) in the *Oxford Super-Scale Cascade*. The primary aim was to evaluate the ability of the commercial solver FLUENT 6.3 to predict the heat transfer coefficient distribution over a representative model of a flat turbine blade tip. The tip gap is constant at 1.5% of blade chord. The relative suitability of the various turbulence models available within FLUENT 6.3 for this particular environment is established and the capability of FLUENT 6.3 to predict the effect on the heat transfer distribution of relative endwall movement is examined. The CFD simulations for this section are run using hexahedral, multiblock meshes generated in ICEM CFD 11. While recent research has suggested that studies into blade tip heat transfer and over-tip leakage performed in low speed, incompressible flow environments may miss certain important features, there is a significant amount of understanding that can still potentially be gained from this research. The work presented in this chapter will aid the computational simulation of such low speed tests, enabling high quality CFD simulations that complement the experimental campaigns and allow the most to be gained from these simplified experiments. Results from this part of the present study have been published in Tang et al. (2010).

Blade chord	1.0 m
Axial chord	0.808 m
Blade span	1.0 m
Blade pitch	0.853 m
Blade turning angle	111.5°
Tip gap	15 mm
(Cascade exit) Reynolds number	4.0×10^5
Freestream inlet velocity	$3.5\,\mathrm{m\,s^{-1}}$
Cascade exit velocity	$7\,\mathrm{m\,s^{-1}}$

Table 3.1: Experimental rig parameters

3.2 Experimental setup

A cursory summary of the experimental details are included here for completeness. Full details of the experiments performed and the results available can be found in Palafox (2006), Palafox et al. (2008) and Palafox et al. (2012). The experimental work used for comparison in this section was performed by Dr Pepe Palafox.

Experiments were performed using a large scale, three passage linear cascade with a blade chord of 1 m, as illustrated in figure 3.1. The aerofoil section used is a low speed version of the RT-27a blade profile (Gregory-Smith and Cleak, 1992), which is representative of a high turning, high work HP turbine blade found in modern civil turbofan aero-engines. This aerofoil geometry is a redesigned blade profile that mimics the blade pressure loading of the (high speed) RT-27a profile at a much lower Mach number. A motorised rubber belt was used to represent the endwall and this could be turned on or off to investigate the effect of relative endwall motion. Tip gaps of 10 mm, 15 mm and 30 mm, representing 1%, 1.5% and 3.0% blade chord, respectively, were tested, although only the results from the 15 mm (1.5% blade chord) tip gap are used for the present study. Key parameters of the experimental rig are detailed in table 3.1.

A *Particle Image Velocimetry* system was used to establish time-averaged velocity vector fields on several planes which were orientated approximately parallel and perpendicular to the primary mainstream flow direction. Heat transfer coefficient

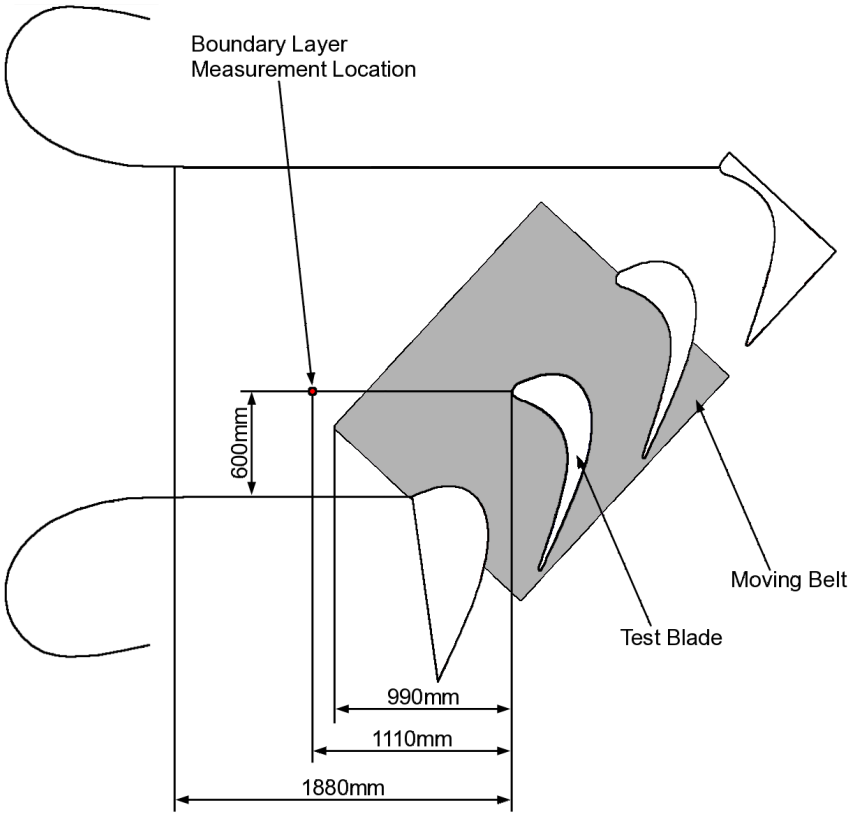

Figure 3.1: Schematic of the experimental test section (Oxford Super-Scale Cascade) (Reproduced from Palafox (2006))

distributions on the (flat) blade tip surface were also measured, using a transient infra-red thermographic technique made possible by a thin copper heater incorporated into the surface of the test blade tip. Heat transfer by radiation, free convection within the hollow blade and lateral conduction in the tip substrate were corrected for. The typical overall uncertainty in the experimental measurement of heat transfer coefficient was estimated to be 5.14%.

3.3 Computational details

The meshes used in this section were purely hexahedral, multiblock meshes generated using ICEM CFD 11 and these were solved using the commercial CFD package FLUENT 6.3. The time-steady formulation of the pressure based solver with the

SIMPLE algorithm for pressure-velocity coupling was used in all cases. A single 64-bit, four-core workstation with 2 Gb of RAM was used for the meshing process, CFD solution and post-processing.

3.3.1 Computational domain and meshing strategy

Two meshing schemes were used in the CFD study. In the first instance, the entire cascade was simulated in an effort to achieve the best possible physical veracity, as shown in figure 3.2a. In doing so, no assumptions regarding periodicity were needed as any artefacts of the experimental rig would be reproduced in the CFD simulations. The computational inlet plane was chosen to be the experimental measurement location of the inlet boundary layer, 1100 mm upstream of the test blade leading edge, as shown in figure 3.1. Note that this was not an axial plane, but rather was chosen to match the experimentally measured boundary layer profile, thus allowing it to be applied as an inlet boundary condition. The computational outlet plane was placed a short distance downstream of the blade trailing edge, where constant static pressure and low velocity gradients were expected.

A fully structured, purely hexahedral, multiblock meshing strategy was adopted; the simplicity of the geometry made this approach viable. It should be noted that FLUENT 6.3 is an unstructured solver and therefore discards the connectivity data from the mesh, negating some of the benefit of using a structured mesh. However, other benefits (in particular, the alignment of grid lines with the predominant flow direction) are still realised. The use of a structured meshing approach allowed fine control over the placement of grid lines and it was decided to align these with the mainstream flow direction, which should aid convergence. Special care was taken to ensure good mesh quality around the aerofoils, minimising cell skewness and avoiding sudden cell size transitions, which required the addition of both inner and outer O-grids, as shown in figure 3.3. The simpler block structure without inner O-grids that has been used in other studies, for example Basson and Lakshminarayana (1995), could not be adopted

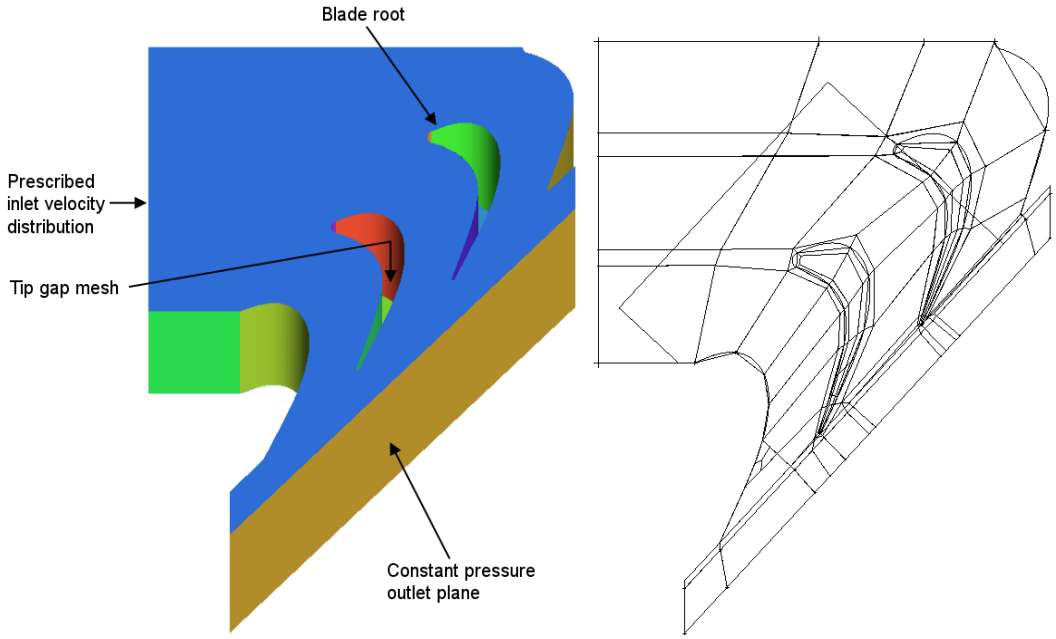

(a) Computational domain (b) Block structure

Figure 3.2: Computational domain and block structure for full cascade simulations

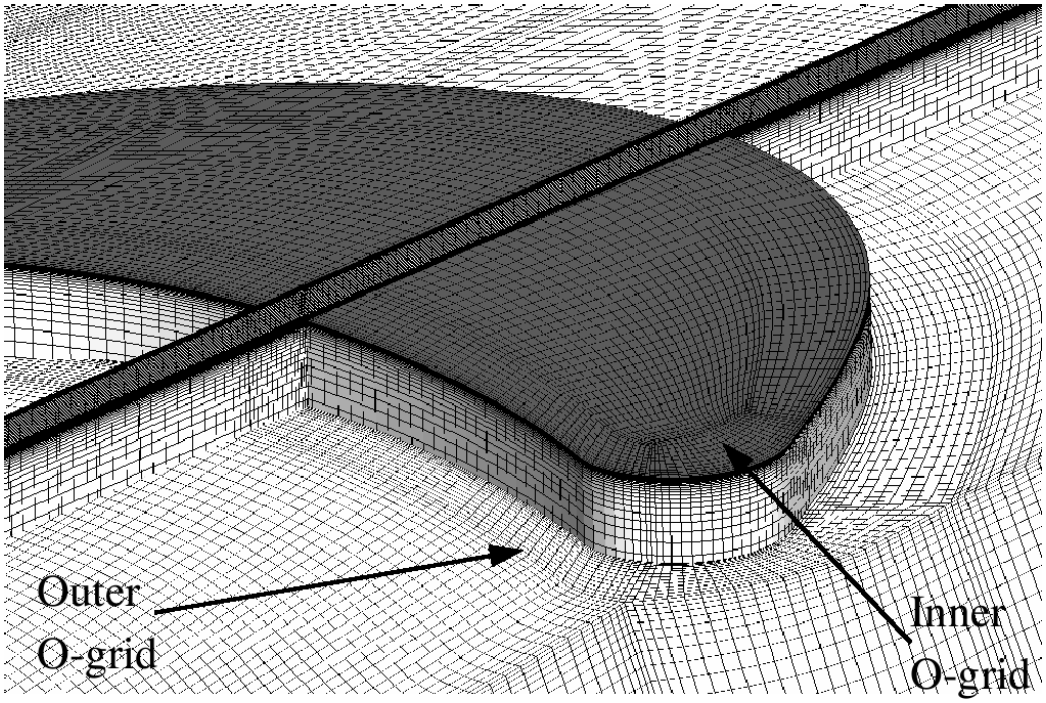

Figure 3.3: Detail of the mesh in the vicinity of the tip gap

due to the thickness of the aerofoil section. A relatively complex block structure was required in the vicinity of the blade trailing edges to ensure appropriate mesh refinement where this was needed; this can be seen in figure 3.2b where the blocking structure in a spanwise plane which passes through the tip gap is shown. The solid lines represent user-defined boundaries between blocks. The precise location of these block boundaries is determined based on the knowledge of the expected flow field and the constraints of the physical geometry. This mesh comprised 5.5 million cells, with 22 nodes in the tip gap and a first cell height of 0.3 mm.

When this meshing scheme was used, however, the wall-adjacent cell y^+ distribution on the blade tip was found to range between 6 and 15. As heat transfer data were the objective of these simulations, a strategy to resolve the boundary layer fully had been adopted and for this wall-adjacent cell y^+ values below five, and preferably below one, were required. An attempt at refining the mesh was made, but insurmountable problems were encountered almost immediately. The large computational domain meant that any further refinement made to the already large mesh resulted in a grid that could not feasibly be solved given the available processing power. Moreover, due to a problem with the mesh generating software used and the complex block structure, it was found that the first cell height in the tip gap could not be reduced below 0.2 mm without severely distorted and partially inverted[1] cells being introduced into the mesh.

As a result of these problems, a second meshing strategy was adopted. The decision was taken to simulate a single blade and impose periodic boundary conditions, as shown in figure 3.4a, rather than to simulate the entire cascade as originally had been intended. Once again, a fully hexahedral mesh was used, which retained the majority of its block structure from the full cascade simulations. However, as only one passage was to be simulated (half of the passage on each side of the test blade), the block structure in the rear section of the cascade could be simplified greatly, as

[1] A partially inverted cell is one in which both positive and negative interior angles between adjacent faces are present. If all interior angles are negative, the cell is fully inverted and may be fixed simply by reversing the order of its vertices. Partial inversion of a cell cannot be eliminated by the reordering of its vertices, because of the cell topology.

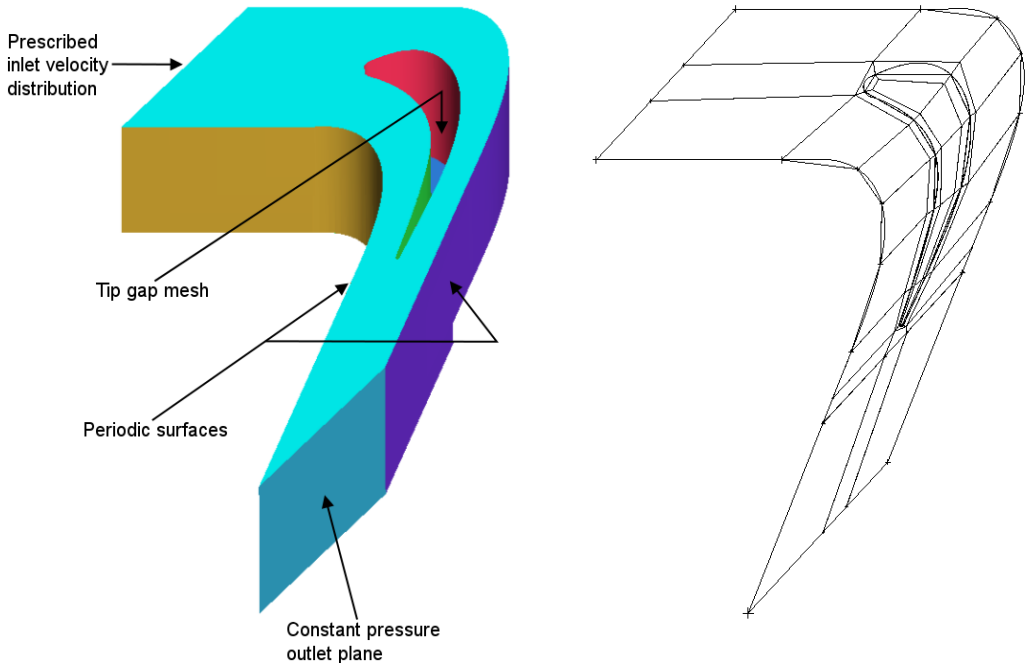

(a) Computational domain (b) Block structure

Figure 3.4: Computational domain and block structure for periodic simulations

can be seen in figure 3.4b. With the imposition of periodic boundary conditions, the inlet plane had to be changed to be parallel to the direction of periodicity. For these periodic simulations, the inlet boundary velocity profile was taken from the converged solution of a full cascade simulation rather than the experimental boundary layer measurements. The reduced cell count from the reduction of physical volume being simulated also allowed the outlet plane to be extended slightly further downstream to ensure that the blade tip region was not affected by the prescribed flow conditions at the computational exit.

3.3.2 Mesh sensitivity testing

One aim of this work was to establish minimum meshing requirements for flow and heat transfer predictions in the tip gap region. In order to achieve this, an investigation into mesh sensitivity was performed that went beyond simple global mesh refinement.

Four tip gap meshes were created using the periodic block structure. The *Coarse mesh* (figure 3.5d) was intended for testing the use of wall functions as the near-wall treatment and was tuned to give wall-adjacent cell y^+ values (as reported[2] by FLUENT 6.3) in the range 30 to 60 across the blade tip. The other meshes were intended to be used with an appropriate near-wall treatment that allows resolution of the boundary layer into the laminar sub-layer, and give wall-adjacent cell y^+ values of below two over the tip surface. y^+ is a non-dimensional measure of the distance normal to the wall, relative to the boundary layer thickness. Sizing the wall-adjacent cell to have a y^+ value below five ensures that the first node is placed within the viscous sub-layer of the boundary layer and that there will be a sufficient number of cells across the boundary layer thickness to allow it to be resolved directly, providing that an appropriate, low-Reynolds number turbulence model is used in the near-wall region. By contrast, if the wall-adjacent cell is expanded to have a y^+ value between 30 and 300, the first node will be located in the fully turbulent, log-law region of the boundary layer; this is the appropriate near-wall meshing approach for the use of wall functions.

The *Very fine mesh* has the thinnest wall-adjacent cells, which are sized to give a maximum wall-adjacent cell y^+ on the blade tip of approximately one. The *Fine mesh* keeps the maximum cell height within the tip gap approximately the same, but has a first cell thickness double that of the *Very fine mesh*. The comparison between simulations run using these two meshes therefore allows the effect of a change in wall-adjacent cell y^+ to be seen. The *Fine (adjusted) mesh* retains the first cell thickness of the *Fine mesh* but has a reduced expansion ratio, thereby reducing the maximum cell thickness within the tip gap. These four meshes are summarised in table 3.2 and illustrated in figure 3.5. The resulting y^+ distributions on the blade tips (run using the Spalart-Allmaras turbulence model) are shown in figure 3.6.

[2]These reported wall-adjacent cell y^+ values are not true y^+ values, as they are based on the (incorrect) computed velocity field. However, it is illustrative of the potential danger that could befall a CFD practitioner if appropriate checks are not made.

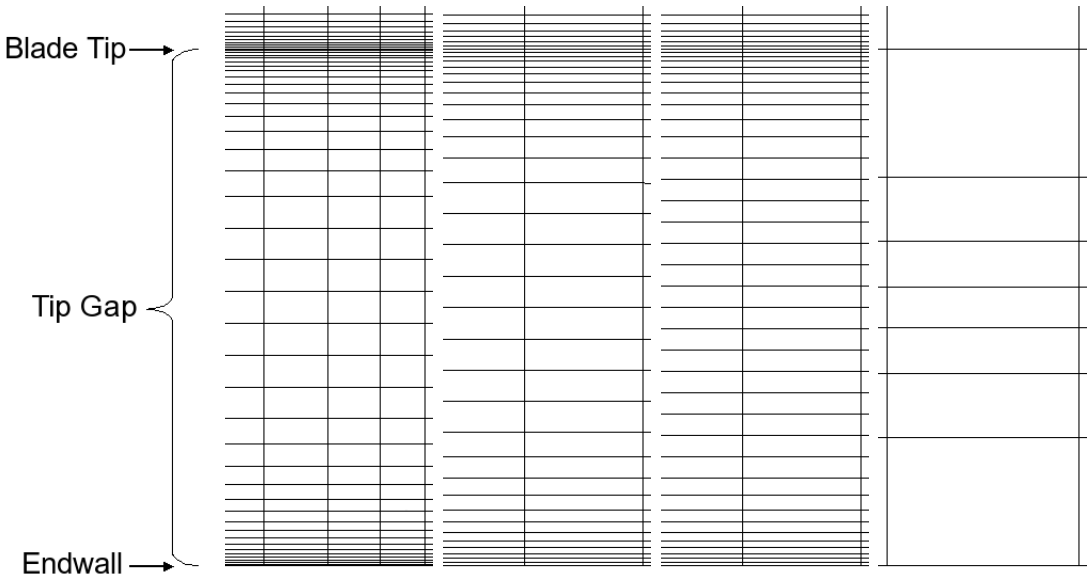

(a) Very fine mesh (b) Fine mesh (c) Fine (adjusted) mesh (d) Coarse mesh

Figure 3.5: Mesh refinement in the tip gap region

3.3.3 Solution and boundary conditions

The time-steady formulation of the pressure based, implicit solver was used, which is a cell-centred, finite volume, pressure-corrector algorithm. The SIMPLE algorithm was used for the pressure-velocity coupling. Second order discretisation was used for all variables alongside an incompressible-ideal-gas density formulation—meaning that density was allowed to vary with temperature but not pressure. Significant underrelaxation of the momentum variable was applied to achieve convergence reliably; an underrelaxation factor of 0.3 was found to give good results.

The blade tip surface had a constant heat flux of $50\,\mathrm{W\,m^{-2}}$ imposed to match the experimental condition and allow Nusselt number to be determined on the test surface. All other walls were adiabatic. A velocity distribution was specified at the inlet plane, taken from the converged solution of a simulation of the entire cascade. An inlet turbulence intensity of 1.2% was applied to match the turbulence level measured in the experiments. A uniform pressure was specified at the outlet plane.

	Very fine	Fine	Fine (adjusted)	Coarse
Number of cells / millions	5.0	2.8	2.8	0.5
Number of nodes across tip gap	40	33	37	8
First cell height in tip gap / mm	0.05	0.1	0.1	3.8
Max. cell height in tip gap / mm	0.94	0.93	0.63	3.8
Max. y^+ on blade tip	1.1	2.0	2.0	55

Table 3.2: Summary of tip gap cell distributions

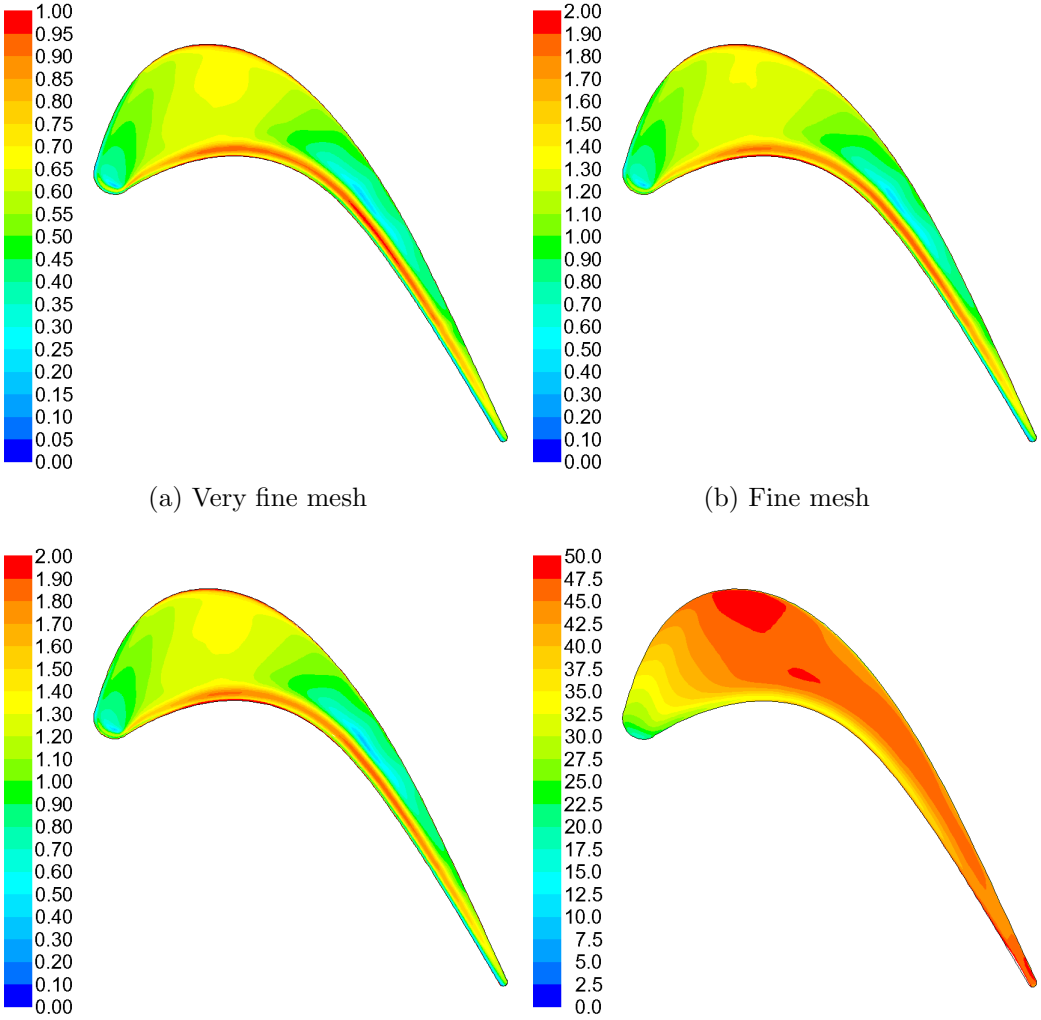

(a) Very fine mesh

(b) Fine mesh

(c) Fine (adjusted) mesh

(d) Coarse mesh

Figure 3.6: Wall-adjacent cell y^+ distributions (Spalart-Allmaras turbulence model) (NB: Scales are different)

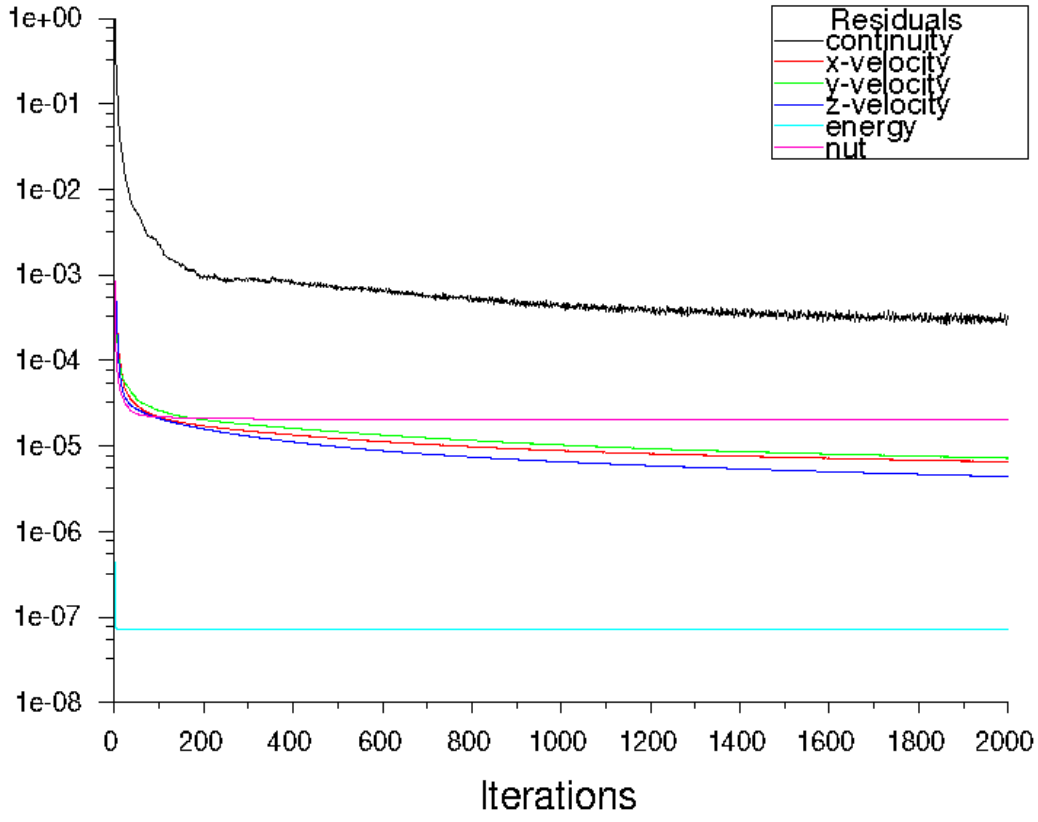

Figure 3.7: Scaled residuals showing a typical convergence history

The criteria used for judging the convergence of a simulation were that the residual histories for all variables were flat and had fallen at least three orders of magnitude (six in the case of the energy variable) and that the integral of Nusselt number over the blade tip surface was invariant with successive iterations. Furthermore, the overall mass imbalance for the entire domain was checked to ensure that it was sufficiently small (below 0.1% of the mainstream mass flow rate). A typical convergence history showing the scaled residuals for each variable is shown in figure 3.7.

3.3.4 Turbulence modelling

For high fidelity flow predictions, the turbulence modelling approach taken must be matched to the flow environment being simulated; increased complexity does not necessarily imply increased accuracy. It is therefore clear that no model can universally be said to be better than the others. Some models may be tuned for particular classes of flows in their implementation in a commercial solver, so the only way of determining the best turbulence model in any given situation is to test all of the available models and compare the results against measured data. The aim of the present study is to assess the best means by which a typically skilled industrial user could obtain reasonably accurate predictions of performance. An extensive test of the turbulence models available through the graphical user interface[3] in FLUENT 6.3 was performed in order to establish the most suitable model for this type of simulation. These, in approximate increasing order of computational cost per iteration, are:

- Spalart-Allmaras (1 equation)
- Standard k-ϵ (2 equations)
- Realisable k-ϵ (2 equations)
- Renormalisation Group Theory (RNG) k-ϵ (2 equations)
- Standard k-ω (2 equations)
- Shear Stress Transport (SST) k-ω (2 equations)
- Reynolds Stress Model (7 equations)

Some of these models (namely, the Spalart-Allmaras and k-ω models) are valid right through the viscosity-affected region and no special treatment is required in the near-wall region other than ensuring sufficient mesh refinement to resolve the velocity gradients. The others (k-ϵ[4] and the RSM) are only valid in the fully turbulent log-law

[3]There are additional turbulence models available through the text user interface. However, these are more specialist models, such as the low-Reynolds number implementations of the k-ϵ model, and are not likely to be of significant benefit compared with the standard ones available through the GUI.

[4]There are low-Reynolds number formulations of the k-ϵ model available through the text user interface which are valid right up to the wall. With the RSM, if enhanced wall treatment is selected, low-Reynolds number modifications are made to the RSM in order to make it valid in the viscous near-wall region.

region and require some other function to bridge the gap to the wall. In these cases, FLUENT 6.3 offers two different approaches for near-wall treatments: *standard wall functions* and *enhanced wall treatment*. Wall functions merely fit empirical functions to the near-wall flow fields for each of the variables being solved for, based on classical boundary layer development. While this usually provides adequate predictions for the flow, it rarely produces accurate heat transfer results, especially in highly turbulated regions. Enhanced wall treatment, however, blends a low-Reynolds number model (a one-equation model by Wolfstein in the case of the k-ϵ models and a low-Re formulation of the RSM in the case of the RSM (Fluent Inc., 2006)) with wall-functions to allow resolution of the boundary layer where the mesh is fine enough, and use of wall functions where it is not. This two-layer near-wall model is then blended with the high-Re turbulence model to give an overall model that is valid across the entire domain. All of the turbulence models were compared using the *Fine (adjusted) mesh* with enhanced wall treatment selected as the near-wall treatment.

3.3.5 Effect of relative endwall motion

An important feature of the experimental rig was the use of a rubber belt to represent the endwall, allowing the effect of the relative motion of the casing on the over-tip leakage flow and blade tip heat transfer to be investigated. This feature was reproduced in the computational domain by defining the area of the cascade sidewall corresponding to the rubber belt as a separate surface during mesh generation, allowing it to be specified as a moving wall to match the experimental setup. The capability of FLUENT 6.3 to capture the effect of relative endwall motion was tested using two simulations with the *Very fine mesh* and the Spalart-Allmaras turbulence model, one with a stationary endwall and the other with the endwall moving. The belt speed was $4.7\,\mathrm{m\,s^{-1}}$, which was the representative blade speed that would produce an axial exit flow direction in the absolute frame of reference, given the blade-relative exit flow angle and speed of the linear cascade. All of the other simulations performed for the

mesh sensitivity testing and turbulence modelling investigation were conducted with a stationary endwall.

3.4 Results

3.4.1 Flow field

Figure 3.8 shows pathlines plotted from a simulation run using the Spalart-Allmaras turbulence model and the *Very fine mesh*. All of the expected flow features that are described in similar low speed, flat tip linear cascade studies found in the open literature are visible. The over-tip leakage flow is roughly parallel to the camber line in the forward part of the blade, and almost perpendicular to the camber line in the latter part. This leakage flow then rolls up into an over-tip leakage vortex as it meets the main passage flow on the suction side of the blade. The mainstream flow also forms a passage vortex that counter-rotates relative to the over-tip leakage vortex, both of which are clearly visible in figure 3.8. A vortex of fluid captured within the separation bubble can also be seen running along the pressure side edge. The over-tip leakage flow separates at the blade tip corner, flowing over the bubble and reattaching on the other side.

In-plane, average velocity data were available from PIV measurements taken in the experimental study. Of particular interest are the data taken on the three secondary flow planes, oriented approximately parallel to the over-tip leakage flow direction in the latter half of the blade, as indicated in figure 3.9. Velocity predictions from the *Very fine mesh* on these planes are compared to those measured experimentally in figures 3.10 to 3.12. In each case, the separation bubble over the sharp-edged pressure side is clearly visible, with the expected acceleration of flow over the bubble and the subsequent flow reattachment.

The qualitative comparison of the flow prediction to the experimental data is very favourable. The peak in-plane velocity of the over-tip leakage jet (at the vena contracta

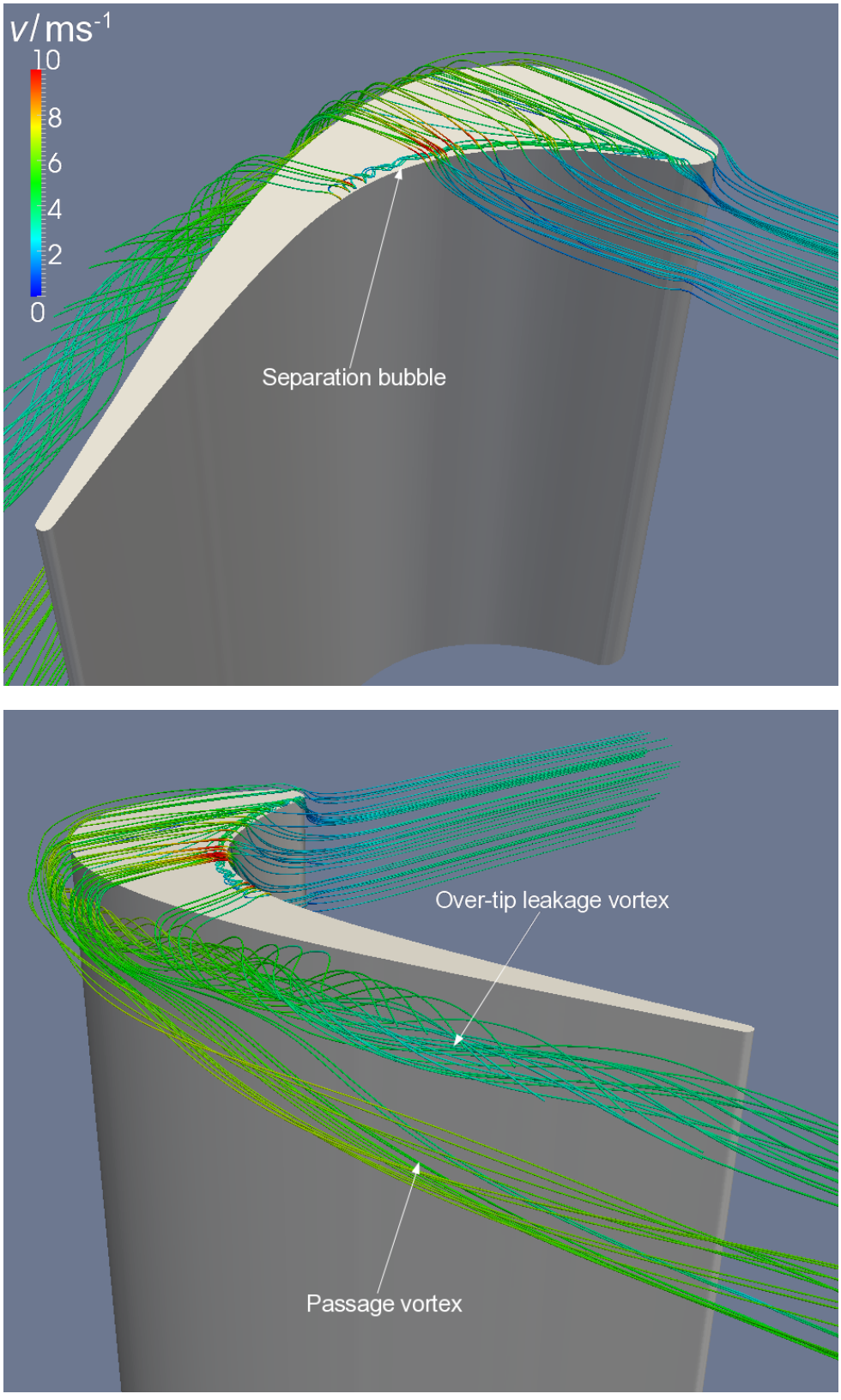

Figure 3.8: Pathlines over the blade tip
(*Very fine mesh*, Spalart-Allmaras turbulence model, endwall stationary)

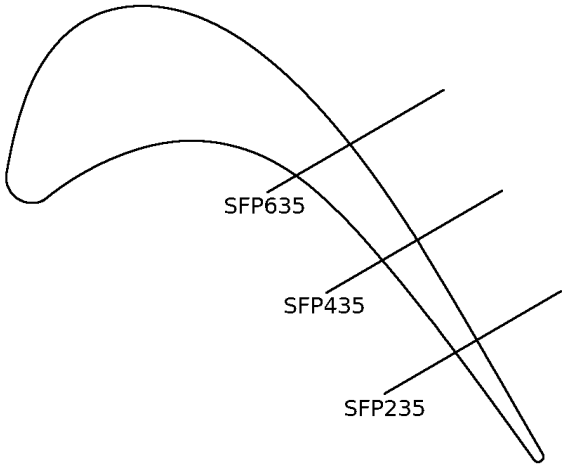

Figure 3.9: Locations of secondary flow planes

throat) is, however, significantly overpredicted by 23%, 18% and 22% for SFP235, SFP435 and SFP635, respectively. Nonetheless, the location of flow reattachment and the size of the separation bubble are simulated extremely well.

3.4.1.1 Mesh sensitivity

Figure 3.13 compares the predicted in-plane velocity contours on SFP435 using the *Very fine mesh* and the *Coarse mesh*. It is evident that the *Coarse mesh* fails to capture the major over-tip leakage flow features in the tip gap region—in particular, the flow separation is entirely absent. This is due to the sparse distribution of mesh points across the tip gap; the wall-adjacent cell is approximately the same thickness as the separation bubble. Thus, the poor performance of the coarse mesh cannot solely, or even significantly, be attributed to the use of wall functions, but rather the coarseness of mesh required for wall functions to be applicable[5].

[5]For wall functions to be valid, the wall-adjacent grid point must be placed within the log-law region of the boundary layer ($30 \lesssim y^+ \lesssim 100$).

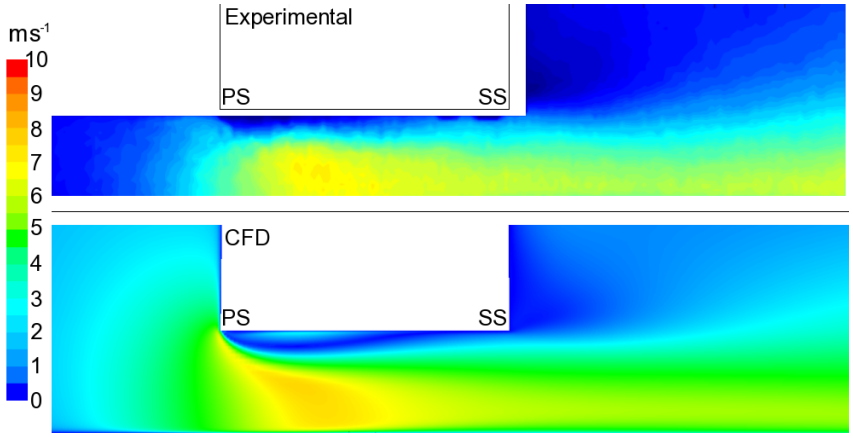

Figure 3.10: In-plane velocity magnitude in tip gap on SFP235
(*Very fine mesh*, Spalart-Allmaras turbulence model, endwall stationary)

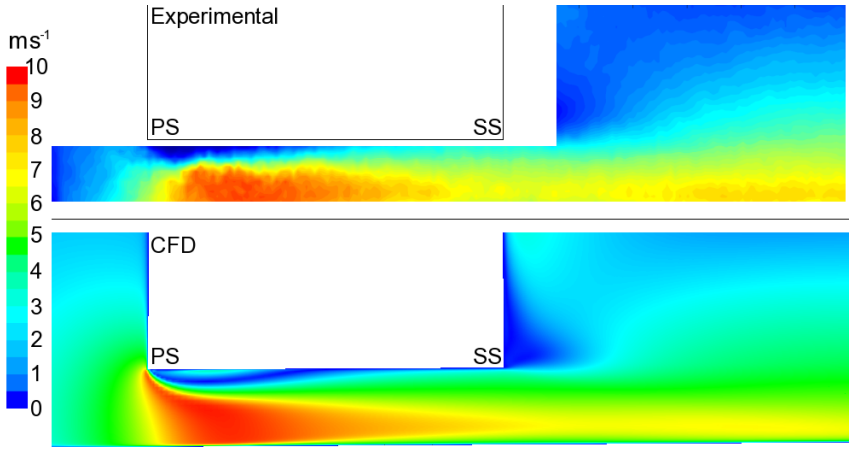

Figure 3.11: In-plane velocity magnitude in tip gap on SFP435
(*Very fine mesh*, Spalart-Allmaras turbulence model, endwall stationary)

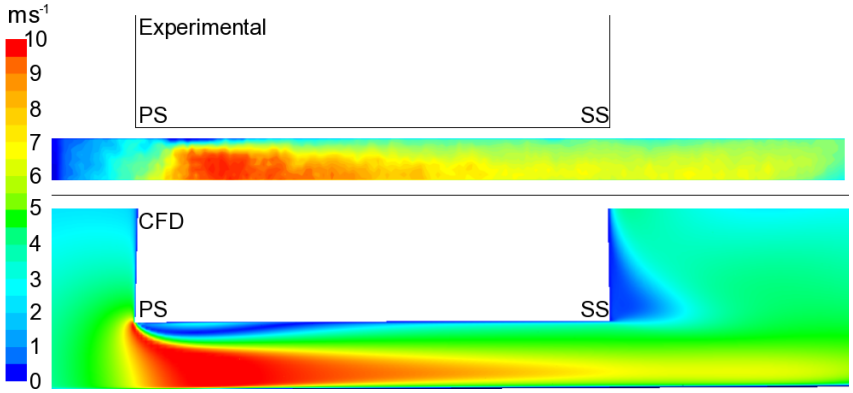

Figure 3.12: In-plane velocity magnitude in tip gap on SFP635
(*Very fine mesh*, Spalart-Allmaras turbulence model, endwall stationary)

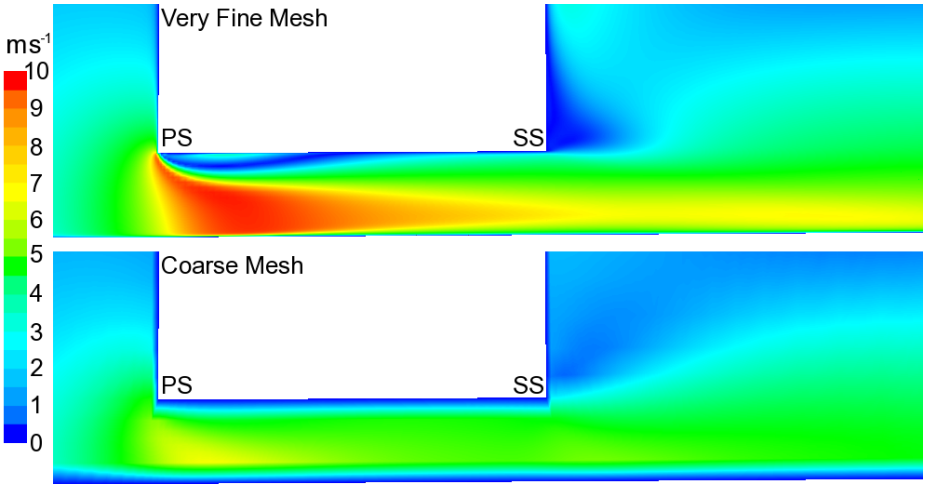

Figure 3.13: In-plane velocity magnitude on SFP435 (*Very fine mesh* and *Coarse mesh*, Spalart-Allmaras turbulence model, endwall stationary)

3.4.2 Heat transfer

The experimental and predicted Nusselt number distributions over the blade tip surface for the different meshes, using blade axial chord as the characteristic length, are shown in figure 3.14. The percentage difference between the experimental and predicted values are shown in figure 3.15. As expected, the erroneous predicted flow field of the *Coarse mesh* leads to a completely incorrectly predicted heat transfer distribution (figure 3.14e). However, the three fine meshes (figures 3.14b to 3.14d) produced excellent qualitative agreement with the experimentally measured data, all capturing the line of enhanced heat transfer of the reattaching flow just inside the pressure side edge and the low heat transfer "sweet spot" by the nose of the blade caused by low local over-tip leakage flow velocity (which can be seen later in figure 3.22a). These characteristic features of the Nusselt number distribution for a flat blade tip at low speed are highlighted in figure 3.16. The predicted distributions from each of the three fine meshes are also indistinguishable, confirming mesh independence.

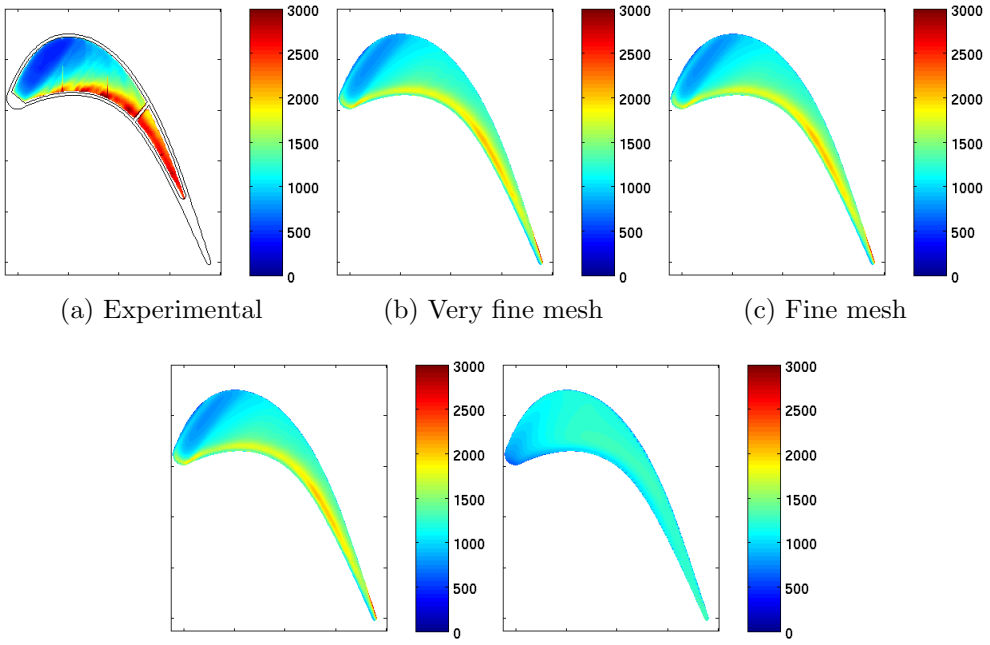

(a) Experimental (b) Very fine mesh (c) Fine mesh

(d) Fine (adjusted) mesh (e) Coarse mesh

Figure 3.14: Blade tip Nusselt number—Mesh sensitivity (Spalart-Allmaras turbulence model, endwall stationary)

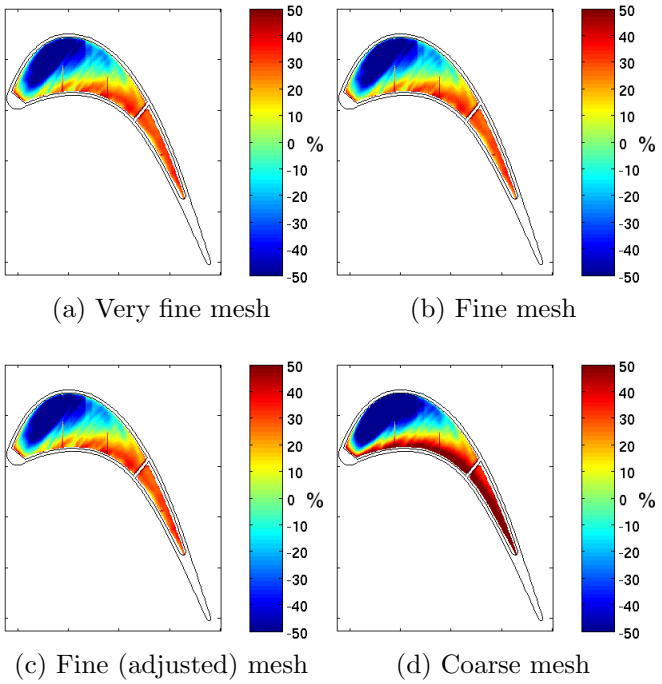

(a) Very fine mesh (b) Fine mesh

(c) Fine (adjusted) mesh (d) Coarse mesh

Figure 3.15: Percentage error in Nusselt number—Mesh sensitivity (Spalart-Allmaras turbulence model, endwall stationary)

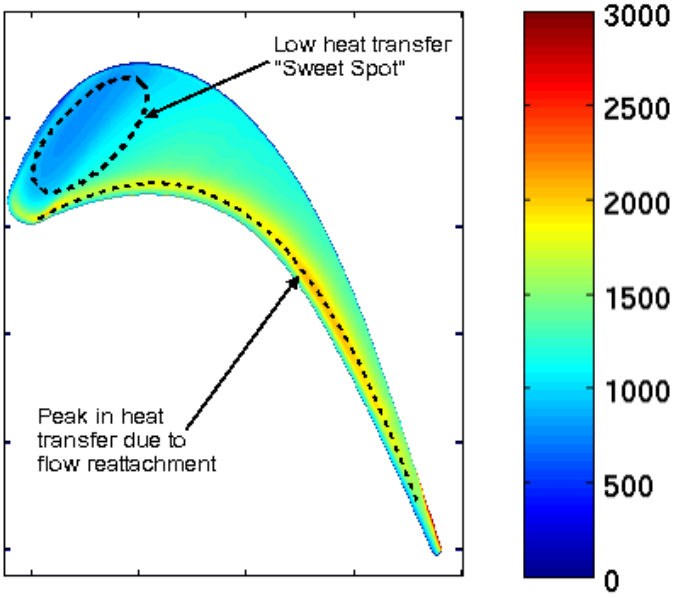

Figure 3.16: Characteristic features of blade tip Nusselt number distribution

3.4.2.1 Turbulence model testing

The blade tip Nusselt number distribution predicted by each of the turbulence models is shown in figure 3.17, along with their deviation from the experimental data (figure 3.18). The overall errors are quantified as the mean absolute error in Nusselt number in figure 3.19[6]. The secondary y-axis on the bar chart shows the mean absolute error in Nusselt number expressed as a percentage of the average experimentally measured Nusselt number.

The performance of most of the models was very similar, typically underpredicting the Nusselt number by 30%–40% in the rear portion of the blade but correctly predicting the size of separation bubble and hence accurately locating the point of reattachment. There were, however, two notable exceptions to this—the standard k-ϵ and standard k-ω models. The standard k-ϵ model performed somewhat better than the majority in terms of the predicted magnitudes of heat transfer, underpredicting Nusselt number by approximately 20%. The standard k-ω model gave an even closer

[6]Note that this is summed only over the area for which experimental data are available and not the entire blade surface.

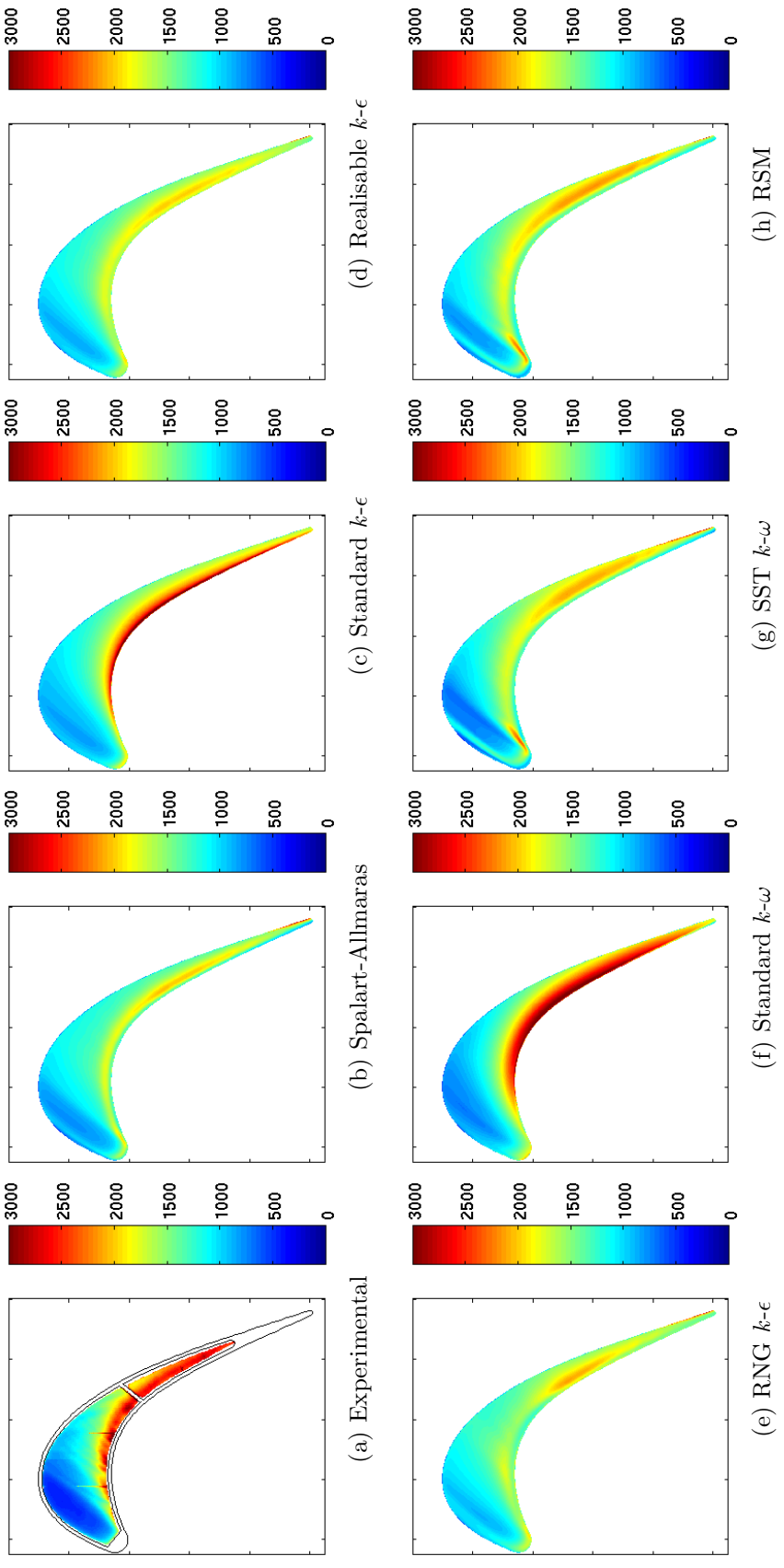

Figure 3.17: Blade tip Nusselt number—Effect of turbulence model (*Fine (adjusted) mesh*, endwall stationary)

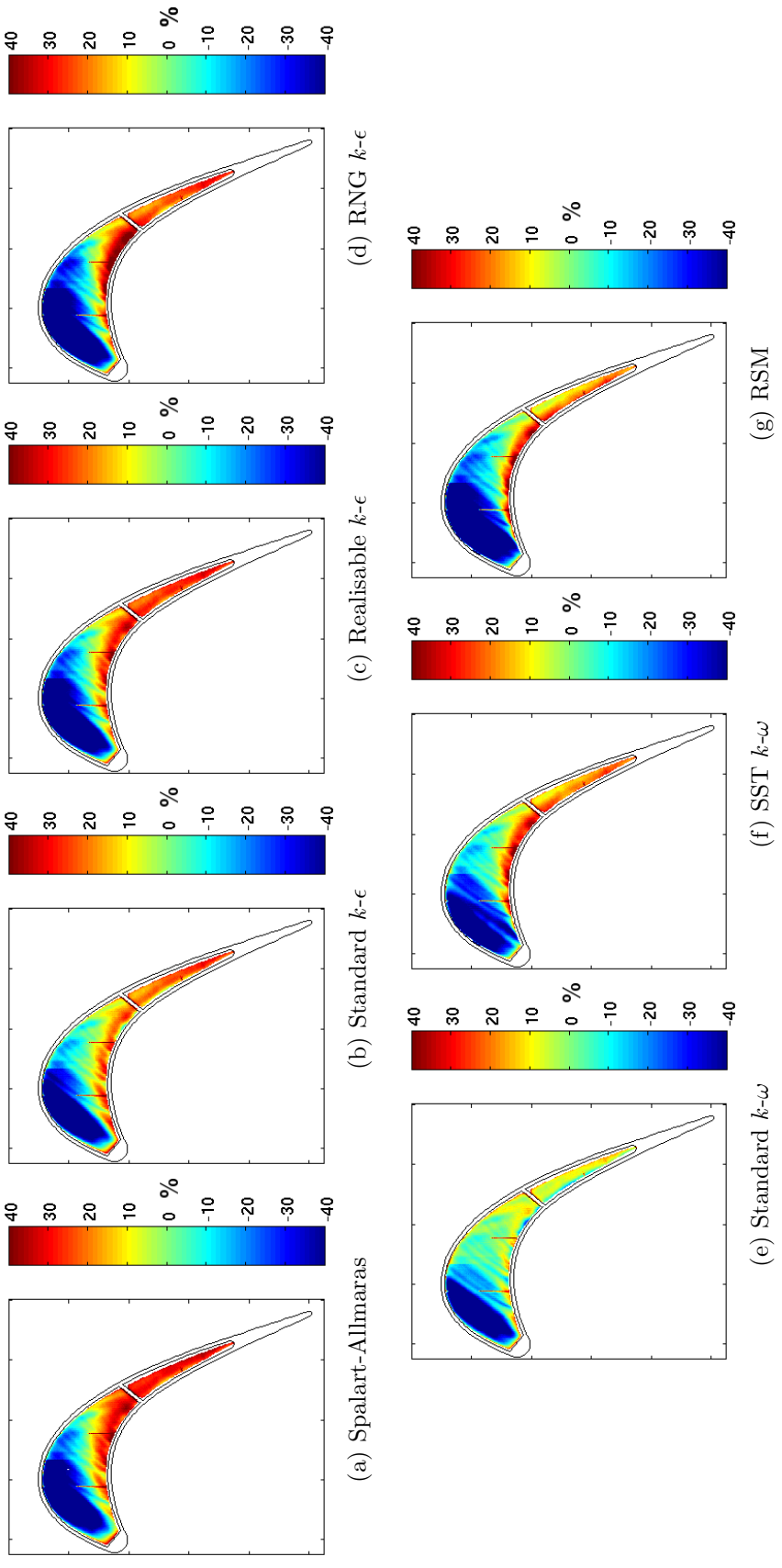

(a) Spalart-Allmaras (b) Standard k-ϵ (c) Realisable k-ϵ (d) RNG k-ϵ

(e) Standard k-ω (f) SST k-ω (g) RSM

Figure 3.18: Percentage error in Nusselt number—Effect of turbulence model (*Fine (adjusted) mesh*, endwall stationary)

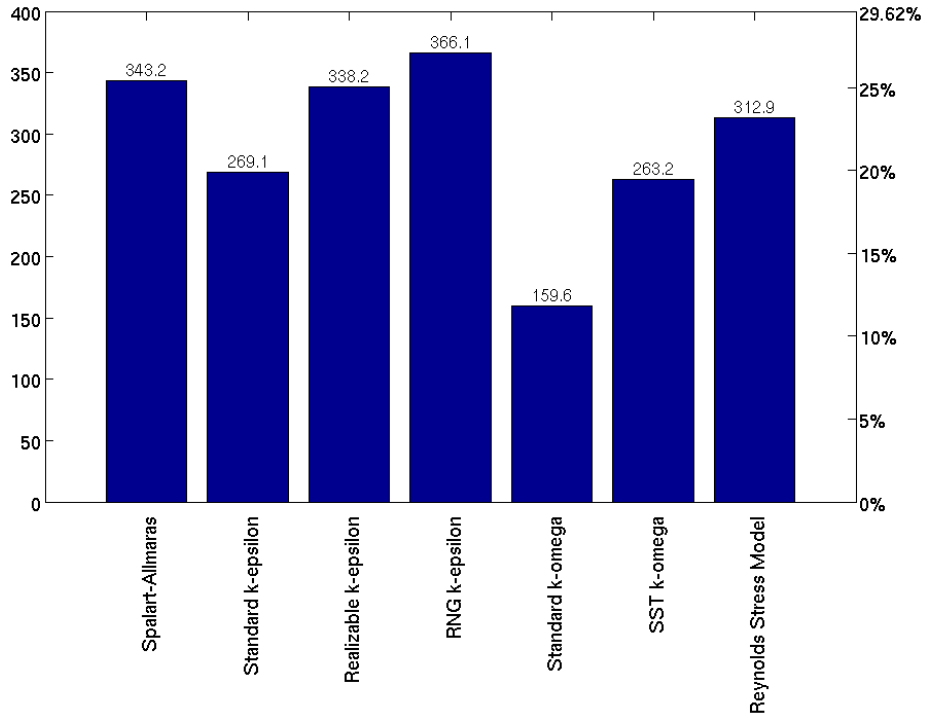

Figure 3.19: Mean absolute error in Nusselt number
(Secondary y-axis is percentage of mean experimental Nu)
(*Fine (adjusted) mesh*, endwall stationary)

estimate, yielding Nusselt numbers within 5%–10% of the experimental results across the tip surface (neglecting the area of low heat transfer in the forward part of the blade). Both of these models, however, suffered from a significant underprediction of the size of the separation bubble, locating the reattachment peak in heat transfer too close to the pressure side edge. The cause of both the elevated blade tip heat transfer levels and the shortened separation is an overprediction of the turbulence within the tip gap region, which is shown in the contours of mid-gap turbulent viscosity (figure 3.20). It can be seen that the levels of turbulent viscosity predicted by the standard k-ω and standard k-ϵ models are an order of magnitude greater than those predicted by the other models.

While it is tempting to conclude from figure 3.19 that the standard k-ω model is the most suitable for predicting blade tip heat transfer in low speed environments, it would not be an appropriate conclusion to draw. Although the shape of the Nusselt

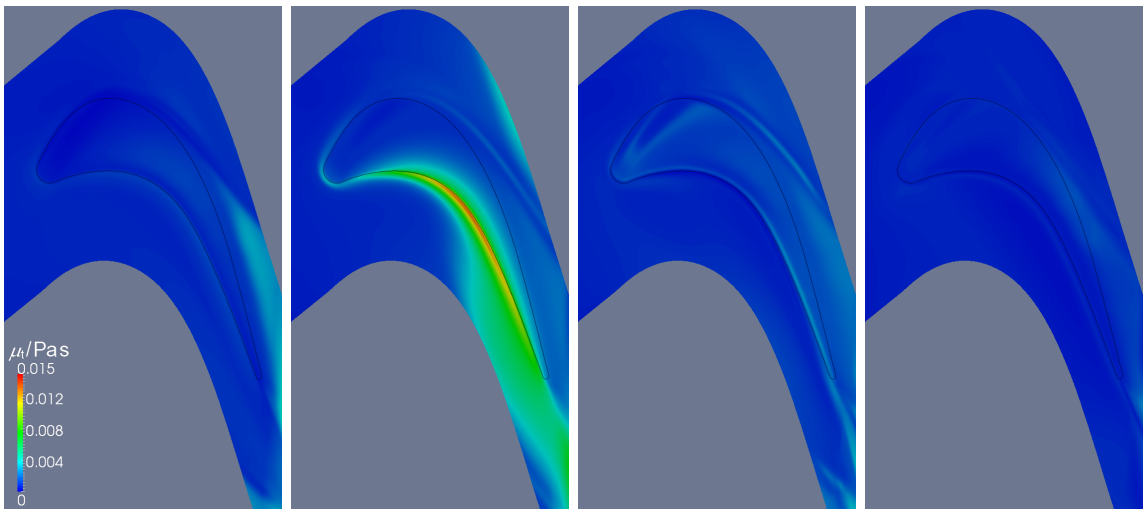

(a) Spalart-Allmaras (b) Standard k-ϵ (c) Realisable k-ϵ (d) RNG k-ϵ

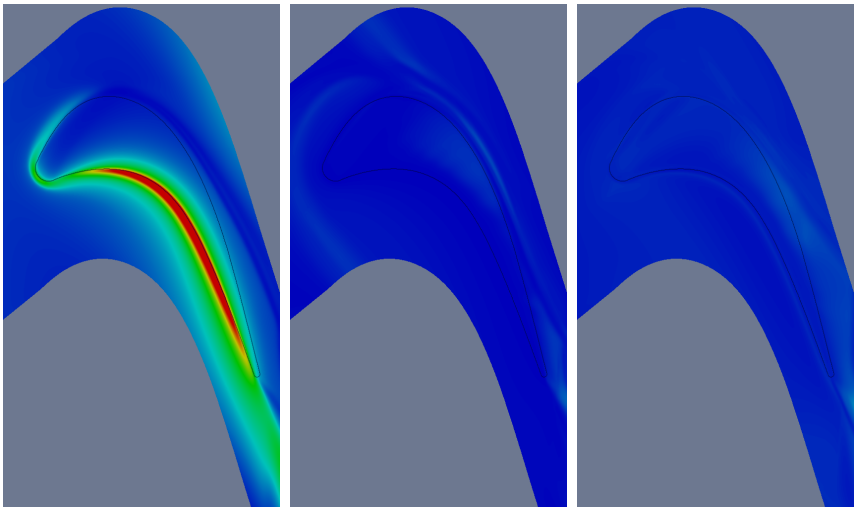

(e) Standard k-ω (f) SST k-ω (g) RSM

Figure 3.20: Mid-gap turbulent viscosity
(*Fine (adjusted) mesh*, endwall stationary)

number distribution on a flat blade tip is only slightly affected by the overprediction of turbulent viscosity, this is unlikely to be true of other blade tip geometries. Other typical unshrouded blade tip shapes, such as squealer tips, have much more significant regions of flow separation than flat blade tips do and the underprediction of the separation bubble size could have a critical impact on the flow structure predicted in the tip gap region. The cavity flow inside a double squealer tip, for instance, can

be very sensitive to small changes to the incoming flow; this is seen later in the CFD simulations of chapter 5. The standard k-ω model and the standard k-ϵ model should therefore be avoided for simulations of this type. The accuracy of the heat transfer and flow predictions from each the other turbulence models were very similar, and so the SST k-ω and realisable k-ϵ models are the recommended turbulence models for use with this type of flow. The extra computational cost associated with the use of the RSM does not, in this result in any significant benefit.

3.4.2.2 Relative endwall movement

The effect of relative endwall movement on the heat transfer distribution was measured experimentally and the data are shown in figures 3.21a and 3.21b. The results from the simulations corresponding to these two cases are shown in figures 3.21c and 3.21d. Once again, the qualitative changes between the stationary endwall and moving endwall cases are captured well computationally. With relative endwall motion, the low heat transfer sweet spot is both broadened and deepened and the separation bubble shortened, moving the reattachment marginally closer to the pressure side edge, which matches the differences observed experimentally.

Figure 3.22 shows pathlines of the over-tip leakage flow, both with and without relative endwall motion. It can be seen that the angle of the over-tip leakage flow for the case with a moving endwall is closer to the axial direction, due to the shear induced by the endwall. This change in direction reduces the velocity mismatch between the over-tip leakage flow and the mainstream flow on the suction side and reduces the extent to which the jet penetrates into the passage before it rolls up into the over-tip leakage vortex. The flow velocity within the tip gap is also significantly reduced, particularly in the forward part of the blade tip region.

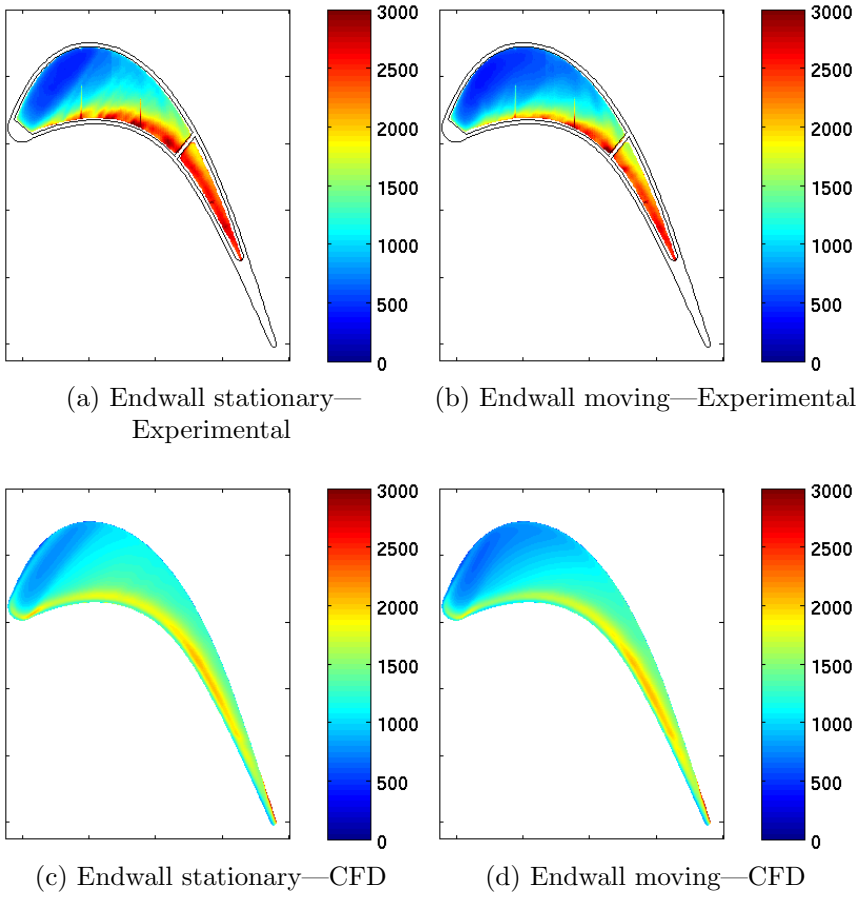

(a) Endwall stationary—Experimental

(b) Endwall moving—Experimental

(c) Endwall stationary—CFD

(d) Endwall moving—CFD

Figure 3.21: Blade tip Nusselt number—Effect of relative endwall motion (*Very fine mesh*, Spalart-Allmaras turbulence model)

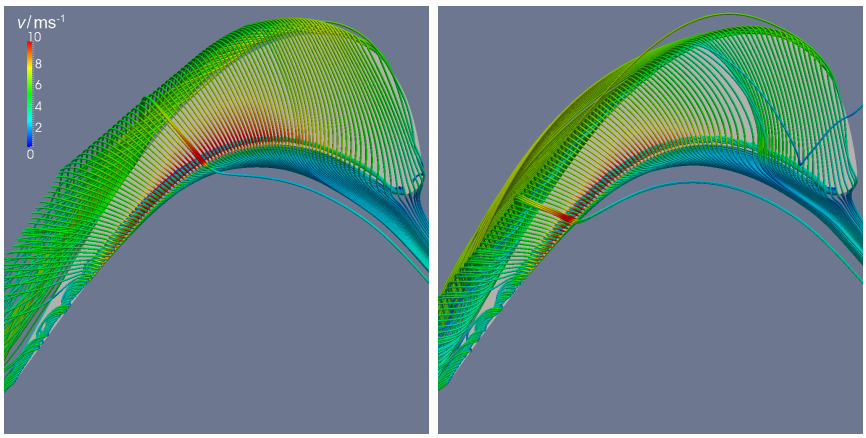

(a) Endwall stationary

(b) Endwall moving

Figure 3.22: Over-tip leakage flow directions—Effect of relative endwall motion (*Very fine mesh*, Spalart-Allmaras turbulence model)

3.5 Chapter summary

In this chapter, a detailed CFD validation study of flow over and heat transfer to the flat blade tip of a large scale, low speed linear cascade was presented. Purely hexahedral, multiblock meshes were generated in ICEM CFD 11 and solved using the pressure based solver of FLUENT 6.3 with the SIMPLE algorithm for pressure-velocity coupling. Mesh insensitivity was confirmed and a thorough test of available turbulence models was performed. Due to the coarseness of mesh required for their use, it was concluded that wall functions were unsuitable for this type of flow. On the flat blade tip, a maximum wall-adjacent cell y^+ value of two was found to be sufficient to achieve mesh independence; further refinement of the mesh within the tip gap provided no change to the blade tip Nusselt number distribution. The standard k-ω and standard k-ϵ models gave the closest match to the experimentally measured magnitudes of Nusselt number in the aft region of the blade tip, but significantly underpredicted the size of the separation bubble and located the flow reattachment too close to the blade tip edge. This was caused by an overprediction of the turbulence levels in the tip gap region by these two turbulence models. The other models tested gave very similar levels of accuracy in their predictions of Nusselt number. The RSM did not produce any significant improvement in accuracy, despite the increase in model complexity and computational cost associated with it.

It is therefore recommended that future studies of blade tip heat transfer in similar, low speed environments should attempt to resolve the boundary layer fully and use a mesh that produces wall-adjacent cell y^+ values below two on the surfaces of interest. The standard k-ω and standard k-ϵ turbulence models should be avoided because of their overprediction of turbulence at the pressure side of the tip gap, which results in relatively poor predictions of the extent of the flow separation. The RSM provided no benefit over simpler RANS models; the SST k-ω and realisable k-ϵ models are therefore the recommended turbulence models for use in this type of flow. It should be noted that all of the turbulence models, except for the standard k-ω and the standard

k-ϵ models, significantly underpredicted the blade tip Nusselt number in the thin section of the blade tip by 30%–40%. This tendancy of these models (in the forms provided within FLUENT 6.3) to underpredict heat transfer should be borne in mind when interpreting any simulation data.

Chapter 4

Uncooled Engine Scale CFD Simulations

4.1 Introduction

This chapter reports a CFD study of the effect of four unshrouded blade tip geometries on the flow field around and heat transfer to an uncooled HP turbine blade typical of those used in modern large civil aero-engines. The blade geometry and boundary conditions are taken from the Rolls-Royce *Environmentally Friendly Engine* (EFE) technology demonstrator engine (Rubin de Cervin and Djelalian, 2006), which is representative of the current cutting edge in large civil aero-engine design. The primary goal is to identify a new unshrouded blade tip geometry for the EFE HP turbine blade that is aerodynamically acceptable but has an improved thermal performance compared to current unshrouded turbine blade tip designs. An unshrouded blade tip design may be considered thermally better if it can more feasibly incorporate cooling features and/or reduce thermal loads to the blade tip. This CFD study, performed in a transonic flow environment, tests several different blade tip geometries at a number of engine-representative tip gaps (varying between 0.45% and 1.34% of blade chord) to establish their relative aerodynamic performances, including their tip gap efficiency exchange rates, defined in equation 2.1 on page 19. The heat transfer to each blade tip is also predicted in order to establish the heat load each geometry would be subjected

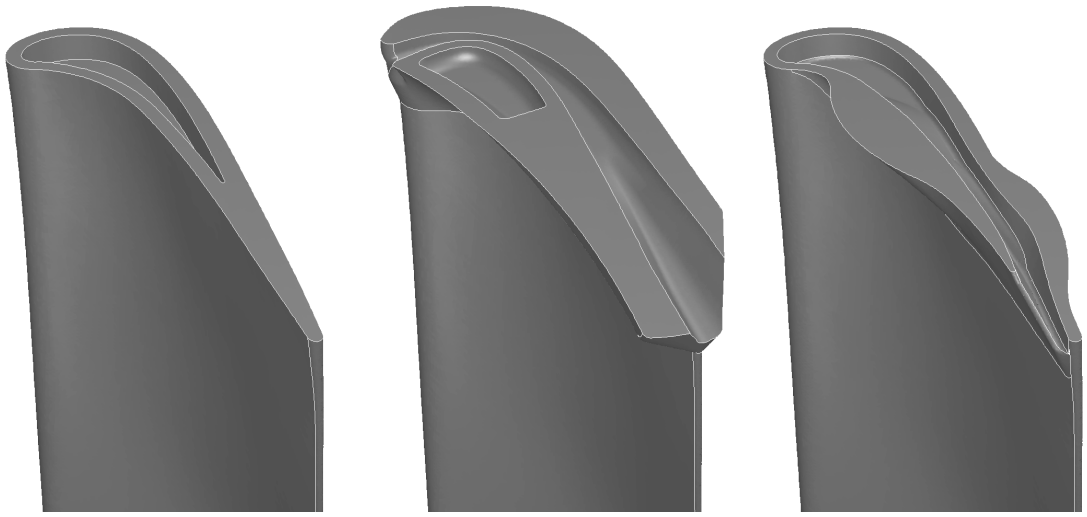

(a) Double squealer (b) Winglet (c) Squealet

Figure 4.1: Tested blade tip geometries

to, which is a preliminary measure of the degree of cooling required. The effect of relative endwall movement is investigated using the double squealer tip geometry. CFD simulations in this section are run using unstructured, hybrid tetrahedral and prism layer meshes generated in ICEM CFD 11 and solved with the time-steady, pressure based solver of FLUENT 6.3 using the realisable k-ϵ turbulence model and the SIMPLE algorithm for pressure-velocity coupling.

4.2 Blade tip geometries

4.2.1 Currently existing geometries

The simplest and most obvious of unshrouded blade tip designs is the flat tip, as investigated in the low speed study detailed in chapter 3. While the flat tip performs very well at very small tip clearances, it has a number of disadvantages—in particular, its performance drops off extremely quickly as tip gap increases. As such, it is not generally employed in real engines and therefore, although it has widely been studied in the literature, it is not examined further in the present work. Perhaps the most

commonly *used* type of unshrouded blade tip design is the squealer tip. These blade tips are characterised by thin rims that extend radially outwards on the pressure side, suction side, camber line or some combination of the three, which act in a similar manner to the fins on a labyrinth seal. Squealer tips have been shown in numerous studies to provide very good aerodynamic performance and can also reduce the heat load to the main blade tip surface. They are lighter than flat tips and are less susceptible to catastrophic damage in the event of a tip rub. The biggest problem with squealer tips, however, is that the rims themselves are often subject to extremely high heat loads and are nearly impossible to cool, as they are too thin to allow holes to be drilled through them to access cooling air directly. This makes the squealer rims extremely vulnerable to damage and reduces their service life considerably. Many patents proposing methods of cooling squealer tips have been filed, for example, Andersen (1979), Butts et al. (1993) and Ammann and Good (2011), but it remains a significant problem without a good solution. Nonetheless, they are often used in small civil aero-engines where the TET is typically lower than in larger engines (Saravanamuttoo et al., 2009). The squealer tip that is usually considered to provide the best compromise between aerodynamic and thermal performance has a rim on both the pressure and suction sides and is known as a *double squealer* or a *cavity tip*. It is used as the baseline case in the present study and is shown in figure 4.1a. The particular double squealer geometry used has a ratio of cavity depth-to-squealer rim thickness of 2.0.

Although all large civil turbofan aero-engines made by Rolls-Royce to date have had shrouded HP turbine blades, there has been some previous work on unshrouded designs. The predecessor technology demonstrator engine to EFE, the *Advanced Near-Term Low Emissions* (ANTLE) engine incorporated a winglet tip on its HP turbine blade. This concept has been further developed for EFE and this EFE winglet design, depicted in figure 4.1b, is used for comparison to the new designs in the present study.

4.2.2 "Squealet" tip design

While the winglet design is significantly lighter than the shrouded blade tip that it replaces, it is still relatively heavy when compared to more traditional unshrouded blade tip designs, such as squealer tips, and provides a much larger wetted surface area for heat transfer. Its advantages are that its tip gap efficiency exchange rate is lower than that of the double squealer design, so the efficiency penalty caused by an increased tip gap is reduced, and that it is not as prone to thermal damage as the thickness of the tip extensions allow film cooling to be used to protect the blade tip. An attempt has been made to bridge the gap between these two designs with a hybrid blade tip geometry that would combine the advantages from both the double squealer tip and the winglet tip—the *"squealet"* tip.

The initial squealet design is illustrated in figure 4.1c. This geometry was designed at Rolls-Royce under guidance from the author of the present study and was based on the early simulation results from the double squealer tip and anecdotal evidence of in-service experience. The design approach used was to start with the double squealer tip and graft features from the winglet on to it to improve the sealing capability of the tip and improve cooling access. In order to reduce the mass flow rate spilling out of the rear of the cavity and over the suction side rim, the back of the cavity was opened to channel the cavity flow all the way through to the trailing edge, resembling the gutter found on the winglet design. Small winglet-like extensions were also introduced in the mid-chord region of the pressure side and towards the trailing edge region of the suction side rims to control the regions of highest velocity over-tip leakage flow and where burnout is most commonly observed in current in-service unshrouded blade tips.

All geometries investigated in this study are idealised and therefore are sharp-edged.

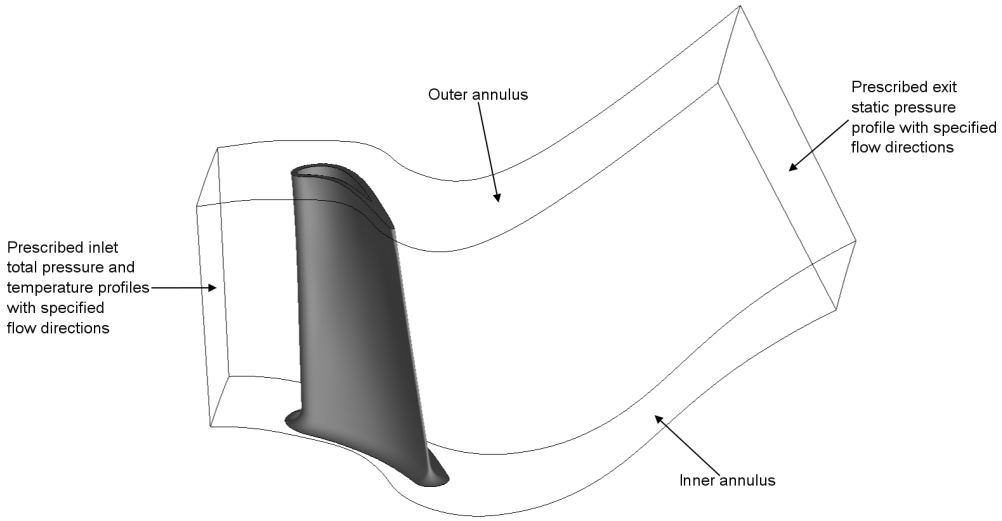

Figure 4.2: Computational domain for engine-representative CFD simulations

4.3 CFD methodology

4.3.1 Meshing

Due to the increase in complexity of the geometries being simulated (and the expected further increase in complexity still to come with the addition of film cooling to the geometry), an unstructured meshing approach was taken for these simulations. The computational domain once again consists of a single blade with periodic boundary conditions and extends from the HP NGV exit plane through to the IP NGV inlet. The geometry is taken from the actual engine and includes the haded transition duct, as shown in figure 4.2.

For each blade tip geometry at each tip gap, a purely tetrahedral mesh was first generated using the Octree mesher of Icem CFD 11, taking care to distribute mesh cells appropriately to ensure adequate refinement in regions of flow complexity, while also avoiding excessive overall cell counts and sudden cell size transitions, as illustrated in figure 4.3a. An example of the typical mesh refinement on the blade tip surface is shown in figure 4.4. Curvature-based mesh refinement was used to ensure that all

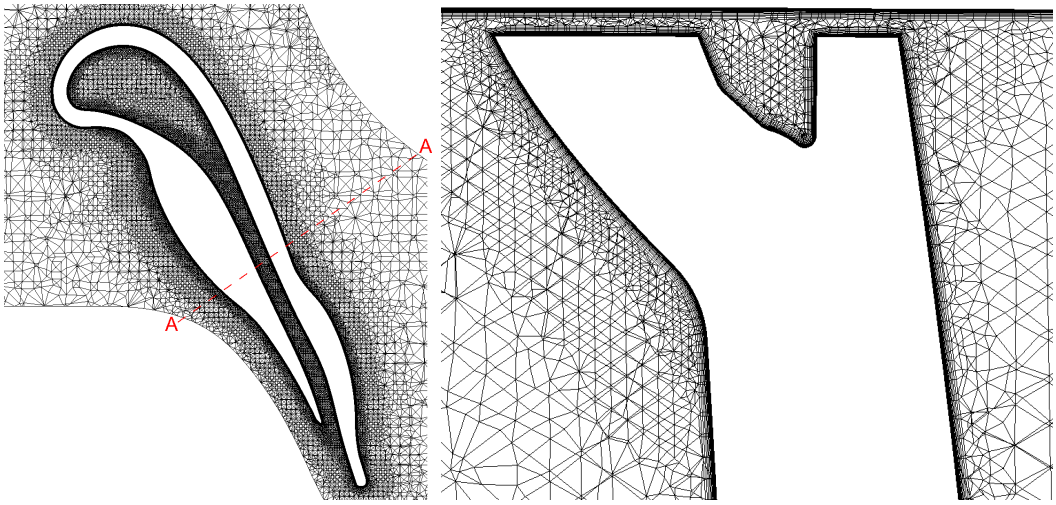

(a) Cutplane through squealet rim (b) Section A—A

Figure 4.3: Typical mesh refinement in the tip gap region

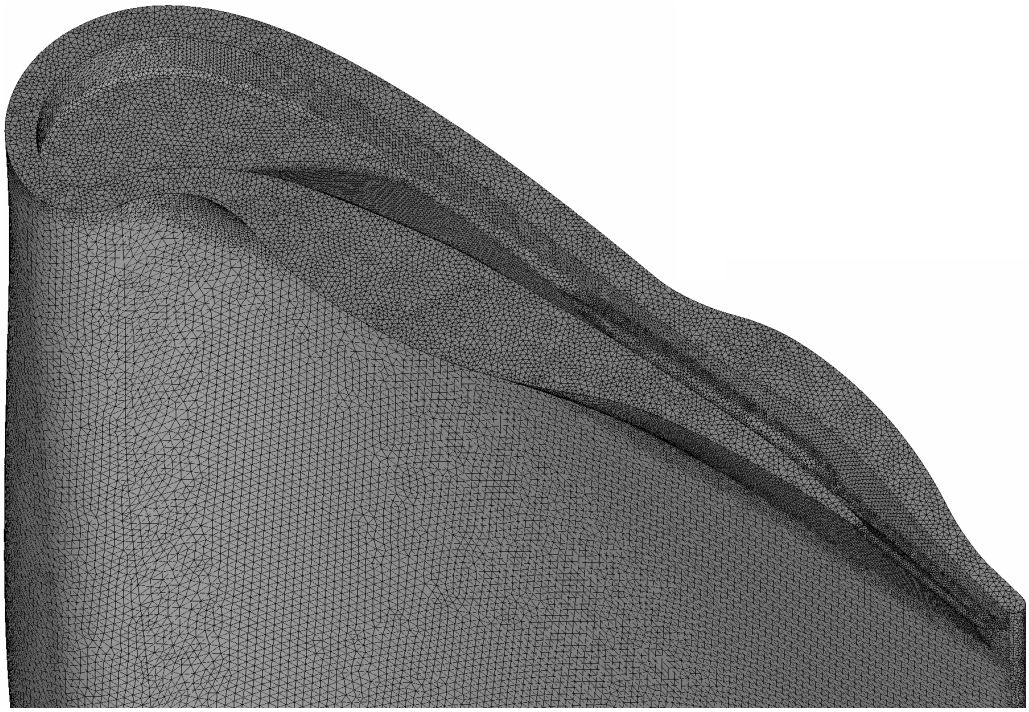

Figure 4.4: Typical mesh refinement on the blade tip surface

salient geometric details were appropriately resolved and expansion ratios[1] of 1.3 or less were specified to ensure the appropriate graduation of cell sizes. The tetrahedral mesh was smoothed globally to produce the highest quality mesh possible, typically achieving a minimum cell quality[2] of above 0.4. Prism layers were then grown from the blade, hub and casing surfaces to ensure that boundary layers would be captured faithfully. The sizing of the first cell height was chosen to produce a suitable wall-adjacent cell y^+ distribution; this was determined by an iterative process of meshing, solving and remeshing as required until the desired y^+ values were achieved. A y^+ distribution of two or less was targeted over the blade tip and near-tip surfaces for high veracity heat flux predictions; this was difficult to achieve in places, however, because of flow impingement or reattachment and high over-tip leakage flow speeds, which result in very thin boundary layers. A typical y^+ distribution achieved is shown in figure 4.5. The number of prism layers was adjusted to leave a thin interface layer of tetrahedral elements between the two sets of prism layers in the tip gap region, as seen in figure 4.3b. This approach yielded first cell thicknesses of $\sim 2\,\mu$m and between 12 and 19 prism layers (depending on tip gap), which is similar to the meshes used in related, earlier CFD simulations performed by Rolls-Royce, for example that reported in Willer et al. (2006), which used 16 prism layers. Smoothing was very carefully applied: the prism layers were initially frozen and smoothing used to return the distorted tetrahedral elements to high quality cells. This was followed by the minimum global smoothing required to bring the minimum cell quality up to 0.1.

[1]The expansion ratio is usually defined as the size ratio of adjacent cells as the cell size increases away from wall surfaces. However, due to the manner in which the Octree algorithm partitions the domain, a gradual transition in cell size is not possible and Octree meshes are characterised by layers of cells of equal size, with the cell size of each layer being double that of the layer beneath it. The thickness of each layer of cells is determined by the expansion ratio; when the expansion ratio raised to the power of the number of cells across the layer is greater than or equal to two, the transition to the next cell size occurs. The expansion ratio therefore continues to control the rate of cell size increase from the walls in an analogous fashion to its use in the context of other meshing algorithms, but is constrained by the inability of the Octree mesher to produce a smooth graduation in cell size.

[2]The reported mesh quality of a cell is defined as the reciprocal of aspect ratio for a tetrahedral cell, the determinant for a hexahedral cell and the minimum of the determinant and warpage for a (triangular) prismatic cell.

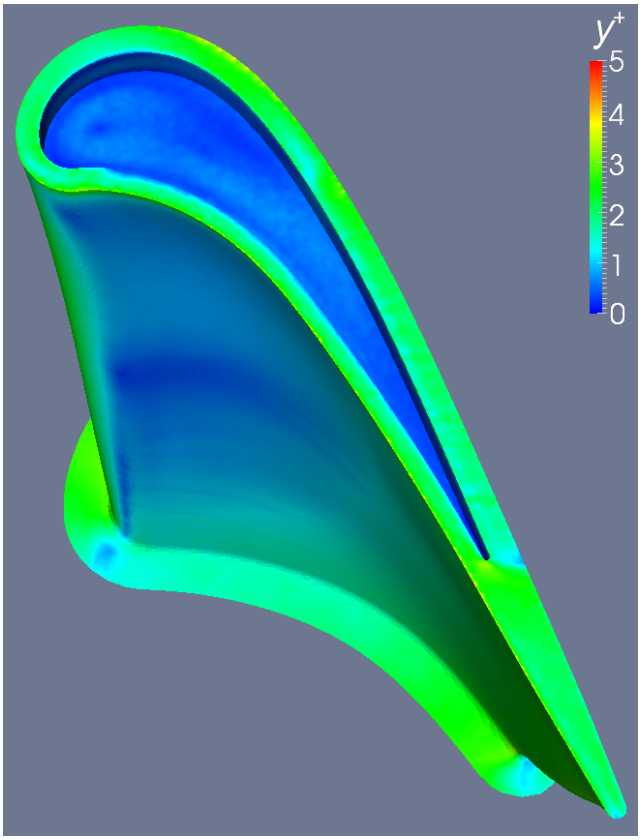

Figure 4.5: Typical achieved wall-adjacent cell y^+ distribution

The smoothing at this latter stage had to be performed with great care to minimise distortion to the boundary layer mesh.

Achieving high mesh quality was of utmost importance in the generation of meshes for these simulations. In order to minimise cell distortion, the cell sizing and growth rates, particularly of the prism layers, were adjusted in problematic areas to ensure that elements of sufficient quality were produced. This was most important on surfaces of high curvature where prism layers were grown, such as the rear corner of the double squealer tip cavity, as without any intervention, the collision of the columns of prism layers grown from the converging sidewalls of the cavity would have resulted in cells with very high aspect ratios. In order to counteract this, prism layer expansion was supressed locally, giving thinner prism layers and thus alleviating the problem.

The sizes of the initial, purely tetrahedral meshes were 2.2–2.6 million cells, which yielded overall final hybrid meshes of 5.0–5.7 million cells. The variation in cell count was caused by the different blade tip geometries and changing tip gap; the cell sizes and expansion ratios were held constant rather than the number of cells. Increases in tip gap were made by trimming the blade tip down to the appropriate radius, so the wetted surface area and blade mass decreased slightly with increasing tip gap. In order that the variation of efficiency of each geometry with tip gap could be established, simulations were run at 0.25 mm, 0.5 mm and 0.75 mm tip gaps, representing 0.45%, 0.89% and 1.34% blade span, respectively.

4.3.2 Solution and boundary conditions

The solver used was, once again, the pressure based, implicit solver of FLUENT 6.3, with the SIMPLE algorithm for pressure-velocity coupling. Although the density based solver is generally regarded as being more appropriate (in terms of stability and speed of convergence) for high speed, compressible flows such as these, the pressure based solver was selected for its relative velocity formulation, as this would be required for the future simulations with film cooling. It had previously been found that CFD simulations run at Rolls-Royce using the absolute velocity formulation, which is the only option with the density based solver, exhibited very uneven velocity profiles at the coolant inlet boundaries caused by truncation errors. The pressure based solver was therefore used for the uncooled CFD simulations to ensure compatibility of the results with the future simulations. By solving the domain in the rotating, blade-relative frame of reference, a time-steady solution could be obtained. This reduced computational requirements to a level that could feasibly be solved on the available hardware. The meshing process and post-processing were conducted on a 64-bit, four-core workstation with 8 Gb RAM. The solver was run on a small, 64-bit cluster with eight nodes, each of which had four cores and 8 Gb RAM.

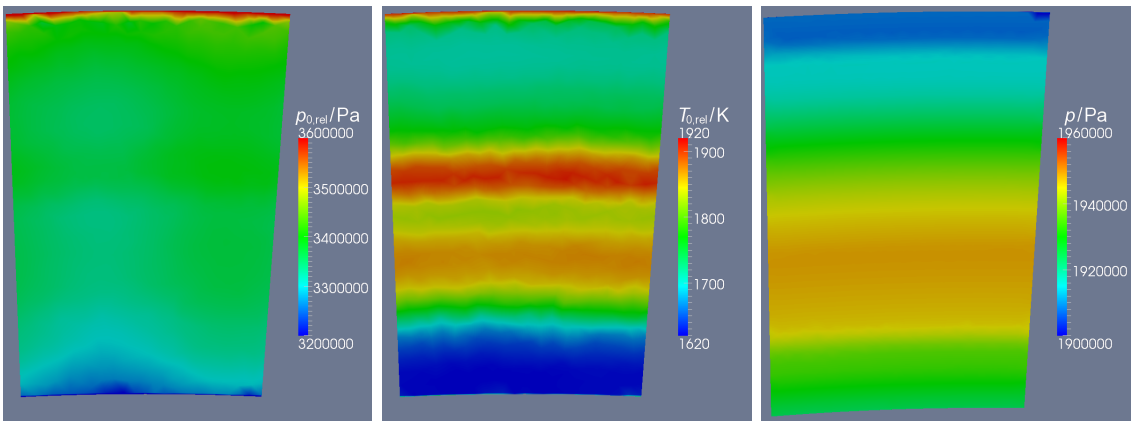

(a) Inlet relative total pressure

(b) Inlet relative total temperature

(c) Exit static pressure

Figure 4.6: Inlet $p_{0,\text{rel}}$ and $T_{0,\text{rel}}$ and exit p boundary condition profiles

The boundary conditions used were engine-realistic and provided by Rolls-Royce from numerical simulations run using their in-house codes. As only a single rotor blade was being simulated in a time-steady, periodic environment, circumferentially averaged total pressure and temperature distributions were imposed at the inlet, along with the appropriate flow directions. The effects of NGV wake passing and circumferential variations of pressure and temperature (e.g. from the combustor exit temperature profile) were therefore not represented in the CFD; the radial variations, by contrast, were included. A radial static pressure profile was similarly applied at the outlet plane. These boundary condition profiles are shown in figure 4.6. Typical mass-averaged flow conditions at the computational inlet and exit planes are given in table 4.1.

Due to the variation in fluid temperature over the blade tip surface, the local adiabatic wall temperature distribution was needed to calculate the appropriate driving temperature for the calculation of heat transfer coefficient. Two simulations were therefore run for each geometry/tip gap combination; one with adiabatic wall boundary conditions on all walls and one with imposed, constant temperature boundary conditions on the blade, tip and shroud surfaces. There is therefore an implied assumption that the flow field is not significantly changed by the wall thermal boundary

Inlet relative total pressure	3.35 MPa
Inlet static pressure	3.02 MPa
Inlet relative total temperature	1760 K
Inlet static temperature	1717 K
Inlet relative velocity	$322\,\mathrm{m\,s^{-1}}$
Inlet relative Mach number	0.40
Inlet relative Reynolds number (based on axial chord)	0.81×10^6
Exit static pressure	1.94 MPa
Exit static temperature	1568 K
Exit relative velocity	$716\,\mathrm{m\,s^{-1}}$
Exit relative Mach number	0.93
Exit relative Reynolds number (based on axial chord)	1.35×10^6
Mass flow rate	$1.81\,\mathrm{kg\,s^{-1}}$
Rotor speed	$1319\,\mathrm{rad\,s^{-1}}$

Table 4.1: Summary of mass-averaged nominal flow conditions

condition. The driving temperature used in the calculation of the heat transfer coefficient was then the difference between the (local) adiabatic wall temperature and the imposed constant wall temperature, i.e.

$$h = \frac{q_{\mathrm{ct}}}{T_{\mathrm{ad}} - T_{\mathrm{ct}}} \tag{4.1}$$

In an effort to maximise comparability with related, previous CFD studies performed in FLUENT at Rolls-Royce, the realisable k-ϵ model was used with enhanced wall treatment. This turbulence model had previously been selected for its good performance in regions of separated flow; a critical feature of over-tip leakage flow. Viscous heating terms in the turbulence model were included, as this was known to make a significant impact in the high shear region found in the tip gap. Real air properties to account for the variation in specific heat, conductivity and viscosity with temperature were input to cover the entire temperature range encountered. The convergence criteria used were very similar to those used previously; that residuals were flat and had dropped by at least three orders of magnitude (six in the case of the energy variable), that the axial drag force on the blade was steady, that either the average blade temperature or average heat flux to the blade (depending on the

boundary conditions used for that simulation) was steady and that the overall mass flux imbalance across the domain was less than 0.1% of the inlet flow.

At convergence, second order discretisation was used for all variables. It was found that the simulations were reasonably unstable and significant underrelaxation was needed to guarantee convergence. This was attributed to the inherent unsteadiness of the flow being pseudo-averaged by use of a time-steady solver. The simulations required some additional care to establish the general flow field without diverging. To achieve convergence, these simulations were initially run with laminar viscosity, first order discretisation and a specified, constant mass flow rate inlet boundary condition of $1.778\,\mathrm{kg\,s^{-1}}$ (with the correct flow directions specified) for ∼100 iterations. The realisable k-ϵ model was then turned on and run for another ∼150 iterations. The inlet boundary condition was then changed to a specified pressure inlet with the appropriate total pressure and temperature distributions. After a further ∼50 iterations, the discretisation scheme was changed to second order, at which point the simulations could be left to converge fully. A typical convergence history is shown in figure 4.7.

No attempt at validation was made, as no suitable experimental data were available. This study was intended solely as a comparative study, so this was not considered to be critical. Additional care was, however, taken to ensure that every solution was physically realistic to minimise the risks of an inappropriate flow solution being accepted.

4.3.3 Mesh sensitivity

Mesh sensitivity was assessed using the revised squealet tip geometry (described later in section 4.5) at a tip gap of 0.5 mm (0.89% blade chord). The same meshing strategy that was used to create the original mesh, described in section 4.3.1, was applied to generate a new, more refined mesh. Applying a global refinement of elements, the overall mesh size was increased by 29% from ∼5.80 million to ∼7.49 million cells. Due

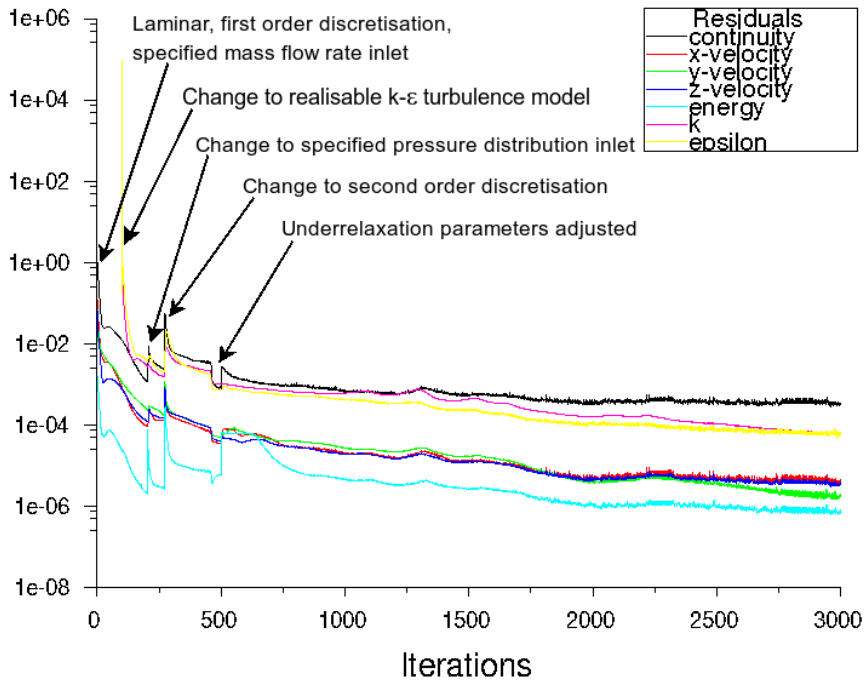

Figure 4.7: Scaled residuals showing a typical convergence history

	Original mesh	Refined mesh	Change
Heat flux / $\mathrm{MW\,m^{-2}}$	2.787	2.855	+2.4%
Heat transfer coefficient / $\mathrm{W\,m^{-2}\,K^{-1}}$	8269	7574	−8.4%
Adiabatic wall temperature / K	1793	1795	+0.1%

Table 4.2: Mesh sensitivity comparison—Average blade tip heat transfer values

to software license availability issues, this mesh sensitivity assessment had to performed using FLUENT 12.0 rather than FLUENT 6.3, which was the solver that was used for the rest of the study. For the purposes of ensuring that a fair comparison could be made, simulations with both meshes were run using the same solver. The solver settings and solution procedure used were identical to those described in section 4.3.2.

The predicted contours of heat flux, heat transfer coefficient and adiabatic wall temperatures for the simulations run with the two different meshes are shown in figure 4.8. There are some noticeable differences between the distributions produced by the meshes; notably, the enhancement of heat transfer coefficient (and hence,

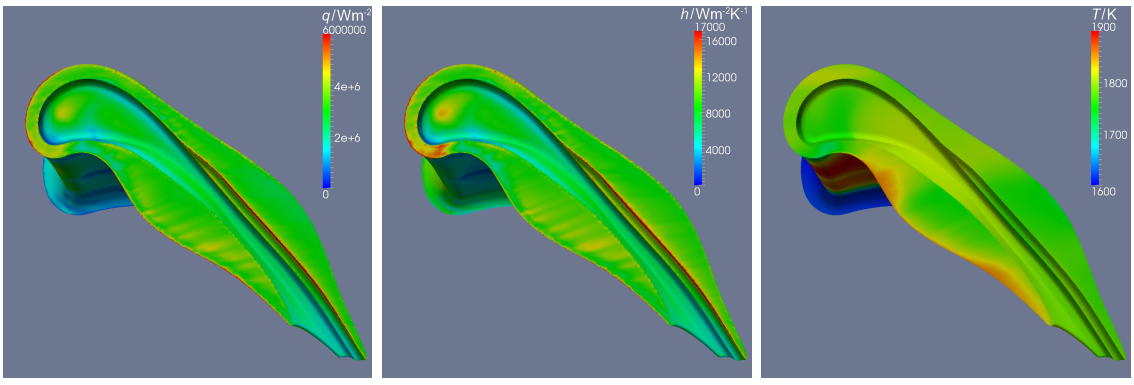

(a) Heat flux
Original mesh

(b) Heat transfer coefficient
Original mesh

(c) Adiabatic wall temperature
Original mesh

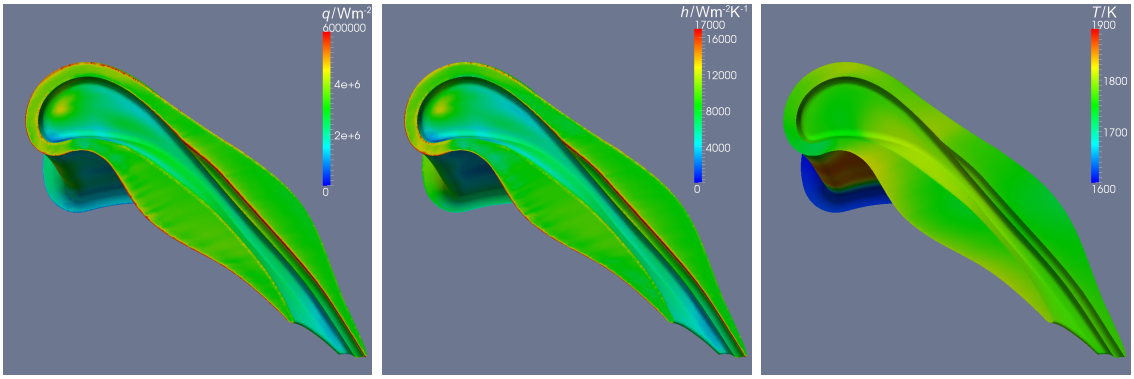

(d) Heat flux
Refined mesh

(e) Heat transfer coefficient
Refined mesh

(f) Adiabatic wall temperature
Refined mesh

Figure 4.8: Mesh sensitivity comparison—Heat transfer predictions

heat flux) caused by flow attachment, both on the pressure side rim and the cavity floor, is slightly attenuated in the refined mesh. The variations in the adiabatic wall temperature distribution over the blade tip are also less pronounced with the finer mesh. However, most importantly, the shape of the distributions predicted by each of the meshes are the same. The area-averaged values of the heat transfer parameters over the blade tip (from ∼90% span outwards) are reported in table 4.2.

Pathlines showing the flow structure in the cavity and the over-tip leakage flow are plotted in figure 4.9. There are again slight differences in the predicted flow paths shown between the two cases. The most obvious of these is that the angle of the over-tip leakage flow towards the rear of the blade tip deviates further from the axial

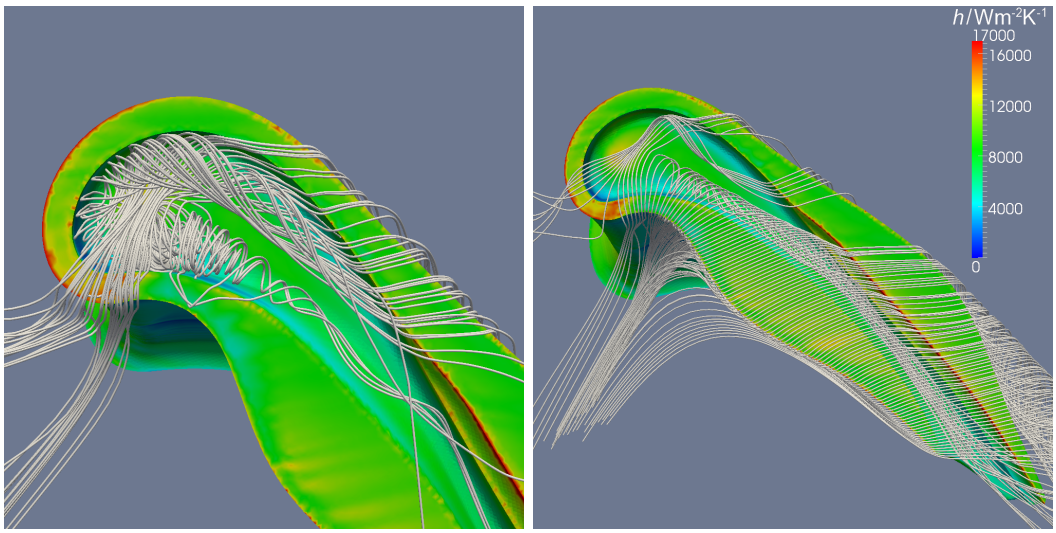

(a) Cavity flow pathlines
Original mesh

(b) Over-tip leakage pathlines
Original mesh

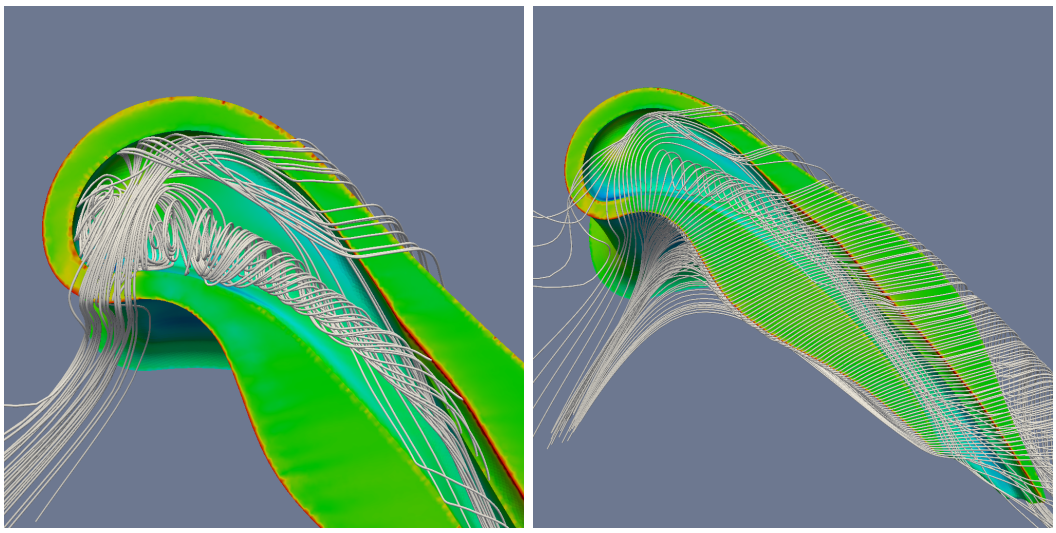

(c) Cavity flow pathlines
Refined mesh

(d) Over-tip leakage pathlines
Refined mesh

Figure 4.9: Mesh sensitivity comparison—Pathlines of over-tip flow

direction in the simulations performed with the refined mesh (figure 4.9d). However, the most important observation is that the predicted flow structure is identical between the two meshes, particularly in the very sensitive front portion of the blade tip cavity (figures 4.9a and 4.9c).

From this study of mesh sensitivity, it can be seen that a small degree of mesh sensitivity is present in the solution. Neither the shape of heat transfer distributions, nor the predicted flow structure are significantly altered with mesh refinement, however. As no suitable experimental dataset was available to allow for the validation of the simulations and the study was hence intended to be comparative rather than quantitative in absolute terms, the small extent of mesh sensitivity exhibited by the simulations run using the original mesh was considered to be acceptable, given the reduction in computational time required to achieve a converged solution.

4.4 Results

4.4.1 Aerodynamic efficiency

In order to compare the aerodynamic performance and tip gap efficiency exchange rates of the different blade tip designs, an exit calculation plane approximately one axial chord downstream of the trailing edge was used, as shown in figure 4.10a. This therefore represents a partially mixed-out plane, in which the footprint of the blade wake and the various vortices are still clearly visible, as can be seen in figure 4.10b. The inlet plane used in calculation of efficiencies was the computational inlet plane.

The row efficiency is defined as

$$\eta_{\mathrm{R}} = \frac{\Delta h}{\Delta h_{\mathrm{s}}} \tag{4.2}$$

which, with an assumption of constant C_{p} and γ, is calculated as

$$\eta_{\mathrm{R}} = \frac{\Delta T}{\Delta T_{\mathrm{s}}} = \frac{\Delta T}{T_{\mathrm{i}} \left(\frac{P_{\mathrm{o}}}{P_{\mathrm{i}}} \right)^{\frac{\gamma-1}{\gamma}}} \tag{4.3}$$

Quantities were mass-averaged over the inlet and outlet planes before the calculation of row efficiency. Two definitions of Δh (and hence, ΔT) can be used, as explained

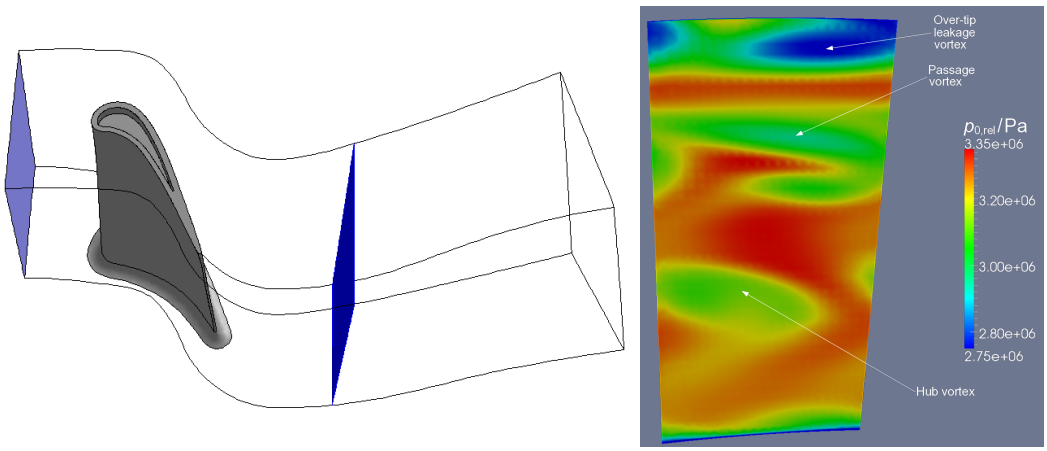

(a) Location of inlet and exit calculation planes

(b) Example exit relative total pressure distribution

Figure 4.10: Planes used for aerodynamic efficiency calculations

in Young and Horlock (2006); either $\Delta h = h_{0\mathrm{i,rel}} - h_{\mathrm{o}}$, which compares the real and isentropic increases in kinetic energy through the blade row, or $\Delta h = h_{\mathrm{i}} - h_{\mathrm{o}}$, which compares the predicted exit kinetic energy against the ideal case. These two definitions of efficiency are referred to as the total-to-static efficiency, $\eta_{\mathrm{R,TS}}$, and the static-to-static efficiency, $\eta_{\mathrm{R,SS}}$, respectively. Although these two definitions give slightly different absolute values, they are compatible in that the predicted trends are consistent across both.

From the calculated row efficiency, an inferred stage efficiency can be determined by the definition given in Harvey (2004)

$$\begin{aligned}\eta_{\mathrm{St}} &= \frac{\left(\frac{\Delta T_{0\mathrm{St,abs}}}{T_{0\mathrm{NGVin}}}\right)}{1-\left[\left(1-\frac{\Delta T_{0\mathrm{St,abs}}}{T_{0\mathrm{NGVin}}}\right)\left(1-\frac{\gamma-1}{2}\mathrm{M}_{\mathrm{i}}^2\left(\frac{1}{\eta_{\mathrm{N}}}-1\right)\right)\left(1-\frac{\gamma-1}{2}\mathrm{M}_{\mathrm{o}}^2\left(\frac{1}{\eta_{\mathrm{R}}}-1\right)\right)\right]} \\ &= \frac{T_{0\mathrm{NGVin,abs}}-T_{0\mathrm{o,abs}}}{T_{0\mathrm{NGVin,abs}}-\left[T_{0\mathrm{o,abs}}\left(1-\frac{\gamma-1}{2}\mathrm{M}_{\mathrm{i}}^2\left(\frac{1}{\eta_{\mathrm{N}}}-1\right)\right)\left(1-\frac{\gamma-1}{2}\mathrm{M}_{\mathrm{o}}^2\left(\frac{1}{\eta_{\mathrm{R}}}-1\right)\right)\right]}\end{aligned} \tag{4.4}$$

This expression compares the actual decrease in absolute total temperature, and hence total enthalpy, across the turbine stage to the decrease in absolute total temperature for an isentropic process operating with the same exit Mach number; i.e.

how much specific work would be extracted by the turbine stage if both the NGV and rotor were 100% efficient. This can be seen by the following manipulation of the factors found in the denominator

$$\begin{aligned} 1 - \frac{\gamma - 1}{2}\mathrm{M}^2 \left(\frac{1}{\eta} - 1\right) &= 1 + \frac{\gamma - 1}{2}\mathrm{M}^2 - \frac{1}{\eta}\frac{\gamma - 1}{2}\mathrm{M}^2 \\ &= \frac{T_0}{T} - \frac{T_0 - T}{\eta T} \\ &= \frac{T_0}{T} - \frac{T_0 - T_\mathrm{s}}{T} \\ &= \frac{T_\mathrm{s}}{T} \end{aligned} \tag{4.5}$$

where the total temperature is taken at the inlet to the blade or vane row and the Mach number and static quantities are taken at the exit.

For clarity, only the static-to-static row efficiency has been used in the calculation of stage efficiency; however, either definition of row efficiency could be used. A constant value of 90.9% was assumed for η_N, which is typical of current NGV efficiency. A tip gap efficiency exchange rate could then be established as $\frac{\Delta \eta_\mathrm{St}}{\Delta \frac{g}{H}}$.

Since these CFD simulations are not validated against experimental measurements, the absolute values of predicted efficiency cannot be trusted to be correct. However, it is the *comparison* between results that is important; both in terms of the relative efficiency at a given tip gap (as this determines which design is most appropriate for an engine with a given design tip clearance) and the tip gap efficiency exchange rate (which indicates the likely degradation in performance over the lifetime of an engine or at different points in a typical engine cycle).

$\eta_\mathrm{R,TS}$ and $\eta_\mathrm{R,SS}$ are plotted in figure 4.11 for the three geometries at tip gaps between 0.25 mm and 0.75 mm. As stated previously, it is evident that although there is clearly an offset between the absolute values of the two definitions of η_R, the trends of the two sets of data, and hence the conclusions that can be drawn from them, are

Double squealer	2.03
Winglet	1.71
Squealet	1.95

Table 4.3: Predicted tip gap efficiency exchange rate

identical. The inferred stage efficiencies, η_{St}, were calculated using $\eta_{\mathrm{R,SS}}$ substituted into equation 4.4 and are plotted in figure 4.12.

The same trends are evident in both the predicted row efficiencies and the inferred stage efficiencies. As expected, the winglet design desensitises the stage efficiency to changes in the tip gap—in other words, for a given increase in tip gap, there is a greater degradation in efficiency using the double squealer design compared with the winglet tip. This is reflected in the smaller tip gap efficiency exchange rate for the winglet tip. The squealet tip, being a hybrid design, has an exchange rate that falls in the range between the double squealer and winglet tips, as expected. There is also an offset in the achieved efficiency, showing that the winglet tip performs better aerodynamically than the double squealer tip over the range of tip gaps investigated. This efficiency offset is largely maintained when the squealet tip is employed, whose predicted efficiency is much closer to that of the winglet than the double squealer tip. The crossover point in efficiency between the winglet and the squealet tip designs is predicted to be at a tip gap of $\sim$0.3 mm, although the exact location of the crossover in efficiency is extremely sensitive to small changes in the predicted efficiencies. The location of the crossover is a crucial metric for the potential application of such a design to a real engine, as it determines what range of tip gaps must be achieved and maintained in order to benefit aerodynamically from the introduction of the new design; however, since the predicted location is so sensitive even to very small changes in either the tip gap exchange rate or the absolute magnitude of efficiency, it is not possible to determine the location of the crossover point with confidence from these data.

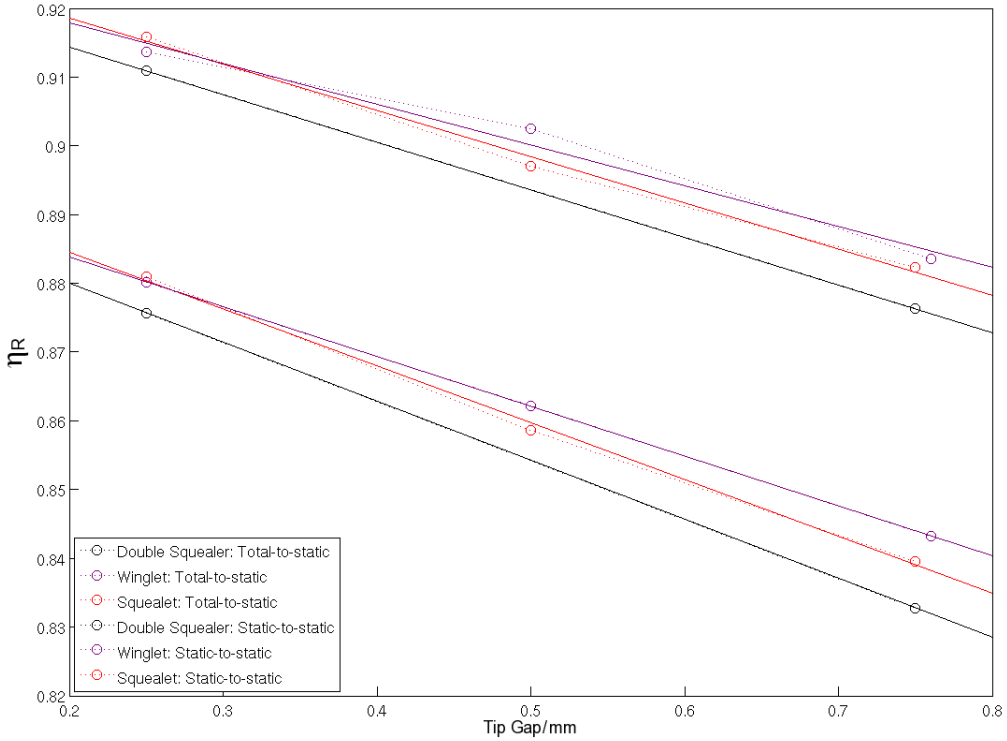

Figure 4.11: Variation in predicted row efficiency with tip gap

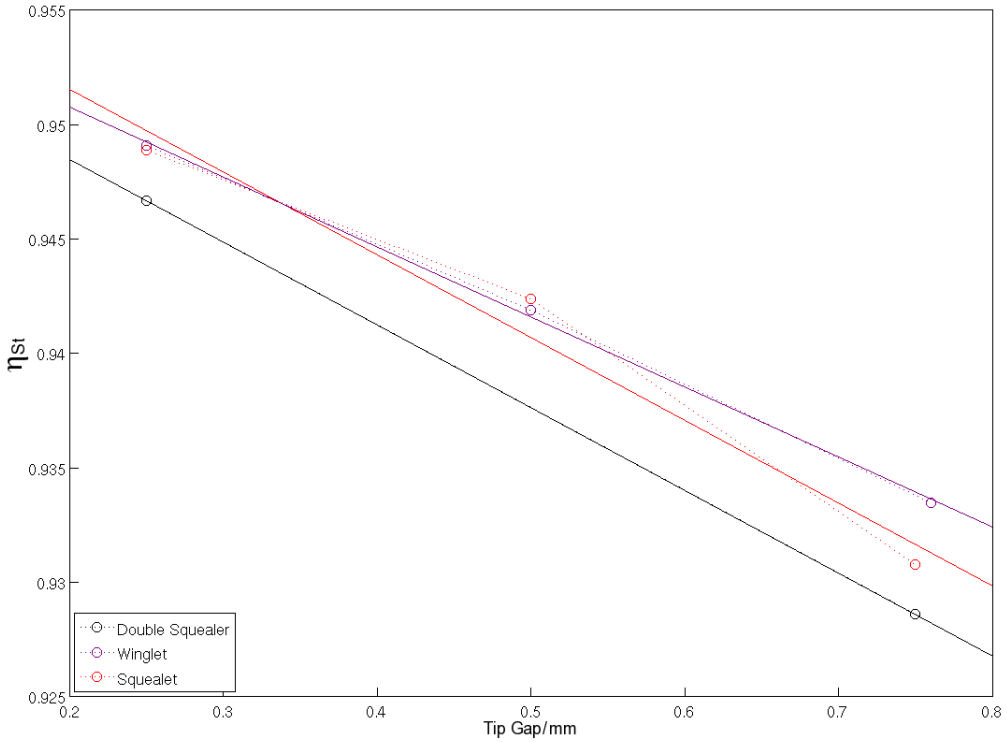

Figure 4.12: Variation in predicted stage efficiency with tip gap

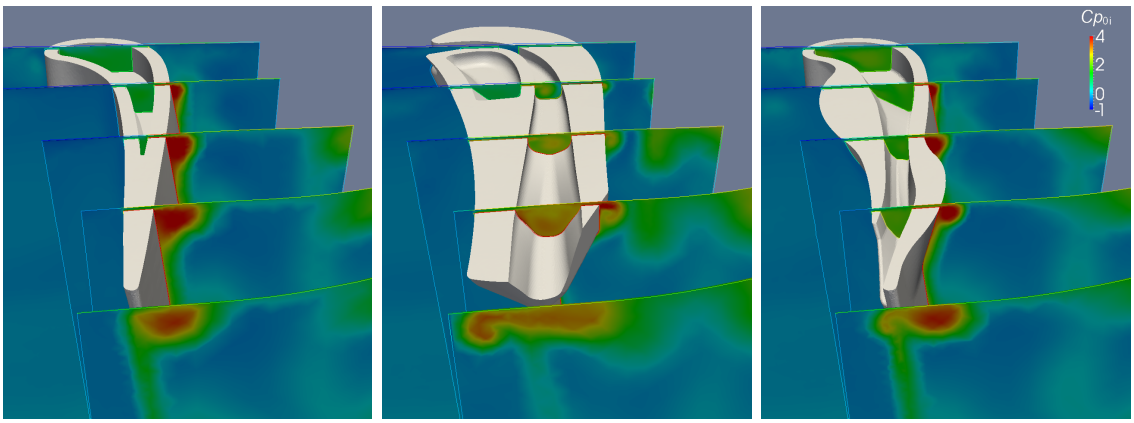

(a) Double squealer (b) Winglet (c) Squealet

Figure 4.13: Cp_{0i} contours at 0.25 mm tip gap

The differences in aerodynamic loss characteristics between the winglet and the squealet tips are caused by changes in the near-tip flowfield. Figure 4.13 shows contours of the pressure loss coefficient, Cp_{0i}, plotted on several transverse planes for the squealet tip and the winglet tip at the 0.25 mm tip gap. Cp_{0i} is defined as

$$Cp_{0i} = \frac{p_{0i,rel} - p_{0,rel}}{\left(\frac{1}{2}\rho v^2\right)_{i,rel}} \tag{4.6}$$

where inlet quantities are mass-averaged before the calculation of Cp_{0i}. With this definition, it should be noted that the pressure loss coefficient can be negative as it is referenced to the mass-averaged total pressure at the inlet.

The over-tip leakage vortex is much reduced in the case of the winglet tip, both in its extent and its depth, reflecting the better sealing capabilities of the winglet tip. This, in turn, likely explains the smaller tip gap efficiency exchange rate of that geometry, as the improved sealing renders the blade tip design relatively insensitive to variations in the tip gap. However, the open entrance to the gutter at the leading edge of the winglet channels more air through the gutter, giving a significantly higher flow velocity within the gutter compared to the other designs. As a result, there is a larger mixing loss within the gutter as the over-tip leakage flow meets the gutter flow with a

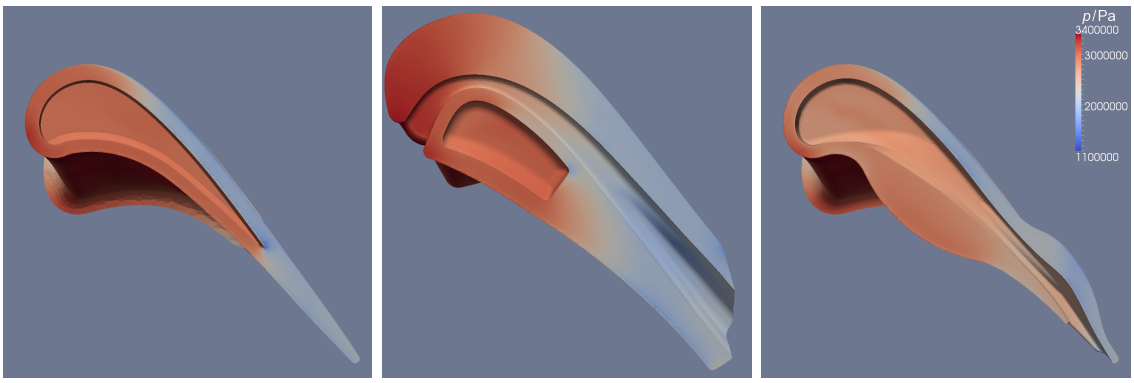

(a) Double squealer (b) Winglet (c) Squealet

Figure 4.14: Blade tip static pressure at 0.25 mm tip gap

greater mismatch in velocity. Thus, the improvement in aerodynamic efficiency due to the reduced over-tip leakage vortex is partially offset by the increased mixing losses within the tip gap itself. The blunt trailing edge of the pressure side of the winglet tip also has a significant contribution to the (uncooled) aerodynamic loss, leaving a large wake behind it. These three sources of loss (the over-tip leakage vortex, the gutter flow mixing losses and the blunt pressure side trailing edge wake) leave a relatively wide footprint in the pressure loss coefficient contours immediately downstream of the blade tip trailing edge.

The increased gutter flow velocity also results in a lower static pressure between the pressure side rim and the suction side rim for the winglet, as can be seen in figure 4.14. This produces a difference in the way the blade tips seal the flow; broadly speaking, it is the pressure side of the winglet tip that does the majority of the sealing, whereas the pressure drop is more evenly distributed across the pressure and the suction sides for the double squealer and squealet tips. This has a direct impact on the over-tip leakage flow velocities in the tip gap, shown in figure 4.15. The winglet tip yields a much higher peak over-tip leakage velocity, with transonic over-tip leakage flow over a much larger portion of the blade tip than the other two designs.

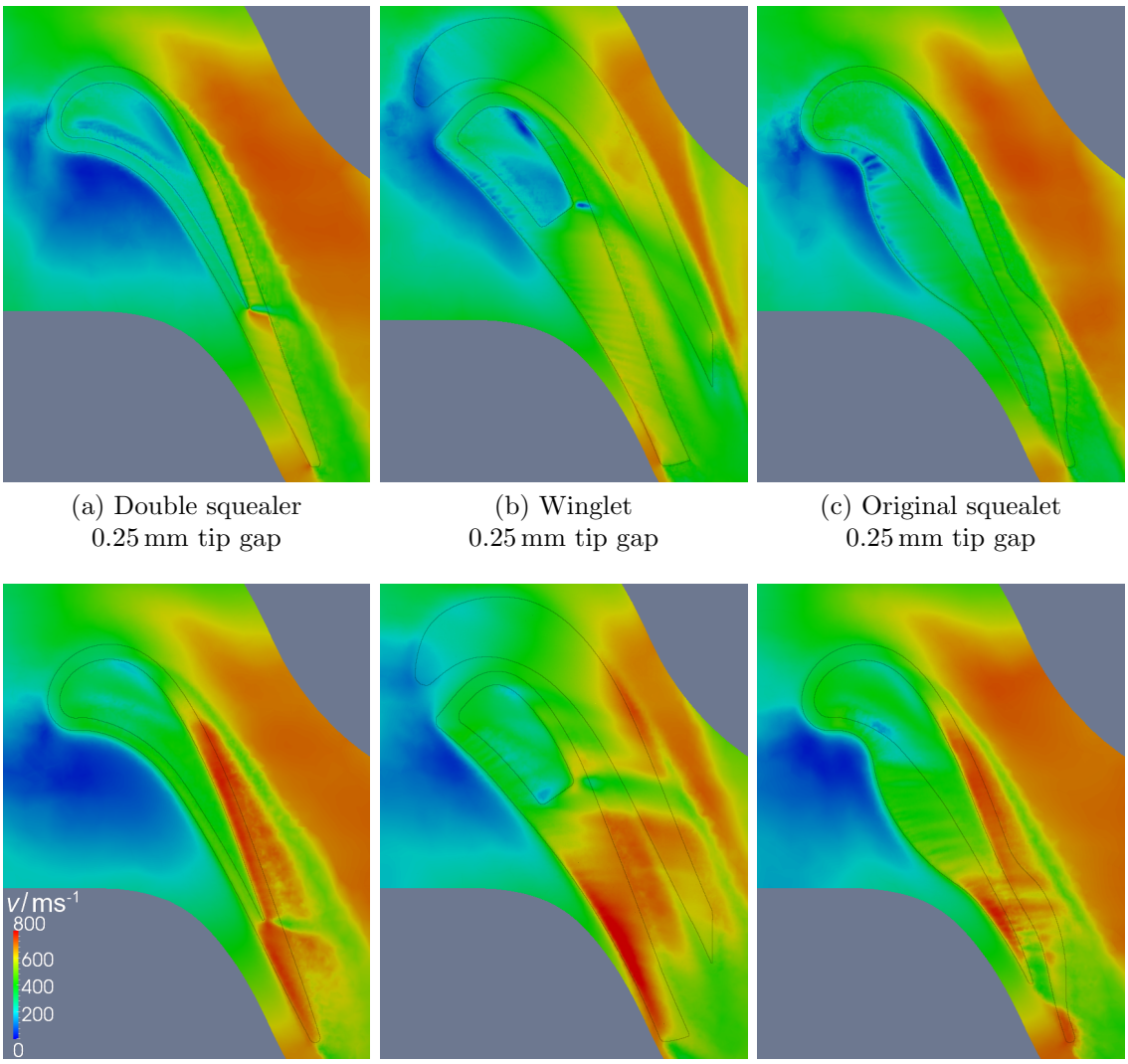

(a) Double squealer 0.25 mm tip gap

(b) Winglet 0.25 mm tip gap

(c) Original squealet 0.25 mm tip gap

(d) Double squealer 0.75 mm tip gap

(e) Winglet 0.75 mm tip gap

(f) Original squealet 0.75 mm tip gap

Figure 4.15: Mid-gap over-tip leakage velocity

The squealet tip is much more similar to the double squealer tip in its flowfield than the winglet tip. The major difference between the two is the open gutter at the rear of the cavity, which allows the squealet tip to maintain a separation between the pressure side and suction side rims right to the trailing edge, thereby slightly mitigating the very high over-tip leakage velocities found at the trailing edge of the double squealer.

4.4.2 Heat transfer

The main intention of this study was to improve the thermal behaviour of the blade tip in order to improve blade life and/or reduce cooling requirements. While the major factor that contributes to the achievement of these goals is the overall heat load to the blade tip, both the adiabatic wall temperature and the heat transfer coefficient distributions are important factors that must be decoupled in order to gain a sufficient understanding of the thermal load on the blade tip to allow it to be controlled. For each tip gap and geometry combination, two simulations were therefore run; one in which the blade and casing surfaces were adiabatic and one where they had constant temperatures imposed—1400 K for the blade and 1500 K for the casing. The local adiabatic wall temperature could then be found directly as the static temperature at the wall from the simulation with adiabatic walls. To find the heat transfer coefficient, an assumption that the imposed wall temperature did not affect the flowfield needed to be made (Day, 1997). The heat transfer coefficient could then be calculated as

$$h = \frac{q_{\mathrm{ct,w}}}{T_{\mathrm{ct,w}} - T_{\mathrm{ad,w}}} \tag{4.7}$$

The overall heat flux to the blade surfaces is presented in figure 4.16, which, when decomposed as described above, produces the heat transfer coefficients plotted in figure 4.17 and the adiabatic wall temperatures plotted in figure 4.18. The Nusselt number based on blade axial chord is also shown in figure 4.19. The Nusselt number is calculated using a local conductivity based on the adiabatic wall temperature.

The shapes of the overall heat flux distributions are very similar to those of the heat transfer coefficient distributions, suggesting that the heat transfer coefficient is the major factor controlling heat transfer to the blade tip and not the driving gas temperature. Indeed, the adiabatic wall temperature distributions are relatively uniform over the blade tip surfaces for all three geometries; although there is some spatial variation, it is not as significant as the variation found in the heat transfer

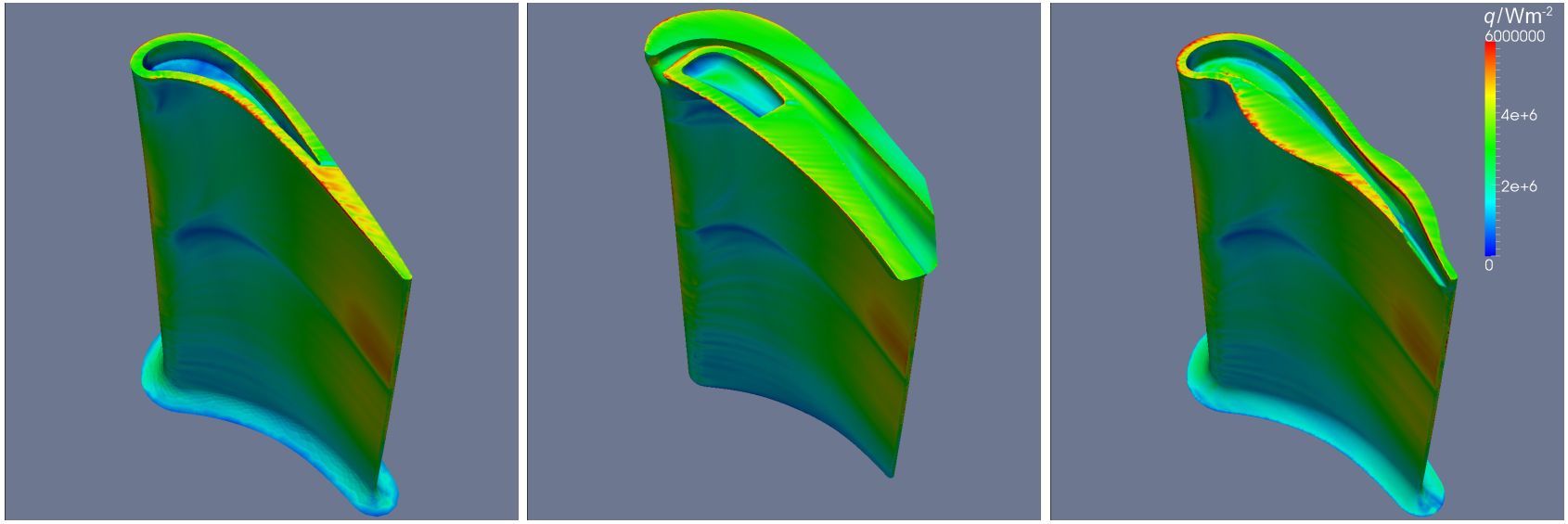

(a) Double Squealer
0.25 mm tip gap

(b) Winglet
0.25 mm tip gap

(c) Original Squealet
0.25 mm tip gap

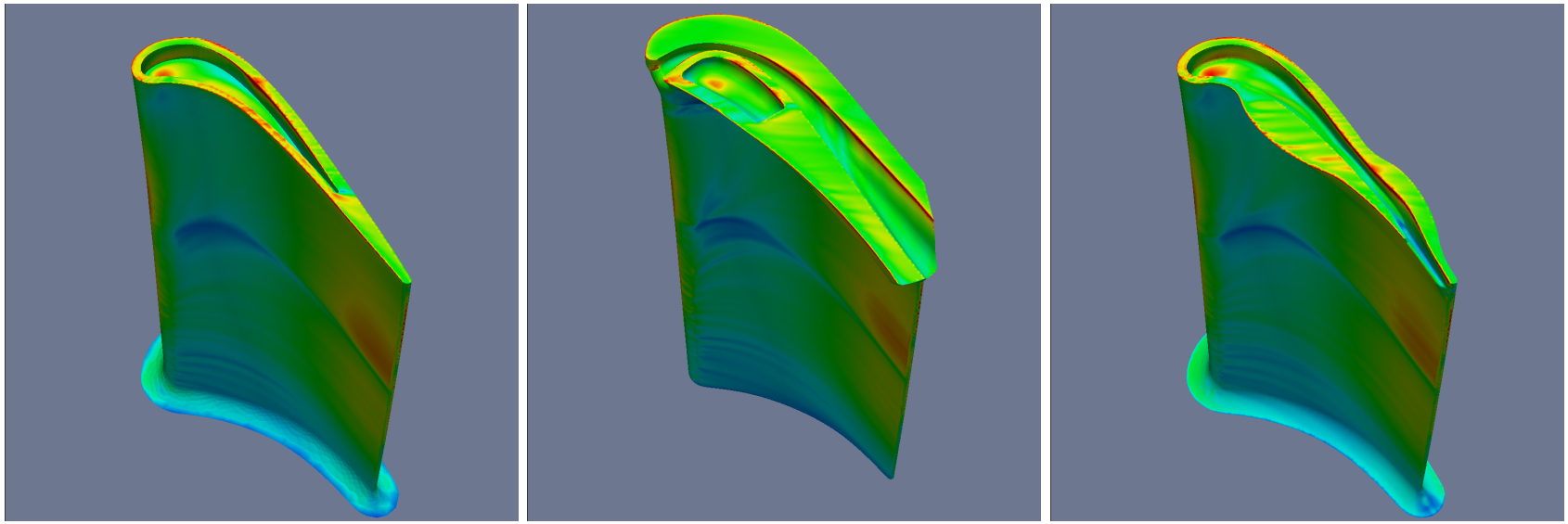

(d) Double Squealer
0.75 mm tip gap

(e) Winglet
0.75 mm tip gap

(f) Original Squealet
0.75 mm tip gap

Figure 4.16: Overall heat flux to blade tip

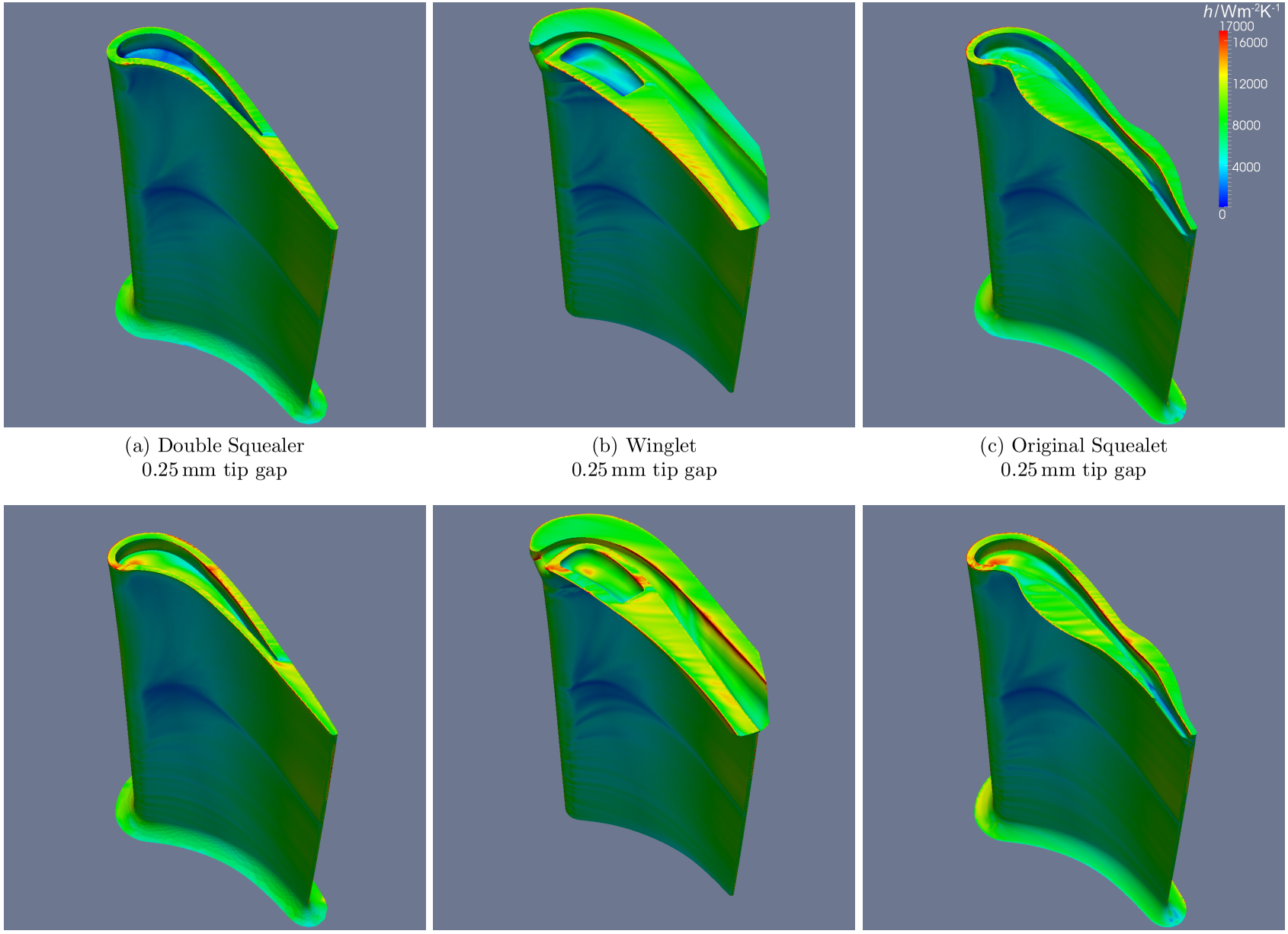

(a) Double Squealer
0.25 mm tip gap

(b) Winglet
0.25 mm tip gap

(c) Original Squealet
0.25 mm tip gap

(d) Double Squealer
0.75 mm tip gap

(e) Winglet
0.75 mm tip gap

(f) Original Squealet
0.75 mm tip gap

Figure 4.17: Heat transfer coefficient

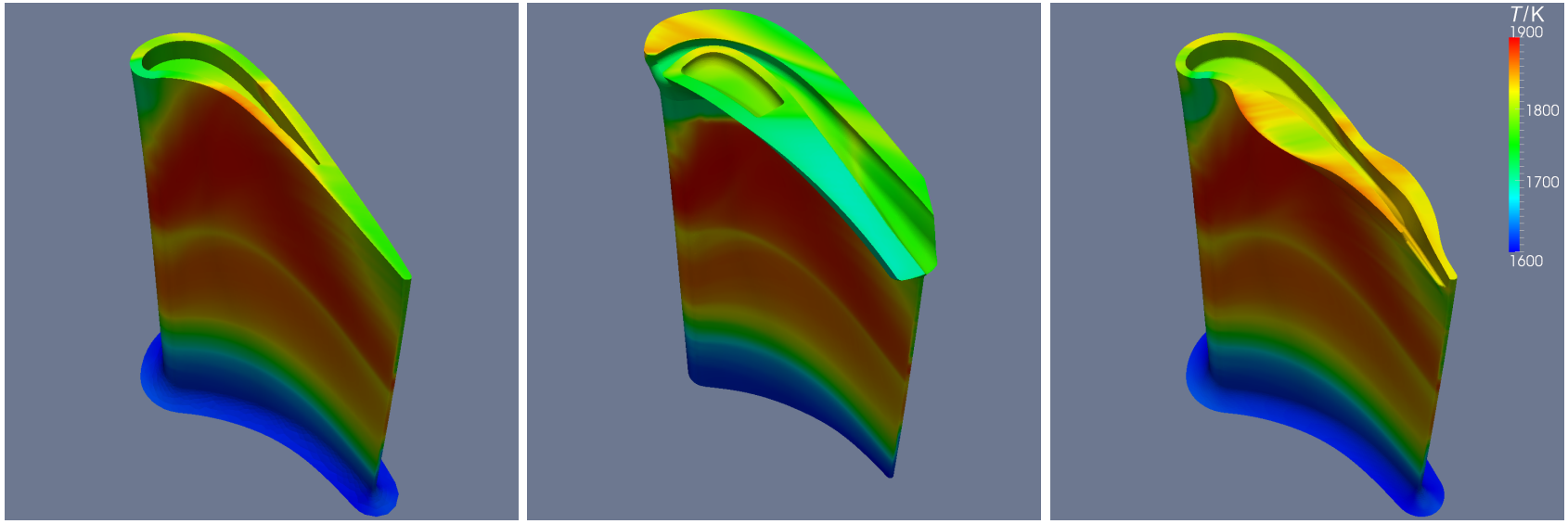

(a) Double Squealer
0.25 mm tip gap

(b) Winglet
0.25 mm tip gap

(c) Original Squealet
0.25 mm tip gap

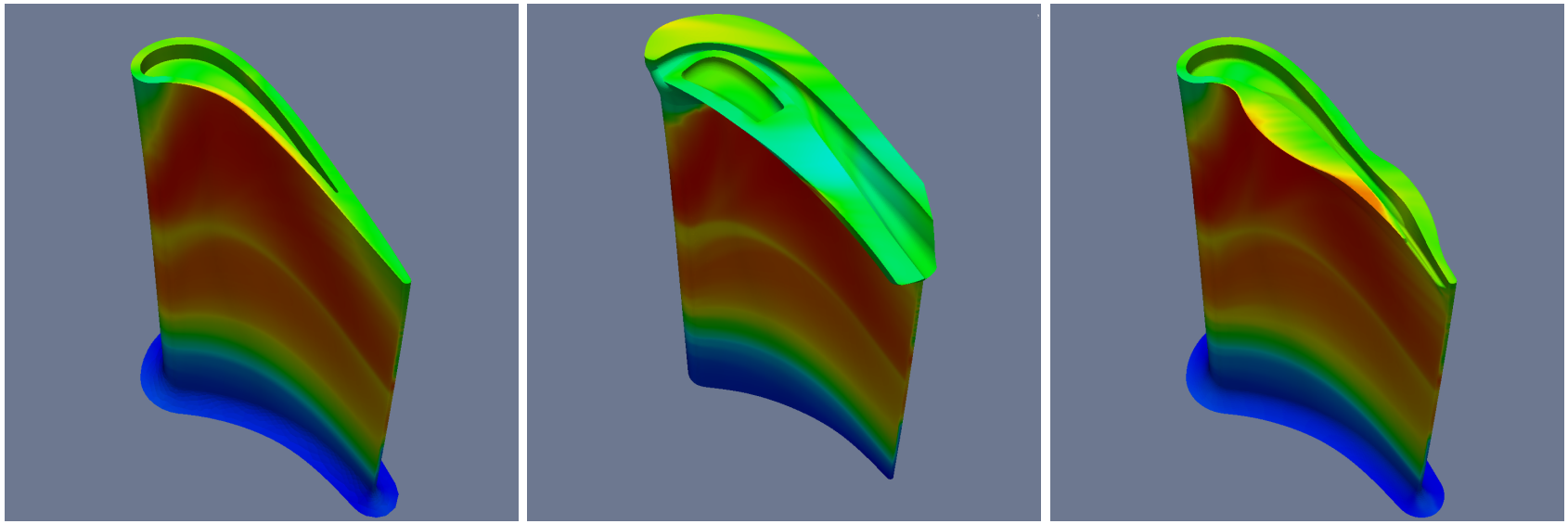

(d) Double Squealer
0.75 mm tip gap

(e) Winglet
0.75 mm tip gap

(f) Original Squealet
0.75 mm tip gap

Figure 4.18: Adiabatic wall temperature

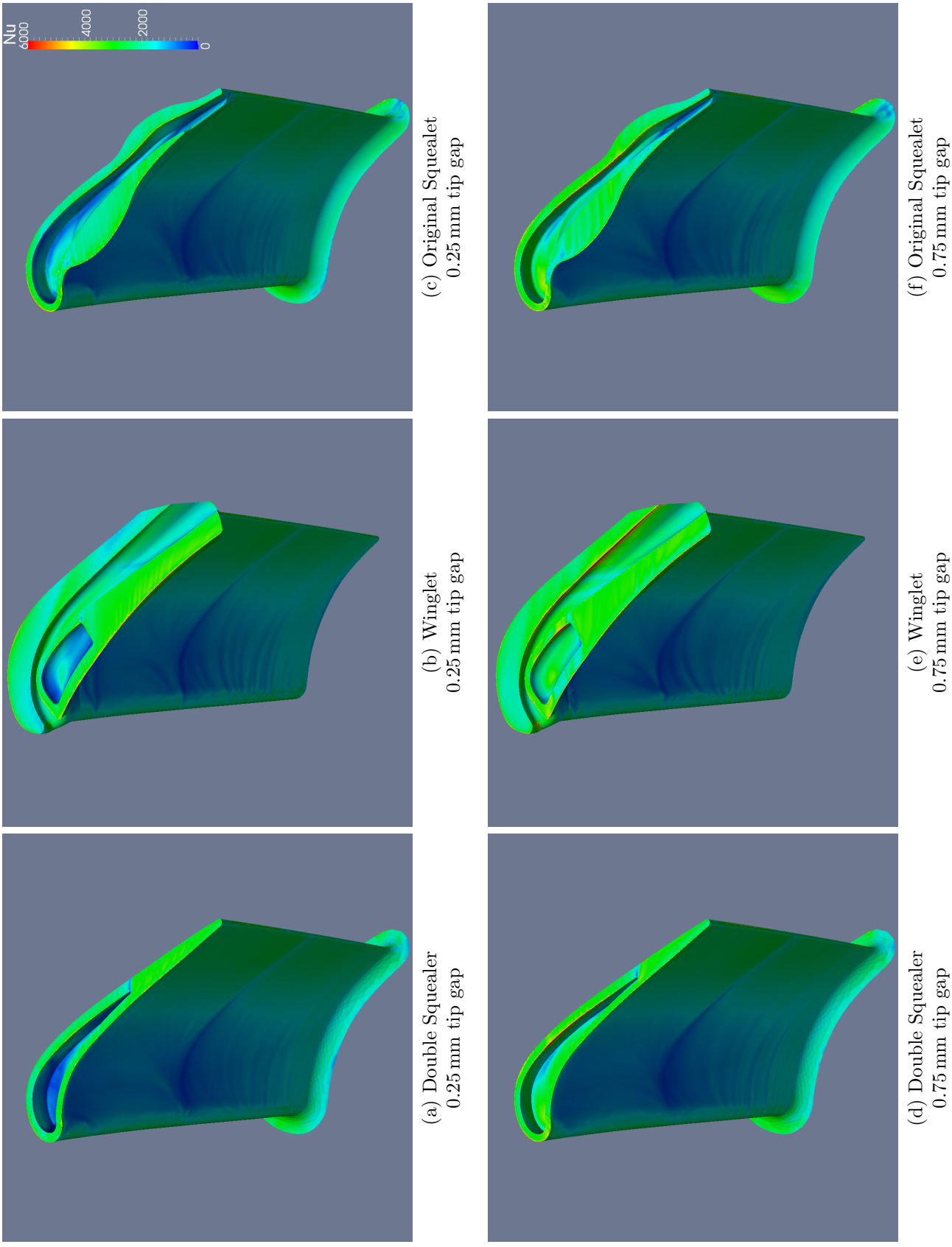

(a) Double Squealer 0.25 mm tip gap

(b) Winglet 0.25 mm tip gap

(c) Original Squealet 0.25 mm tip gap

(d) Double Squealer 0.75 mm tip gap

(e) Winglet 0.75 mm tip gap

(f) Original Squealet 0.75 mm tip gap

Figure 4.19: Nusselt number

coefficient distributions. High heat transfer coefficients are observed in all three geometries on the pressure side-facing, inner edge of the suction side rims, caused by the impingement of the over-tip leakage flow. Recessed areas, such as the cavity and gutter floors, generally exhibit much lower levels of heat transfer coefficient, being largely sheltered from the high velocity over-tip leakage flows. There are significant impingement hot spots on these surfaces, however, near the leading edge of the double squealer and squealet tips and in the cavity of the winglet tips, where the over-tip leakage flow separates from the upstream rim and reattaches on to the floor.

Across all three geometries, the same trends in heat transfer are seen as the tip gap increases from 0.25 mm to 0.75 mm. The heat transfer coefficients on the tip broadly increase with increasing clearance, particularly on the radially outermost surfaces. This increase in heat transfer coefficient can be attributed to the increased over-tip leakage flow velocities seen in the tip gap region at the larger tip clearance, shown in figure 4.15. There are also significantly stronger impingements on to the floors of the cavities in all three designs, resulting in more pronounced local peaks in the contours of heat transfer coefficient. Such hot spots can exacerbate the problem of thermal loading by introducing thermal stresses that further reduce the lifetime of a blade tip. On the blade aerofoil surfaces away from the near-tip region, there is no discernable effect of changing tip gap or blade tip geometry on the heat transfer coefficient. This confinement of the effect of tip geometry to a relatively small region near the blade tip is as expected and has previously been reported in the open literature (for example, Yamamoto et al. (1994b)).

The increase in heat transfer coefficient is slightly offset by a small decrease in the average driving gas temperature. However, the drop in the adiabatic wall temperature is small compared to the changes in heat transfer coefficient; the average adiabatic wall temperature for the double squealer blade tip (from ∼90% span outwards) is reduced by 14.6 K. There is therefore an overall increase in heat flux with tip gap, as seen in figure 4.16. The reduction in adiabatic wall temperature at the larger tip

gap is not caused by a drop in viscous heating due to decreased shear as might be expected; it is still observable if the simulations are run without viscous heating terms. Its origin is a combination of two other factors related to the reduced shear. The first is purely one of convection; the relative movement of the casing over the blade tip has the effect of reducing the near-tip angle of incidence, which has a large effect on the way that flow leaks over the blade tip. Figure 4.20 shows pathlines seeded from the cooler, near-casing region for the double squealer geometry. This relatively cool flow leaks over the blade tip and covers around two-thirds of the tip in the case of the 0.75 mm tip gap, but only spills over a very small portion of the trailing edge at the smaller tip clearance. The over-tip leakage flow, in the latter case, is thus comprised exclusively of the hotter flow that migrates from close to mid-span up the pressure side of the aerofoil to the tip region. The second reason also results from the change in incidence angle, which reduces the near-tip blade loading at the smaller tip gap. As a result, over-tip leakage flow expands to a lower pressure at larger tip gaps, thereby resulting in a lower temperature. This increase in the expansion of the over-tip leakage flow is shown in figure 4.21.

The heat flux and heat transfer coefficient distributions in figures 4.16 and 4.17 have a distinct striping parallel to the over-tip leakage flow direction on all of the large, flat areas of the blade tips—this is most easily seen on the winglet and squealet pressure side extensions. This feature is clearly unrealistic and is a computational artefact that would be impossible to explain physically. Its roots lie in the time-steady formulation of the simulations and is explained by figure 4.22. The over-tip leakage flow spilling over the pressure side edge (white pathlines) interacts with the separation bubble flow along its upper edge (blue pathlines). This interaction is forced by the time-steady formulation to be resolved as a coherent, spatially repeating feature where the over-tip leakage flow periodically breaks through over the separation bubble and is channeled into these narrow streams, which are seen to line up with the stripes in the heat flux distribution. This striping may therefore be interpreted as an artefact of

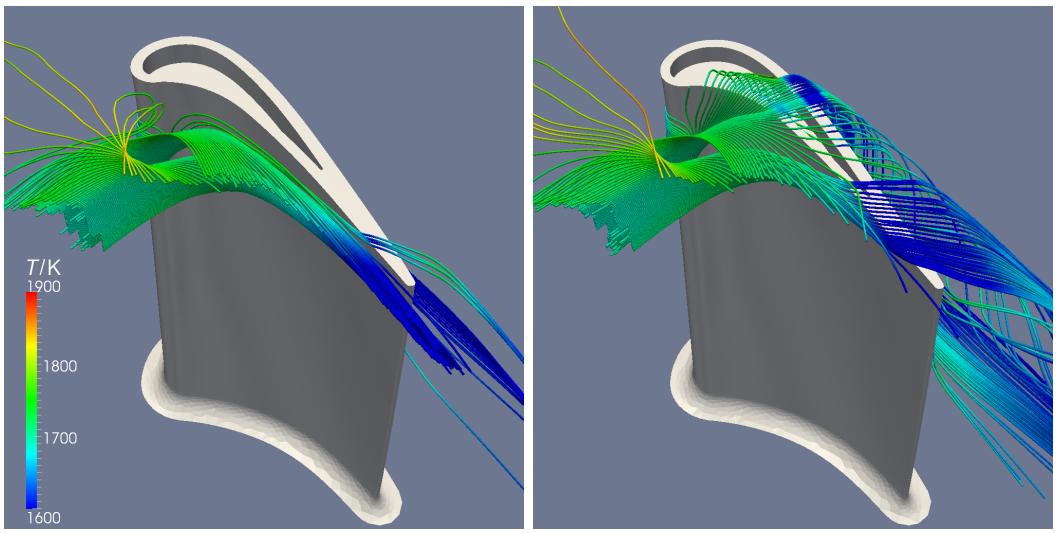

(a) 0.25 mm tip gap (b) 0.75 mm tip gap

Figure 4.20: Effect of tip gap on near-casing flow
(Pathlines are seeded from identical locations)

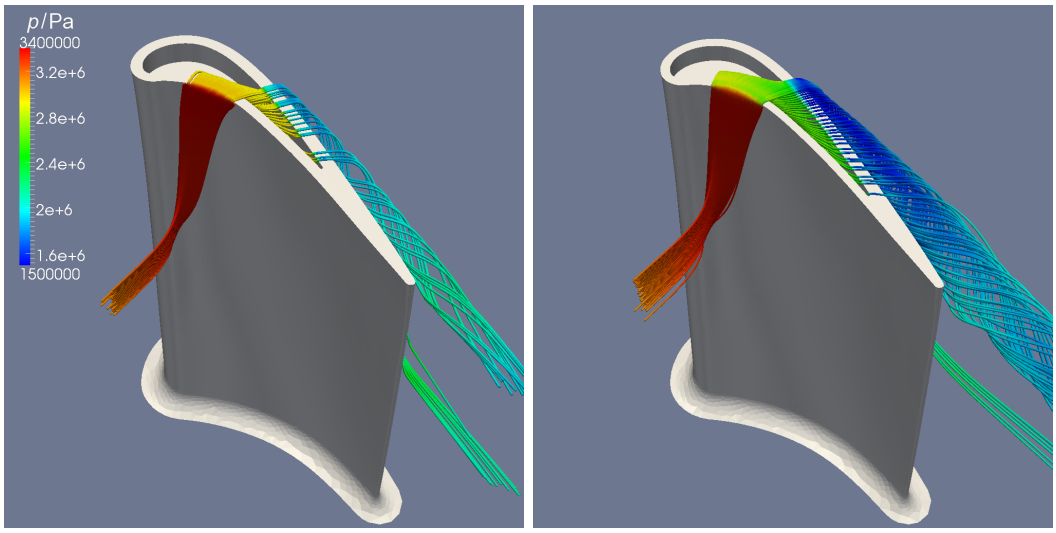

(a) 0.25 mm tip gap (b) 0.75 mm tip gap

Figure 4.21: Effect of tip gap on over-tip leakage flow expansion
(Pathlines are seeded from identical locations)

mesh sensitivity; indeed, the prominence of this striping is significantly reduced in the heat transfer results for the refined mesh, shown in figure 4.8d. As identical meshing strategies and cell sizing had been applied to each geometry and tip gap combination,

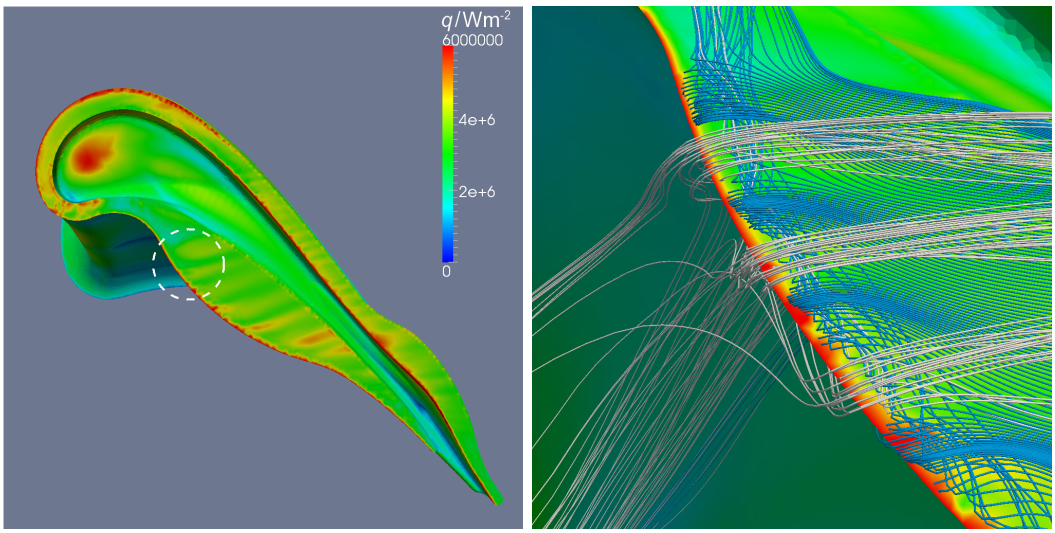

Figure 4.22: Stripes in heat flux on squealet at 0.75 mm tip gap
(blue pathlines: separation bubble flow, white pathlines: over-tip leakage flow)

the effect of this mesh sensitivity should be consistent across all cases and it should not affect the reported comparisons.

The region of extremely high heat transfer located on the inner edge of the suction side rim of all three geometries poses an especially difficult problem for blade tip cooling. The cause of this high thermal load is the impingement of over-tip leakage flow directly on to the corner as it crosses from the pressure side to the suction side. The over-tip leakage flow is then divided by the sharp corner, with part of the flow being directed into the cavity/gutter and the remainder continuing over the suction side rim and rolling up into the over-tip leakage vortex. The streamlines at the corner therefore split and diverge, as illustrated in figure 4.23. Any cooling air bled out on to either the cavity wall or the suction side squealer rim would hence be convected away from the area where it is most needed, leaving the rim exposed and vulnerable to damage.

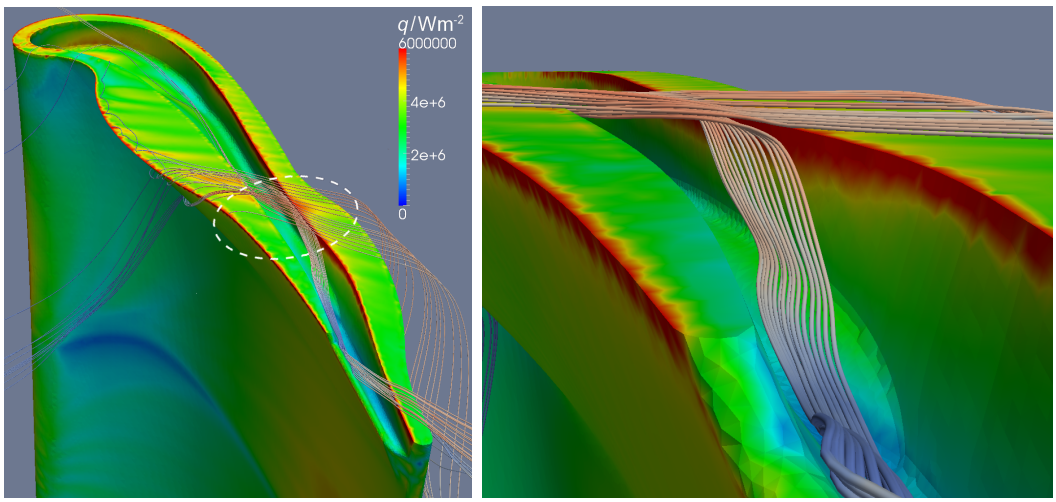

Figure 4.23: Blade heat flux and diverging flow over squealet inner suction side rim

4.5 Squealet tip design revision

Based on the generally encouraging results produced by the initial CFD simulations of the first squealet design, a second iteration of the squealet geometry was produced. The design revision was again performed by Rolls-Royce, with guidance from the author. The revised squealet tip geometry, shown in figure 4.24b, takes into account some additional manufacturing constraints that had been neglected in the initial design process, while also incorporating some new features aimed at tackling problem areas highlighted by the CFD results. The most obvious of these new additions is the tip shelf along the inner edge of the suction side rim. This feature was introduced in an effort to tackle the line of extremely high heat transfer coefficient caused by the impinging over-tip leakage flow by providing a feature that enables direct access to cooling air. This region would otherwise be impossible to cool, as coolant ejected elsewhere would be convected away from this edge by the diverging flow. The tip extension on the suction side was enlarged to accommodate internal features that supply the tip shelf with coolant. The pressure side extension was also slightly enlarged in an attempt to improve the control of the over-tip leakage flow. The plan area of

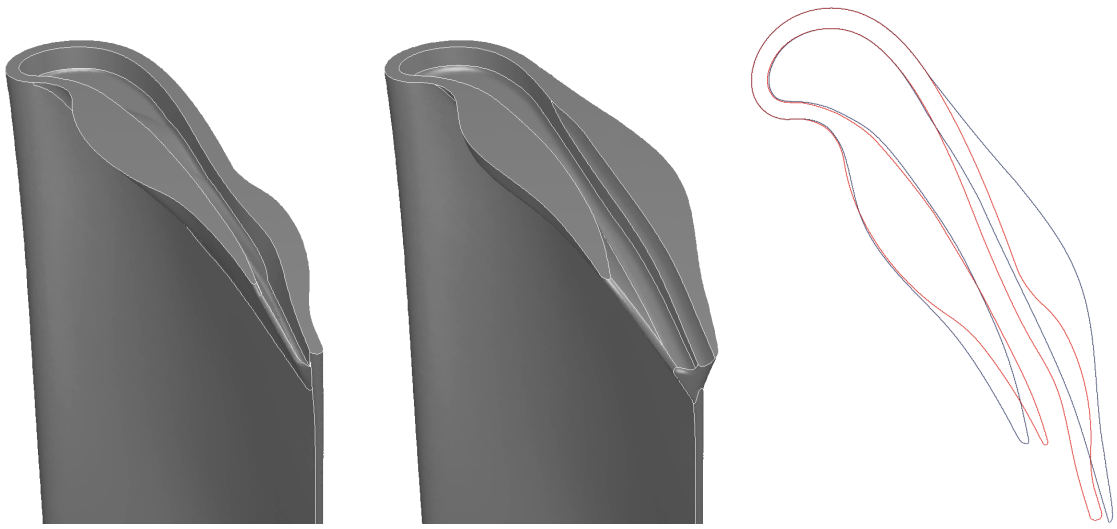

(a) Original squealet (b) Revised squealet (c) Plan area comparison (red: original; blue: revised)

Figure 4.24: Squealet tip geometry revision

the squealet tip (not including the tip shelf, shown in figure 4.24c) increased by 27% as a result of the widened extensions.

4.5.1 Aerodynamic efficiency

Figure 4.25 and figure 4.26 show the predicted static-to-static efficiencies. Once again, only static-to-static efficiencies are shown; precisely the same trends are evident in the total-to-static efficiencies.

The differences in the predicted tip gap efficiency exchange rates between all four geometries are very small, and a reasonably small peturbation in the result of a single simulation could potentially have a significant impact on the predicted tip gap efficiency exchange rate, relative to the observed differences. Some degree of caution is therefore advised in interpreting these data; these CFD predictions show that the aerodynamic sensitivities of the four tested blade tip geometries to tip clearance are similar, but the magnitudes—and possibly even the relative order—of their aerodynamic performances are not necessarily certain.

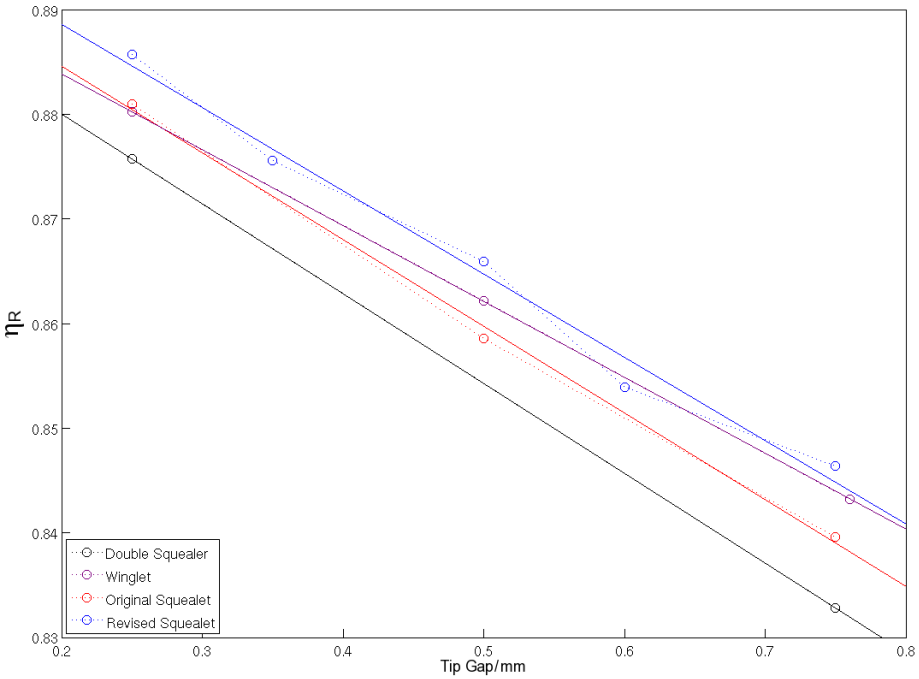

Figure 4.25: Variation in predicted row efficiency with tip gap

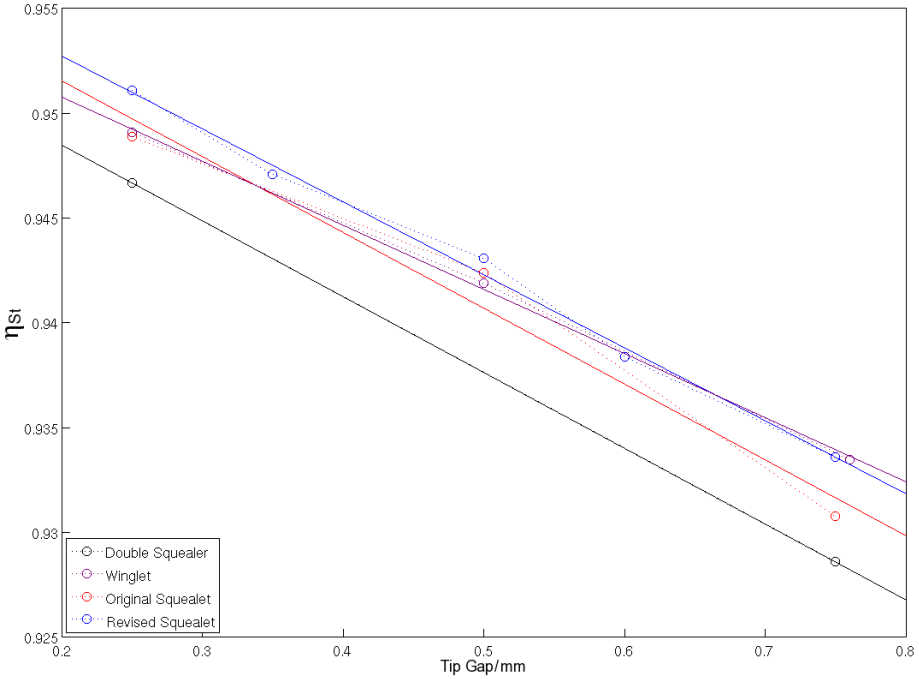

Figure 4.26: Variation in predicted stage efficiency with tip gap

Double squealer	2.03
Winglet	1.71
Original squealet	1.95
Revised squealet	2.03

Table 4.4: Predicted tip gap efficiency exchange rate

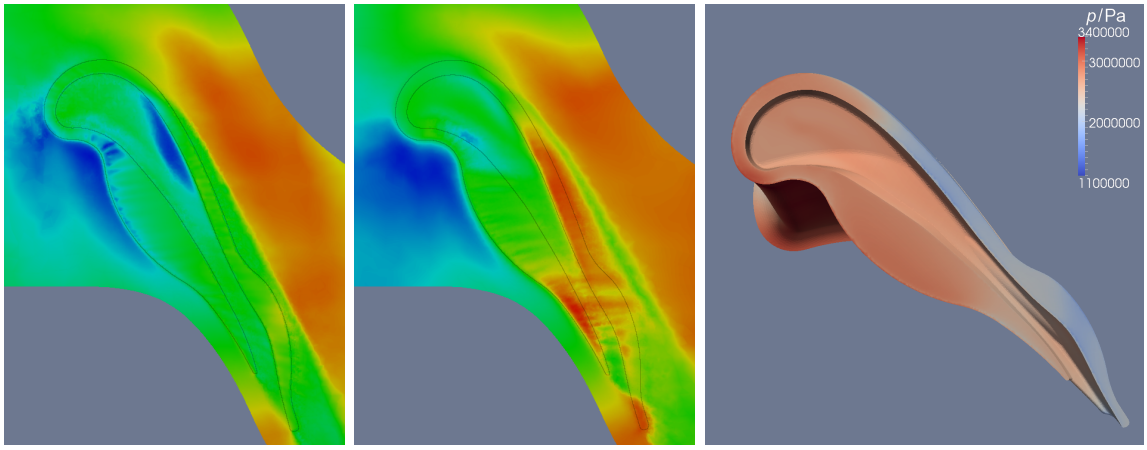

(a) Mid-gap over-tip velocity Original squealet 0.25 mm tip gap

(b) Mid-gap over-tip velocity Original squealet 0.75 mm tip gap

(c) Blade tip static pressure Original squealet 0.25 mm tip gap

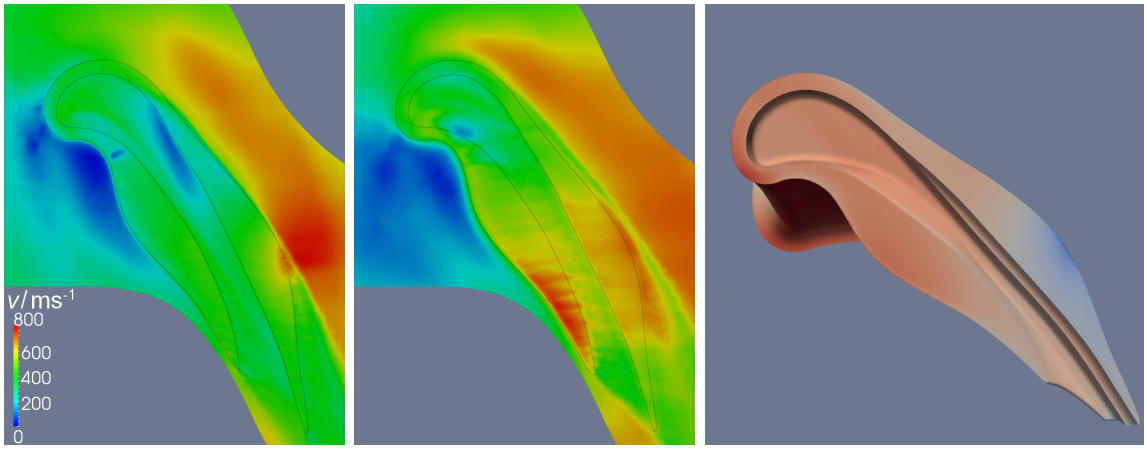

(d) Mid-gap over-tip velocity Revised squealet 0.25 mm tip gap

(e) Mid-gap over-tip velocity Revised squealet 0.75 mm tip gap

(f) Blade tip static pressure Revised squealet 0.25 mm tip gap

Figure 4.27: Blade tip static pressure and over-tip leakage velocity

The revised squealet tip has a very similar flow field to the original squealet tip from which it was derived, which has resulted in a similar tip gap exchange rate. The offset in efficiency is caused by an improvement in the sealing of the over-tip leakage flow, resulting in reduced over-tip leakage velocities over the tip gap and a reduced mass flow rate entering the high-loss over-tip leakage vortex; this is shown in figures 4.27d and 4.27e. The revised squealet design has larger tip extensions and is more similar to a winglet tip than the original squealet design, which produces a static pressure distribution somewhere between that of the original squealet design and the winglet tip, shown in figure 4.27f. The reasonably subtle changes in pressure distribution over the blade tip surface help reduce the high pressure gradient found over the mid-chord suction side rim on the original squealet design, which controls the high over-tip leakage velocities seen in that region previously.

Comparing the $Cp_{0\mathrm{i}}$ contours of the revised squealet, plotted in figure 4.28b, to those of the other geometries (figure 4.13), it can be seen that the loss development characteristics of the revised squealet tip design lie between those of the original squealet tip and the winglet tip geometries. The increased separation between the two squealet rims allows a greater degree of mixing of the over-tip leakage flow and an increased aerodynamic loss generation to occur in the gutter. This region of flow with high aerodynamic loss coefficient is convected to the trailing edge, resulting in a wider pressure loss wake downstream of the blade tip. This change, however, is relatively small and the shape of the wake profile remains much closer to that of the original squealet tip than the winglet tip.

4.5.2 Heat transfer

The heat load on the revised squealet tip is shown in figure 4.29, once again decomposed into heat transfer coefficient (figure 4.30) and adiabatic wall temperature (figure 4.31), with Nusselt number calculated as before (figure 4.32). The same trends seen in the heat transfer coefficient and adiabatic wall temperature distributions in the original

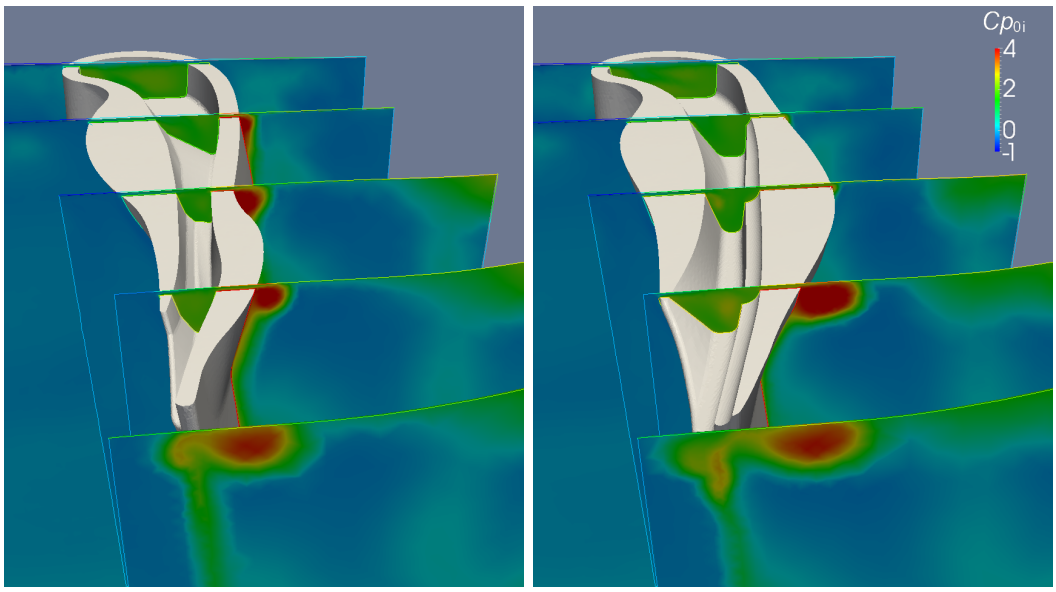

(a) Original squealet (b) Revised squealet

Figure 4.28: Cp_{0i} contours at 0.25 mm tip gap

three tip geometries are reproduced in the results for the revised squealet tip. The heat flux levels for the new design are very similar to those found previously, although the enlarged tip extensions increase the blade tip surface area, so the total heat transfer rate to the surface increases slightly from the initial squealet design to the revised blade tip. The wetted area of the revised squealet still remains significantly lower than the winglet tip, however, so the overall heat load (and hence, cooling requirement) is still reduced by comparison.

The overall thermal load incurred by the different tip geometries is summarised in the graphs in figure 4.33. These data are gathered for the tip surfaces from a radius of 0.3678 m (approximately 90% span) outwards. Figure 4.33a plots the total heat transfer rate into the blade tip, which is the single most important measure of thermal performance for each design, as it represents the total energy flux that must be removed from the blade by the cooling system (or be prevented from reaching the blade in the first place). Since the levels of heat transfer coefficient seen across the four designs are broadly similar, the majority of the difference in total heat transfer

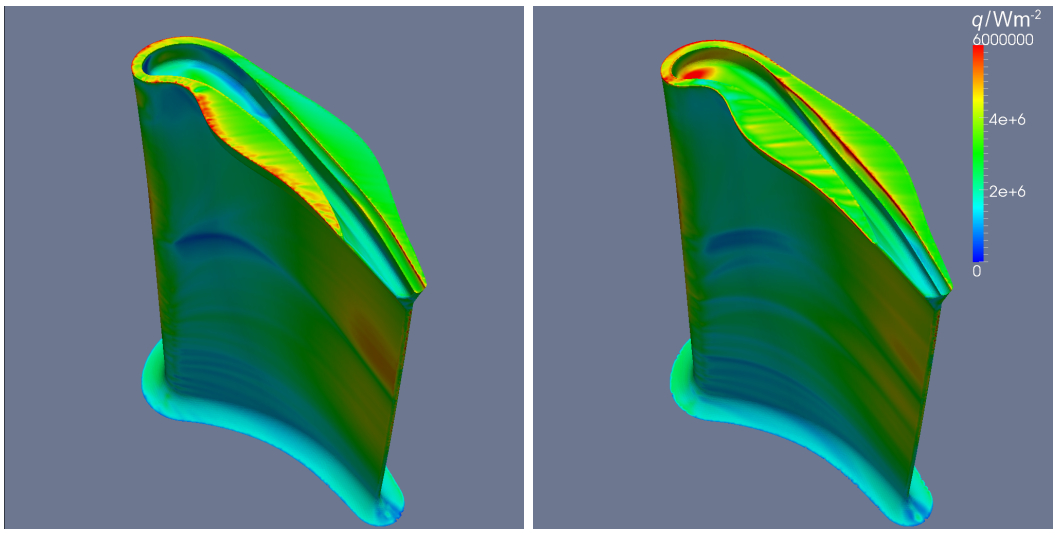

(a) 0.25 mm tip gap (b) 0.75 mm tip gap

Figure 4.29: Overall heat flux to revised squealet tip

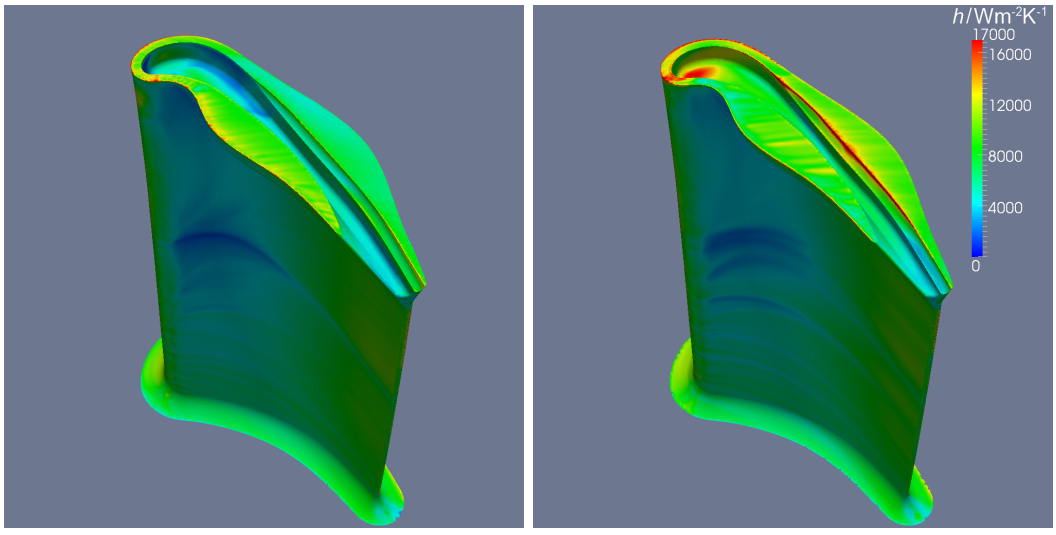

(a) 0.25 mm tip gap (b) 0.75 mm tip gap

Figure 4.30: Revised squealet heat transfer coefficient

rate seen reflects the differences in the wetted surface area. The revised squealet (at a tip gap of 0.5 mm) shows an increase in total heat load of 28% compared with the double squealer tip, but a reduction of 14% compared to the winglet tip; for comparison, the revised squealet has 24% more wetted area than the double squealer

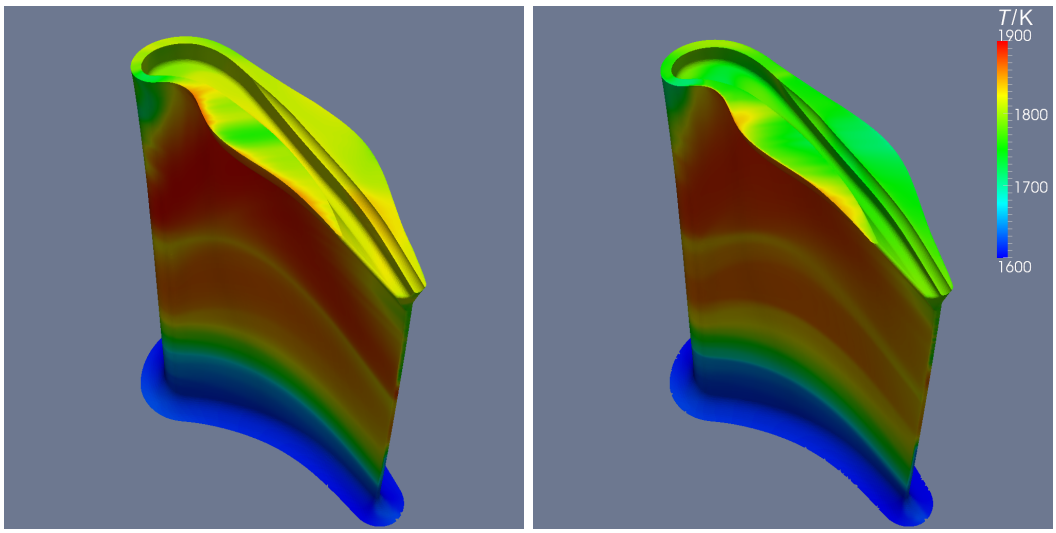

(a) 0.25 mm tip gap (b) 0.75 mm tip gap

Figure 4.31: Revised squealet adiabatic wall temperature

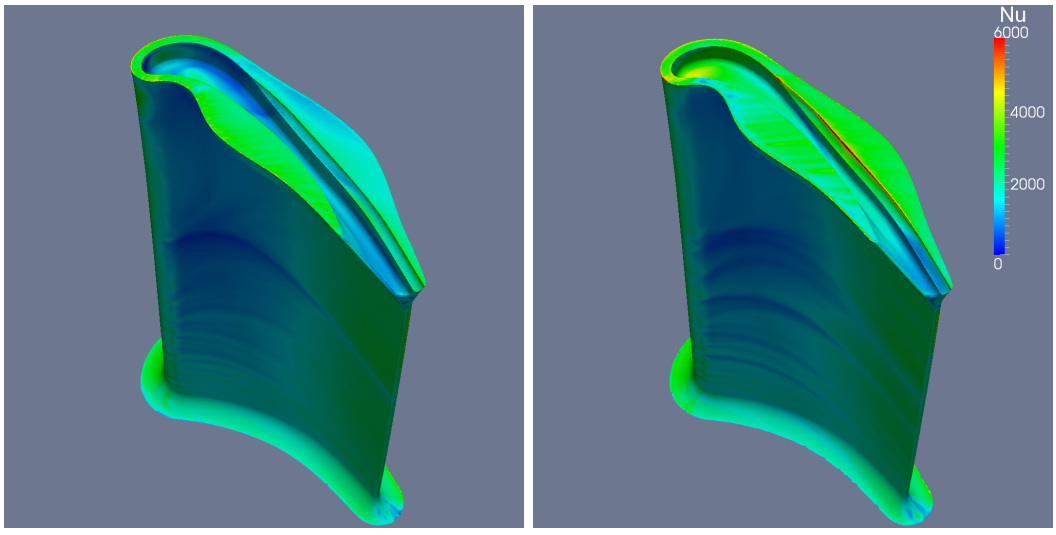

(a) 0.25 mm tip gap (b) 0.75 mm tip gap

Figure 4.32: Revised squealet Nusselt number

tip and 16% less than the winglet tip. Figure 4.33b plots the integral of heat transfer coefficient over the surface area, or hA product. Although this quantity is not as directly relevant in determining the overall cooling requirement as the total heat transfer rate is, it is generally the one used by Rolls-Royce as it is largely independent

of inlet temperature profile. It therefore allows the thermal performance of the rotor blade to be tracked even if the combustor outlet temperature traverse is changed. The hA product puts the squealet designs slightly closer to the double squealer in thermal performance than suggested by the total heat transfer rate data, with a 21% increase in hA product at 0.5 mm for the revised squealet tip. The reduction from the winglet is also 21%; significantly larger than when measured by total heat transfer rate. The discrepancy between these two measures is a reflection of the slightly lower adiabatic wall temperature for the winglet tip and the slightly higher adiabatic wall temperature for the double squealer tip, visible in figure 4.18.

In both the graphs of total heat transfer rate and hA product, there is little variation in heat transfer with changing tip gap, with a small peak typically seen near the middle of the range of tip clearances investigated. This is caused by the combination of two competing effects; as the tip gap increases, the over-tip leakage flow velocities broadly increase, resulting in thinner boundary layers and generally increasing heat transfer coefficients. However, in these simulations, the increase in tip gap was modelled by trimming the blade tip model down to the appropriate radius, therefore reducing the wetted surface area of the blade over which heat transfer occurs and consequently reducing both the total heat transfer rate and hA product. If the tip clearance had been adjusted by increasing the radius of the over-tip casing instead, these quantities would be expected to increase monotonically with tip gap.

In calculating the heat transfer coefficient using equation 4.7, an assumption is made that the flowfield is not altered by the imposed wall temperature boundary condition. In order to test this, four separate simulations were run using the revised squealet geometry at a tip gap of 0.5 mm: one with adiabatic wall boundary conditions applied to the blade surfaces and the other three with constant imposed wall temperatures of 1350 K, 1400 K and 1450 K. The heat transfer coefficient could then be calculated using any pair of simulations. The resulting heat transfer coefficient distributions are shown in figure 4.34 and the differences between them in figure 4.35.

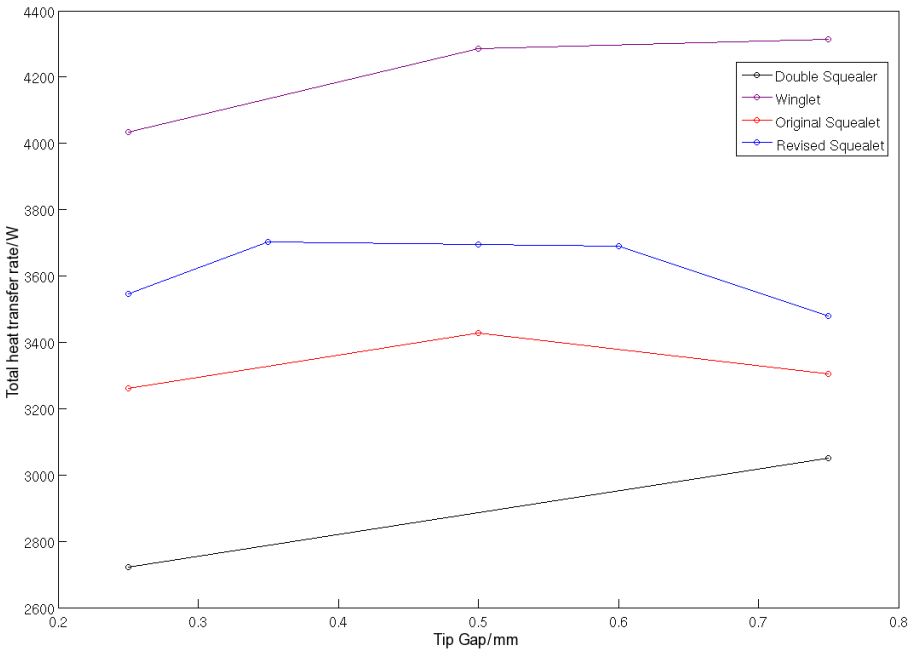

(a) Total heat transfer rate

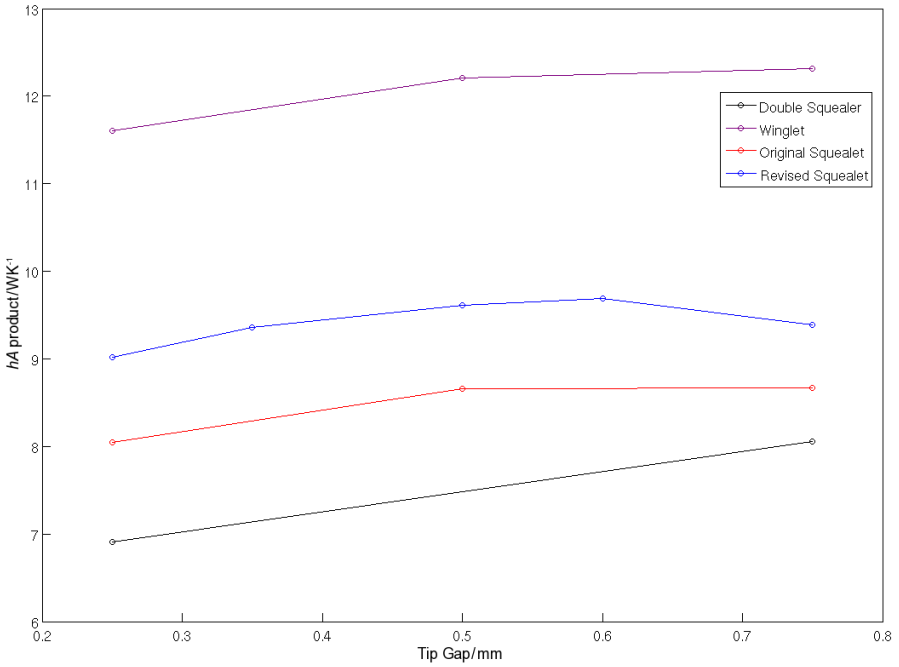

(b) hA product

Figure 4.33: Overall blade tip thermal load

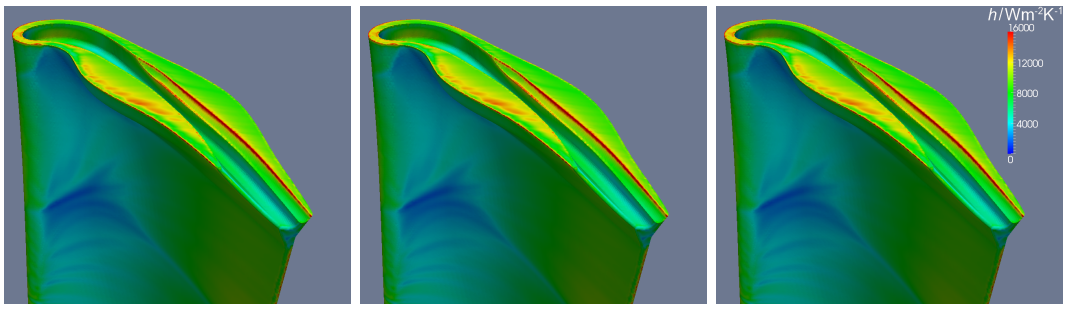

(a) Adiabatic-1350 K (b) Adiabatic-1400 K (c) Adiabatic-1450 K

(d) 1350 K-1400 K (e) 1400 K-1450 K (f) 1350 K-1450 K

Figure 4.34: HTC distributions calculated by different methods

It is clear that there are slight differences in the heat transfer coefficient distributions calculated using the various methods and as such, the imposition of a constant wall temperature does have some effect on the detailed flowfield around the blade. However, these differences are small and localised and are generally restricted to small displacements of features rather than large scale variations in the shape of the distribution. Even the absolute magnitude of the predicted heat transfer coefficient is largely unaffected by which pair of simulations is used in the calculation; the maximum deviation from the mean for the average blade tip heat transfer coefficient over all of the six calculation methods shown in figure 4.34 is just 0.7%. As no suitable validation data for the CFD simulations are available and the depth of this study is thus limited to the direct comparison of different geometries, the assumption that the imposition of constant wall temperatures has no significant effect on the flowfield is considered justified.

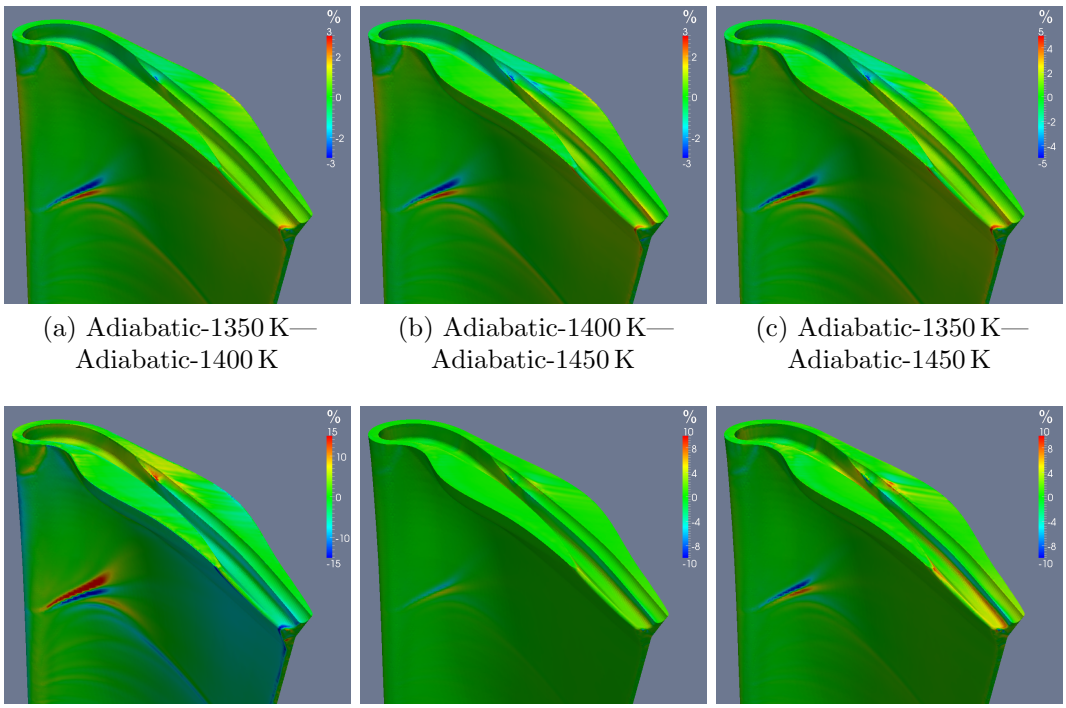

(a) Adiabatic-1350 K—Adiabatic-1400 K

(b) Adiabatic-1400 K—Adiabatic-1450 K

(c) Adiabatic-1350 K—Adiabatic-1450 K

(d) Adiabatic-1350 K—1350 K-1450 K

(e) 1350 K-1400 K—1350 K-1450 K

(f) 1350 K-1400 K—1400 K-1450 K

Figure 4.35: Differences between HTC distributions calculated by different methods (NB: Scales are different)

4.6 Relative endwall movement

Much of the experimental data available in the open literature on the subject of turbine blade over-tip leakage flow and heat transfer have been obtained from linear cascade environments with stationary endwalls. These experimental rigs simulate the pressure distribution around the aerofoil, but neglect the effects of blade rotation and the relative movement of the endwall past the blade tip. The opportunity was taken to investigate the impact of one of these features in an engine-realistic environment; that of relative endwall motion. The case of the double squealer tip at a tip gap of 0.75 mm was used as a testbed, selected as being the case most similar to unshrouded blades currently used in real engines. Two more simulations were run for this geometry (one with adiabatic walls and one with constant temperature walls) with the entire endwall

surface (shown in figure 4.2) rotating at the same speed as the blade. In this way, any effects of the rotating frame of reference (such as buoyancy forces) would still be present, but without the relative endwall motion, enabling the effects of the two features to be decoupled and isolated.

Figure 4.36 shows the development of the over-tip leakage vortex, visualised through contours of pressure loss coefficient. The shear from the relative motion of the endwall reduces the distance that the over-tip leakage flow penetrates across the passage on the suction side of the blade, forcing it to roll into a smaller, tighter vortex that is pushed up closer to the suction side of the blade. Although the shear induced by the relative endwall motion does reduce the over-tip leakage velocity in the forward part of the tip gap slightly, shown in figure 4.37, the general migration of air up the pressure side of the blade is unaffected and so the adiabatic wall temperature is virtually identical with or without relative endwall motion, as can be seen in figure 4.38. The introduction of relative endwall motion increases the over-tip leakage flow velocity in the aft portion of the blade, however, exhibiting the same rearward shift in the mass-flow rate distribution that was observed in the low speed experimental studies of Tallman and Lakshminarayana (2001b) and Palafox (2006).

A very small variation in temperature distribution is seen, but it is confined to the blade tip, mostly at the leading edge. This is caused by the change in the near-tip flow incidence angle, which alters the flow structure in and around the front of the cavity. Without relative endwall motion, the over-tip leakage flow enters the cavity from the leading edge and forms a single, wide cavity vortex occupying the full extent of the cavity that gradually exits over the entire length of the suction side rim (figure 4.39a). By contrast, when the shear from the endwall motion is present, flow leaks over the squealer rim from further around on the suction side, remaining confined to a region by the crown of the cavity and forming a tight, counter-rotating vortex before once again spilling over the suction side rim (figure 4.39b). The rest of the cavity is filled with flow that leaks over the early pressure side rim that forms a separate cavity vortex.

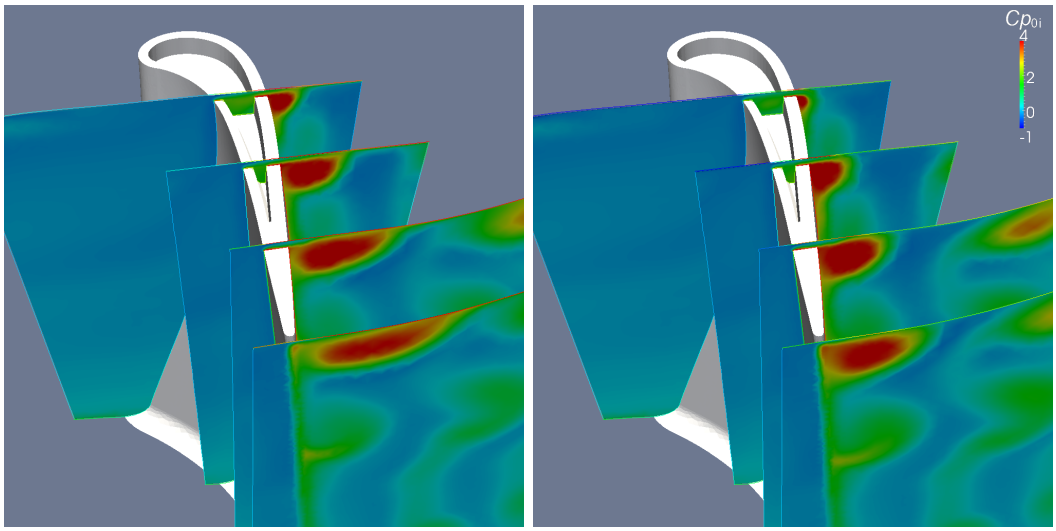

(a) No relative endwall motion (b) With relative endwall motion

Figure 4.36: Effect of relative endwall motion on Cp_{0i} pressure loss coefficient

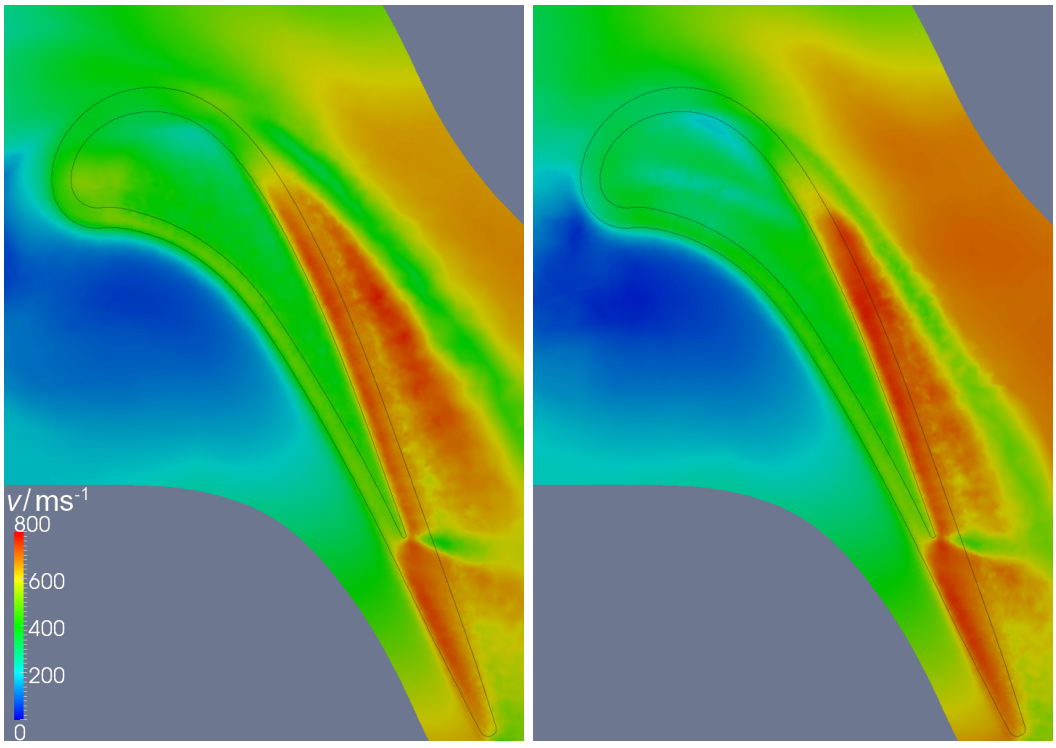

(a) No relative endwall motion (b) With relative endwall motion

Figure 4.37: Effect of relative endwall motion on mid-gap over-tip flow velocity

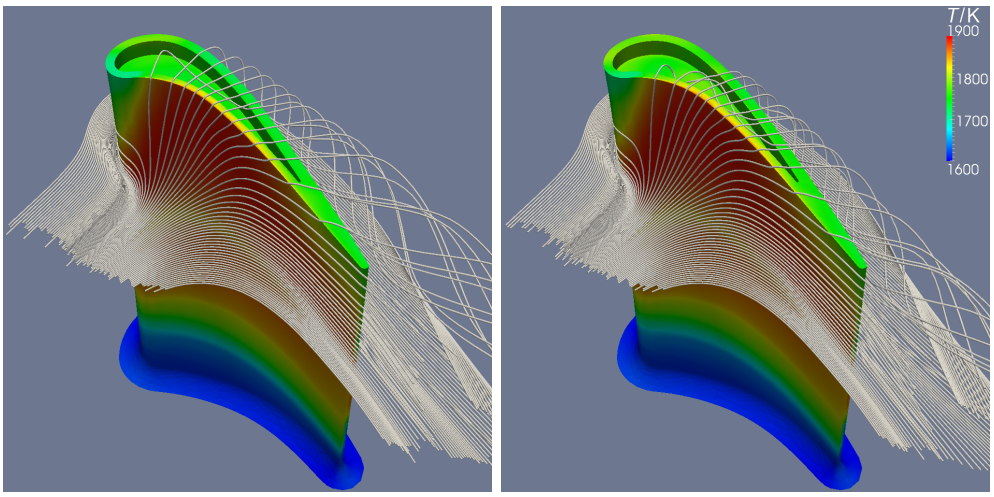

(a) No relative endwall motion (b) With relative endwall motion

Figure 4.38: Effect of relative endwall motion on adiabatic wall temperature

This change in flow structure, particularly around the leading edge, drives the minor change in the adiabatic wall temperature distribution, but has a more significant effect on the heat transfer coefficient distribution, particularly around the reattachment hot spot on the cavity floor. In the absence of relative endwall movement, the wide cavity vortex results in a broad streak of high heat transfer coefficient where the incoming flow impinges in slightly different locations depending on exactly where around the rim it enters the cavity. A much smaller peak is seen in the case where relative endwall motion is present, due to the split cavity flow. This difference in heat transfer distributions is somewhat reassuring as it implies that results from the simplified case omitting relative endwall movement (as is the case in most linear cascade studies) will generally overpredict the heat load that the blade tip is subjected to. In this case, the introduction of relative endwall movement reduced the total heat transfer rate to the double squealer tip (from ∼90% span outwards) by 1.7%. However, the change in cavity flow field casts some doubt over the veracity with which such experiments would be able to capture the detailed flow fields in and around complex tip geometries.

The same general effects of relative endwall motion are observed in these high speed CFD simulation results as were seen in the low speed work reported in chapter 3:

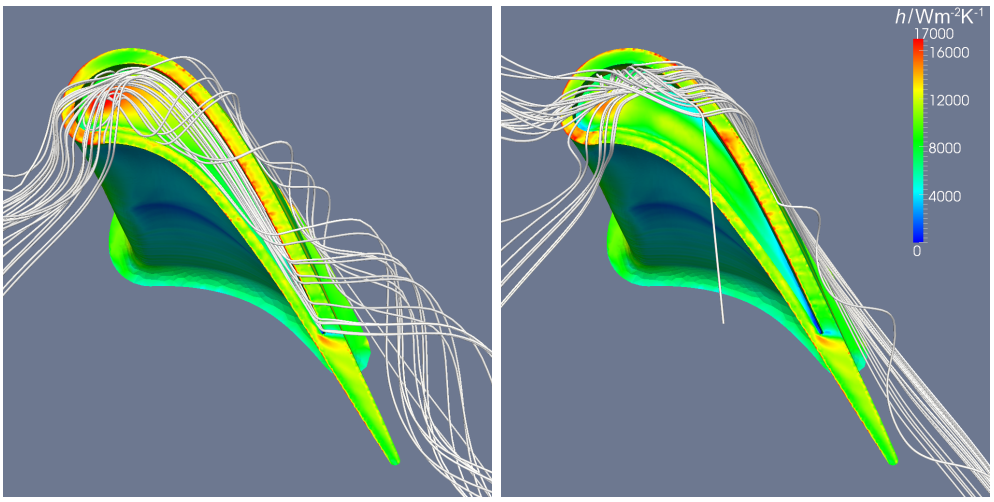

(a) No relative endwall motion (b) With relative endwall motion

Figure 4.39: Effect of relative endwall motion on cavity flow and HTC

the over-tip leakage velocity is reduced in the forward part of the blade, the over-tip leakage mass flow rate balance is moved towards the rear, the over-tip leakage vortex occupies a smaller space and does not penetrate as far across the passage and there is a modest reduction in overall heat flux to the blade tip. However, there is a much more significant change in the flow structure in the over-tip region than was observed previously. This is most likely caused by the change in blade tip geometry (i.e. the use of a double squealer tip instead of a flat tip) rather than a difference in behaviour between high speed and low speed flows.

4.7 Chapter summary

In this chapter, an engine-realistic, time-steady CFD investigation into the aerodynamic and thermal behaviour of an uncooled turbine blade with different blade tip geometries has been presented. The tip gap was varied over a range of 0.25 mm–0.75 mm, or 0.45%–1.34% blade chord. Unstructured, hybrid tetrahedral and prism layer meshes were generated in ICEM CFD 11 and solved using the steady, pressure based solver of FLUENT 6.3 with the realisable k-ϵ turbulence model with enhanced wall treatment

and the SIMPLE algorithm for pressure-velocity coupling. The baseline geometry tested was a basic double squealer tip, which was compared to the existing EFE winglet design. A hybrid design drawing features from both of these, the squealet tip, was introduced, tested, refined and tested again. The aerodynamic performance of the blade tip design was primarily measured by the tip gap efficiency exchange rate; both variants of the squealet tip were found to have a very similar performance to the baseline double squealer geometry in this regard, slightly inferior to that of the winglet tip. There was an improvement in absolute efficiency, however, with the revised squealet tip predicted to perform better than the winglet tip over the majority of the range of tip gaps tested. Very similar levels of heat transfer coefficient were seen across all blade tip designs, so the total heat load received by the revised squealet tip was reduced compared to the winglet by approximately 14%, primarily due to the reduction in wetted surface area. The effect of relative endwall motion was also investigated using the double squealer blade tip geometry at the 0.75 mm tip gap. Endwall movement was found to reduce the incidence angle of over-tip leakage flow, altering the structure of the flow within the tip gap region and dividing the cavity flow into two smaller vortices. This change reduced the extent of the impingement hot spot on the cavity floor caused by the over-tip leakage flow entering the cavity at the leading edge.

Chapter 5

Cooled Engine Scale CFD Simulations

5.1 Introduction

This chapter reports a continuation of the CFD study of the squealet tip using the same aerofoil and external boundary conditions as before. This section concerns the development towards a practical blade tip that could be used in a real engine by the addition of film cooling. This is performed at a single tip gap of 0.5 mm (0.89% blade chord). A simplified internal core and film cooling holes are added to the blade tip region, taking into account restrictions regarding placement of features due to manufacturing tolerances, and then a "manual optimisation" of the cooling configuration is undertaken by sealing off some of the cooling holes but leaving others open. All of the CFD simulations detailed in this chapter are run using an unstructured tetrahedral mesh with prism layers generated in ICEM CFD 12 and once again solved with the time-steady, pressure based solver of FLUENT 6.3 using the realisable k-ϵ turbulence model and enhanced wall treatment and the SIMPLE algorithm for pressure-velocity coupling.

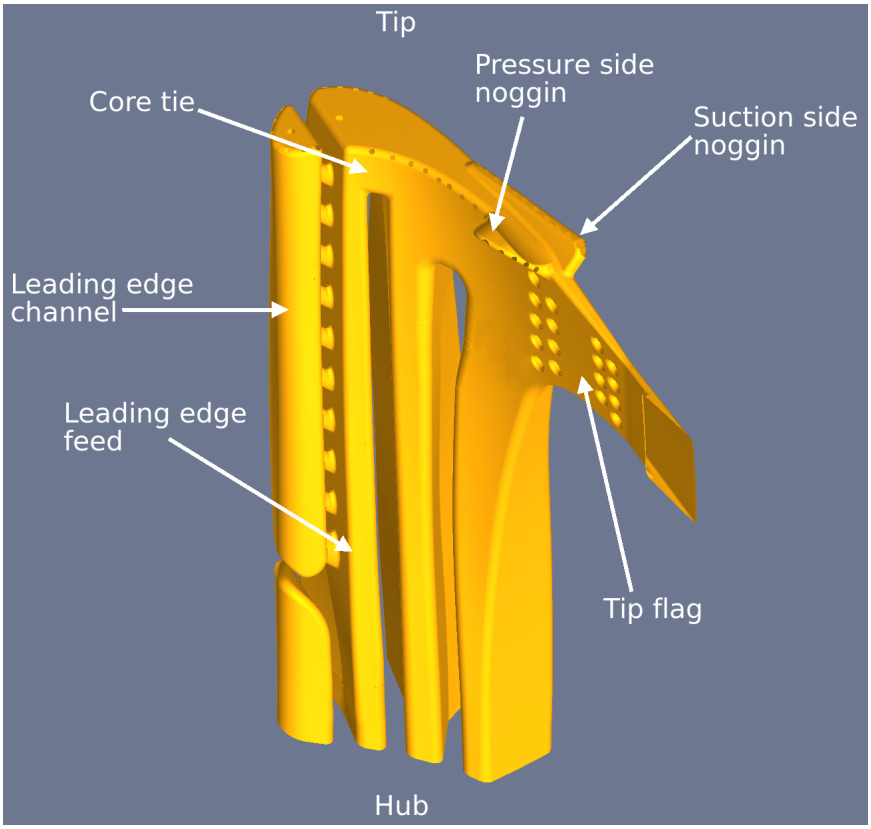

Figure 5.1: EFE blade internal cooling core

5.2 Cooling geometry

The initial possible locations of cooling holes were identified by Rolls-Royce, using the revised squealet tip design from the previous chapter as the external geometry. The internal core geometry was the existing core designed for use with the EFE winglet tip, shown in figure 5.1, to which no modifications were made. This meant that there was a noggin (a small bulge in the top of the core) on the suction side, to which a chordwise cooling gallery was connected. A similar feature also existed on the pressure side, although it was not needed. The cooling gallery was used to reduce the required length of the cooling holes near the trailing edge in order to allow a greater cooling air mass flow rate in this critical region. The cooling gallery was 0.8 mm in diameter, but exited the blade surface through a 0.5 mm diameter dust hole. This had been achieved in practice on the winglet tip by welding the gallery exit

closed and then redrilling the smaller diameter exit; a similar scheme is represented schematically in the geometry as a sharp, sudden contraction close to the gallery exit. As many cooling holes of diameter 0.38 mm as could be fit in a single row in the blade near-tip region were located to connect the internal core to the external aerofoil surfaces, taking into account manufacturability requirements—in particular, a minimum separation of approximately 1.0 mm was required between adjacent hole centrelines to accommodate stress limitations. Larger, 0.5 mm diameter dust holes were also located on the top of each radial internal passage and at the top of each noggin to allow any debris in the cooling air supply to be expelled from the blade. In addition to the manufacturing constraints, the EFE blade was designed to be compatible with an abrasive blade tip/abradable casing liner technology intended to improve casing circularity and concentricity. This introduced the further requirement that no cooling holes break out on to the squealet rim, as the abrasive rocks used for the cutting material on the blade tips would be attached to this surface. In total, 44 cooling holes were included on this cooling design, plus five dust holes and the suction side cooling gallery exit. This initial cooling design is shown in figure 5.2.

5.3 CFD strategy

As the most time-consuming part of the previous CFD study by far was the meshing of the computational domain, a decision was taken to create a single mesh that would allow different cooling configurations to be tested without the need for remeshing. While this would significantly increase the complexity of the meshing process, that process would only have to be conducted once. In order to achieve this, cover surfaces were created to cap each end of every cooling hole; one flush with the external blade surface and one flush with the internal core. By partitioning the flow domain in this way, the mesh within each cooling hole could be defined as a separate computational volume, independent of both the internal core and the mainstream air channel. Thus,

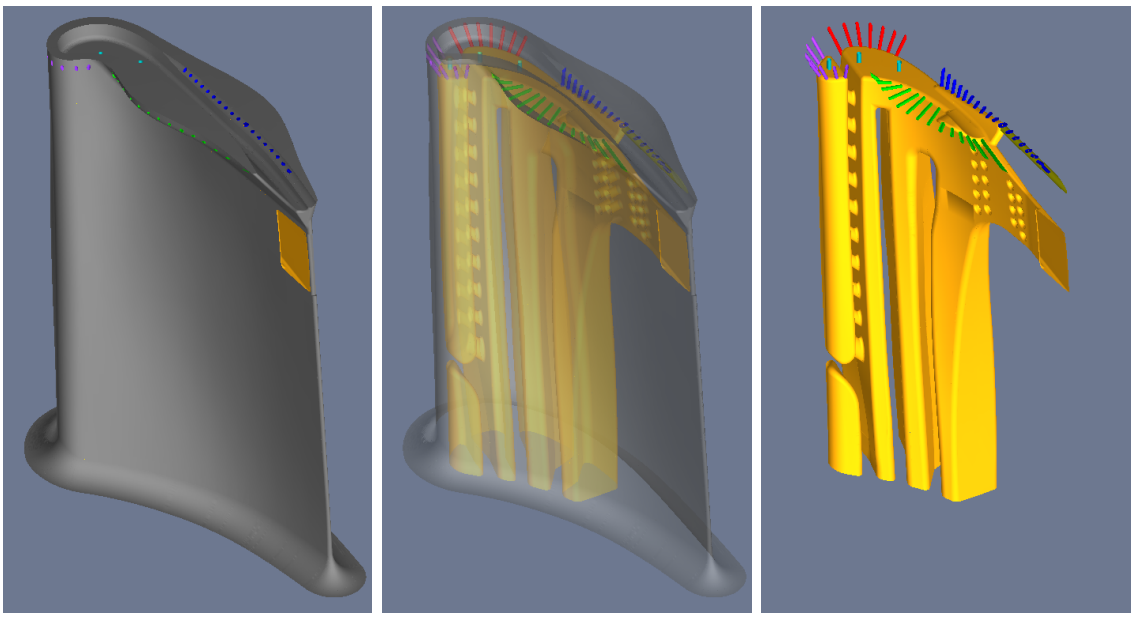

(a) External (b) Transparent (c) Internal

Figure 5.2: Original external and internal cooled squealet tip geometry

the mesh within the cooling hole regions could be specified as being solid zones (turning off the convection terms of the solver) to seal them off, allowing different cooling configurations to be simulated. In order to maximise the definition of the velocity profile at the cooling hole exits, conformal mesh boundaries were enforced over all of the cooling hole cover surfaces.

The meshes were generated with a similar method to that used for the meshes created for the uncooled simulations described in the previous chapter, this time using Icem CFD 12. The Octree mesher was once again employed for the tetrahedral mesh generation.

5.3.1 Geometry simplification

Many problems were encountered in the development of the meshing process due to the complexity of the geometry. Critically, insurmountable difficulties arose while extruding prism layers from the external surfaces, with many highly distorted and

partially inverted[1] cells being produced, mainly in the region around the tip flag exit at the trailing edge. In an attempt to circumvent these issues, local cell refinement was increased greatly, constrained only by the limits of the maximum mesh size that could be generated with the available memory on the computer used for meshing. The excessive distortion still remained despite the reduced cell size.

In order to solve the meshing problems, the computational geometry was simplified. The most significant modification made was to terminate the tip flag in a computational exit before it broke through the aerofoil surface, meaning that any cooling flow through the tip flag was removed from the simulation without it joining the mainstream flow. As the trailing edge slot feed was absent from the initial geometry and was not in any case to be simulated, it was felt that the detailed flow field around the tip flag exit was already less than entirely representative of the real blade and that the removal of the tip flag–mainstream interface was not critical. By maintaining the tip flag geometry in all other respects and placing a pressure outlet at its extremity, the internal cross-flow conditions in the core at the entrance to the cooling holes were still correctly simulated, so this change would only have a minor effect on the coolant supply to the blade tip. The core itself was also simplified slightly. The leading edge channel was disconnected from the leading edge feed to form two separate passages and the whole core was trimmed to a radius just below the extent of the tip flag. These two changes were made solely to reduce mesh size rather than to alleviate any specific meshing-related problems. The core tie joining the top of the leading edge channel to the first passage of the multipass was kept in place, however, as its removal could potentially have altered the cross-flow conditions at the inlets to the cooling holes in the region and hence the resulting mass flow rates and velocity distributions through them.

While the first attempts at meshing were being made, some concerns had been raised over the squealet design in the trailing edge region being inadequately cooled. The opportunity presented by the delay caused by the meshing problems and subsequent

[1] See footnote on page 63.

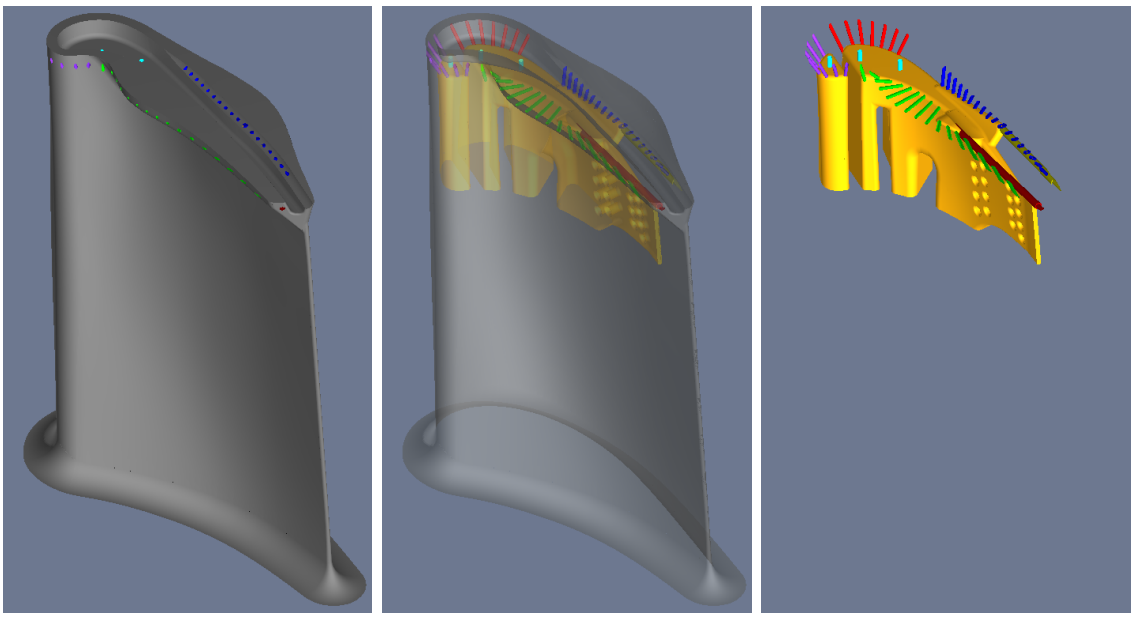

(a) External (b) Transparent (c) Internal

Figure 5.3: Final external and simplified internal squealet tip geometry

alterations to the internal geometry was seized and some modifications were also made to the external squealet design by Rolls-Royce. The pressure side squealet rim was thickened and lengthened, allowing a cooling gallery to be inserted on the pressure side in addition to the one already present on the suction side. This cooling gallery greatly reduced the length of cooling hole needed to reach the trailing edge and also allowed an extra two holes to be located on the pressure side. This relatively minor change to the external blade tip geometry is not expected to have a large impact on its aerodynamic performance, although the blunt pressure side trailing edge may leave a larger wake as on the winglet tip, which would decrease the efficiency; this would likely be in the form of an offset in efficiency, rather than a change in the tip gap efficiency exchange rate. The revised external geometry and simplified internal geometry are shown in figure 5.3.

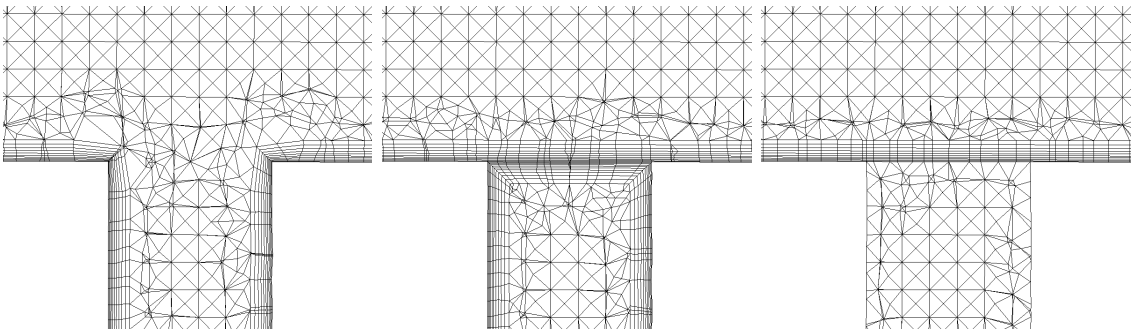

(a) Uncapped cooling holes (b) Capped cooling holes (c) Capped cooling holes, compromise

Figure 5.4: Prism layer meshing options (schematic)

5.3.2 Meshing compromise

In spite of the simplifications made to the cooling system geometry, some further problems were encountered in the meshing process as a result of the decision to cap the cooling holes with cover surfaces. Without cover surfaces, prism layers could be grown over the external aerofoil surfaces and bent around into the inside of the cooling holes and the interior surfaces of the core, shown schematically in figure 5.4a. The cooling hole covers prevent this, as the prism layers have to continue across the face of the cover surfaces. The ideal meshing approach in this case, would therefore be to have a second set of prism layers grown on the interior of the cooling hole volume which bend around the inner side of the end cap (figure 5.4b). Although this technique would result in a double-thickness of prism layers over the cover surface, it would otherwise be impossible to maintain a conformal interface without creating very narrow pyramidal cells at the interface. This double layer of prism cells is unlikely to affect accuracy adversely, but does cause a small overhead in cell count.

While this approach would give a good distribution of prismatic cells with only the small expense of a slight increase in mesh size, it was found not to be possible in the case of the cooled squealet tip geometry. Due to the external shape of the squealet tip, some of the cooling holes exited the blade at very acute angles relative to the blade

surface, particularly in the concave region of the blade tip on the pressure side. These tight angles between the cover surfaces and the cooling hole walls made the addition of prism layers in the interior of the cooling hole impossible, resulting in highly distorted and often inverted cells near the cooling hole exit. A compromise therefore had to be made to allow a valid mesh to be generated. Prism layers were retained over the external aerofoil and outer cooling hole covers and also on the interior of the blade core and the inner covers, but the mesh within the cooling holes themselves would be purely tetrahedral (figure 5.4c). This allowed boundary layer growth to be simulated correctly in the cooling flow leading to the entrance of the cooling holes and also in the mainstream where the cooling flow would exit. However, the boundary layer growth within the length of the cooling holes themselves would not be captured accurately, thereby affecting the discharge coefficient of each hole and hence the cooling mass flow rate passed through it. The velocity profile at the cooling hole exit would also be affected slightly. While this is clearly not ideal, it was felt that the uncertainties introduced by this compromise would be acceptable in the context of the aims of the study and the other approximations already introduced.

The final mesh was created in an analogous method to the uncooled blade tip meshes of chapter 4. Purely tetrahedral meshes were first generated using the Octree mesher, covering the mainstream air channel external to the blade and the blade core but *not* inside the cooling holes. The two portions of the mesh were therefore not connected at this point. The mesh was smoothed globally and then prism layers grown over the blade, tip, hub and core surfaces. Following the same careful smoothing procedure applied to the previous hybrid meshes, the two discrete sections of the mesh were joined by filling the cooling hole volumes with tetrahedral elements, ensuring conformal interfaces were maintained. The mesh was then smoothed one final time to bring the minimum quality of the elements up to an acceptable level.

The finished mesh consisted of 7.6 million tetrahedral cells and 6.9 million prismatic cells, giving an overall cell count of 14.5 million. 15 prism layers were used with a first

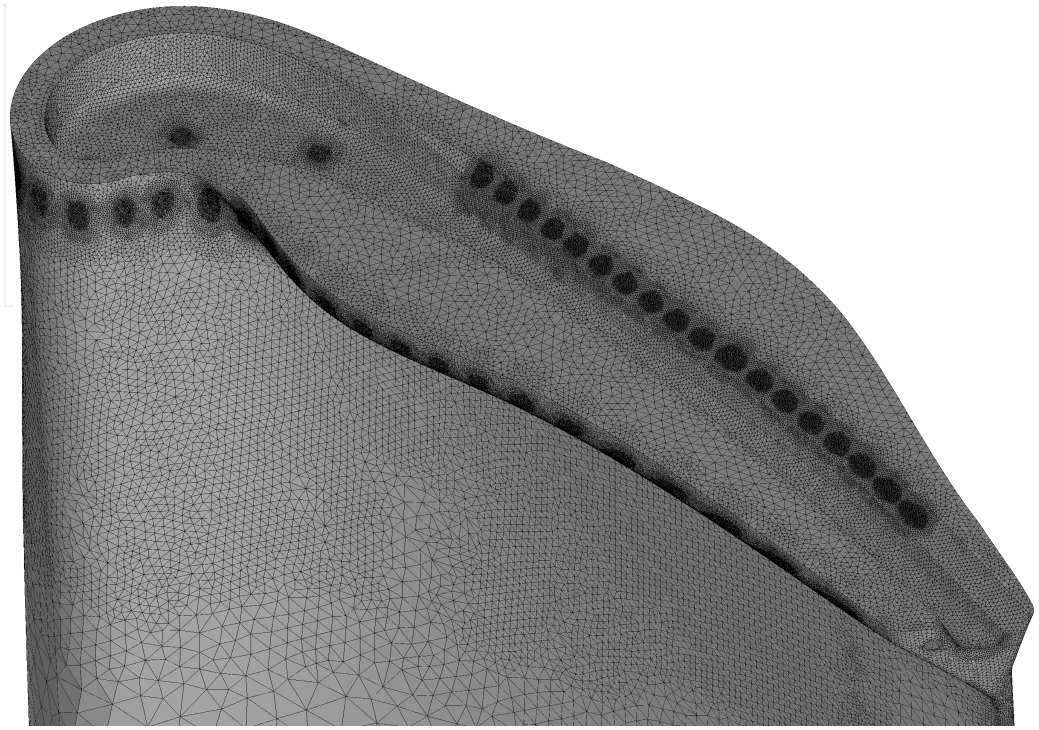

Figure 5.5: Mesh refinement on the blade tip surface

cell height of 2 μm. The minimum cell quality[2] value was 0.0279; however, there were only 43 cells with a cell quality below 0.1 and these were clustered in a non-critical region inside the suction side gallery where there is an abrupt contraction immediately upstream of the dust hole exit. The mesh refinement on the blade tip surface is shown in figure 5.5

5.3.3 Solution and boundary conditions

As this section of the study is a direct continuation of the uncooled investigation described in the previous chapter, the solver setup and boundary conditions used were kept the same where possible. The extent of the computational domain is identical to that used previously, covering a single blade in a periodic environment from the HP NGV exit plane to the IP NGV inlet plane, as shown in figure 4.2. The external boundary conditions used were identical to those used for the CFD study without

[2]See footnote on page 92.

film cooling described in chapter 4, which are detailed in section 4.3.2 and shown in figure 4.6. Once again, the time-steady, pressure based solver of FLUENT 6.3 with the SIMPLE algorithm for pressure-velocity coupling was used in its relative velocity formulation with the realisable k-ϵ turbulence model and enhanced wall treatment. Heat transfer coefficient distributions were calculated in exactly the same way as before, using the results from two simulations; one with adiabatic walls and one with constant temperature walls. In order to maintain sufficient heat transfer for the calculation of heat transfer coefficient in regions of high film cooling effectiveness, a much lower imposed wall temperature of 1100 K was used for the cooled blade tip simulations. The computational hardware used for these simulations was identical to that described in the previous chapter.

A single set of boundary conditions were required to allow the direct comparison between different cooling configurations. The internal cooling boundary conditions were taken from flow simulations performed by Rolls-Royce using their in-house network analysis codes, run for the EFE winglet tip. These analyses did not account for the absence of cooling holes not associated with the blade tip cooling configuration in the present simulations (i.e. the cooling holes located lower down the blade on the aerofoil surfaces) or the change in porosity of the blade tip cooling design, which would alter the internal core pressures. The internal boundary conditions used are summarised in figure 5.6, which were used as being realistic and representative of the appropriate coolant feed conditions. Once again, consistency and comparability between the different cooling configurations being assessed were the priorities rather than absolute veracity compared with the real engine build.

5.3.4 Cooling configurations

The six cooling configurations tested numerically are shown in figure 5.7. This relatively small number of configurations covers most viable cooling variants possible using arrangements of the single meshed cooling scheme. The latter ones were selected based

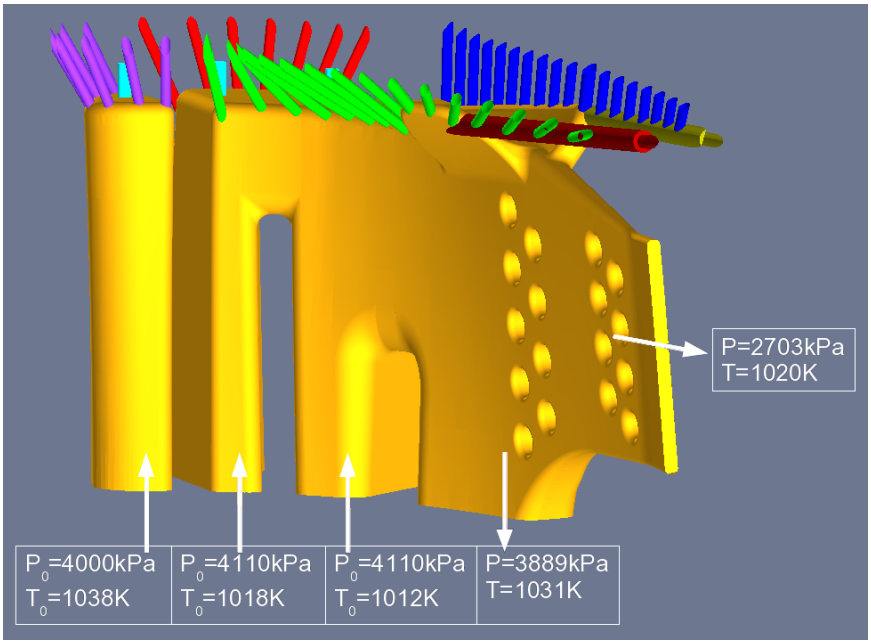

Figure 5.6: Internal cooling boundary conditions

on the results of configurations (a)–(d). The goal of the exercise was to minimise the coolant mass flow rate while still maintaining sufficient cooling across the entire blade tip, judged primarily by the local adiabatic wall temperature distribution, which is the key driver of metal temperature given the high external heat transfer coefficients. Temperature gradients were minimised where possible, as these induce thermal stresses which can reduce blade life. The only means of changing the cooling configuration used was the selective blocking of the film cooling holes; there was no scope within this study for their resizing or movement.

5.4 Results

The adiabatic wall temperatures reported represent the influence of convection, viscous heating and film cooling effectiveness, but do not capture lateral conduction within the solid or heat pick-up by the cooling air within the interior of the blade. The effect of internal cooling can be significant; cooling holes placed in such a way that

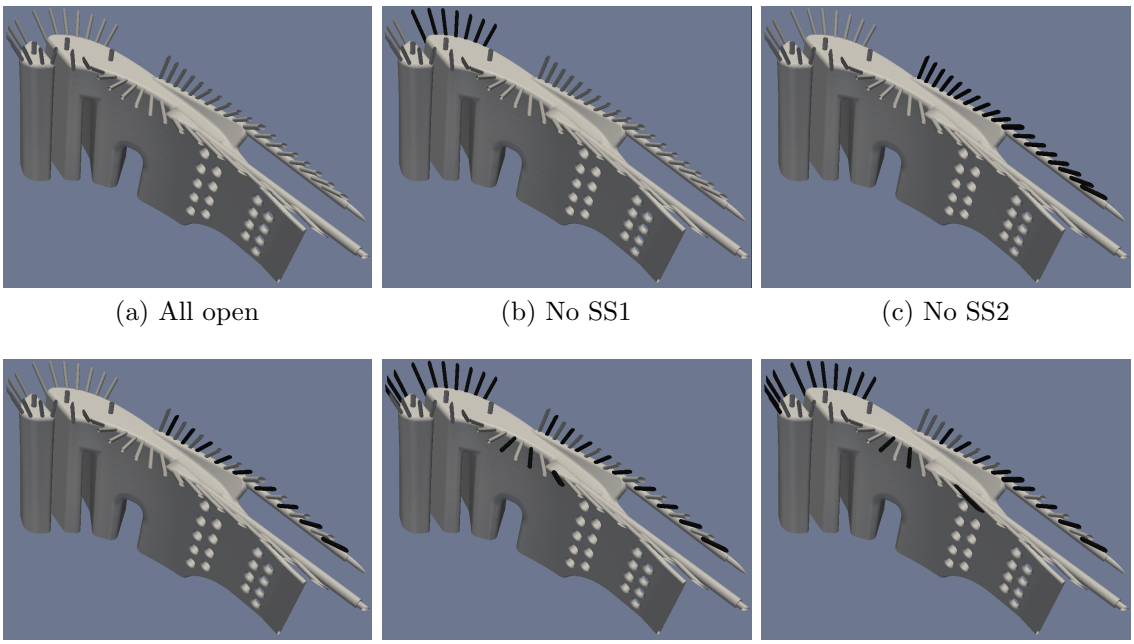

(a) All open (b) No SS1 (c) No SS2

(d) Odd SS2 only (e) Config 1 (f) Config 2

Figure 5.7: Tested cooling configurations
(grey = open, black = closed)

they do not form effective films on the external surfaces can still provide useful thermal protection to the blade. The extension of these simulations to predict blade metal temperatures would require a conjugate heat transfer approach to account for conduction through the solid region. Although this would undeniably be useful and provide a more accurate assessment of the overall cooling performance than the pure CFD investigation performed here, it would likely have been too slow to feed back into the design process for the real engine builds.

The heat transfer predictions for all six cooling configurations are shown in figures 5.8 to 5.13. The heat transfer coefficient distributions predicted are broadly similar to those seen in the uncooled simulations, though modulated by the presence of film cooling. Regions of very high heat transfer coefficient remain around the suction side tip shelf and at the reattachment line along the pressure side corner, but with additional augmentation around and downstream of the blown cooling holes.

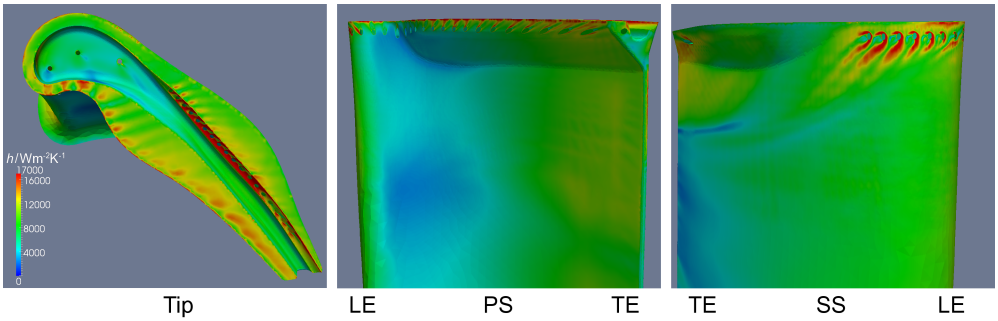

(a) Heat transfer coefficient

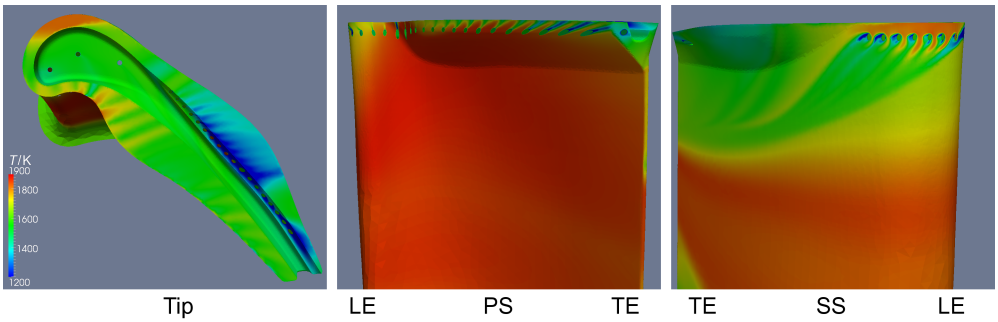

(b) Adiabatic wall temperature

Figure 5.8: HTC and adiabatic wall temperature—*All open* configuration

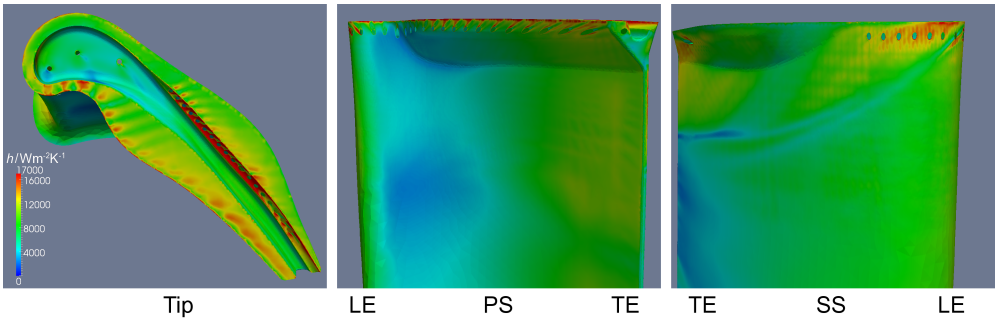

(a) Heat transfer coefficient

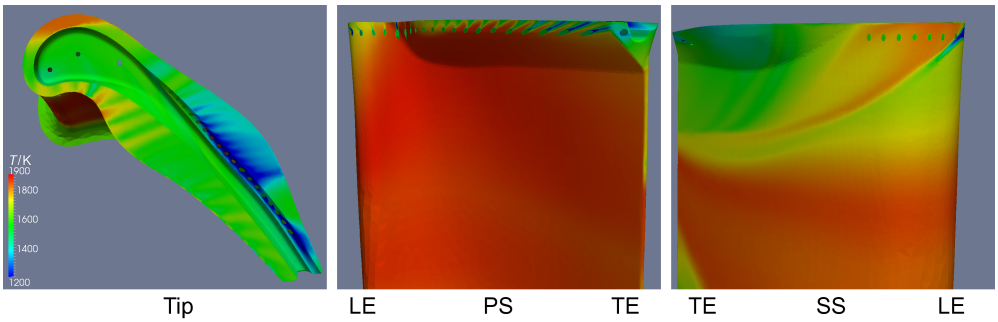

(b) Adiabatic wall temperature

Figure 5.9: HTC and adiabatic wall temperature—*No SS1* configuration

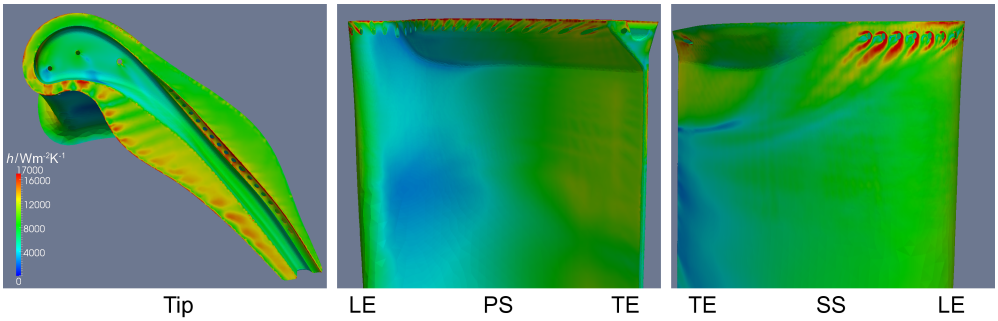

(a) Heat transfer coefficient

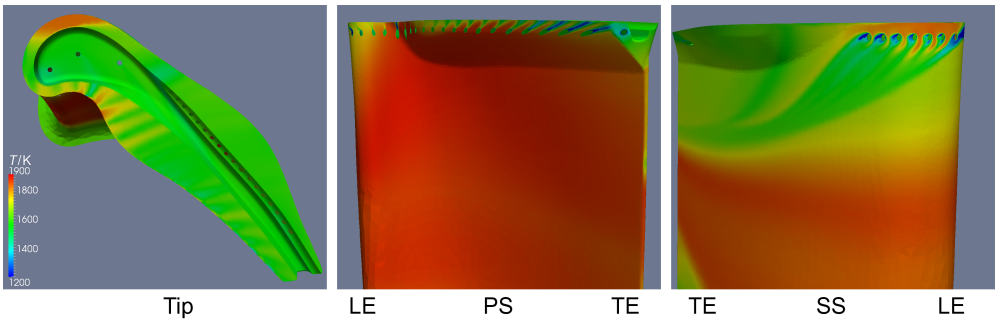

(b) Adiabatic wall temperature

Figure 5.10: HTC and adiabatic wall temperature—*No SS2* configuration

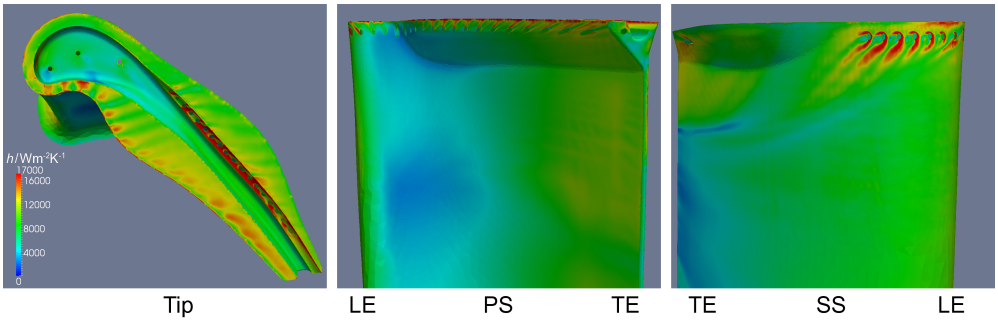

(a) Heat transfer coefficient

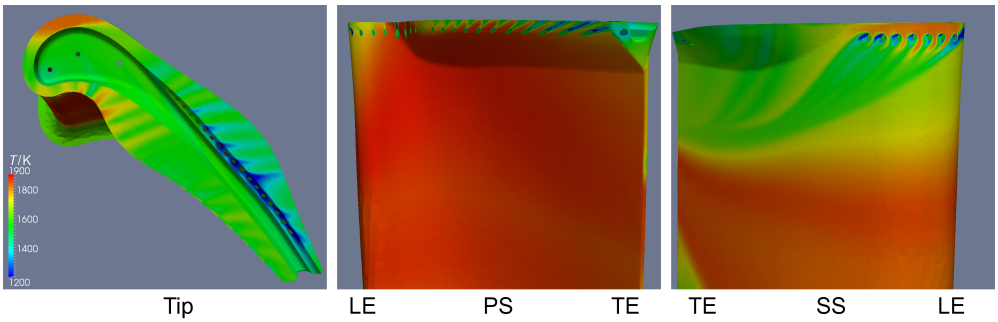

(b) Adiabatic wall temperature

Figure 5.11: HTC and adiabatic wall temperature—*Odd SS2 only* configuration

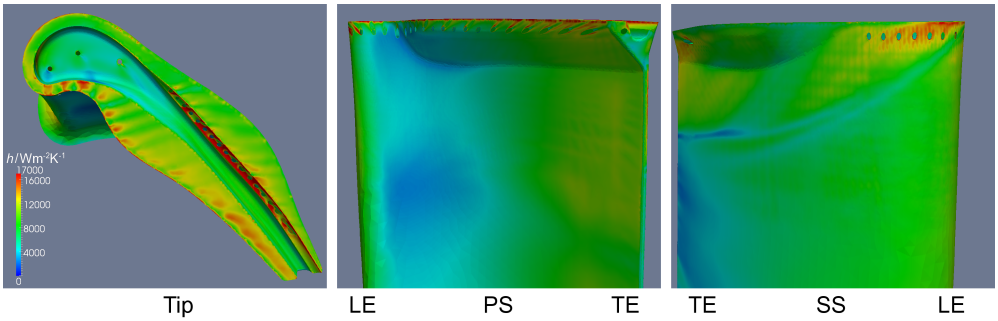

(a) Heat transfer coefficient

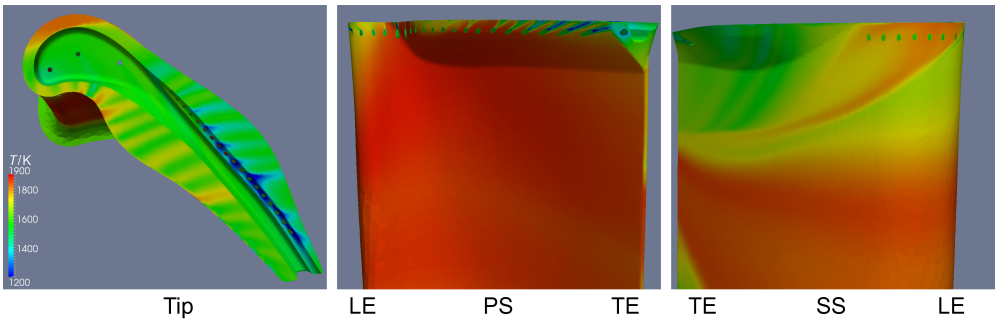

(b) Adiabatic wall temperature

Figure 5.12: HTC and adiabatic wall temperature—*Config 1* configuration

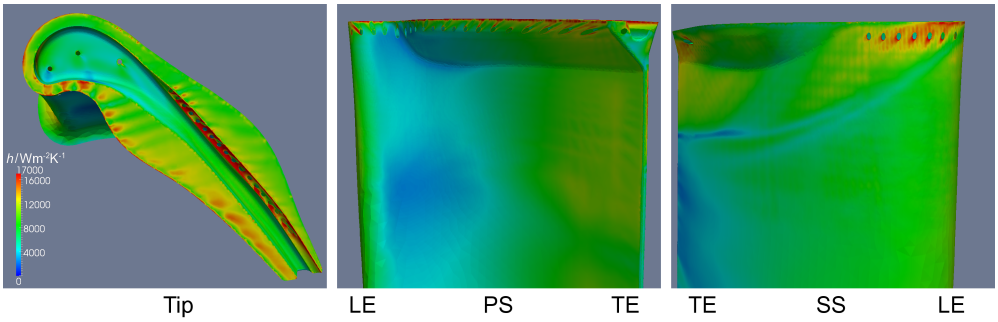

(a) Heat transfer coefficient

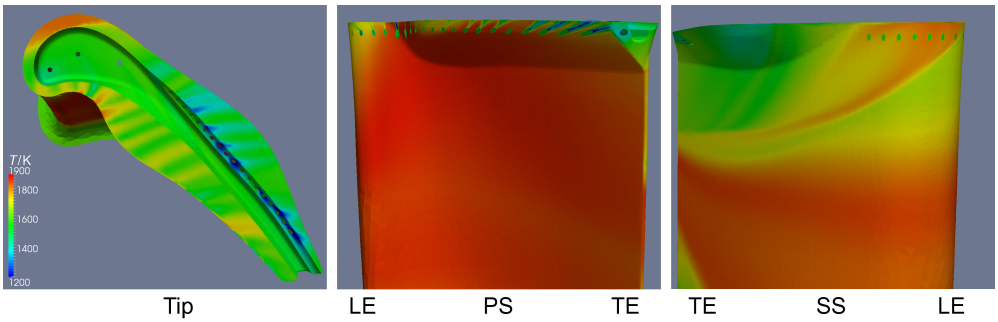

(b) Adiabatic wall temperature

Figure 5.13: HTC and adiabatic wall temperature—*Config 2* configuration

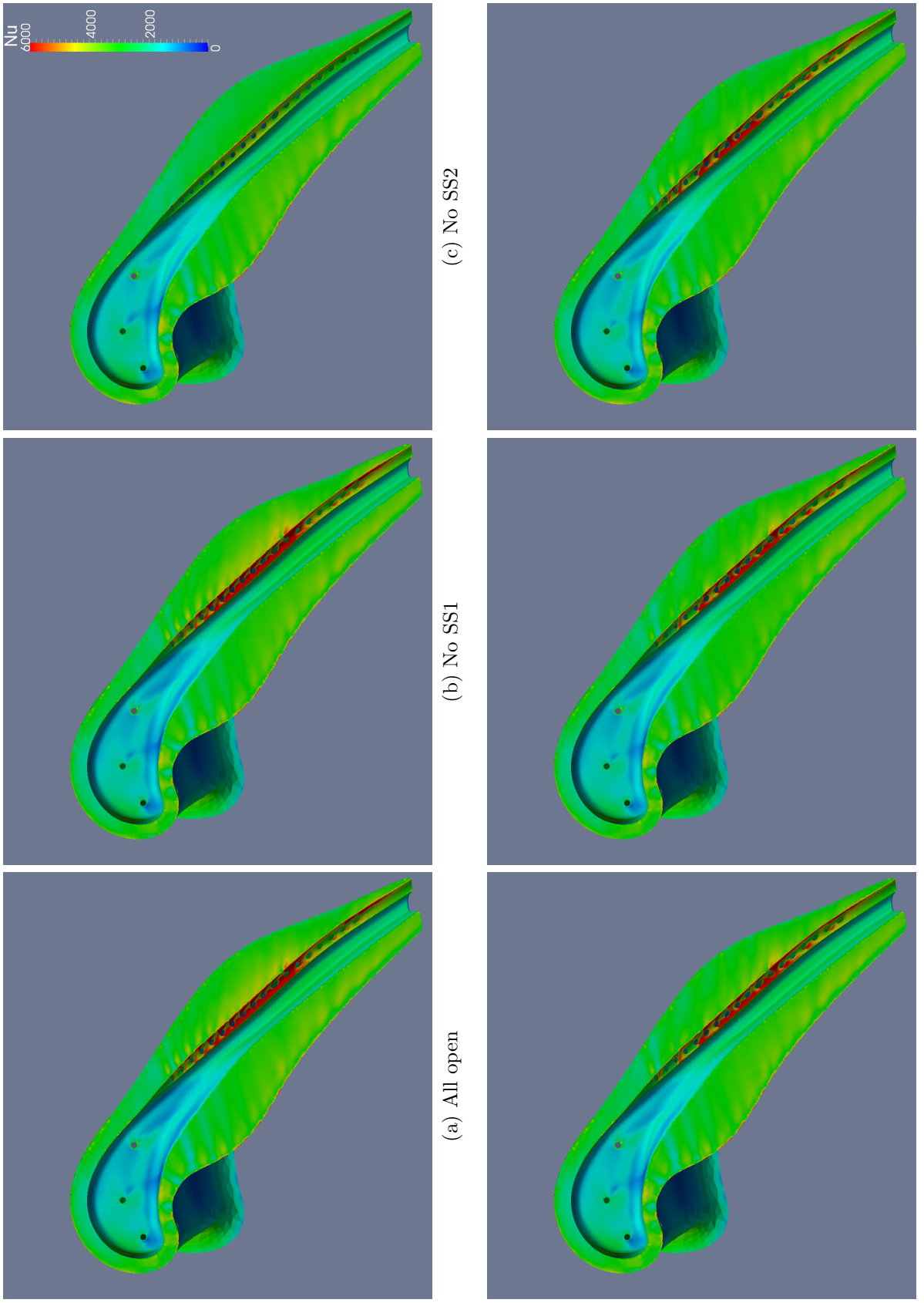

(a) All open (b) No SS1 (c) No SS2

(d) Odd SS2 only (e) Config 1 (f) Config 2

Figure 5.14: Nusselt number

The output of cooling air has only minor, localised effects on the general tip gap flowfield and the coolant is carried over the tip by the over-tip leakage flow, leaving its footprint in the adiabatic wall temperature distributions. The striped pattern seen in both the heat transfer coefficient and adiabatic wall temperature distributions is indicative of minimal film spreading and mixing; however, the underprediction of coolant spreading following film cooling ejection is a common problem for RANS models (Harrison and Bogard, 2008), so it is possible that the discrete hot and cold streaks would not be as distinct in reality as suggested here.

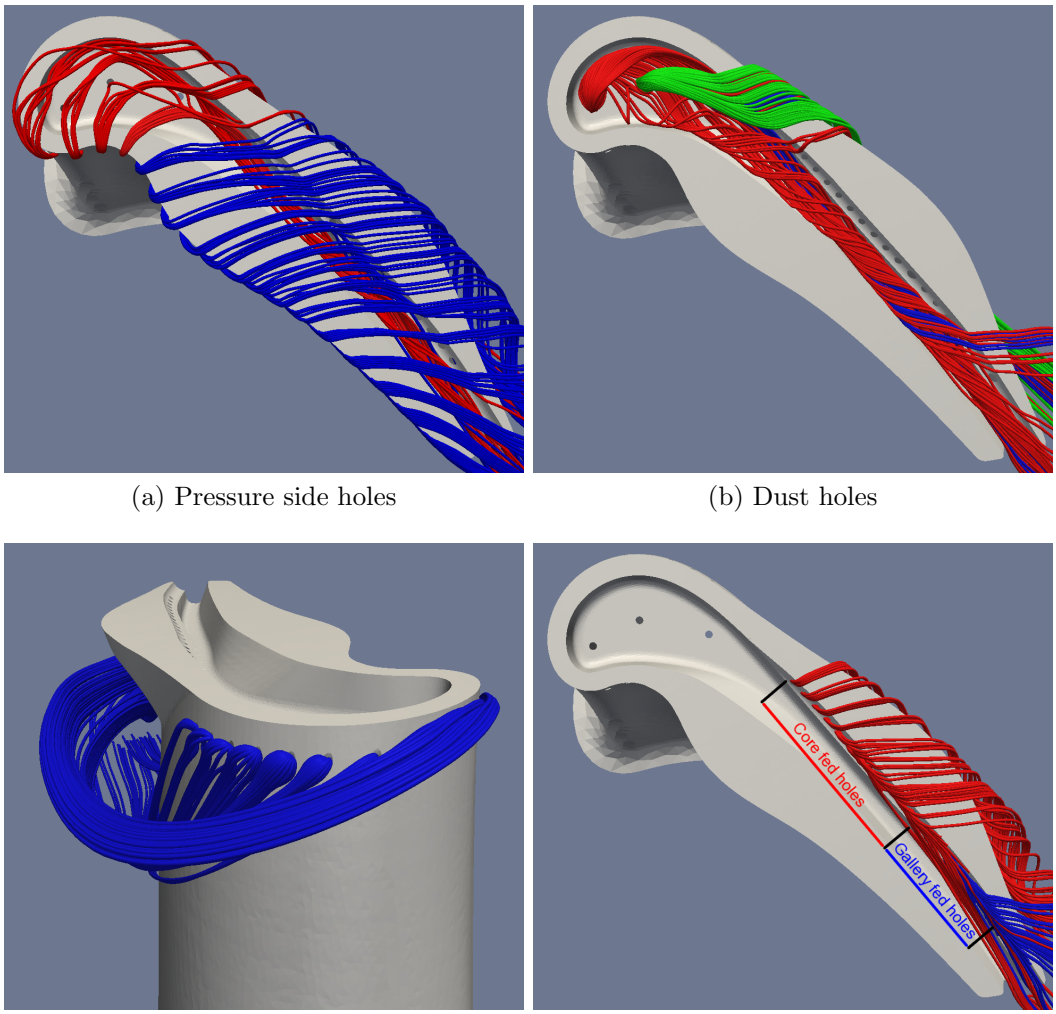

(a) Pressure side holes

(b) Dust holes

(c) Suction side holes

(d) Tip shelf holes

Figure 5.15: Coolant pathlines for *All open* configuration

It can be seen in figure 5.15 that the direction in which the coolant is swept is entirely determined by the location of ejection. Almost all of the cooling air from the pressure side holes is carried straight over the top of the blade tip, bypassing the gutter entirely; only a small portion of the flow (pathlines coloured red in figure 5.15a), from the first few of these holes closest to the leading edge, enters the cavity at all. The coolant film from the pressure side holes therefore covers both the pressure and suction side rims, which is reflected in the relatively low adiabatic wall temperatures on the suction side rim of the *No SS2* configuration (figure 5.10b), despite the absence of any tip shelf cooling flow. The flow within the cavity is instead dominated by the flow from the first dust hole (red in figure 5.15b), which remains almost entirely in the confines of the gutter, diluting the over-tip leakage flow that forms the wide cavity vortex. By contrast, the flow from the second dust hole (coloured green) spills almost immediately over the suction side rim to join the over-tip leakage vortex. Flow from the third dust hole (coloured blue) is divided between these two paths, with part of the coolant leaving the tip gap in a similar way and the remainder mixing with the flow from the first dust hole in the gutter. The fact that so much of the cooling air from the second and third dust holes is immediately lost from the blade tip to the over-tip leakage vortex suggests that this aspect would be a good candidate for further improvement in the cooling design. By repositioning and/or angling these holes (with minor adjustments made as necessary to the top of the internal core to ensure that they continued to work as dust holes), the air flow through the holes could be redirected for a more efficient expediture of coolant that maximised the utilisation of its cooling capacity. Such an optimisation would clearly be beneficial, but is beyond the scope of the present study.

The cooling air issuing from the holes on the suction side of the blade is swept back down the blade and away from the tip region, mostly being loosely entrained in the passage vortex (figure 5.15c). As a result, these holes have only a small effect on

the results of this pure CFD investigation; as noted previously, their impact would be more significant if internal heat pick-up was simulated.

The tip shelf holes have a more direct effect on the adiabatic wall temperature distributions on the blade tip, with some of the cooling air sweeping over the suction side squealet rim and the remainder channeled down the tip shelf itself towards the trailing edge. There is a noticeable divide in the behaviour of the flow; the air from the cooling holes connected directly to the core (coloured red in figure 5.15d) is mostly captured by the over-tip leakage flow and carried over the rim to the over-tip leakage vortex. The holes further back that are connected to the suction side cooling gallery (coloured blue) have a lower pressure ratio across them, resulting in a lower momentum cooling flow that does not penetrate into this strong cross flow. The cooling air from these holes is kept within the channel of the tip shelf until very close to the trailing edge where it begins to spill over the rim. This behaviour is rather useful, as the extreme trailing edge of the blade tip is difficult to cool and has been noted as a particularly vulnerable region of the blade tip from the limited in-service experience available. It is possible, therefore, that small changes to the size and shape of the cooling gallery could be used to tune the variation in pressure ratio across the tip shelf cooling holes and thus control the cooling air that protects the trailing edge region. Pathlines are seeded from all of the cooling holes in the tip shelf in figure 5.15d; the gap between the red pathlines and blue pathlines in the figure accurately reflects this difference in predicted behaviour between the holes directly connected to the core and the holes connected to the gallery.

As there are so many factors influencing the choices made for cooling configuration, it is difficult to measure and compare their overall performances objectively. Two important metrics are plotted in figure 5.16; total cooling air mass flow rate and total blade tip heat transfer rate. The "blade tip" for the latter is defined as all of the external surfaces down to a radius of 0.3678 m (approximately 90% span). There is an obvious trade-off between coolant mass flow rate and total heat transfer rate, as

is to be expected. The mass flow rate is clearly not the only factor governing the variation in thermal load though. The tip shelf cooling flow appears to be particularly important in reducing the total heat transfer rate, but it is clearly excessive in the *All open* configuration; removing every other hole (and hence approximately halving the coolant mass flow rate to the tip shelf) produces just a 2% increase in heat transfer rate; there is a further 6% increase when it is eliminated entirely. Moreover, total heat transfer rate cannot take into account the variation in temperature over the blade tip. If, for example, the equilibrium metal temperature on the suction side squealet rim is sufficiently low without any tip shelf cooling flow, it could still outlast a hotter portion of the blade tip and so further cooling in the region would not provide any benefit to blade life. However, short of a full thermal analysis including conduction, there is no way to predict the equilibrium metal temperatures, so total heat transfer rate remains the most appropriate single measure of goodness. The final configuration produced by the "manual optimisation", *Config 2*, reduces the cooling air mass flow requirement by 38% for an increased total heat transfer rate of 7% compared to the *All Open* configuration.

The reduction in heat flux due to film cooling can be expressed as the *Net Heat Flux Reduction* (NHFR), a quantity introduced by Sen et al. (1996). NHFR is defined as

$$\text{NHFR} = \frac{q_{\text{without cooling}} - q_{\text{with cooling}}}{q_{\text{without cooling}}} \tag{5.1}$$

and is particularly useful because it can be estimated from measurements taken in an experimental rig without reproducing real engine coolant-to-mainstream and mainstream-to-wall temperature ratios. NHFR therefore allows the effect of film cooling on heat flux in an engine environment to be shown from experimental rig data. The present simulations were performed at engine scale, with engine-realistic temperatures, so NHFR is calculated directly as in equation 5.1; this is presented in figure 5.17. The heat flux distribution without cooling air is obtained from a simulation run using the same mesh but with all cooling holes sealed.

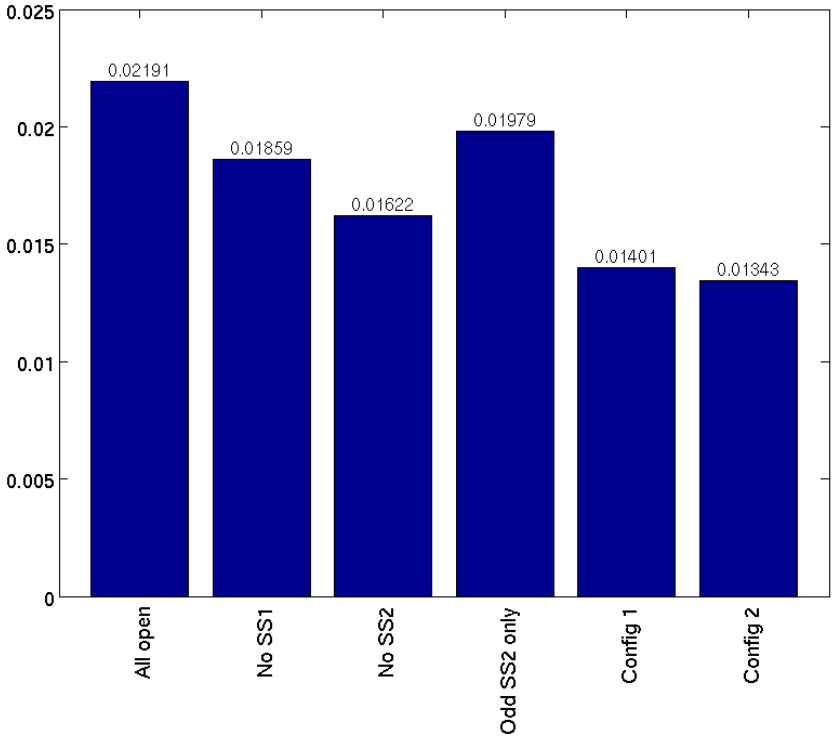

(a) Total coolant mass flow rate / $\mathrm{kg\,s^{-1}}$

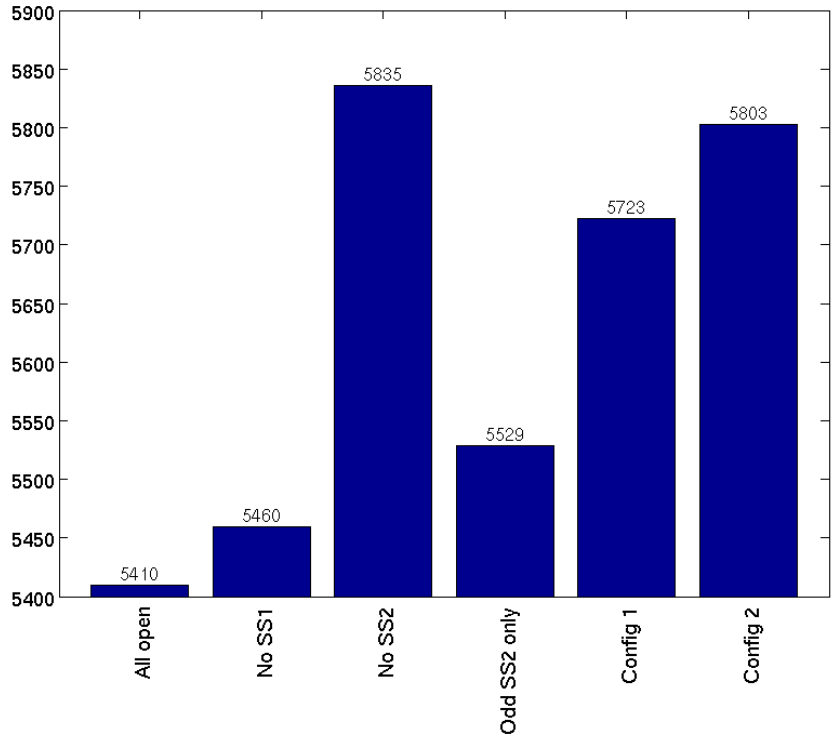

(b) Total blade tip heat transfer rate / $\mathrm{W\,m^{-2}}$

Figure 5.16: Total coolant mass flow rate and total blade tip heat transfer rate

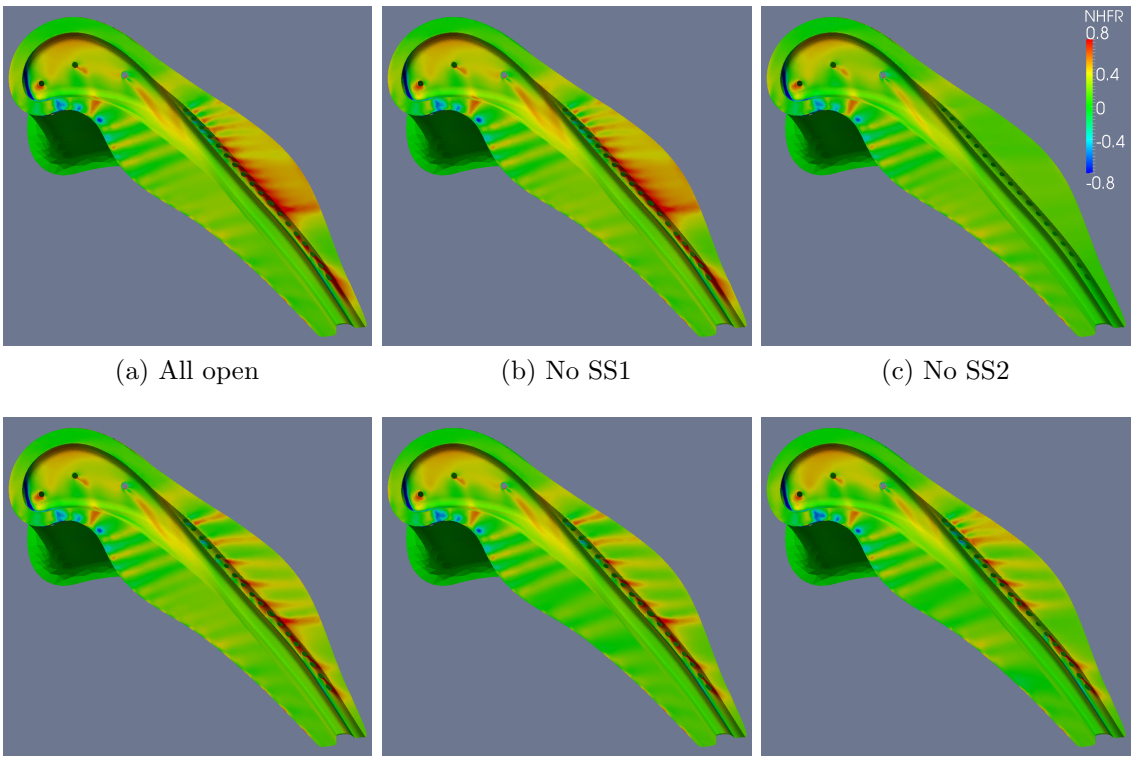

(a) All open (b) No SS1 (c) No SS2

(d) Odd SS2 only (e) Config 1 (f) Config 2

Figure 5.17: Net heat flux reduction

The net heat flux reduction is negative in the space between the coolant paths in the concave part of the pressure side squealet rim. This reflects an increase in local heat flux into the blade when film cooling is introduced, which is caused by the local augmentation of heat transfer coefficient by the film cooling air combined with poor film cooling effectiveness. Because of the shape of the external aerofoil in this region, it is difficult to produce good film coverage using discrete cooling holes here; future design revisions may benefit from a small reshaping of the pressure side tip extension to make this area more amenable to film cooling. It should be noted that the tendancy of RANS turbulence models to underpredict the spreading of film cooling flows may have exacerbated this issue and that the regions of negative NHFR may not be as significant in reality as are suggested by these simulation results; a more detailed examination of this region would be needed to eliminate the risk entirely. NHFR

remains positive over the rest of the blade tip, indicating that the film cooling air reduces the thermal load elsewhere.

5.5 Addition of extra cooling holes

While the inclusion of cooling flows has reduced the adiabatic wall temperatures over the majority of the blade tip, there remains a high temperature region on the squealet rim at the crown of the blade across all of the tested cooling configurations. This hot spot is identifiable in the 0.25 mm tip gap uncooled blade tip simulations as well, but is not nearly as prominent; with film cooling, it is the hottest part of the entire blade tip surface. This island of high temperature persists because it is very difficult to get coolant to this area, due to the flow structure around the forward portion of the blade tip. As can be seen in figure 5.18, little of the flow in this region has traversed much of the blade tip surface, making it difficult to entrain cooling air into the over-tip leakage flow to reach this area.

In an effort to solve this problem, four additional holes were added to the geometry as shown in figure 5.19. The first of these new holes is a vertical dust hole, intended as a replacement for the dust hole at the end of the leading edge channel. This repositioning could be accommodated with minor reshaping of the top of the internal geometry of the core and is designed to allow the cooling flow expelled from the dust hole to be advected to the inner side of the blade crown, providing cooling without drawing any additional cooling air. The other three holes are angled so that they blow cooling air on to this surface directly, similar to those described in Correia (2001). Their axes pass directly through the squealet rim and as such, machining them by traditional methods would require drilling through the rim itself. These holes are therefore not manufacturable by traditional techniques and have been located as a possibility for future manufacturing technologies, such as *Virtual Pattern Casting* (Frasier et al., 2011), that will allow cooling holes to be cast directly in place. They

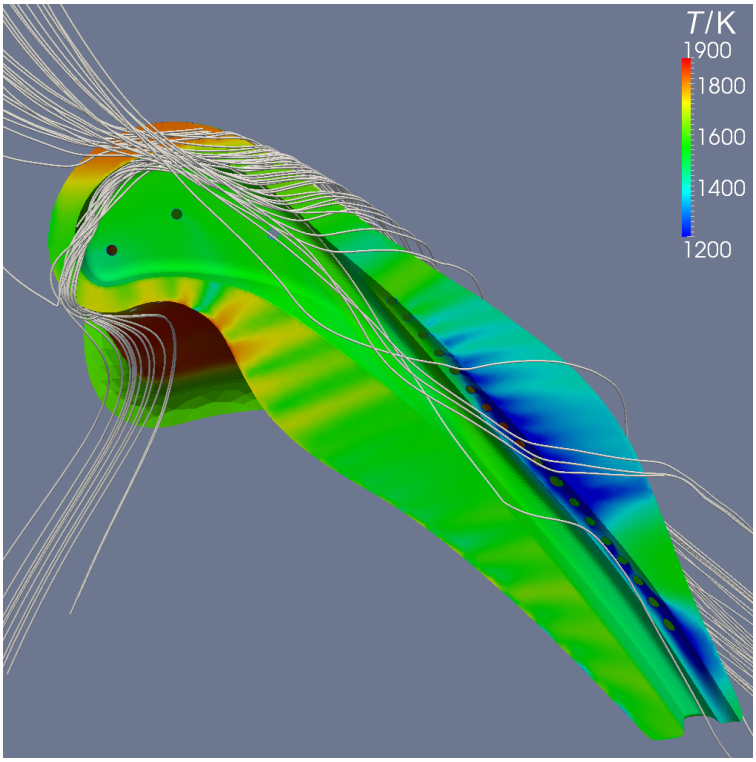

Figure 5.18: Pathlines around suction side hot spot (*All open* configuration)

could potentially be manufactured using currently available techniques by drilling directly through the squealet rim and then optionally back-filling the holes in the rim; this could potentially cause local stress problems in the rim, however.

The generation of the hybrid mesh used in the first part of this chapter was a long and arduous process, taking several months to complete successfully, even with the compromise eventually made in the mesh. This additional exploratory study was therefore performed on a purely tetrahedral mesh with no prism layers. By doing this, the mesh was reduced to 9.85 million cells, with a minimum cell quality of 0.20. Simulations using this new mesh were significantly faster to converge due to both the reduced cell count and the increased mesh quality. However, it is recognised that a significant reduction in simulation accuracy, particularly with regards to heat transfer predictions, will have been introduced by the elimination of the boundary layer mesh.

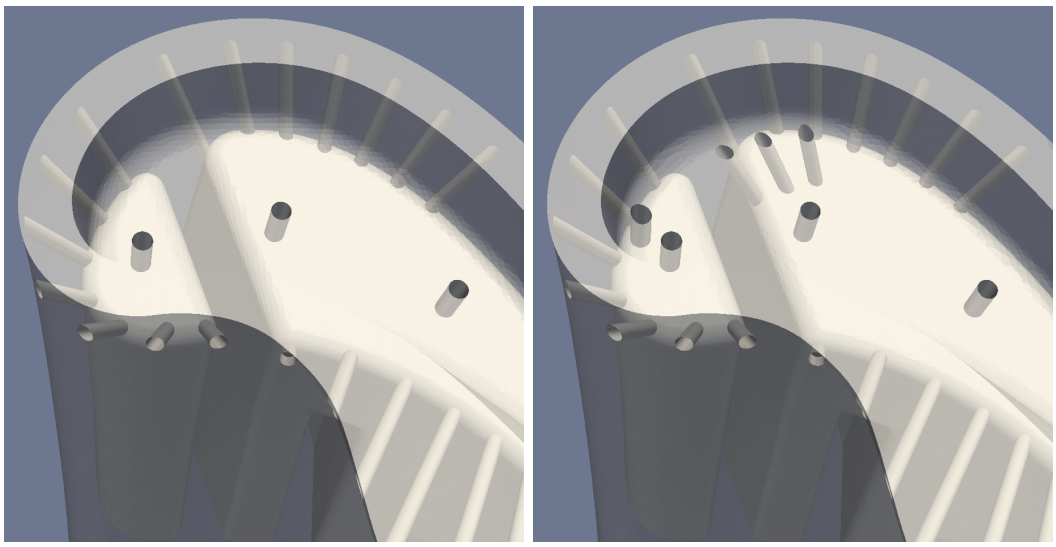

(a) Original cooling hole layout (b) New cooling hole layout

Figure 5.19: Location of extra cooling holes

Three configurations were tested with the new mesh, illustrated in figure 5.20. The *"All open"* configuration replicates the original *All open* configuration—i.e. with all of the new holes sealed—and is intended to allow the results from the new, purely tetrahedral mesh to be compared against the results from the original, hybrid tetrahedral and prism layer mesh to give some indication of the scale of error that has been introduced. *New holes 1* replicates the final configuration from the previous section (*Config 2*), but with the first dust hole repositioned and all three of the new cooling holes open. This configuration, therefore, is not manufacturable with current techniques, so a second variant, *New holes 2*, was also tested. This configuration is identical to *Config 2*, but with the first dust hole repositioned in an attempt to cool the crown of the blade tip. As all of the cooling holes have line-of-sight access, *New holes 2* is currently manufacturable.

Figures 5.21 and 5.22 show a comparison of the heat transfer data from the original *All open* configuration run on the two meshes. The predicted adiabatic wall temperatures compare very well, with only minor differences present between the distributions, for example the more pronounced striping over the pressure side squealet

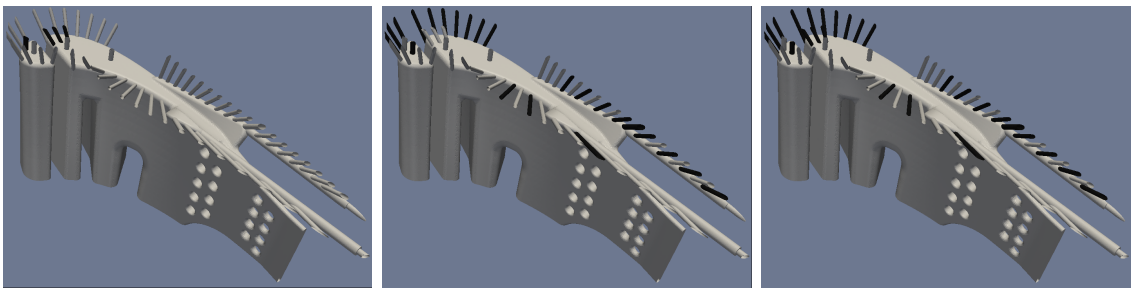

(a) *"All open"* (b) *New holes 1* (c) *New holes 2*

Figure 5.20: Cooling configurations with extra holes
(grey = open, black = closed)

rim for the purely tetrahedral mesh. The predicted heat transfer coefficients are slightly more distinct, although good similarity still remains. The predicted levels are very close together, but there is a much clearer separation and subsequent reattachment of the flow over the pressure side edge (and on the suction side near the tip shelf) with the purely tetrahedral mesh. Importantly though, the overall character of the predicted flow field remains identical despite this discrepancy in the detail.

The comparison of heat transfer coefficient in the forward part of the blade is not as good, however. A large hot spot is present on the floor of the cavity in the purely tetrahedral mesh results that is not found in the hybrid mesh data. There is also a significant increase in heat transfer coefficient on the outer squealet rim by the leading edge. Both of these differences are caused by a change in flow, illustrated in figure 5.23. A slight change to the way flow enters the cavity at the leading edge has a large impact on the structure of the flow in the forward part of the cavity. In the case of the hybrid mesh, the cavity flow originates from a lower radius, flowing over the leading edge region and forming a large vortex that dominates the cavity flow. With the purely tetrahedral mesh, by contrast, the over-tip leakage flow that enters the cavity is largely drawn from the region adjacent to the casing, which subsequently impinges upon the cavity floor, causing the hot spot. In each case, the flow enters the cavity at approximately the same location, crossing the squealet rim close to the

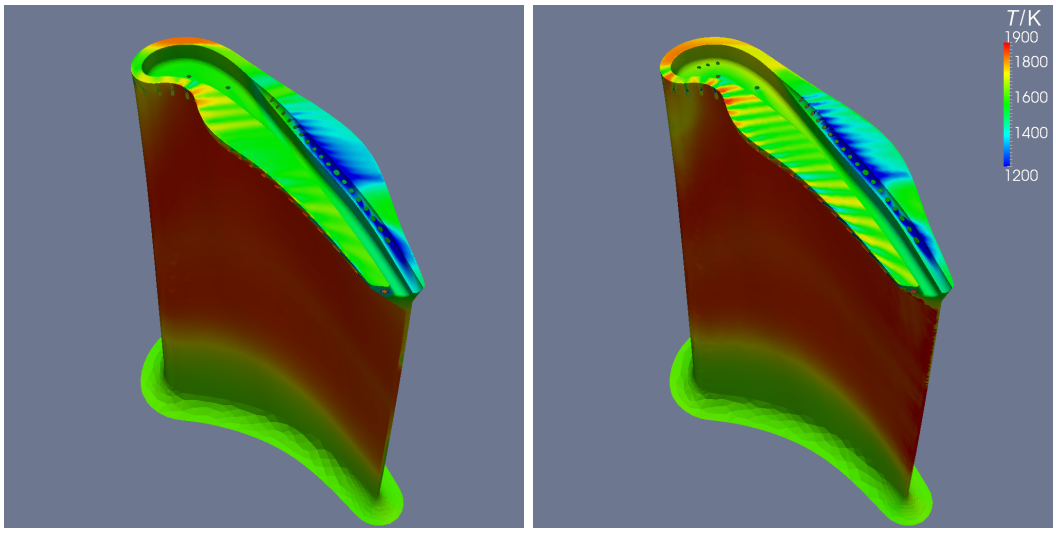

(a) Hybrid mesh (b) Purely tetrahedral mesh

Figure 5.21: Mesh comparison—Adiabatic wall temperature
(Cooling configurations are identical; additional cooling holes are sealed)

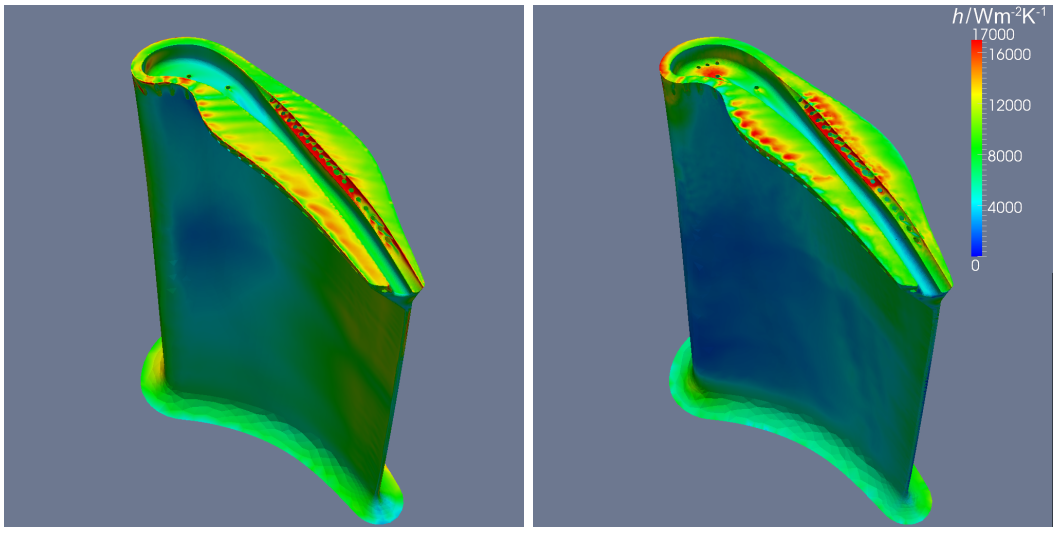

(a) Hybrid mesh (b) Purely tetrahedral mesh

Figure 5.22: Mesh comparison—Heat transfer coefficient
(Cooling configurations are identical; additional cooling holes are sealed)

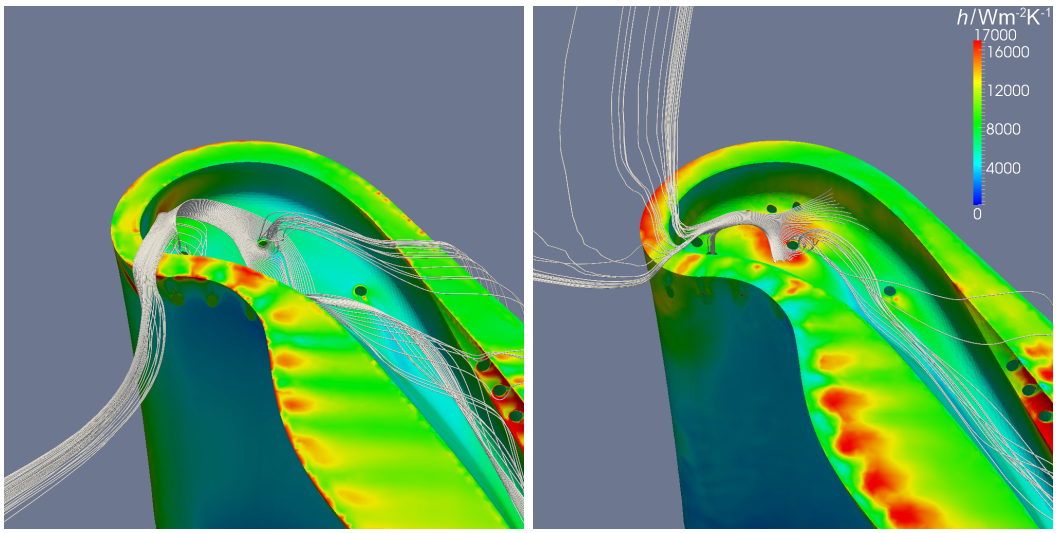

(a) Hybrid mesh (b) Purely tetrahedral mesh

Figure 5.23: Mesh comparison—Heat transfer coefficient and pathlines (Cooling configurations are identical; additional cooling holes are sealed)

leading edge, but as the flow originates from different locations, the flow entry angle is changed dramatically. This relatively minor difference has a large impact on the cavity flow structure, which can be seen more clearly in figure 5.24.

It is clear that there is considerable mesh sensitivity present and that the omission of prism layers has resulted in a noticable change in the cavity flow. However, although the differences are evidently significant, they are not irreconcilably large. The flow and heat transfer predictions for the latter two-thirds of the blade tip region remain very well matched and the purely tetrahedral mesh simulation is an excellent—if a little coarse—approximation in this region. Even in the cavity where the differences are most pronounced, the salient features of the over-tip leakage flow (e.g. gross flow direction, separation and reattachment) are still captured to some extent. Providing that these differences are recognised, additional understanding can still be gained from the simulations run using this purely tetrahedral mesh. With the omission of prism layers, the area-averaged values of heat flux, adiabatic wall temperature and

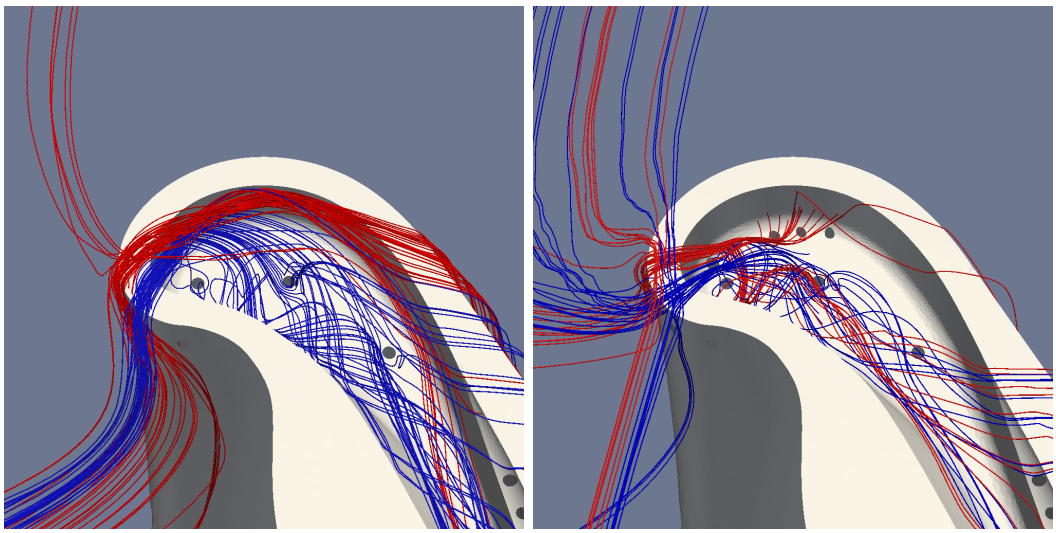

(a) Hybrid mesh (b) Purely tetrahedral mesh

Figure 5.24: Mesh comparison—Cavity flow formation
(Cooling configurations are identical; additional cooling holes are sealed)

heat transfer coefficient from ∼90% span outwards are changed by −6.1%, +1.2% and −10.6%, respectively.

The heat transfer predictions for the three cooling configurations with the new mesh are shown in figures 5.25 to 5.27. There is a prominent region of enhanced heat transfer seemingly centred around the sealed dust hole for both the *New holes 1* and *New holes 2* configurations. This feature is rather unusual, and could easily be dismissed as an artifice of the geometry or the mesh, for example caused by a wake from a cover surface that was not quite flush with the cavity floor, as it is centred around a cooling hole that is effectively not present. However, as can be seen in figure 5.29, it is not caused by a problem with the CAD geometry, but rather is coincident with the position of initial attachment of the over-tip leakage flow on to the floor of the blade tip cavity. This is, therefore, a feature that would always have been present were it not for the exact placement of the original dust hole. The blowing from that first dust hole interrupted the impingement of the over-tip leakage flow on the cavity floor, suppressing the peak in heat transfer coefficient now visible.

Aside from that unexpected feature, the additional cooling holes and relocated dust hole cause very little change to the overall adiabatic wall temperature and heat transfer coefficient distributions. Figure 5.30 shows a detail of the adiabatic wall temperature distributions around the inner rim in the vicinity of the additional cooling holes. The new cooling holes in the *New Holes 1* configuration (figure 5.30b) have a very clear effect on the local temperature, blowing directly on to the squealer rim and resulting in very high film cooling effectiveness on the inner surface. While the new cooling holes leave a clear footprint in the adiabatic wall temperature distribution, the relocated dust hole alone (*New holes 2* configuration in figure 5.30c) has very little impact. Although the air from this dust hole appears to be convected to the correct place (grey pathlines in figure 5.31), its effect on the adiabatic wall temperature is minimal. It therefore appears that the relocation of the dust hole was unsuccessful,

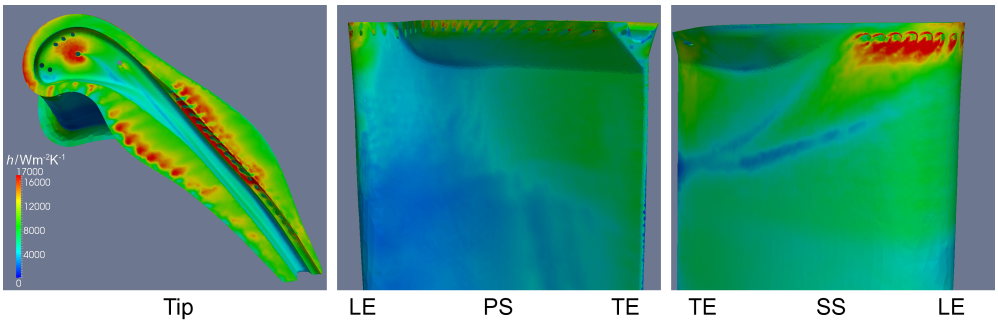

(a) Heat transfer coefficient

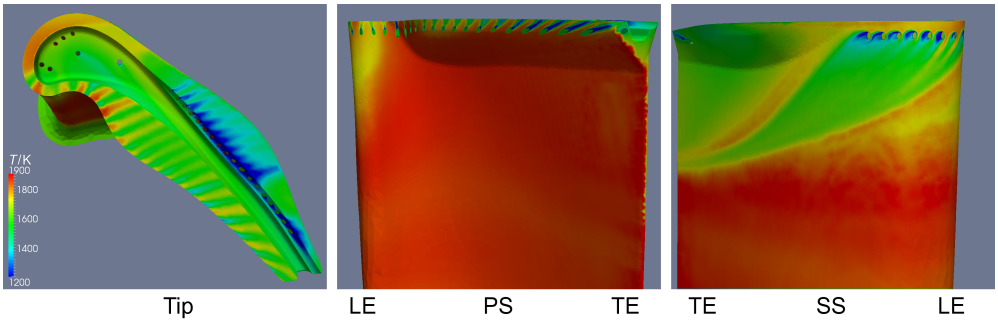

(b) Adiabatic wall temperature

Figure 5.25: *"All open"* cooling configuration results (purely tetrahedral mesh)

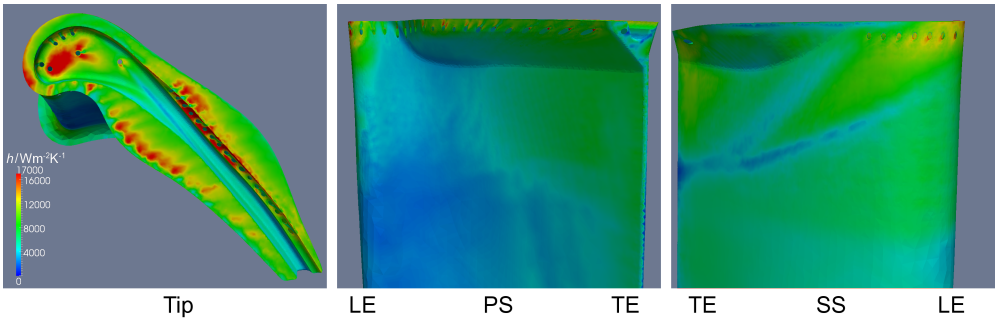

(a) Heat transfer coefficient

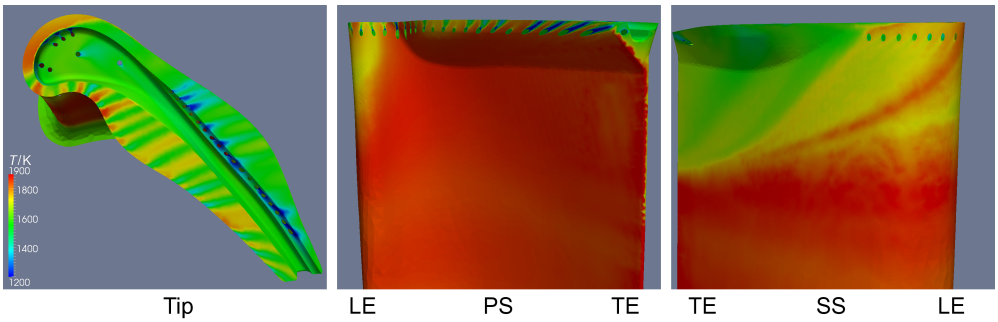

(b) Adiabatic wall temperature

Figure 5.26: *New holes 1* configuration results (purely tetrahedral mesh)

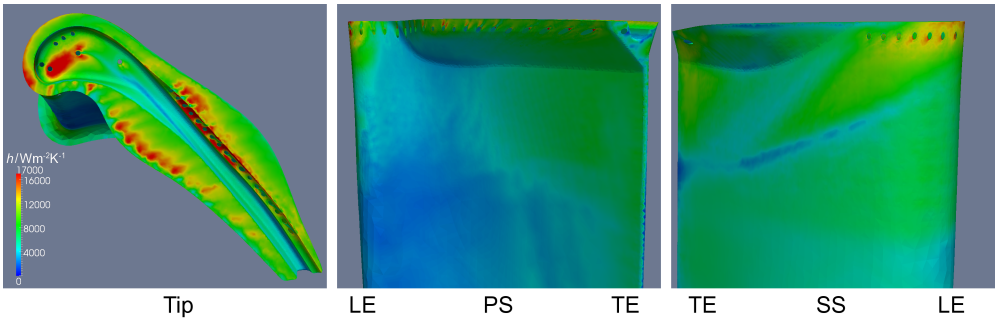

(a) Heat transfer coefficient

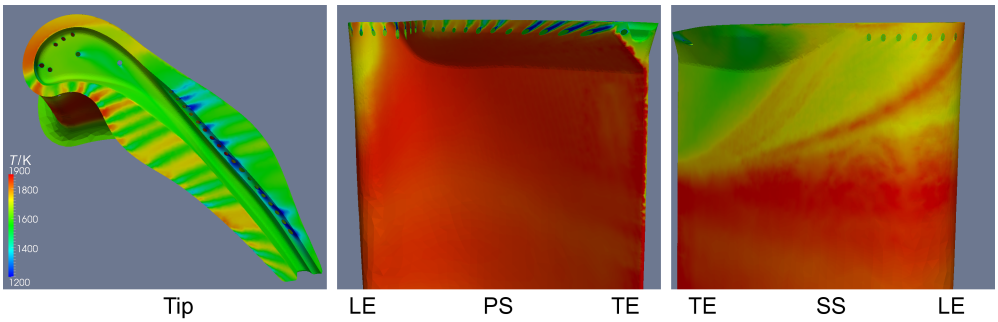

(b) Adiabatic wall temperature

Figure 5.27: *New holes 2* configuration results (purely tetrahedral mesh)

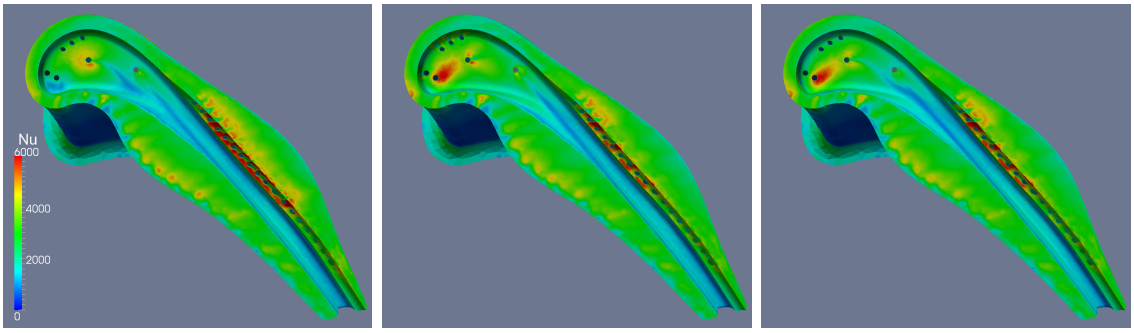

(a) *"All open"* (b) *New holes 1* (c) *New holes 2*

Figure 5.28: Nusselt number (purely tetrahedral mesh)

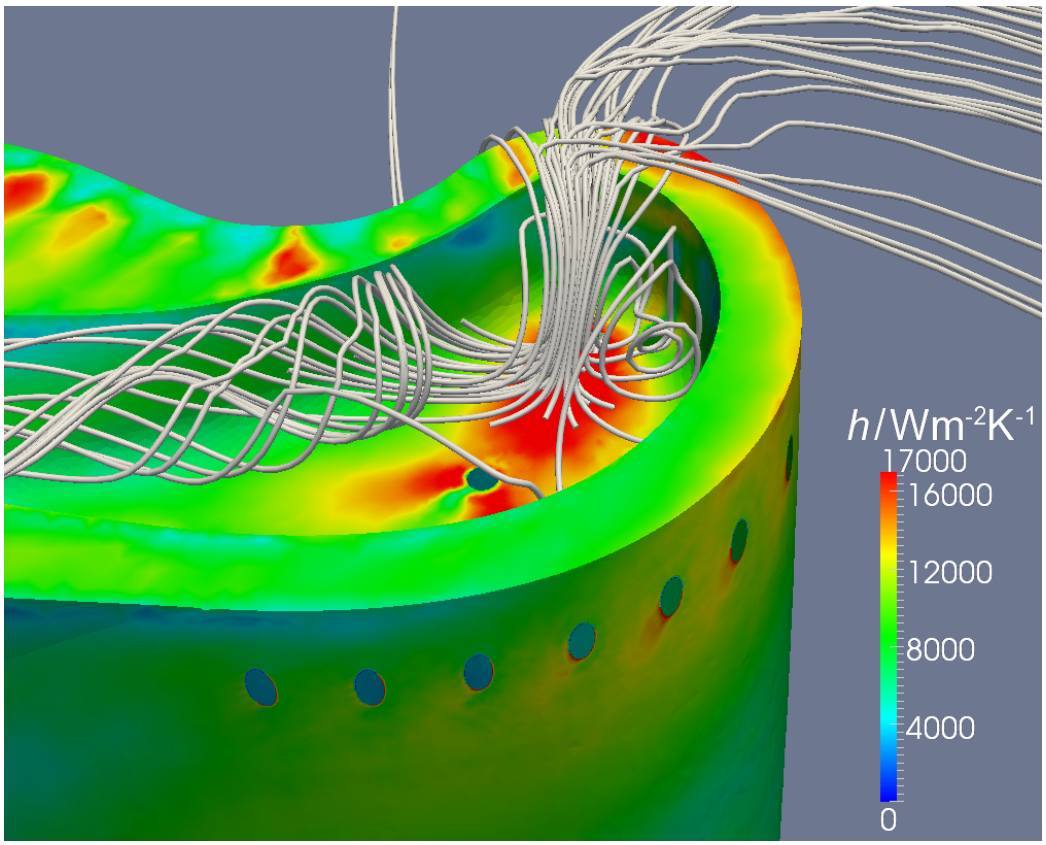

Figure 5.29: Cavity floor impingement hot spot (*New holes 1* configuration)

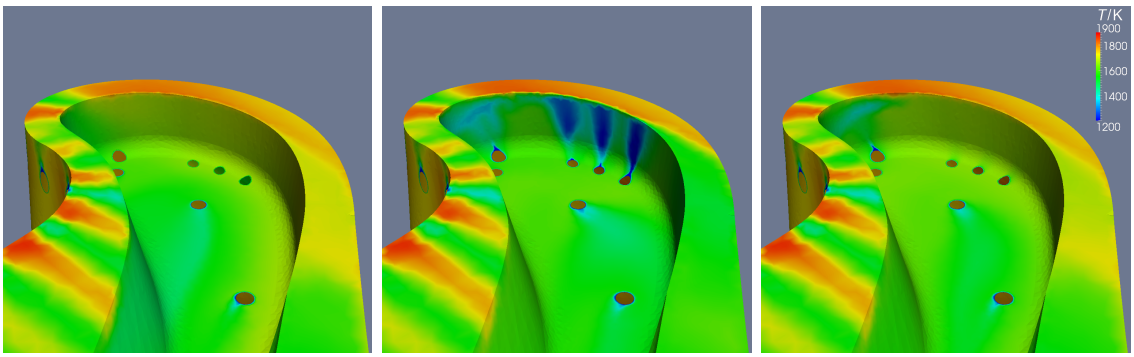

(a) *"All open"* (b) *New holes 1* (c) *New holes 2*

Figure 5.30: Adiabatic wall temperatures around inner suction side rim

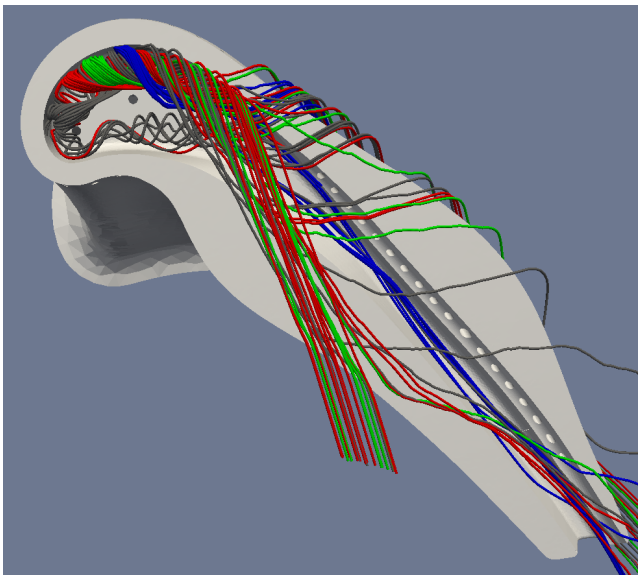

Figure 5.31: Coolant pathlines from the new holes
(grey = relocated dust hole, red/green/blue = new cooling holes)

increasing the heat transfer to the cavity floor (as it no longer disrupts the impinging flow) while providing little benefit at the blade crown.

The pathlines in figure 5.31 show that cooling air from all three new cooling holes and the relocated dust hole are bound into a tight recirculation that holds it close it to the inner suction side rim over the entire crown of the blade tip. As this cooling air is not convected to the outer surface of the rim, the removal of heat would have to be achieved by conduction through the metal. Some form of conduction analysis would

therefore have to be performed in order to ascertain whether or not these measures would be sufficient to reduce the local metal temperatures enough to prevent damage to the squealer rim.

Although some of the cooling air from these holes leaves the cavity in the expected way over the suction side rim to join the over-tip leakage vortex, much of it crosses the tip gap and reaches the stationary over-tip casing and is dragged back over the pressure side edge. This could potentially be useful if the casing liner requires additional cooling as the blade passes over it, but otherwise some changes to the cooling layout could be made to keep the cooling air close to the blade tip to maximise the efficiency of its use. However, these observations regarding the path that the cooling air takes must be taken with some degree of caution. The new cooling holes are located in the region of the cavity near the leading edge where significant discrepancies between the purely tetrahedral mesh and the hybrid mesh results were observed, and the attachment of cooling air to the over-tip casing could feasibly be affected by the build up of the boundary layer there.

The new cooling holes do provide an interesting possibility to improve cooling air utilisation. It was noted in the previous section that the air flowing through the second dust hole, close to which the new cooling holes are located, is lost over the suction side rim almost immediately and provides little benefit in cooling the blade tip. Indeed, this dust hole is required to allow the expulsion of debris from the internal passage rather than specifically being located for thermal protection. It is possible, therefore, that the second dust hole could be eliminated altogether if the inclined cooling holes were widened sufficiently to act as dust holes (potentially requiring minor reshaping of the core as well); by doing this, the overall coolant mass flow rate could be decreased while simultaneously increasing the flow of cooling air to this critical and difficult to cool region. Speculating further, if the new cooling holes were formed by drilling through the squealet rim and if these holes were subsequently left open, it might even be possible to draw some of the impinging cooling air or the cooling air

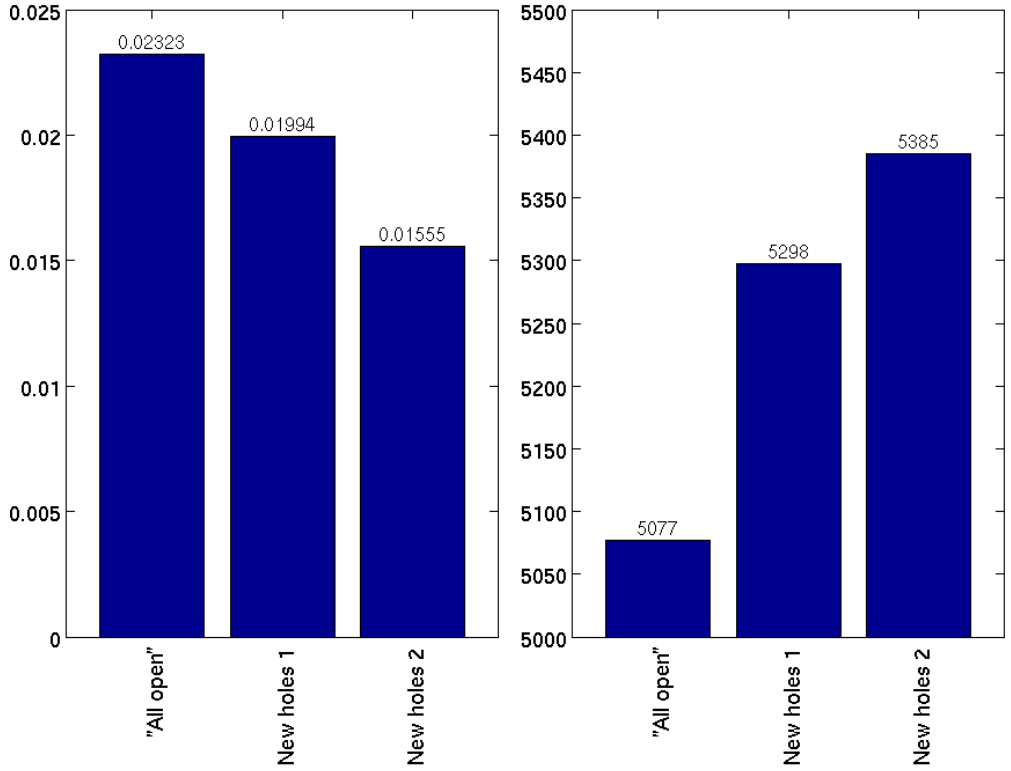

(a) Total coolant mass flow rate / $\mathrm{kg\,s^{-1}}$

(b) Total blade tip heat transfer rate / $\mathrm{W\,m^{-2}}$

Figure 5.32: Total coolant mass flow rate and total blade tip heat transfer rate

bound up in the vortex located on the inner rim surface through the holes in the rim and provide some degree of internal cooling for the rim itself.

Overall cooling air mass flow rate requirements and total blade tip heat transfer rate for the simulations run with the purely tetrahedral mesh are plotted in figure 5.32. Comparing the *New holes 1* and the *New holes 2* configurations, it can be seen that the addition of the three additional cooling holes close to the crown of the blade tip cause a large increase in the total required coolant mass flow rate of 28%, compared with the case that merely has the repositioned dust hole. A direct comparison to figure 5.16 is not possible, as the absence of prism layers in the mesh causes significant changes to both the coolant mass flow rate and the blade tip heat transfer; for the *All open* cooling configuration, there is a 6% increase in predicted coolant mass flow

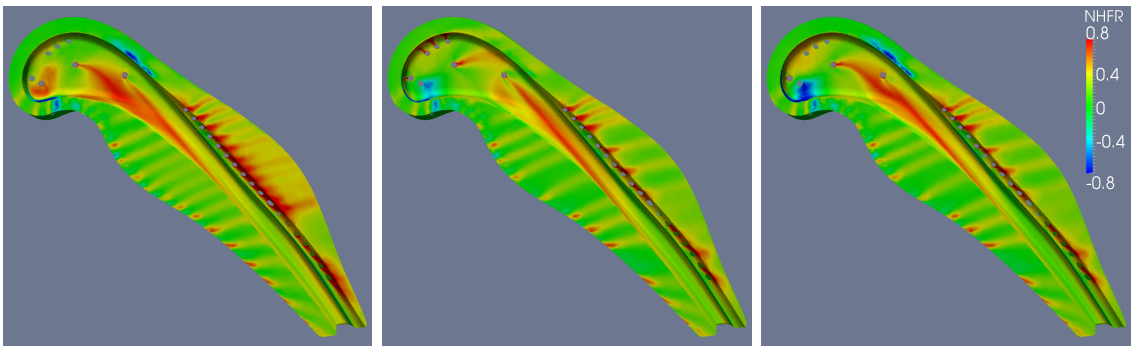

(a) *"All open"* (b) *New holes 1* (c) *New holes 2*

Figure 5.33: Net heat flux reduction

rate and a 6% decrease in total blade tip heat transfer rate when the simulation is run without prism layers. The *New holes 1* and *New holes 2* cooling configurations show increases in total blade tip heat transfer rate of 4.3% and 6.1%, respectively, over the *"All open"* cooling configuration, which compares favourably to an increase of 7.3% seen for the *Config 2* cooling configuration when compared to the *All open* configuration modelled with a comparable meshing strategy. The corresponding decreases in required coolant mass flow rates for the *New holes 1*, *New holes 2* and *Config 2* configurations were 14%, 33% and 39%, respectively. Net heat flux reduction distributions are shown in figure 5.33, although caution is once again advised in interpreting these data, as the mesh used for these simulations lacks prism layers.

5.6 Chapter summary

In this chapter, an engine-realistic, time-steady CFD investigation into the thermal performance of various blade tip cooling schemes has been presented. This was conducted at a single blade tip clearance of 0.5 mm (0.89% blade chord) with a slightly amended version of the revised squealet tip introduced in chapter 4. A simplified version of the internal core used with the EFE winglet was used as a base for the cooling configurations, to which as many cooling holes as could be

placed without violating manufacturing constraints were added. The cooling holes were capped at both ends with cover surfaces and a hybrid tetrahedral and prism layer mesh was generated in ICEM CFD 12 with each cooling hole specified as a separate fluid volume, allowing them to be left open or sealed as solid regions merely by changing the boundary condition specification in the solver. Solution was once again performed with the time-steady, pressure based solver of FLUENT 6.3 with the SIMPLE algorithm for pressure-velocity coupling, using the realisable k-ϵ turbulence model and enhanced wall treatment to maintain compatibility with the previous simulations. Six cooling configurations were tested initially and a significant reduction of cooling air consumption of 38% was achieved, at the expense of an increase of 7% in total blade tip heat transfer rate, compared to the intial cooling configuration with all holes open. The cooling holes exiting on the suction side of the blade did not provide useful film coverage over the blade tip, as the cooling air was swept away from the region. It was also found that adequate coverage of the tip shelf and suction side rim could be achieved with relatively few holes in the tip shelf, despite the relatively small degree of spreading of the cooling air that was observed. This was, in part, due to the good film coverage over both the pressure side and suction side squealet rims that was produced by the pressure side cooling holes. It was also found that the cooling gallery on the suction side reduced the pressure ratios across the cooling holes located on the tip shelf towards the rear of the blade. These reduced pressure ratios resulted in lower momentum cooling flows that improved the coverage of the trailing edge of the blade tip. Thermal gradients across the blade tip were also reduced by the selective blocking of cooling holes. A high temperature region remained on the squealet rim at the blade crown, so a further cooling geometry was tested with three additional holes (though these are not manufacturable using current techniques and were designed with future manufacturing techniques in mind) and the relocation of the first of the dust holes. Due to time constraints, this extra cooling geometry was tested using a purely tetrahedral mesh without prism layers, which exhibited some mesh sensitivity

in the forward part of the blade tip. The relocation of the dust hole was found to have a detrimental effect on thermal performance, providing little effective cooling on the squealet rim but resulting in a significant increase in heat transfer coefficient where the dust hole had previously been. This result was somewhat unexpected and highlights that the placement of the dust hole for the leading edge channel is absolutely critical because of the sensitivity of the flow in the forward part of the cavity. By contrast, the additional cooling holes displayed excellent cooling performance and could potentially be used in place of the second dust hole, to some extent mitigating the extra cooling air required to feed them.

Chapter 6

High Speed Linear Cascade Experimental Testing

6.1 Introduction

This chapter covers an experimental study performed using the High Speed Linear Cascade (HSLC) facility at the Osney Thermofluids Laboratory, Oxford University, a transonic, 1.9× scale blowdown facility. The squealet design from the CFD study reported in chapter 5 is transformed for use in the linear cascade environment and test pieces are manufactured by stereolithography. Aerodynamic loss measurements are taken at nominal tip gaps of 0.48 mm, 0.95 mm and 1.4 mm (0.25 mm, 0.5 mm and 0.75 mm at engine-equivalent scale, or 0.45%, 0.89% and 1.34% blade chord) with an uncooled blade tip (with no cooling holes present and clean external geometry) by a downstream traverse using a three-hole probe and a single-hole probe for the near-casing region. Heat transfer measurements are taken with the same test blade tip by a transient, infra-red thermographic method at the 0.89% and 1.34% blade chord tip gaps. Thermal tests are additionally conducted at the intermediate tip gap (0.89% blade chord) on a test blade with film cooling with the same cooling hole locations as in chapter 5.

6.2 Experimental methodology

6.2.1 HSLC facility

Only a cursory overview of the HSLC facility is presented here. Extensive details of the experimental setup are available in O'Dowd (2010), which records the initial commissioning of the experimental rig and details all of its features. The experimental arrangement is also described in O'Dowd et al. (2011b), Zhang et al. (2011a), O'Dowd et al. (2010) and Zhang et al. (2011b). The development of the measurement and analysis techniques used in this chapter and the commissioning of the experimental facility itself were performed by Dr Devin O'Dowd and Dr Qiang Zhang and the present author gratefully acknowledges their contributions.

A schematic of the HSLC facility in overview is shown in figure 6.1, with a detail of the test section. Photos of the same are shown in figure 6.2. The HSLC test section is a four passage linear cascade at 1.9× scale, fully enclosed within the outlet plenum. The aerofoil section for the cascade is taken from the EFE HP turbine blade at 90% span. The HSLC is a blowdown facility, venting air from two 30 m^3 storage tanks through the test section to an exhaust at atmospheric pressure. The mainstream supply pressure from the tanks is nominally 2750 kPa, which is regulated to the appropriate inlet pressure for the test section by a Spirax-Sarco 'C' series cage design control valve driven by an SP200 electropneumatic smart positioner, controlled by an Ascon gammadue series X5 process controller. This process controller allows for full PID control, fed back from a pitot-static probe located at the inlet to the test section, allowing the pressure ratio across the test section to be set and maintained as the storage tanks are depleted and the supply pressure drops. Since the study of O'Dowd (2010), the exhaust pipes have been connected to a detuner for acoustic noise control, extending their length by approximately 20 m and hence increasing the back-pressure in the outlet plenum downstream of the blade row. The regulated total pressure set at the inlet to the test section has therefore been increased by ∼20%

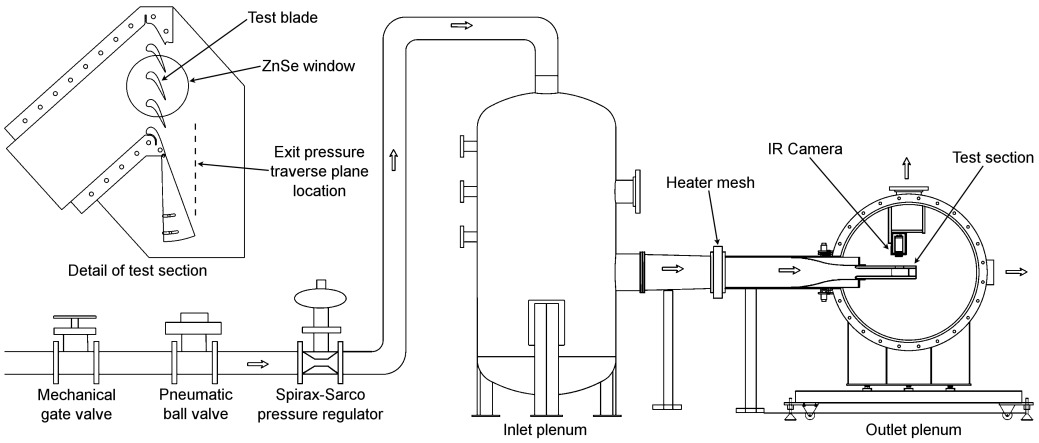

Figure 6.1: Schematic of the HSLC
(CAD drawings courtesy of Dr Qiang Zhang)

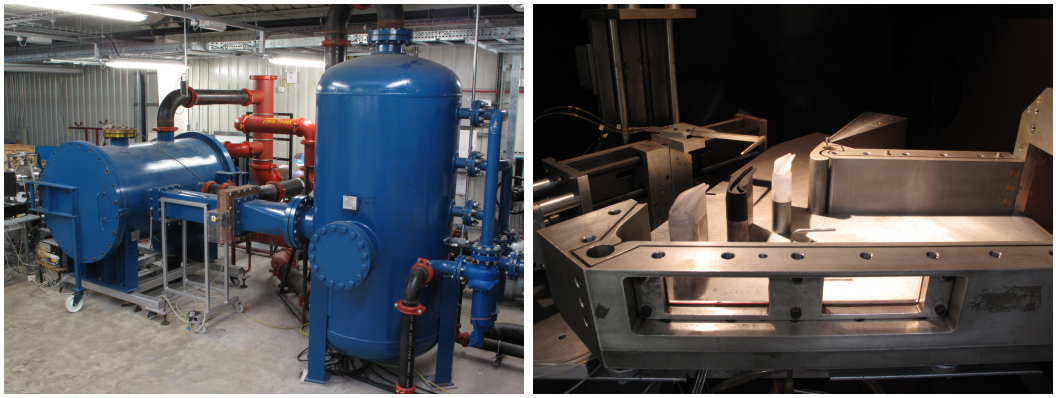

(a) Overview (b) Test section

Figure 6.2: Photos of the HSLC

to match the original pressure ratio and maintain the Mach number distribution, resulting in a small increase in Reynolds number of approximately 15%. Details of the nominal flow conditions for the HSLC are given in table 6.2.

6.2.2 Aero-thermal scaling for the HSLC

The dimensional analysis required for correct aero-thermal scaling of the flow through a turbine stage was presented in section 1.5. This analysis showed that aerodynamic similarity will approximately be achieved for an experiment using air as the test fluid

Blade chord	78.5 mm
Axial chord	47.7 mm
Blade pitch	68.4 mm
Blade turning angle	110°
Test section passage height	71.8 mm
Scale	1.9

Table 6.1: Summary of HSLC geometry parameters

Inlet total pressure	239 kPa
Inlet static pressure	227 kPa
Inlet Mach number	0.28
Inlet velocity	$93.9\,\mathrm{m\,s^{-1}}$
Inlet Reynolds number (based on axial chord)	0.69×10^6
Exit static pressure	123 kPa
Isentropic exit Mach number	1.02
Pressure ratio ($p_{0\mathrm{i}}/p_{\mathrm{o}}$)	1.94

Table 6.2: HSLC nominal flow conditions

providing that Reynolds number, Mach number, pressure ratio and specific speed are all matched. The HSLC flow conditions, summarised in table 6.2, match the first three dimensionless groups to the nominal (blade-relative) engine conditions; the specific speed is clearly meaningless in the context of a linear cascade with stationary blades. Similarity in heat transfer additionally requires gas-to-wall temperature ratio to be matched—this was not possible in the experimental rig. This discrepancy may be corrected for using the correlation proposed by Fitt et al. (1986).

$$\frac{\mathrm{Nu}}{\mathrm{Nu}_{\mathrm{Incompressible}}} = \left(\frac{T}{T_{\mathrm{w}}}\right)^{0.25} \tag{6.1}$$

The gas-to-wall temperature ratio for the HP turbine blade in a real engine environment is typically ∼1.5, whereas that achieved in the HSLC was ∼1.1. The correlation therefore indicates that Nusselt numbers measured in the HSLC environment should be scaled up by approximately 7.5% for engine-representative heat transfer.

6.2.3 Geometry transformation

The external geometry of the test blade tip for use in the HSLC was a linearised version of the geometry used in the cooled CFD simulations of chapter 5. The external, 3D geometry was first trimmed to 90% span and then a coordinate transformation applied, substituting z-coordinate for radius and y-coordinate for circumferential location to remove the annularity. A blend was then used to join the resultant profile to the exact aerofoil shape found on the pre-existing base blades of the test section smoothly.

Due to the relatively small scale of the test section, there was only sufficient room within the new blade tip for a single coolant plenum. The varying feed pressures supplied by the various channels of the leading edge channel, leading edge feed and the multipass (and the cross flow resulting from this variation) could therefore not be replicated. A simple coolant plenum was inserted into the geometry, with representative noggins on the upper surface for the two cooling galleries to attach to. To locate the cooling holes and cooling galleries in the linearised geometry, the points on the centreline of each hole where it broke the external aerofoil surface and the internal core surface were taken and put through the same coordinate transformation that the external surfaces had been. These two transformed points were then joined by a straight line to form the axis of the cooling hole in the test piece. The results of the deannularisation process can be seen in figure 6.3.

The test blade tips were manufactured by stereolithography by Gemini Prototyping Ltd. using DSM Somos WaterShed XC 11122 resin. Two sets of test blade tips were produced; one uncooled set with only the external geometry present, and one with the cooling configuration printed directly in the SLA process. The two different blade tips are shown directly from SLA printing in figure 6.4. These were bolted on to metal base blades in the cascade (as can be seen in figure 6.2b) to increase the rigidity of the test blades compared to manufacturing the whole blade out of resin (O'Dowd, 2010). Three small pins were also used in the thin trailing edge region to hold the blade tip

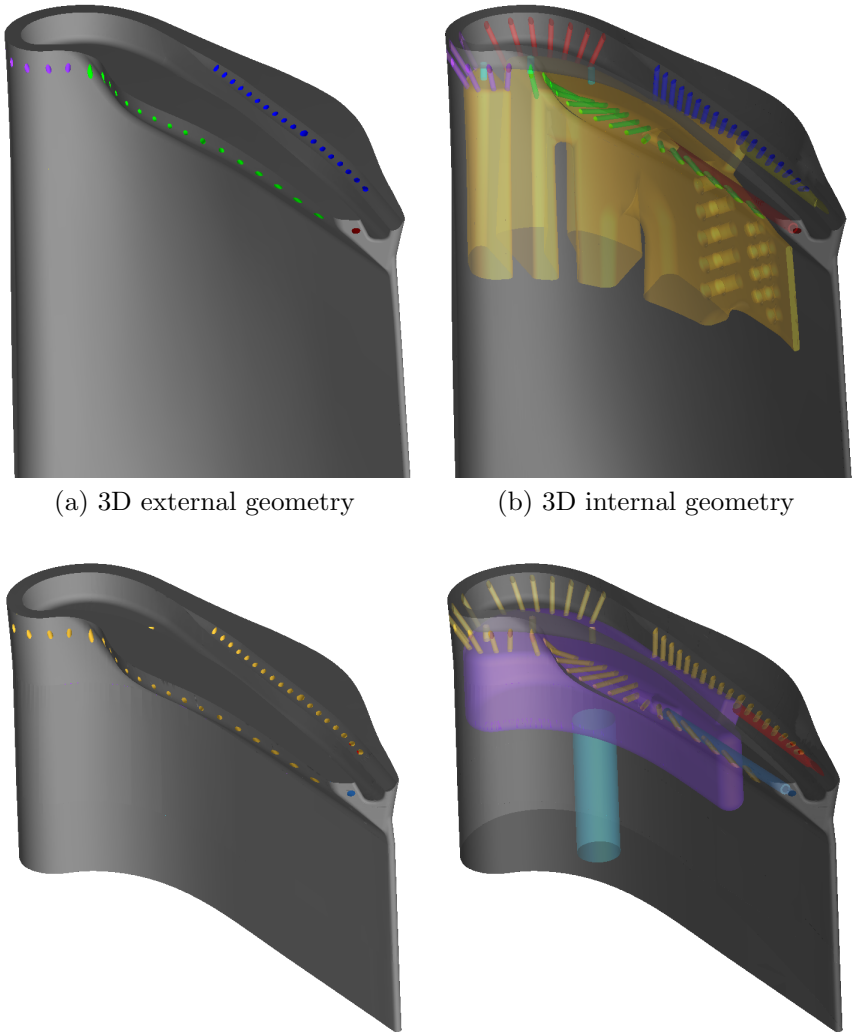

(a) 3D external geometry (b) 3D internal geometry

(c) Linearised external geometry (d) Linearised internal geometry

Figure 6.3: Linearisation of the test geometry

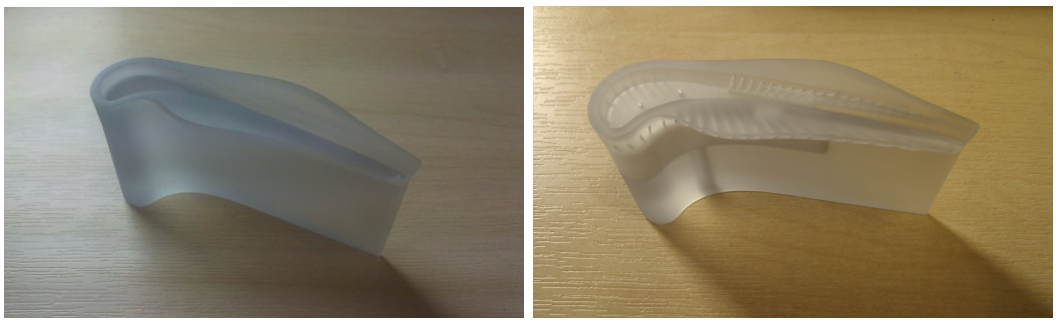

(a) Uncooled blade tip (b) Cooled blade tip

Figure 6.4: SLA blade tip models

to the base blade and prevent the relatively flexible plastic tip from deforming under aerodynamic load in this weak area.

6.2.4 Aerodynamic loss measurements

Aerodynamic loss measurements were accomplished by the downstream traverse of a three-hole probe, driven by two stepper motors controlled by LabVIEW 8.6. This three-hole probe had been calibrated over a yaw angle range of $\pm 60°$ and a Mach number range of 0.6 to 1.3 (O'Dowd, 2010). Due to the thickness of the three-hole probe stem, the probe tip could only be traversed to a minimum distance of 4 mm from the over-tip casing. In order to get closer to the endwall, a much thinner single-hole probe was traversed with the same system, allowing measurements to be taken down to 0.5 mm from the casing. Data were recorded with the single-hole probe at yaw angles of $+6°$, $0°$and $-10.5°$, taking care to ensure that the probe tip was in the same position at each alignment, allowing the single-hole probe to act as a pseudo three-hole probe. An estimate of the total pressure in the near-wall region could then be obtained by simple interpolation. There is some inherent error in the loss measurements, however, as only a three-hole probe rather than a four-hole probe was used, so variations in pitch angle could not be accounted for. However, at a $20°$ yaw angle, the centre hole pressure measurement was just 2.8% lower than the true total pressure (O'Dowd, 2010), so this error is expected to be small. Both the three-hole probe and the single-hole probe were constructed from stainless steel tubing with an outer diameter of 0.7 mm supported on a tapered sting with a maximum diameter of 7 mm, so the blockage of the probe is not expected to have a significant effect on the measurements. The traverse gear with three-hole probe attached is visible in the background of figure 6.2b.

The probe was traversed at a constant spanwise distance, with the probe pausing to collect data at 26 pitchwise locations, covering a single blade pitch. To allow sufficient time for flow settling, data gathering and probe movement at each location, a relatively

long run time of 59 seconds for each traverse of the probe was needed, during which time the supply pressure typically dropped from ∼2750 kPa to ∼2200 kPa. The Spirax-Sarco pressure regulator was therefore run with full PID control for the aerodynamic tests, which compensated for the decreasing supply pressure but introduced a small oscillation of approximately ±2.5% in total pressure at the inlet to the test section at a frequency on the order of 1 Hz. This variation in inlet total pressure results in a variation in exit isentropic Mach number of ±2.0%. To minimise the impact of this slight variation on the downstream pressure measurements, the pressures measured by the probe were recorded as differential pressures relative to the inlet total pressure.

Each downstream pressure survey was a composite of probe traverses taken at 11 spanwise heights. Three of these were taken with the single-hole probe, requiring three traverses per spanwise location for the different orientations of the probe, so each survey is the composite of 17 separate experimental runs.

6.2.5 Heat transfer measurements

The measurement of both heat transfer coefficient and adiabatic wall temperature distributions across the test blade tip was performed simultaneously by a transient infra-red thermographic method. A heater mesh (Ireland et al., 2001) is located upstream of the test section, which is powered by a Drake Power Systems high power DC power supply rated at 100 V, 1.5 kA and can produce a near-instantaneous step change of approximately 20°C in the mainstream flow temperature. A FLIR Systems, Inc. A325 infra-red camera was used to measure the surface temperature of the model blade tip, which was painted black to provide a uniformly high emissivity. The tip was viewed through a 10 cm diameter, IR-transmissive window made of Zinc-Selenide. The A325 IR camera measures the surface temperature over the range −20°C–120°C, digitising it as a 16-bit greyscale value. It provides a 320 × 240 resolution at a 60 Hz refresh rate. A 10 mm lens was used, giving a 45° × 33.8° field of view. The IR camera was mounted in an anti-vibration housing vertically above the test blade tip to allow a

clear and unobstructed view over the entire upper surface. Calibration of the greyscale signal was performed in situ; the uncooled test blade tip was instrumented with a 0.0254 mm fast-response thermocouple on the cavity floor to facilitate this. There was insufficient space on the cooled blade tip for a calibration thermocouple, so the calibration coefficients derived from the uncooled test at the same tip gap were used.

As the thermal conductivity of the SLA resin is low, semi-infinite, one-dimensional conduction could be assumed, providing the test duration was sufficiently short to ensure that the thermal pulse did not penetrate the full thickness of the model. The thermal pulse penetration depth is given by $4\sqrt{\alpha t}$ (Schultz and Jones, 1973). WaterShed XC 11122 has a manufacturer-quoted thermal diffusivity of $1.274 \times 10^{-7}\,\mathrm{m^2 s^{-1}}$. The test duration for the heat transfer tests for the uncooled blade tip was 3.5 s (from heater mesh activation), giving a minimum blade thickness of ∼2.7 mm to avoid violating the semi-infinite assumption, which was easily achieved. Due to the hollow cooling plenum within the cooled blade tip, the thickness of material under the cavity floor was just 2.3 mm, so the analysis period was restricted to 1.5 s, reducing the penetration depth to ∼1.7 mm. The semi-infinite conduction assumption is still violated, however, around the edges of the blade tip and in the vicinity of cooling holes and other features in the geometry.

The impulse response method of Oldfield (2008) was used to construct the local heat flux history at each location on the surface given its temperature history, measured by the IR camera. These instantaneous heat flux and surface temperature pairs are linked by

$$q = h(T_{\mathrm{ad}} - T_{\mathrm{w}}) \tag{6.2}$$

The local heat transfer coefficient could thus be obtained from the gradient and the adiabatic wall temperature from the x-intercept of the $q{\sim}T_{\mathrm{w}}$ plot from a single transient test. An example $q{\sim}T_{\mathrm{w}}$ plot for a single pixel location is shown in figure 6.5.

The measurement uncertainty associated with the heat transfer measurements taken using this method with the HSLC facility is fully documented in O'Dowd (2010)

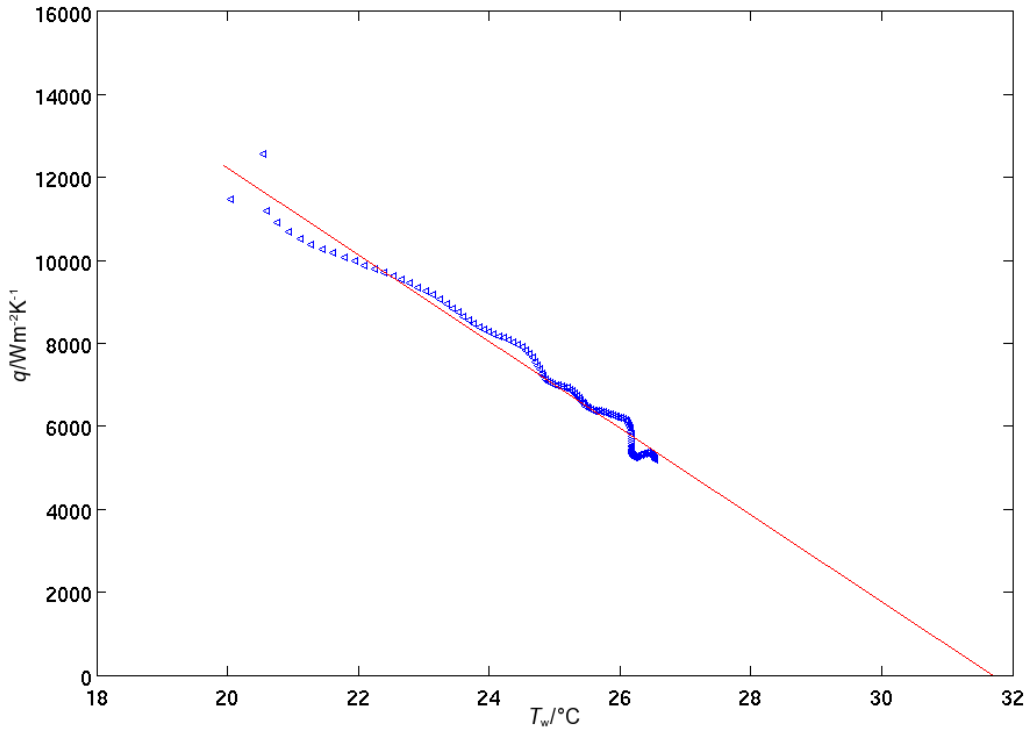

Figure 6.5: $q{\sim}T_{\mathrm{w}}$ plot for an example pixel location ($h = 1046\,\mathrm{W\,m^{-2}\,K^{-1}}$, $T_{\mathrm{ad}} = 31.7\,^{\circ}\mathrm{C}$)

and O'Dowd et al. (2011a). The uncertainty in the measurands in this experimental campaign are essentially identical to those which he considered. These uncertainties were estimated to be 9.5% in heat transfer coefficient and 1.2 K in adiabatic wall temperature and these values apply equally well to the measurements conducted in the present study. This estimate took into account the uncertainties in the material properties, the measurement of gas and wall temperatures and in the regression analysis performed.

6.2.5.1 Thermal product measurement

As WaterShed XC 11122 had not been used for heat transfer measurements previously, its thermal product, $\sqrt{\rho c k}$, needed to be measured. This was done by comparison against another material of known thermal product. The shutter rig used for this purpose is pictured in figure 6.6. It consists of a hot air gun clamped to point vertically

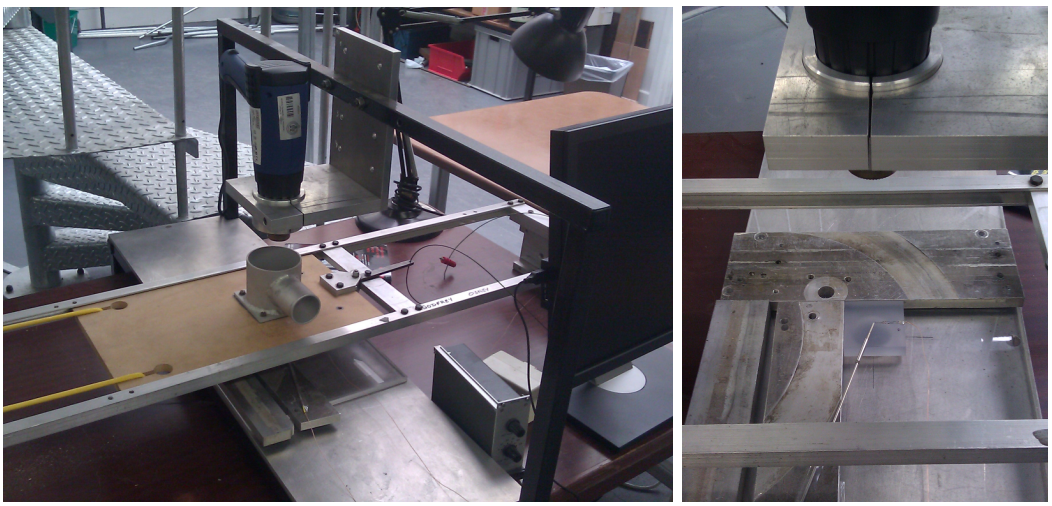

Figure 6.6: Photos of the shutter rig

downwards on to a specimen block of the material under test. Between the hot air gun and the specimen block is a sprung shutter that redirects the hot air flow away from the test piece. At the start of the test, the shutter is released and rapidly slides away, allowing the jet of hot air from the hot air gun to impinge upon the specimen block and heat it up. The surface temperature of the specimen block is recorded by a surface mount thermocouple, while the gas temperature history is recorded by another thermocouple suspended just above the test piece.

Under the one-dimensional, semi-infinite conduction assumption, for a step-change in gas temperature, the solution of the heat equation yields the expression for surface wall temperature (Schneider, 1955)

$$\frac{T_\mathrm{w} - T_\mathrm{i}}{T_\mathrm{g} - T_\mathrm{i}} = 1 - \mathrm{e}^{\left(\frac{h^2 t}{\rho c k}\right)} \mathrm{erfc}\left(\frac{h\sqrt{t}}{\sqrt{\rho c k}}\right) \tag{6.3}$$

This can be generalised to account for gradual gas temperature changes by the superposition of incremental step changes in gas temperature, resulting in the expression

$$T_\mathrm{w} - T_\mathrm{i} = \sum_n \left\{ \left(1 - \mathrm{e}^{\left(\frac{h^2 (t-t_n)}{\rho c k}\right)} \mathrm{erfc}\left(\frac{h\sqrt{t-t_n}}{\sqrt{\rho c k}}\right)\right) (\Delta T_\mathrm{gas})_n \right\} \tag{6.4}$$

Performing this test initially with a material of known thermal product, the effective heat transfer coefficient on the surface of the test piece can be determined by taking the measured gas temperature history and finding the heat transfer coefficient that produces the wall temperature history (calculated using equation 6.4) that fits the measured wall temperature history best. Subsequently substituting the specimen block for an identical one made from the material of unknown thermal product, the heat transfer coefficient can be assumed to be unchanged and the thermal product used as the variable for best-fit.

For the present case, Perspex was used as the material with known thermal product, equal to $569 \pm 29\,\mathrm{J\,s^{-\frac{1}{2}}\,m^{-2}\,K^{-1}}$ (Ireland, 1987). This yielded a heat transfer coefficient of $250 \pm 13\,\mathrm{W\,m^{-2}\,K^{-1}}$ and a thermal product for WaterShed XC 11122 of $654 \pm 34\,\mathrm{J\,s^{-\frac{1}{2}}\,m^{-2}\,K^{-1}}$.

6.2.5.2 Film cooling

A 650 kPa pressurised air supply line was available for the provision of cooling air. This was connected directly to an inlet coolant plenum which was located in the containment formed by the HSLC mainstream outlet plenum. In order to ensure that the film cooling air was at a lower temperature than the mainstream air, even in the high Mach number over-tip flow region towards the trailing edge, it had to be cooled below ambient temperature before being supplied to the test blade. This was achieved by the use of three vortex tubes, connected to the inlet coolant plenum in parallel. The output lines from all three vortex tubes were then connected via a solenoid valve to the bottom of the test blade, feeding the internal blade plenum. The inclusion of the solenoid valve allowed the cooling system to be set up in advance of each test run and for the piping to be pre-cooled without pre-cooling the test blade itself. During each test run, the solenoid valve was triggered fractionally before the heater mesh activation, redirecting the cold air flow from an overboard exhaust up into the test blade. The cooling system can be seen in figure 6.7.

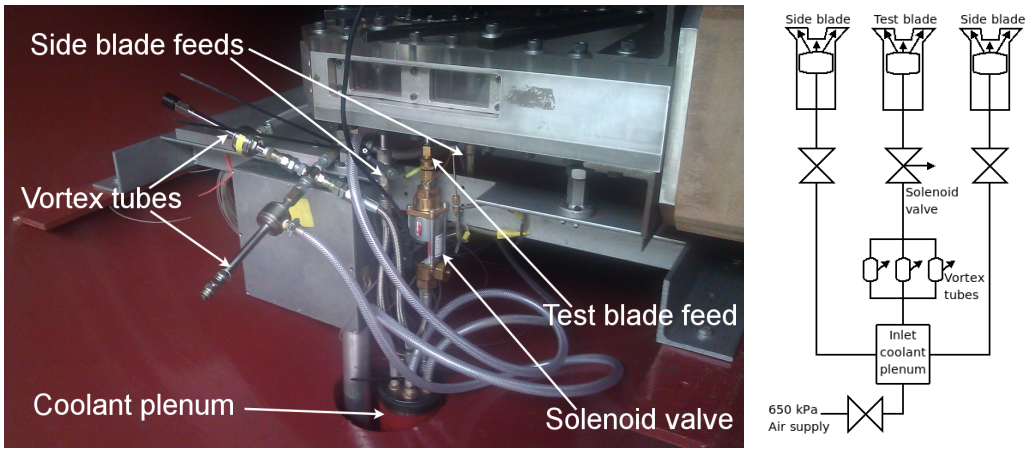

(a) Photo (b) Schematic

Figure 6.7: Cooling air supply system

By moving the vortex tubes from upstream to downstream of the inlet coolant plenum, the coolant-to-mainstream total pressure ratio was increased from 1.08 (O'Dowd, 2010) to 1.11. This is an improvement, although the nominal design total pressure ratio is 1.2 (specified by Rolls-Royce as the best compromise, given the single coolant chamber within the blade). During the cooled heat transfer tests, the cooling air was supplied at approximately 10°C to the test blade, giving a mainstream-to-coolant total temperature ratio of 1.1. This is similar to what had been achieved by O'Dowd (2010), which also falls short of the target ratio of 1.5 that is typical of real engine conditions. An additional improvement made to the cooling supply system was that the two side blades could be fed with uncooled cooling air taken directly from the inlet coolant plenum to maintain cascade periodicity. This rectifies an omission that had previously been identified as a significant flaw with earlier heat transfer measurements on cooled blade tips conducted with this facility.

6.3 Uncooled blade tip results

6.3.1 Aerodynamic loss

Two loss coefficients are used to quantify the aerodynamic losses downstream of the blade row: the pressure loss coefficient, Cp_0, and the kinetic energy loss coefficient, ζ. Cp_0 measures the drop in total pressure across the blade row and is defined in a similar way to $Cp_{0\mathrm{i}}$ in equation 4.6, but is non-dimensionalised by mass-averaged, mid-span exit dynamic head.

$$Cp_0 = \frac{p_{0\mathrm{i}} - p_0}{\left(\frac{1}{2}\rho v^2\right)_{\mathrm{e,mid-span}}} \tag{6.5}$$

ζ represents the exit kinetic energy of the flow compared with an isentropic expansion through the same pressure ratio and is defined as

$$\zeta = 1 - \frac{1 - \left(\frac{p}{p_0}\right)^{\frac{\gamma-1}{\gamma}}}{1 - \left(\frac{p_{\mathrm{e,mid-span}}}{p_{0\mathrm{i}}}\right)^{\frac{\gamma-1}{\gamma}}} \tag{6.6}$$

Figure 6.8 shows the Cp_0 pressure loss coefficient distributions for the squealet tip, which can be compared to those from a flat tip (reproduced from O'Dowd (2010)) in figure 6.9. The traverse location is one axial chord downstream of the blade trailing edge, as marked on figure 6.1. The x-axis represents distance from the geometric passage centreline and is normalised by blade pitch. The y-axis represents spanwise location, normalised by passage height. Measurements above $z/H = 0.97$ were taken using the single hole probe. It should be remembered that the Reynolds number of the cascade is ∼15% different between the two cases. There is also some uncertainty regarding the tip gap; due to the manufacturing tolerances of the test section, there was a very significant variation in tip gap which was particularly important at the smallest tip gap (nominally 0.45% blade chord). The observed variation in tip gap was considerably smaller (in relative terms) at the nominal 0.89% and 1.34% tip gaps. The real tip clearances measured using feeler gauges are quantified in table 6.3.

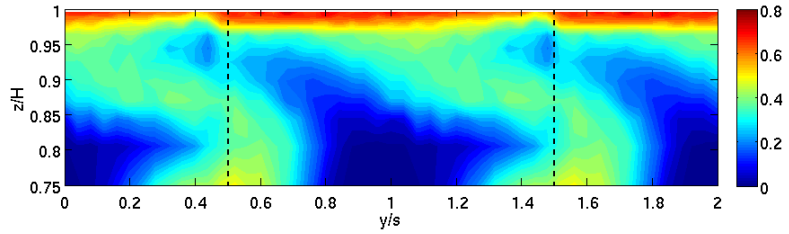

(a) 0.45% tip gap

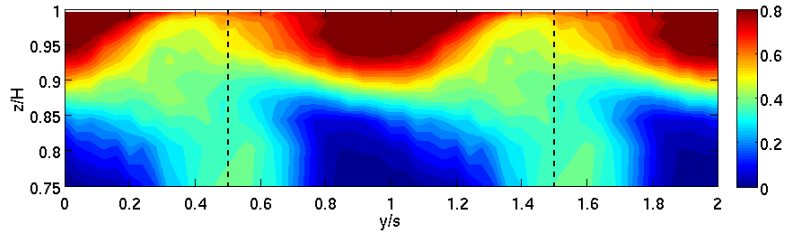

(b) 0.89% tip gap

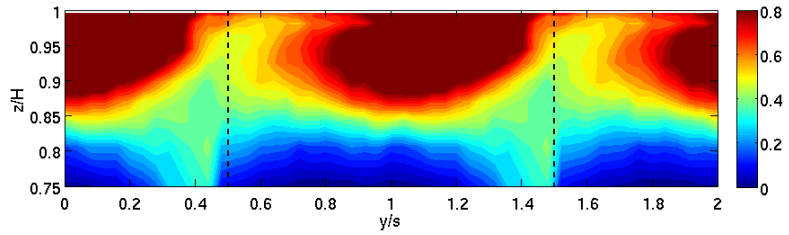

(c) 1.34% tip gap

Figure 6.8: Squealet tip downstream Cp_0 pressure loss coefficient (Dashed lines indicate geometric trailing edge locations)

Measurements were taken at the trailing edge and near mid-chord; access to the leading edge was not possible due to the high turning angle of the aerofoil. Assuming both the endwall and blade tip surfaces were flat, these measurements have been extrapolated in table 6.3 to provide an estimate of the tip clearance at the leading edge.

The measured variations in the actual tip clearance are large and are likely to be a significant source of error in the experimental data, particularly at the smallest tip gap tested. At all three tip clearances, the extrapolated "leading edge" tip gap is close to the nominal tip gap, while the tip clearance closes up towards the trailing edge. It was observed in chapter 5 that the flow structure within the tip gap region is most sensitive to the way that the over-tip leakage flow enters the forward part of the

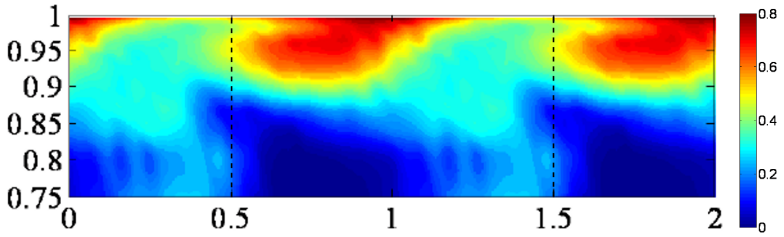

(a) 0.45% tip gap

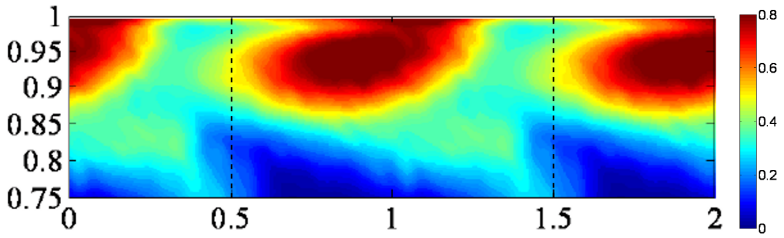

(b) 0.89% tip gap

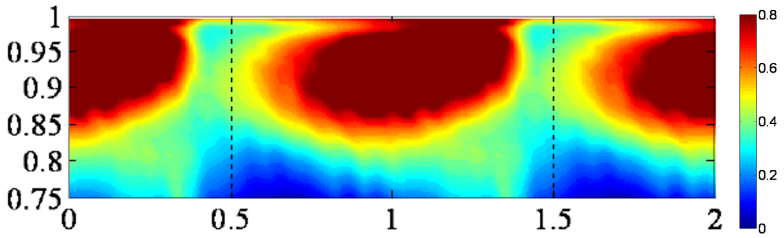

(c) 1.34% tip gap

Figure 6.9: Flat tip downstream Cp_0 pressure loss coefficient
(Reproduced from O'Dowd (2010))
(Dashed lines indicate geometric trailing edge locations)

cavity, so it is believed to be unlikely that the observed variation in tip clearance will drastically alter the character of the over-tip leakage flow, as the error in tip gap at the leading edge is small. However, the large reduction in tip clearance towards the trailing edge will increase the resistance to the over-tip leakage flow in the aft region, reducing the total over-tip leakage mass flow rate and the resulting aerodynamic loss associated with it. Care must therefore be taken in the interpretation of the data, and the potential limitations on the experimental accuracy caused by the uncertainty in tip clearance must be appreciated. This effect is likely to be non-linear and will have greater influence at smaller tip clearances, due to the increased proportional size of the variation relative to the actual tip clearance.

Nominal tip gap		Measured tip gap / mm			Variation	
% blade chord	/ mm	Trailing edge	Mid-chord	"Leading edge" (extrapolated)	/ mm	% nominal tip gap
0.45%	0.48	0.24	0.35	0.46	0.22	46%
0.89%	0.95	0.75	0.88	1.01	0.26	29%
1.34%	1.43	1.32	1.38	1.44	0.12	8%

Table 6.3: Measured tip clearances

The over-tip leakage vortex loss core increases in both extent and depth with increasing tip gap, as expected. The centre of the vortex also shifts further away from the blade suction side, moving noticeably to the right in figure 6.8 (the over-tip leakage flow in this figure is left-to-right, with a clockwise over-tip leakage vortex). Comparing figures 6.8 and 6.9, the predicted loss of the squealet tip is very similar to that of the flat tip at the nominal 0.89% and 1.34% tip gaps, with marginally smaller but stronger loss cores visible for the squealet tip. The loss profile is significantly reduced at the 0.45% tip gap, with the lossy region confined to a small band near the casing and a very large, almost inviscid region elsewhere. However, the results at the nominal 0.45% tip gap may be somewhat misleading due to the uncertainty in the actual tip gap, which was observed to be much smaller than intended.

Downstream Mach number profiles for the region surveyed by the three-hole probe are plotted in figure 6.10. These are largely the inverse of the pressure loss coefficient contours; where aerodynamic losses are high, exit Mach numbers are low and vice-versa. The peak downstream Mach number measured in the freestream away from the tip leakage vortex is approximately 1.2. With the pressure ratio applied across the linear cascade, however, the exit Mach number should be 1.0, as reflected in the nominal flow conditions in table 6.2. This discrepancy reflects a problem with the application matrix of the three-hole probe for Mach number derived from the calibration of the probe; a similar discrepancy can be seen in the equivalent data reported in O'Dowd (2010), which used the same probe and calibration. The three-hole probe application

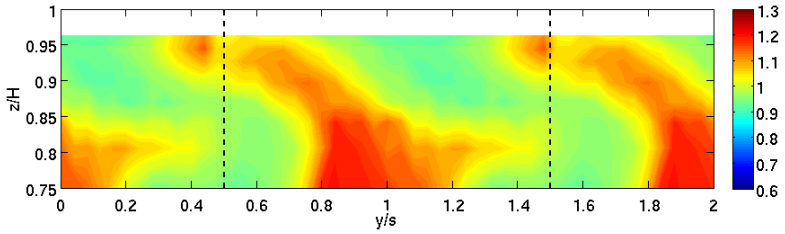

(a) 0.45% tip gap

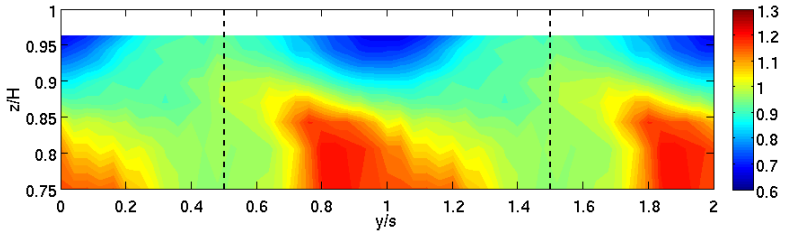

(b) 0.89% tip gap

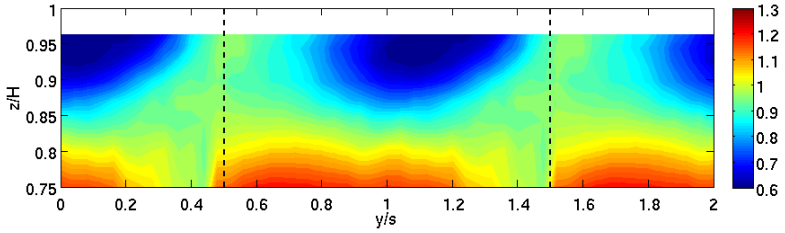

(c) 1.34% tip gap

Figure 6.10: Squealet tip downstream Mach number
(Dashed lines indicate geometric trailing edge locations)

matrix for total pressure is independent of the matrix for Mach number, so there is no implication that a similar error exists in the measurements of aerodynamic loss.

The aerodynamic loss of the squealet tip is presented in terms of the ζ kinetic energy loss coefficient in figure 6.11 to allow comparison against the loss data available for the winglet tip (figure 6.12). This figure is generated from the same raw pressure data as the Cp_0 profiles of figure 6.8.

The squealet tip shows a significantly reduced over-tip leakage vortex compared with the winglet at both the 0.89% and 1.34% tip gaps. The loss cores for the squealet are more discrete, being clearly separated by a low-loss region, whereas the winglet results show adjacent cores to be much closer together. This reflects the wide wake left by the winglet tip due to its blunt trailing edge, identified in chapter 4. It is reiterated

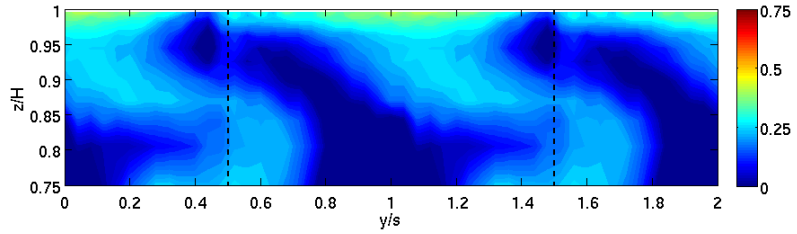

(a) 0.45% tip gap

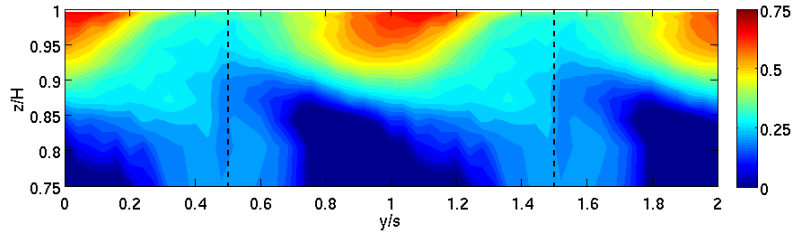

(b) 0.89% tip gap

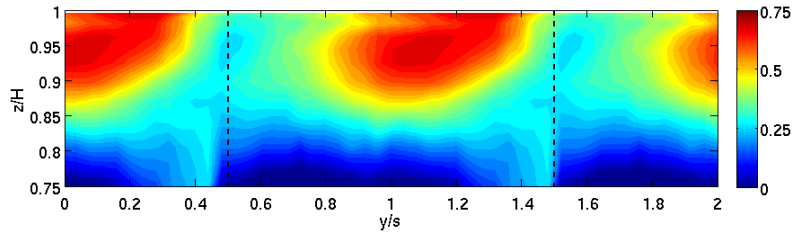

(c) 1.34% tip gap

Figure 6.11: Squealet tip downstream ζ kinetic energy loss coefficient (Dashed lines indicate geometric trailing edge locations)

here that the model used for these tests was an *uncooled* version of the final design of the squealet used in the CFD simulations with cooling presented in chapter 5.

6.3.2 Heat transfer

The measured heat transfer coefficient and Nusselt number distributions for the uncooled squealet tip are presented in figure 6.13. As expected, the heat transfer coefficient is generally increased at the larger tip gap. There is a strong reattachment peak on the cavity floor near the leading edge, as had been predicted in the previous CFD simulations of the 3D blade. The line of reattachment along the pressure side edge is somewhat more prominent than had been suggested by those simulations, and

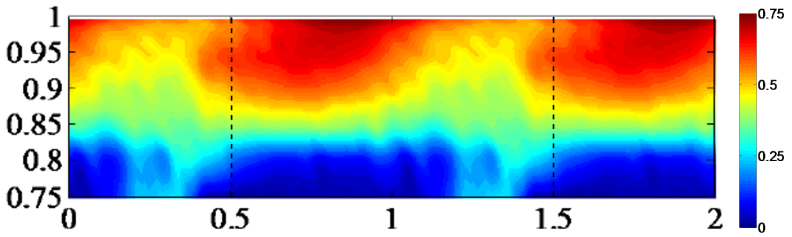

(a) 0.89% tip gap

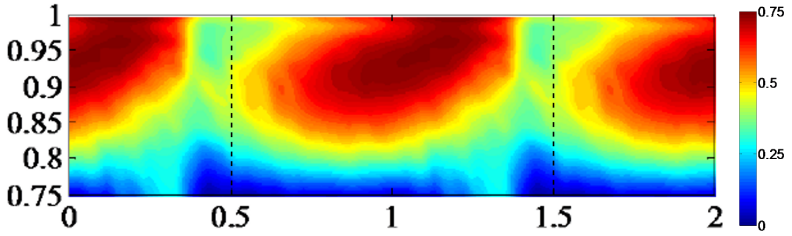

(b) 1.34% tip gap

Figure 6.12: Winglet tip downstream ζ kinetic energy loss coefficient
(Reproduced from O'Dowd (2010))
(Dashed lines indicate geometric trailing edge locations)

the Nusselt number on the squealet rim is a lot higher relative to the cavity floor and gutter.

With the higher heat transfer coefficients seen on the rim, there is an obvious patch of low heat transfer coefficient on the concave portion of the pressure side rim, just upstream of the pressure side tip extension. This is likely caused by the over-tip leakage flow separating as it passes over the sharp pressure side edge but not reattaching on to the upper rim surface, resulting in low heat transfer coefficients. This patch of low heat transfer coefficient remains, despite the fact that 3D conduction effects could be expected to result in an overprediction of heat transfer in this thin portion of the squealet rim. It is also noted that the tip shelf region does not have noticeably higher measured heat transfer coefficients than the rest of the squealet rim.

There are fine striations visible in the heat transfer coefficient distributions on the pressure side squealet rim, approximately aligned with the expected over-tip leakage flow direction. These are believed to have been caused by small peturbations in the test blade tip surface, either stemming from the SLA printing process or caused by

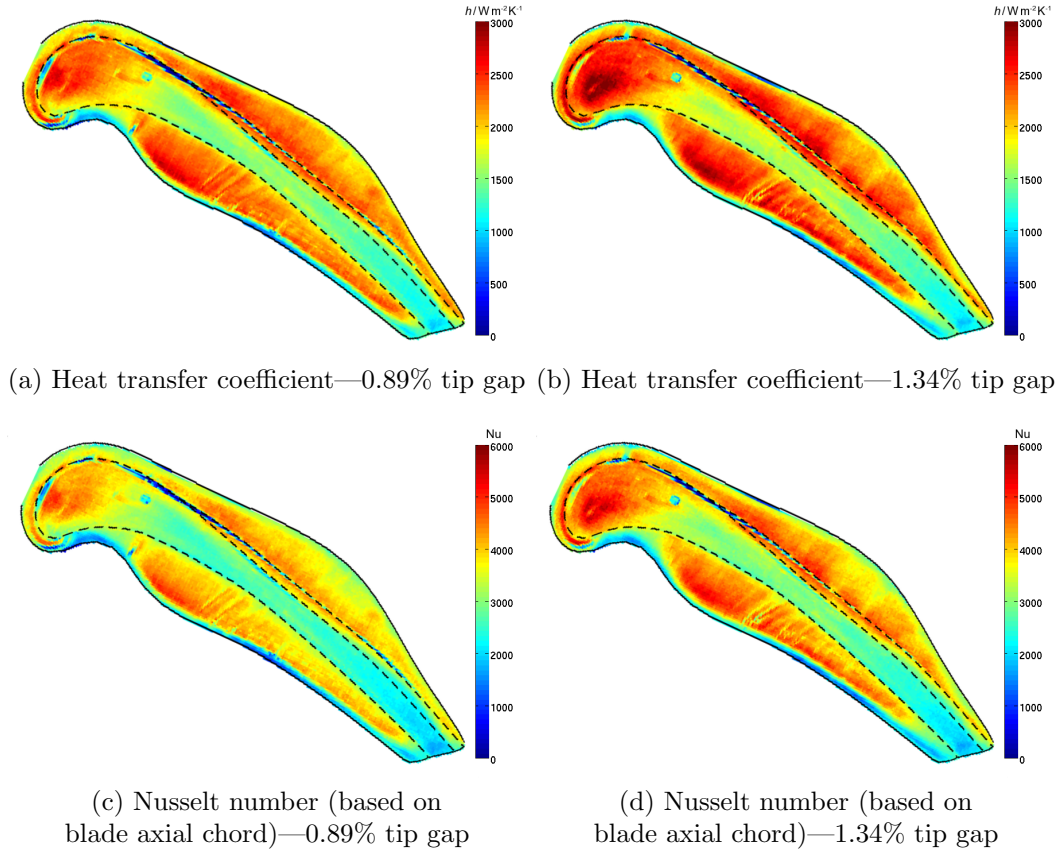

(a) Heat transfer coefficient—0.89% tip gap (b) Heat transfer coefficient—1.34% tip gap

(c) Nusselt number (based on blade axial chord)—0.89% tip gap

(d) Nusselt number (based on blade axial chord)—1.34% tip gap

Figure 6.13: Uncooled squealet tip heat transfer results

imperfections in the paint layer. If this really is the cause, the sensitivity of the heat transfer distributions on the blade tip surface to surface roughness may require further investigation, particularly in the context of the application of abrasive rocks to the blade tip surfaces for use with abradable over-tip casing liners.

6.4 Cooled blade tip results

Heat transfer coefficients and adiabatic wall temperature measurements taken for the cooled blade tips are shown in figure 6.14, along with the equivalent Nusselt number distributions. Only heat transfer data are available; no aerodynamic loss measurements were attempted for the configurations with film cooling due to time constraints. Two film cooling configurations were tested; the *All open* configuration

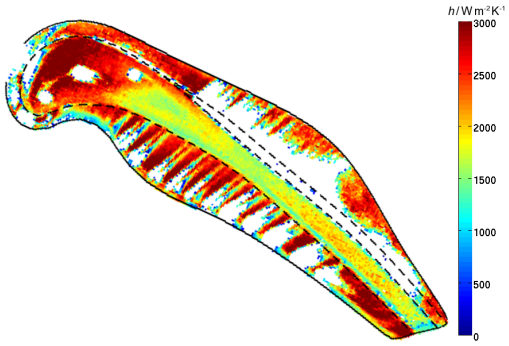

(a) Heat transfer coefficient—*All open*

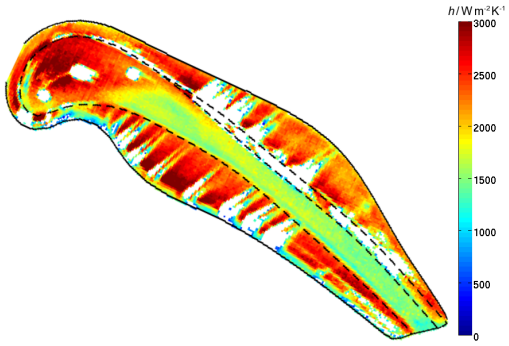

(b) Heat transfer coefficient—*Config 2*

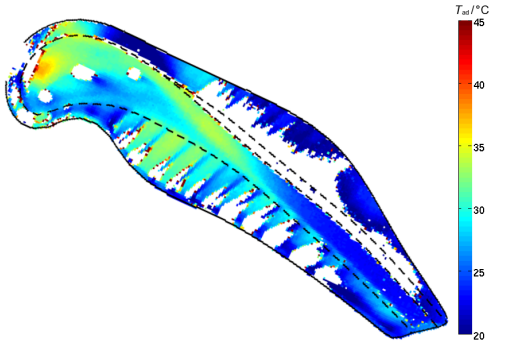

(c) Adiabatic wall temperature—*All open*

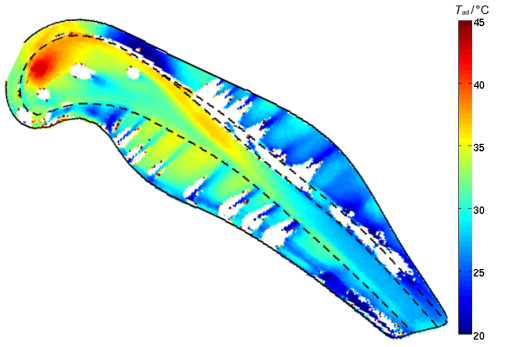

(d) Adiabatic wall temperature—*Config 2*

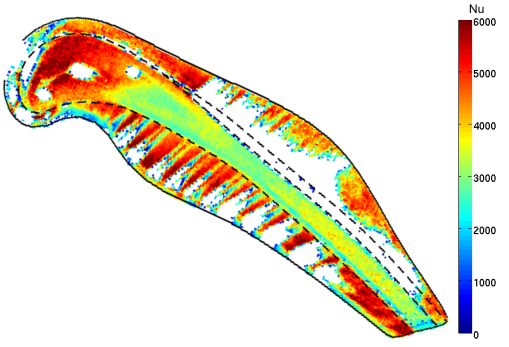

(e) Nusselt number (based on blade axial chord)—*All open*

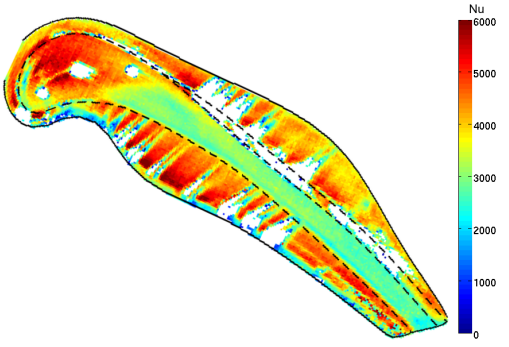

(f) Nusselt number (based on blade axial chord)—*Config 2*

Figure 6.14: Cooled squealet tip heat transfer results (1.34% tip gap)

and the *Config 2* configuration (shown in figure 5.7). The latter was achieved by using an epoxy resin to seal the appropriate cooling holes on the test blade permanently. The inlet pressure to the cooling plenum was then adjusted to maintain the blade plenum-to-mainstream pressure ratio with the decreased coolant flow area.

The gaps in the data are in regions of high film cooling effectiveness; the cooling air supplied to the blade was at ∼10°C and the difference between the coolant temperature and the initial blade temperature was insufficient to produce sufficient heat transfer to allow heat transfer coefficient to be determined. This was reflected by a failure in the processing of the transient IR data—where insufficient heat transfer occurred, the regression analysis of the $q{\sim}T_{\mathrm{w}}$ plot (performed using the *mldivide* (backslash) operator in MATLAB) would fail and produce a line of best fit with positive gradient, indicating a negative heat transfer coefficient. A mask was therefore applied to remove any negative values in the heat transfer coefficient map and the corresponding adiabatic wall temperatures.

Comparing the adiabatic wall temperature results from the HSLC (figure 6.14) to the equivalent cooled CFD simulations (figures 5.8 and 5.13) qualitatively, the agreement is good. The convection of film cooling flows is largely replicated, with a heavily over-cooled region found on the suction side squealet rim and a slightly under-cooled region in the forward part of the pressure side squealet extension. The hot spot previously seen at the crown of the blade is present. The subtle change in behaviour of the tip shelf cooling holes before and after the suction side gallery entrance is also visible, with the characteristic drop and subsequent recovery in film cooling effectiveness towards the trailing edge of the suction side squealet rim.

The largest difference between the CFD predictions and the experimental data is found in the leading edge region on the cavity floor. The over-tip leakage flow in the HSLC impinges on a spot halfway between the first dust hole and the suction side squealet rim, with a resultant peak in both adiabatic wall temperature and heat transfer coefficient. By contrast, as had been noted in chapter 5, the CFD simulations predict the reattachment to occur exactly over the dust hole, so it is deflected by the coolant flow. As a result, no reattachment peak is observed in the CFD predictions in this region. This discrepancy is not entirely unexpected; it was seen from the mesh sensitivity test that the flow in the forward part of the blade tip cavity is highly

sensitive, with small changes to the incoming over-tip leakage flow greatly affecting the flow structure within the cavity. The HSLC lacks rotation, relative endwall movement, inlet pressure and temperature flow profiles and the twisted, fully-3D blade shape of the real engine, all of which could have a significant effect on the near-tip flow. Observing the early suction side rim for the two cooling configurations in the HSLC, there is a region of missing data for the *All open* configuration (indicating an area of high cooling effectiveness) but not for the *Config 2* configuration. This suggests that flow from one of the holes near the leading edge that was blocked off for the *Config 2* case was being swept over the blade tip to cool the suction side rim. The flow from these holes was seen to be swept away from the tip region in the CFD simulations, further implying that the incidence angle in the blade tip region is altered in the linear cascade environment.

Heat transfer coefficients are increased compared with the uncooled case, as is expected with the presence of film cooling. Although it is somewhat difficult to see due to the areas of missing data, regions near the sealed cooling holes in the *Config 2* configuration have lower measured heat transfer coefficients than similar regions in the *All open* case. Comparing figure 6.14e and 6.14f with 5.14a and 5.14f, generally higher heat transfer levels are observed in the HSLC compared with the CFD predictions.

6.5 CFD simulation

In order to gain an indication of the reliability of the computational simulations of chapters 4 and 5, a CFD simulation of the experimental cascade was performed using an analogous computational strategy to those of the engine-representative simulations presented previously. A single blade of the HSLC, without film cooling, was simulated with (translationally) periodic boundaries; this simulation was performed at the largest tip gap tested experimentally, 1.34% blade chord, so that the uncertainties regarding the actual tip clearance of the experimental results would be minimised. The

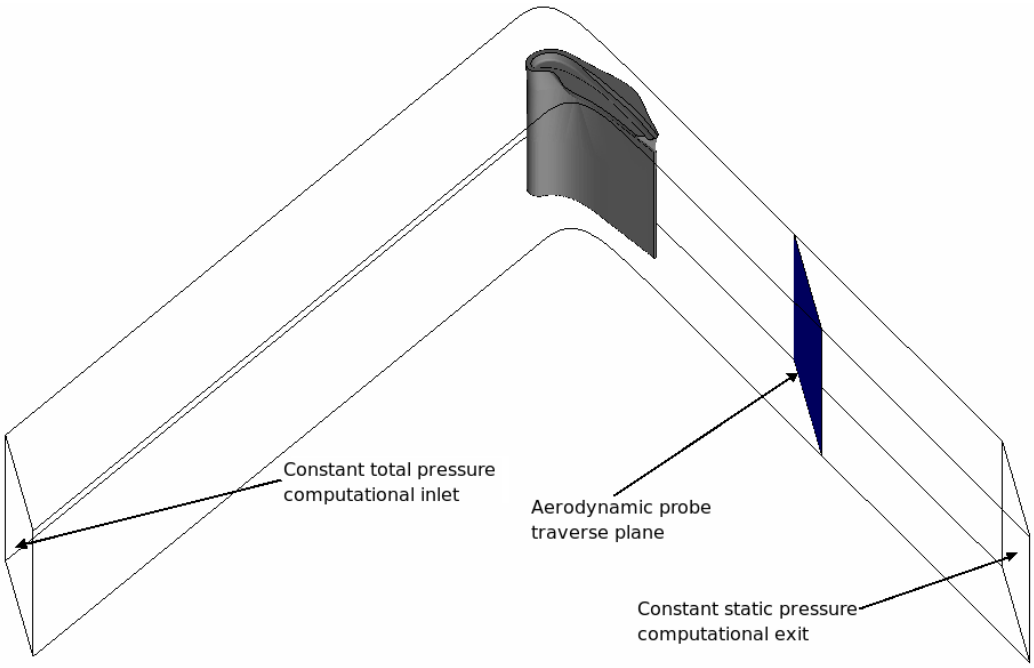

Figure 6.15: Computational domain for the linear cascade CFD simulations

computational domain runs from the inlet to the HSLC test section to approximately 2.5× blade axial chord downstream of the blade trailing edge, as shown in figure 6.15.

A hybrid unstructured tetrahedral and prism layer mesh was generated using the Octree mesher of ICEM CFD 12, using the techniques described in section 4.3.1. The finished mesh was 5.53 million cells large. The mesh refinement on the blade tip surface is shown in figure 6.16. Once again, due to issues with software license availability, this CFD simulation was solved using FLUENT 12.0 rather than FLUENT 6.3. In order to maximise the comparability with the previous CFD studies, the solver settings were kept the same as far as possible—the realisable k-ϵ turbulence model with enhanced wall treatment was used, along with the time-steady pressure based solver with the SIMPLE algorithm for pressure-velocity coupling. A constant total pressure boundary condition at the inlet and a constant static pressure boundary condition at the outlet were applied, their values being those of the nominal HSLC conditions specified in table 6.2.

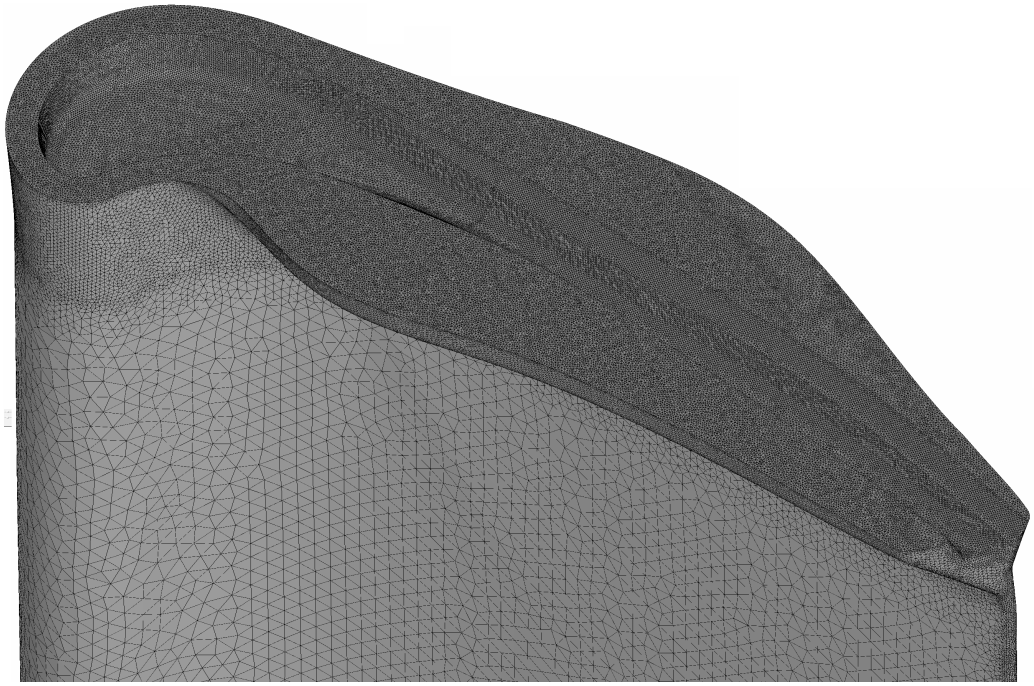

Figure 6.16: Mesh refinement on the blade tip surface

Figure 6.17 shows the predicted Cp_0 pressure loss coefficient, ζ kinetic energy loss coefficient and Mach number distributions at the downstream aerodynamic probe traverse plane from the CFD simulation, which can be compared to the equivalent experimental data plotted in figures 6.8c, 6.11c and 6.10c, respectively. The over-tip leakage vortex aerodynamic loss core is predicted to be smaller than was measured experimentally, and is displaced by approximately one third of a blade pitch further away from the blade suction side. This reduction in the size of the over-tip leakage vortex results in a significant underprediction in the area-averaged aerodynamic loss coefficients of 36% in Cp_0 and 42% in ζ over the area plotted in figures 6.8c, 6.11c and 6.17.

The downstream Mach number predicted by the CFD simulation is significantly lower than what was measured in the HSLC—as explained previously in section 6.3.1, this is caused by a problem with the calibration of the three-hole probe for Mach number. The pressure loading on the blade at mid-span is presented as isentropic

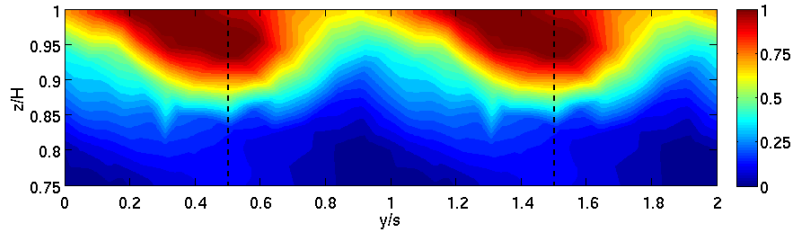

(a) Cp_0 pressure loss coefficient

(b) ζ kinetic energy loss coefficient

(c) Mach number

Figure 6.17: Uncooled linear cascade CFD downstream aerodynamic results (1.34% tip gap—Dashed lines indicate geometric trailing edge locations)

Mach number in figure 6.18, with both experimental data and the numerical prediction from the CFD simulation plotted. The agreement between the experimental and computational data here provides confidence that the experimental aerodynamic conditions have been appropriately matched in the simulation. The freestream Mach number predicted by the CFD simulation is 1.0 and matches the cascade exit Mach number expected from the pressure ratio across the linear cascade.

The predicted heat transfer coefficient and Nusselt number distributions over the blade tip surface are shown in figure 6.19, which can be compared to the equivalent experimental data plotted in figures 6.13b and 6.13d. The predicted magnitudes of Nusselt number are consistent with those from the engine-representative CFD simulations presented in chapter 4 and are reduced compared with those measured

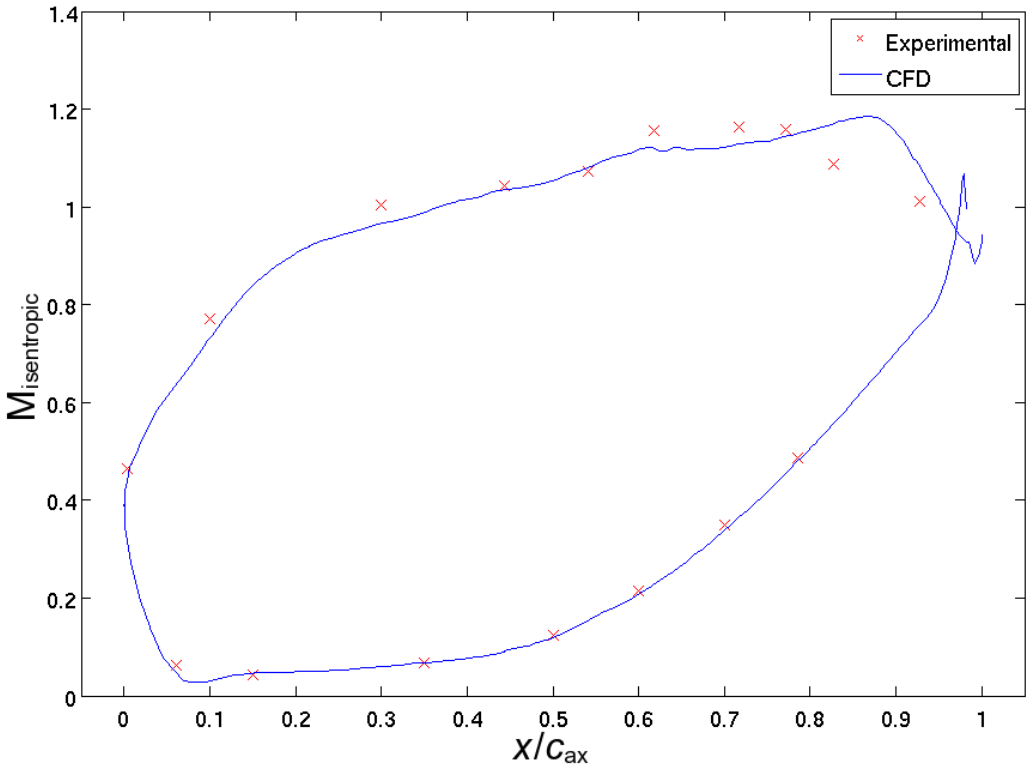

Figure 6.18: Mid-span isentropic Mach number showing blade pressure loading (Experimental data courtesy of Dr Qiang Zhang)

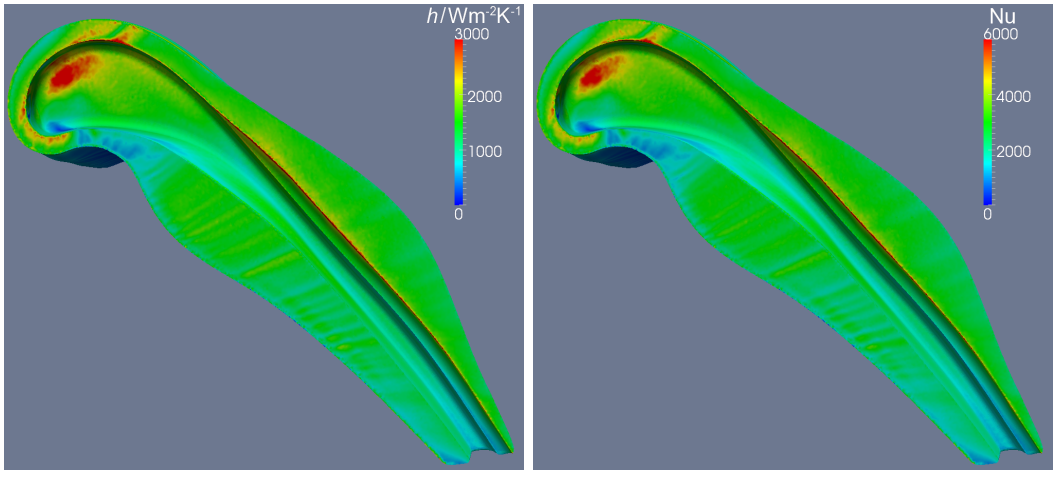

(a) Heat transfer coefficient (b) Nusselt number

Figure 6.19: Uncooled linear cascade CFD heat transfer results (1.34% tip gap)

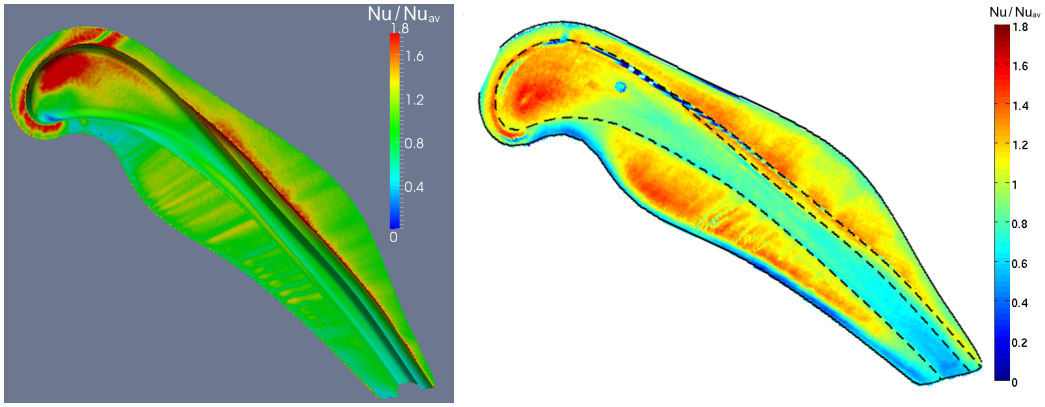

(a) CFD (b) Experimental

Figure 6.20: CFD and experimental Nusselt number normalised by average blade tip Nusselt number (1.34% tip gap)

experimentally. This confirms the tendancy of the computational strategy used to underpredict the levels of blade tip heat transfer coefficient; additionally, the size of the reattachment hotspot on the cavity floor is significantly underpredicted by the simulation.

Figure 6.20 shows the blade tip Nusselt number distributions from both the CFD and the experiment, normalised by average blade tip Nusselt number. There is a significant difference in the shape of the distributions on the pressure side squealet tip extension, suggesting that the flow separation and reattachment over the pressure side edge are not well captured by the simulation. Similarly, the separation of over-tip leakage flow at the leading edge and its subsequent reattachment on to the cavity floor are not modelled accurately, although the absolute value of Nusselt number at the reattachment location is approximately correct in this instance. By contrast, other salient features of the shape of the measured Nusselt number distribution are reproduced in the computational results. The regions of low heat transfer on the concave portion of the early pressure side rim and at the extreme trailing edge of the pressure side extension are present in the predicted distributions. The enhancement of heat transfer on the surface of the rim at the blade tip leading edge is also captured

well and the above average heat transfer to the suction side squealet tip extension is present, although its magnitude is somewhat underpredicted by the simulation.

The comparison between the numerical and experimental data illustrates that FLUENT struggles to model regions of separated flow accurately and has a general tendancy to underpredict the magnitudes of heat transfer on the blade tip surface. These observations should not only be remembered when considering the results from chapters 3, 4 and 5, but also for any similar studies performed in the future. However, the same comparison also shows that the CFD methodology applied is still useful as a design tool; while the limitations of the predictions must be remembered, key flow features and their effects on heat transfer distributions are appropriately resolved.

6.6 Chapter summary

In this chapter, details of an experimental investigation conducted using the High Speed Linear Cascade, a transonic, 1.9× scale blowdown facility have been presented. The squealet tip geometry was transformed for use in a linear cascade environment and the film cooling holes were repositioned in their equivalent locations with a single cooling air feed plenum. Test blade tips were manufactured by stereolithography from WaterShed XC 11122 resin, whose thermal product was measured. Aerodynamic loss measurements were performed using an uncooled, clean version of the transformed geometry by traversing a three-hole probe and a single-hole probe one axial chord downstream of the blade row. This was performed at three nominal tip gaps of 0.45%, 0.89% and 1.34% blade chord. The uncooled squealet tip exhibited a similar aerodynamic loss at this location to the flat tip blade and a significantly reduced loss compared to the winglet tip tested by O'Dowd (2010). Heat transfer measurements of the uncooled blade tip were taken at the 0.89% and 1.34% tip gaps using a transient infra-red thermographic technique, with the mainstream flow heated by an upstream heater mesh fed by a high power DC electrical supply. Calibration of the IR camera

was accomplished in situ, by virtue of a fast-response thermocouple located on the test blade tip surface. The heat transfer data were processed by the impulse response method of Oldfield (2008), applying a semi-infinite, 1D conduction assumption to calculate the heat transfer coefficient maps across the squealet tip surface. Heat transfer data were taken and processed using the same technique for the film-cooled test blade tips, with cooled film cooling air supplied by the use of vortex tubes. This was performed for two cooling configurations, the *All open* and the *Config 2* configurations, at a single tip gap of 0.89% blade chord. Good qualitative agreement was seen between the adiabatic wall temperature distributions measured in the HSLC and those predicted in the CFD simulations of the previous chapter, although generally higher Nusselt numbers were recorded in the HSLC data than were predicted by the CFD simulations. Additionally, there was some evidence of changes to the flowfield in the forward part of the blade; this was ascribed to the inherent simplifications of the linear cascade environment—the stationary frame of reference and the absence of relative endwall motion. A CFD simulation of the uncooled experimental linear cascade environment at the 1.34% blade chord tip clearance was performed using a single blade with translationally periodic boundary conditions. The predicted size of the over-tip leakage vortex was smaller than had been observed in the experimental results, which resulted in a large underprediction of the magnitude of the area-averaged aerodynamic loss. The magnitudes of the blade tip Nusselt number predicted by the linear cascade simulation were similar to those obtained in the engine-representative CFD simulations and generally lower than the values measured in the HSLC. Discrepancies in the shape of the Nusselt number distribution were observed in the vicinity of regions of separated flow (on the pressure side squealet extension and in the cavity close to the leading edge) but other salient features of the distribution that were observed experimentally were reproduced in the simulation data.

Chapter 7

Conclusion

7.1 Summary of work

This thesis documents work performed in the investigation of the thermal performance of unshrouded blade tip designs for high pressure turbine blades in large civil turbofan aero-engines, with some consideration also given to aerodynamic loss.

A comprehensive test of turbulence models available through the GUI of the commercial CFD solver FLUENT 6.3 was performed, using experimental data taken by Palafox (2006) as the test case and validation dataset. This setup was a large scale, low speed linear cascade with a flat blade tip, using a low speed version of the RT-27a HP turbine aerofoil. All computation was performed at a tip gap of 1.5% blade chord on a single blade in a time-steady, periodic environment. Fully structured, hexahedral, multiblock meshes were used, generated using ICEM CFD 11. Seven different turbulence models were tested; Spalart-Allmaras, standard k-ϵ, realisable k-ϵ, RNG k-ϵ, standard k-ω, SST k-ω and the Reynolds stress model, using the enhanced wall treatment for all cases. It was found that all of the expected flow phenomena were captured well by all of the turbulence models. The standard k-ω and standard k-ϵ models gave the closest match to the experimentally measured magnitudes of blade tip Nusselt number in the aft of the blade tip, but significantly overpredicted the turbulence levels in the tip gap region and placed the reattachment too close to the blade tip edge. All of the other turbulence models tested exhibited very similar

performances to each other and correctly located the line of flow reattachment. No increase in accuracy was achieved by the use of the RSM compared with the simpler RANS models; consequently, the SST k-ω and realisable k-ϵ models are therefore recommended as the most suitable turbulence models for use in this type of flow. Relative endwall motion was also simulated, and good qualitative agreement with the experimental data was observed. This section of research was published in the *Journal of Turbomachinery* as Tang et al. (2010).

A hybrid unshrouded blade tip geometry, the squealet tip, was introduced, drawing design elements from a double squealer tip and a winglet tip. This was tested numerically against the two geometries from which it was derived and subsequently against a later design revision of the squealet tip, using the EFE HP turbine blade as the test blade geometry. FLUENT 6.3 was once again used as the solver, this time with unstructured, hybrid tetrahedral and prism layer meshes generated with ICEM CFD 11. Engine-realistic boundary conditions were specified, including radial pressure and temperature profiles at the inlet and exit to the computational domain. Computation was again performed with a time-steady formulation, using a single blade with periodic boundaries. Tip gaps were varied between 0.45% and 1.34% blade chord. The aerodynamic performance of the four blade tip geometries (without film cooling) was examined by the calculation of the predicted row efficiencies and inferred stage efficiencies at a partially mixed-out plane, approximately one axial chord downstream of the blade row. The revised version of the squealet design was predicted to have a tip gap efficiency exchange rate equal to that of the double squealer tip and higher than that of the winglet tip, but with a reduction in aerodynamic losses compared to both over the majority of the range of tip gaps investigated. Heat flux and heat transfer coefficient levels across the revised squealet tip geometry were similar to those predicted for both of the base designs, but with a significant reduction in wetted surface area compared to the winglet and hence a reduction in total blade tip heat flux of 14%. Although the total heat flux for the squealet tip still exceeded that of the

double squealer tip, it was designed to be more amenable to film cooling. The effect of relative endwall motion was also investigated numerically, using the double squealer tip as a test bed. The near-tip incidence angle was seen to be reduced by the endwall movement, which altered the flow structure with the blade tip cavity significantly, although the resultant effect on the heat transfer coefficient distribution was relatively small.

A simplified version of the EFE internal cooling core was used to add film cooling holes to the squealet tip geometry. Numerical simulations of the cooled blade tip were performed at the 0.89% blade chord tip gap in FLUENT 6.3 on unstructured, hybrid tetrahedral and prism layer meshes created using ICEM CFD 12. Each cooling hole was capped at both ends with a cover surface and the fluid volume contained within specified as a separate computational volume, allowing the cooling holes to be sealed off or opened up independently. Six different film cooling configurations were assessed by selectively sealing cooling holes while leaving others open. The intention was to minimise the cooling air consumption while maintaining an adequate cooling performance. A reduction of coolant mass flow rate of 38% was achieved compared with the *All open* configuration, at the expense of a 7% increase in total blade tip heat flux. Cooling holes exiting on the blade suction side were found not to contribute to expedient film cooling of the blade tip, as the cooling air issued from these holes was swept away from the tip region. The cooling holes exiting on the pressure side, by contrast, provided good film coverage over the majority of both the pressure side and suction side squealet rims. This allowed the tip shelf to be adequately cooled with relatively few holes kept open locally. The suction side cooling gallery reduced the pressure ratios across the tip shelf cooling holes towards the trailing edge, resulting in lower momentum cooling flows that improved blade tip trailing edge coverage. The effect of some additional cooling holes and a relocated dust hole was also investigated in an attempt to improve cooling of the blade tip crown. This investigation was performed using a purely tetrahedral mesh. The placement of the dust hole in the

front of the blade tip cavity was found to be crucial to the local heat transfer levels, as the cooling air flow could moderate the high heat transfer coefficients caused by the attachment of over-tip leakage flow on to the cavity floor. This required the dust hole to be appropriately placed to interrupt the attaching flow, however. The extra cooling holes were located to blow cooling air directly on to the inner squealet rim and were effective at reducing local adiabatic wall temperatures, but required large amounts of cooling air to feed.

The squealet blade tip was tested experimentally in the High Speed Linear Cascade, a transonic blowdown facility. The tip geometry was straightened to remove its annularity and the cooling holes repositioned in their equivalent positions, along with a simple, single cooling plenum within the blade tip. Test pieces were manufactured by stereolithography from WaterShed XC 11122 resin, whose thermal product was measured. Aerodynamic loss measurements were taken using uncooled versions of the linearised blade tip by the downstream traverse of a three-hole and a single-hole probe at 0.45%, 0.89% and 1.34% blade chord tip gaps. The aerodynamic loss of the squealet tip was seen to be similar to that of a flat blade tip and lower than that of a winglet tip, tested by O'Dowd (2010). Heat transfer measurements were taken for the uncooled blade tip by a transient, infra-red thermographic technique, using an electric heater mesh upstream of the test section to heat the mainstream flow. Calibration of the IR camera was performed in situ, using a thermocouple located on the test blade tip surface. Heat transfer measurements were also performed using the same technique for the cooled blade tip. Two cooling configurations were tested at the 0.89% blade chord tip gap. Cooled cooling air was supplied from three vortex tubes to the test blade, with uncooled cooling air supplied to the side blades to maintain the periodicity of the cascade. The qualitative comparison of the experimental adiabatic wall temperature maps against the 3D CFD results was good, although generally higher Nusselt numbers were recorded than were predicted by the engine-representative CFD simulations. Some differences were noted in the forward part of the blade tip; these

were attributed to the simplifications to the environment made in the linear cascade, such as the lack of relative endwall motion. A CFD simulation of the experimental linear cascade environment without cooling was performed at the 1.34% tip clearance. This was conducted with a single blade in a translationally periodic environment. The size of the over-tip leakage vortex was predicted to be smaller than had been observed experimentally, resulting in a large underprediction of the area-averaged aerodynamic loss coefficients. The magnitudes of the predicted blade tip Nusselt number distribution were similar to those of the previous engine-representative CFD simulations and lower than the magnitudes observed in the experimental data. Differences in the shape of the Nusselt number distribution were observed in the vicinity of regions of separated and reattaching flow, but other salient features were replicated in the computational data.

7.2 Conclusions and research outcomes

Additional insight into the overall understanding of heat transfer to unshrouded turbine blade tips has been gained over the course of the study presented in the present thesis. From the low speed, incompressible study of chapter 3, specific details of the conditions required for high veracity computational simulations of blade tip heat transfer have been identified; namely that wall functions are inappropriate for use in such simulations and the boundary layer flows must instead be fully resolved, and that the standard k-ϵ and realisable k-ϵ models overpredict the turbulence levels at the pressure side entrance to the tip gap region and should be avoided. Additionally, the Reynolds stress model provided no increase in accuracy, so does not justify the extra computational cost. These observations will aid any similar computational studies that may be performed in the future.

The greatest contributions of the present study, however, stem from the development of the squealet tip. The initial design philosophy of the squealet tip has been validated,

showing that the approach that was taken to create a hybrid, unshrouded blade tip design produces a geometry whose aerothermal behaviour lies somewhere in between those of the two parent designs, the double squealer tip and the winglet tip. In this way, the most fundamental outcome of the study is the verification that a spectrum in over-tip flow characteristics and performance that runs from a double squealer tip to a winglet tip exists and hence that it is feasible to blend the physical geometries in some way to attempt to harness some of the performance characteristics of each. This spectrum is illustrated in the results of chapter 4, where the original squealet tip showed characteristics that more closely resembled the double squealer tip than the revised squealet, yet both sets of results included some of the character of each parent design.

Another significant outcome of the present research is the highlighting of the sensitivity of the over-tip flow field around double squealer-like blade tips to the forward part of the cavity. The tremendous importance of the detail of the flow near the leading edge of the cavity had not previously been appreciated. It has been seen that apparently minor changes in the flow near the leading edge can affect the overall flow structure and the resultant heat transfer distribution over the entire blade tip. This observation presents a potentially significant opportunity to condition of the over-tip leakage flow by applying small changes to the forward part of the blade tip, harnessing this sensitivity. The need for extremely accurate flow predictions in this region is made even more critical by the reattachment hotspot located on the cavity floor near the leading edge; it was observed that if the location can be predicted accurately, the appropriate positioning of a dust hole can suppress the impingement of the flow onto the cavity floor and eliminate the hotspot entirely.

The understanding required for the effective application of film cooling flows to the squealet tip design specifically, and more generally to double squealer-like blade tips, has been expanded significantly. Film cooling air delivered from cooling holes exiting the near-tip pressure side surfaces provides excellent coverage over almost all

of the blade tip and can provide the bulk of the required film cooling coverage for the blade tip. Cooling air delivered to holes exiting the near-tip suction side surfaces, by contrast, is swept away from the blade tip region and such holes are ineffective for film cooling provision. The tip shelf was introduced and demonstrated to be an effective device for the local cooling of a high heat load region that is prone to thermal damage. The combination of the tip shelf and the cooling gallery used to supply the cooling holes located on it has shown significant potential for the fine control of cooling air delivery in the region, allowing the distribution of coolant to be improved and vulnerable areas that had previously been extremely difficult to cool, such as the trailing edge of the blade tip, to be better protected.

7.3 Recommendations for future work

The primary achievement of the work presented in this thesis has been the introduction of a new unshrouded blade tip design and the demonstration of its viability, both computationally and experimentally. This new blade tip geometry, the squealet tip, shows the potential for improved blade tip life compared with the double squealer tip, while offering a significant reduction in both weight and wetted surface area compared with the winglet tip. This will become more and more important if the current trends of increasing TET and rotor speed continue. It is therefore suggested that future work would best focus on the development of this promising potential new tip design into a true contender for use in a real engine. A formal optimisation on the cooling configuration would be a significant step forward towards this goal, although this should perhaps be preceded by some form of optimisation on the external geometry. The hot spot on the crown of the blade, identified in chapter 5 should be investigated in more detail, as there is every possibility that it could be eliminated by reshaping the forward section of the blade tip. The flow field for the whole of the cavity and gutter has been seen to be very sensitive to minor details of the flow near the leading

edge of the tip; there is therefore potential for this to be harnessed and for minor alterations to be made here to condition the cavity and gutter flow better. It has already been shown by Mischo et al. (2008) that relatively small changes to the profile of a double squealer tip can dramatically alter the structure of the flow within its cavity; the character of the flow in the forward portion of the squealet tip originates from the double squealer-like geometry at the front of the blade, so similar reprofiling could be expected to yield comparable results.

The observation that the pressure ratios across the tip shelf cooling holes are reduced by the cooling gallery presents a significant opportunity for improvements in blade tip cooling design. The trailing edge region of the blade tip is difficult to cool; the cooling gallery provides a potential way in which the momentum flux of cooling air supplied nearby could be tuned to bathe this problematic region in coolant. Further investigation into this possibility is needed before it can be employed in a real engine, however.

The data from the High Speed Linear Cascade provides an excellent dataset for use in CFD validation. Its unique combination of high spatial resolution blade tip heat transfer measurements with film cooling in the transonic flow regime offers a valuable opportunity for the development of CFD codes and the improvement of turbulence models. The benefits of this would run in both directions as well; by running validated CFD simulations on the HSLC test section, further understanding of the flow within the cascade could be obtained. There has been some work performed in this regard already, linked with the development of Rolls-Royce's CFD suite, HYDRA, but it has largely been restricted to the flat blade tip geometry. This work should be extended to encompass the squealet, double squealer and winglet tips as well.

This programme of research has considered only the over-tip leakage flow and blade tip heat transfer in steady flow. This assumption was a significant, but necessary, simplification of a highly complex environment. Unsteady effects, such as combustor hot streak or NGV wake passing, could affect even the time-mean flow and heat transfer;

this was observed in Atkins et al. (2008), where unsteady interactions between the NGV and the rotor blade potential fields resulted in a significant increase in the time-averaged heat load. There are few such studies that have considered the effects of unsteadiness on unshrouded blade tip performance and heat transfer specifically and hence these effects are relatively poorly understood. Further research into unsteady interactions in the HP turbine stage environment and specifically their effects on unshrouded blade tips would be very beneficial.

References

A. R. Abu Talib. *Detailed investigation of the low-temperature analogy of an aircraft engine standard fire-test.* DPhil thesis, Oxford University, 2003.

S. Acharya, H. Yang, S. V. Ekkad, C. Prakash, and R. Bunker. Numerical simulation of film cooling on the tip of a gas turbine blade. In *Proceedings of the ASME Turbo Expo 2002: Power for Land, Sea and Air*, 2002. 3rd–6th June 2002, Amsterdam, The Netherlands (GT-2002-30553).

S. Acharya, H. Yang, C. Prakash, and R. Bunker. Numerical study of flow and heat transfer on a blade tip with different leakage reduction strategies. In *Proceedings of the ASME Turbo Expo 2003: Power for Land, Sea and Air*, 2003. 16th–19th June 2003, Atlanta, Georgia, USA (GT-2003-38617).

S. Acharya, G. Kramer, L. Moreaux, and C. Nakamata. Squealer tip heat transfer with film cooling. In *Proceedings of the ASME Turbo Expo 2010: Power for Land, Sea and Air*, 2010. 14th–18th June 2010, Glasgow, UK (GT2010-23688).

J. Ahn, S. Mhetras, and J. C. Han. Film-cooling effectiveness on a gas turbine blade tip using pressure-sensitive paint. *Journal of Heat Transfer*, 127(5):521–530, May 2005.

H. W. Allen and M. G. Kofskey. *Visualization study of secondary flows in turbine rotor tip regions.* Technical Report TN-3519, NACA, 1955.

A. A. Ameri. Heat transfer and flow on the blade tip of a gas turbine equipped with a mean-camberline strip. *Journal of Turbomachinery*, 123(4):704–708, Oct 2001.

A. A. Ameri. Numerical simulation of flow and heat transfer in the tip region of turbine blades. In *Turbine Blade Tip Design and Tip Clearance Treatment*, 2004. ISBN 2-930389-51-6. Von Karman Institute Lecture Series VKI-LS 2004-02, 19th–23rd January 2004, Brussels.

A. A. Ameri and R. S. Bunker. Heat transfer and flow on the first-stage blade tip of a power generation gas turbine: Part 2—Simulation results. *Journal of Turbomachinery*, 122(2):272–277, Apr 2000.

A. A. Ameri and D. L. Rigby. A numerical analysis of heat transfer and effectiveness on film cooled turbine blade tip models. In *Fourteenth International Symposium on Air Breathing Engines*, 1999. ISBN 1-56347-357-7. 5$^{\text{th}}$–10$^{\text{th}}$ September 1999, Florence, Italy.

A. A. Ameri and E. Steinthorsson. Prediction of unshrouded rotor blade tip heat transfer. In *Proceedings of the ASME Turbo Expo 1995: Land, Sea and Air*, 1995. 5$^{\text{th}}$–8$^{\text{th}}$ June 1995, Houston, Texas, USA (95-GT-142). Also published as NASA Contractor Report 198542, Oct 1996.

A. A. Ameri and E. Steinthorsson. Analysis of gas turbine rotor blade tip and shroud heat transfer. In *Proceedings of the ASME Turbo Expo 1996: Land, Sea and Air*, 1996. 10$^{\text{th}}$–13$^{\text{th}}$ June 1996, Birmingham, UK (96-GT-189). Also published as NASA Contractor Report 198541, Oct 1996.

A. A. Ameri, E. Steinthorsson, and D. L. Rigby. Effect of squealer tip on rotor heat transfer and efficiency. *Journal of Turbomachinery*, 120(4):753–759, Oct 1998.

A. A. Ameri, E. Steinthorsson, and D. L. Rigby. Effects of tip clearance and casing recess on heat transfer and stage efficiency in axial turbines. *Journal of Turbomachinery*, 121(4):683–693, Oct 1999.

A. A. Ameri, D. L. Rigby, E. Steinthorsson, J. Heidmann, and J. C. Fabian. Unsteady analysis of blade and tip heat transfer as influenced by the upstream momentum and thermal wakes. *Journal of Turbomachinery*, 132(4):041007, Oct 2010.

L. J. Ammann and R. R. Good. *System for cooling turbine blades*. US Patent US 0176929, Jul 2011.

R. H. Andersen. *Tip cooling for turbine blades*. US Patent US 4142824, Mar 1979.

N. R. Atkins, S. J. Thorpe, and R. W. Ainsworth. Unsteady effects on transonic turbine blade-tip heat transfer. In *Proceedings of the ASME Turbo Expo 2008: Power for Land, Sea and Air*, 2008. 9$^{\text{th}}$–13$^{\text{th}}$ June 2008, Berlin, Germany (GT2008-51177). To be published in *Journal of Turbomachinery*.

Gm. S. Azad, J. C. Han, and R. J. Boyle. Heat transfer and flow on the squealer tip of a gas turbine blade. *Journal of Turbomachinery*, 122(4):725–732, Oct 2000a.

Gm. S. Azad, J. C. Han, S. Teng, and R. J. Boyle. Heat transfer and pressure distributions on a gas turbine blade tip. *Journal of Turbomachinery*, 122(4):717–724, Oct 2000b. Previously published as 2000-GT-194 in *Proceedings of the ASME Turbo Expo 2000: Power for Land, Sea and Air*.

A. Basson and B. Lakshminarayana. Numerical simulation of tip clearance effects in turbomachinery. *Journal of Turbomachinery*, 117(3):348–359, Jul 1995.

T. Behr, A. I. Kalfas, and R. S. Abhari. Control of rotor tip leakage through cooling injection from the casing in a high-work turbine: Experimental investigation. In *Proceedings of the ASME Turbo Expo 2007: Power for Land, Sea and Air*, 2007. 14^{th}–17^{th} May 2007, Montreal, Canada (GT2007-27269).

T. Behr, A. I. Kalfas, and R. S. Abhari. Desensitization of the flowfield from rotor tip-gap height by casing-air injection. *Journal of Propulsion and Power*, 24(5): 1108–1116, Sep–Oct 2008.

J. P. Bindon. The measurement of tip clearance flow structure on the end-wall and within the clearance gap of an axial turbine cascade. In *Proceedings of the Institution of Mechanical Engineers: Turbomachinery—Efficiency prediction and improvement*, 1987. ISBN 0-85298-630-0, 1^{st}–3^{rd} Sep 1987, Cambridge, UK (C273/87).

J. P. Bindon. The measurement and formation of tip clearance loss. *Journal of Turbomachinery*, 111(3):257–263, Jul 1989.

J. P. Bindon and G. Morphis. The development of axial turbine leakage loss for two profiled tip geometries using linear cascade data. *Journal of Turbomachinery*, 114 (1):198–203, Jan 1992.

T. C. Booth, P. R. Dodge, and H. K. Hepworth. Rotor-tip leakage: Part I—Basic methodology. *Journal of Engineering for Power*, 104(1):154–161, Jan 1982.

R. J. Boyle, J. E. Haas, and T. Katsanis. *Comparison between measured turbine stage performance and the predicted performance using quasi-3D flow and boundary layer analyses*. Technical Report TM-83640, NASA, 1984.

E. Buckingham. On physically similar systems; Illustrations on the use of dimensional equations. *Physical Review*, 4(4):345–376, Oct 1914.

R. S. Bunker. A review of turbine blade tip heat transfer. *Annals of the New York Academy of Sciences*, 934(1):64–79, May 2001.

R. S. Bunker. Blade tip heat transfer and cooling techniques. In *Turbine Blade Tip Design and Tip Clearance Treatment*, 2004. ISBN 2-930389-51-6. Von Karman Institute Lecture Series VKI-LS 2004-02, 19^{th}–23^{rd} January 2004, Brussels.

R. S. Bunker. Axial turbine blade tips: Function, design, and durability. *Journal of Propulsion and Power*, 22(2):271–285, Mar–Apr 2006.

R. S. Bunker and J. C. Bailey. Blade tip heat transfer and flow with chordwise sealing strips. In *Proceedings of the 8^{th} International Symposium on Transport Phenomena and Dynamics of Rotating Machinery (ISROMAC–8), Volume 1*, pages 548–555, 2000. ISBN 0-9652469-8-1. 26^{th}–30^{th} March 2000, Honolulu, Hawaii, USA.

R. S. Bunker and J. C. Bailey. Effect of squealer cavity depth and oxidation on turbine blade tip heat transfer. In *Proceedings of the ASME Turbo Expo 2001: Power for Land, Sea and Air*, 2001. 4th–8th June 2001, New Orleans, Louisiana, USA (2001-GT-0155).

R. S. Bunker, J. C. Bailey, and A. A. Ameri. Heat transfer and flow on the first-stage blade tip of a power generation gas turbine: Part 1—Experimental results. *Journal of Turbomachinery*, 122(2):263–271, Apr 2000.

D. Butts, J. G. Nourse, and R. C. Simmons. *Tip cooled blade.* US Patent US 5261789, Nov 1993.

C. Camci, D. Dey, and L. Kavurmacioglu. Tip leakage flows near partial squealer rims in an axial flow turbine stage. In *Proceedings of the ASME Turbo Expo 2003: Power for Land, Sea and Air*, 2003. 16th–19th June 2003, Atlanta, Georgia, USA (GT-2003-38979).

K. S. Chana and T. V. Jones. An investigation on turbine tip and shroud heat transfer. *Journal of Turbomachinery*, 125(3):513–520, Jul 2003. Previously published as GT-2002-30554 in *Proceedings of the ASME Turbo Expo 2002: Power for Land, Sea and Air*.

G. Chen, W. N. Dawes, and H. P. Hodson. A numerical and experimental investigation of turbine tip gap flow. In *Proceedings of the AIAA/SAE/ASME/ASEE 29th Joint Propulsion Conference*, 1993. 28th–30th June 1993, Monterey, California, USA (AIAA-93-2533).

B. C. Y. Cheong and S. C. Diamond. *Blade for a rotor.* US Patent US 0098554, Apr 2010.

D. G. Cherry, C. P. Lee, C. Prakash, A. R. Wadia, B. D. Keith, and S. R. Brassfield. *Turbine blade having angled squealer tip.* US Patent US 6672829, Jan 2004.

J. R. Christophel, E. Couch, K. A. Thole, and F. J. Cunha. Measured adiabatic effectiveness and heat transfer for blowing from the tip of a turbine blade. *Journal of Turbomachinery*, 127(2):251–262, Apr 2005a.

J. R. Christophel, K. A. Thole, and F. J. Cunha. Cooling the tip of a turbine blade using pressure side holes—Part I: Adiabatic effectiveness measurements. *Journal of Turbomachinery*, 127(2):270–277, Apr 2005b.

J. R. Christophel, K. A. Thole, and F. J. Cunha. Cooling the tip of a turbine blade using pressure side holes—Part II: Heat transfer measurements. *Journal of Turbomachinery*, 127(2):278–286, Apr 2005c.

M. K. Chyu, H. K. Moon, and D. E. Metzger. Heat transfer in the tip region of grooved turbine blades. *Journal of Turbomachinery*, 111(2):131–138, Apr 1989.

V. H. S. Correia. *Impingement cooled airfoil tip.* US Patent US 6231307, May 2001.

N. A. Cumpsty and J. H. Horlock. Averaging nonuniform flow for a purpose. *Journal of Turbomachinery*, 128(1):120–129, Jan 2006.

C. R. B. Day. *Aerodynamics of an annular film-cooled turbine cascade.* DPhil thesis, Oxford University, 1997.

J. D. Denton. Loss mechanisms in turbomachines. *Journal of Turbomachinery*, 115 (4):621–656, Oct 1993.

J. D. Denton and N. A. Cumpsty. Loss mechanisms in turbomachines. In *Proceedings of the Institution of Mechanical Engineers: Turbomachinery—Efficiency Prediction and Improvement*, 1987. ISBN 0-85298-630-0, 1st–3rd Sep 1987, Cambridge, UK (C260/87).

D. Dey and C. Camci. Development of tip clearance flow downstream of a rotor blade with coolant injection from a tip trench. In *Proceedings of the 8th International Symposium on Transport Phenomena and Dynamics of Rotating Machinery (ISROMAC–8), Volume 1*, pages 572–579, 2000. ISBN 0-9652469-8-1. 26th–30th March 2000, Honolulu, Hawaii, USA.

D. Dey and C. Camci. Aerodynamic tip desensitization of an axial turbine rotor using pressure side tip platform extensions. In *Proceedings of the ASME Turbo Expo 2001: Power for Land, Sea and Air*, 2001. 4th–8th June 2001, New Orleans, Louisiana, USA (2001-GT-0484).

F. Didier, R. Dénos, and T. Arts. Unsteady rotor heat transfer in a transonic turbine stage. In *Proceedings of the ASME Turbo Expo 2002: Power for Land, Sea and Air*, 2002. 3rd–6th June 2002, Amsterdam, The Netherlands (GT-2002-30195).

P. T. Dishart and J. Moore. Tip leakage losses in a linear turbine cascade. *Journal of Turbomachinery*, 112(4):599–608, Oct 1990.

R. P. Dring and H. D. Joslyn. Measurement of turbine rotor blade flows. *Journal of Engineering for Power*, 103(2):400–405, Apr 1981.

M. G. Dunn and C. W. Haldeman. Time-averaged heat flux for a recessed tip, lip, and platform of a transonic turbine blade. *Journal of Turbomachinery*, 122(4):692–698, Oct 2000.

M. El-Ghandour, M. K. Ibrahim, K. Mori, and Y. Nakamura. Effects of tip cavity depth, width and location on the leakage flow in an axial turbine cascade. *Journal of Fluid Science and Technology*, 5(3):558–573, 2010a.

M. El-Ghandour, K. Mori, and Y. Nakamura. Desensitization of tip clearance effects in axial flow turbines. *Journal of Fluid Science and Technology*, 5(2):317–330, 2010b.

ERCOFTAC Special Interest Group on "Quality and Trust in Industrial CFD". *Best Practice Guidelines*. Technical report, European Community On Flow, Turbulence And Combustion, Jan 2000. Version 1.0.

A. D. Fitt, C. J. P. Forth, B. A. Robertson, and T. V. Jones. Temperature ratio effects in compressible turbulent boundary layers. *International Journal of Heat and Mass Transfer*, 29(1):159–164, Jan 1986.

Fluent Inc. FLUENT 6.3 *User's Guide*. Fluent Inc., Centerra Resource Park, 10 Cavendish Court, Lebanon, NH 03766, USA, Sep 2006.

D. J. Frasier, M. E. Schlienger, and M. Kush. *Method for production of a ceramic casting mold system*. European Patent Application EP 2359958, Aug 2011.

Z. Gao, D. Narzary, S. Mhetras, and J. C. Han. Effect of inlet flow angle on gas turbine blade tip film cooling. In *Proceedings of the ASME Turbo Expo 2007: Power for Land, Sea and Air*, 2007. 14th–17th May 2007, Montreal, Canada (GT2007-27066).

S. G. Gegg, N. J. Heidegger, and R. A. Mikkelson. Computational modeling and thermal paint verification of film-cooling designs for an unshrouded high-pressure turbine blade. In *Proceedings of the ASME Turbo Expo 1999: Land, Sea and Air*, 1999. 7th–10th June 1999, Indianapolis, Indiana, USA (99-GT-330).

B. Glezer. Thermo-mechanical design factors affecting turbine blade tip clearance. In *Turbine Blade Tip Design and Tip Clearance Treatment*, 2004. ISBN 2-930389-51-6. Von Karman Institute Lecture Series VKI-LS 2004-02, 19th–23rd January 2004, Brussels.

J. A. H. Graham. Investigation of a tip clearance cascade in a water analogy rig. *Journal of Engineering for Gas Turbines and Power*, 108(1):38–46, Jan 1986.

A. Granovskiy, M. Kostege, and N. Lomakin. Parametrical investigation of turbine stages with open tip clearance for the purpose of stage efficiency increase. In *Proceedings of the ASME Turbo Expo 2010: Power for Land, Sea and Air*, 2010. 14th–18th June 2010, Glasgow, UK (GT2010-22876).

D. G. Gregory-Smith and J. G. E. Cleak. Secondary flow measurements in a turbine cascade with high inlet turbulence. *Journal of Turbomachinery*, 114(1):173–183, Jan 1992.

M. Guillaume. *Propulseur par réaction sur l'air*. French Patent FR 534801, Apr 1922.

E. E. Halila, D. T. Lenahan, and T. T. Thomas. *High pressure turbine test hardware detailed design report*. Technical Report CR-167955, NASA, Jun 1982.

K. L. Harrison and D. G. Bogard. Comparison of RANS turbulence models for prediction of film cooling performance. In *Proceedings of the ASME Turbo Expo 2008: Power for Land, Sea and Air*, 2008. 9th–13th June 2008, Berlin, Germany (GT2008-51423).

N. W. Harvey. Aerothermal implications of shroudless and shrouded blades. In *Turbine Blade Tip Design and Tip Clearance Treatment*, 2004. ISBN 2-930389-51-6. Von Karman Institute Lecture Series VKI-LS 2004-02, 19th–23rd January 2004, Brussels.

N. W. Harvey and K. Ramsden. A computational study of a novel turbine rotor partial shroud. *Journal of Turbomachinery*, 123(3):534–543, Jul 2001.

N. W. Harvey, D. A. Newman, F. Haselbach, and L. Willer. An investigation into a novel turbine rotor winglet: Part 1—Design and model rig test results. In *Proceedings of the ASME Turbo Expo 2006: Power for Land, Sea and Air*, 2006. 8th–11th May 2006, Barcelona, Spain (GT2006-90456).

D. K. Hennecke. Heat transfer problems in aero-engines. In D. E. Metzger and N. H. Afgan, editors, *Heat and Mass Transfer in Rotating Machinery*, pages 353–379. Hemisphere Publishing Company, Washington, DC, USA, 1984.

F. J. G. Heyes, H. P. Hodson, and G. M. Dailey. The effect of blade tip geometry on the tip leakage flow in axial turbine cascades. *Journal of Turbomachinery*, 114(3): 643–651, Jul 1992.

T. Hofer and T. Arts. Aerodynamic investigation of the tip leakage flow for blades with different tip squealer geometries at transonic conditions. In *Proceedings of the ASME Turbo Expo 2009: Power for Land, Sea and Air*, 2009. 8th–12th June 2009, Orlando, Florida, USA (GT2009-59909).

T. Hofer, M. Legrand, L. Pons, and T. Arts. Aerodynamic investigation of the leakage flow for a blade with a squealer tip at transonic condictions. In F. Heitmeir, F. Martelli, and M. Manna, editors, *Proceedings of the 8th European Conference on Turbomachinery Fluid Dynamics and Thermodynamics*, pages 1483–1493, 2009. ISBN 978-3-85125-036-7, 23rd–27th Mar 2009, Graz, Austria.

E. M. Hohlfield, J. R. Christophel, E. L. Couch, and K. A. Thole. Predictions of cooling from dirt purge holes along the tip of a turbine blade. In *Proceedings of the ASME Turbo Expo 2003: Power for Land, Sea and Air*, 2003. 16th–19th June 2003, Atlanta, Georgia, USA (GT-2003-38251).

J. H. Horlock, D. T. Watson, and T. V. Jones. Limitations on gas turbine performance imposed by large turbine cooling flows. *Journal of Engineering for Gas Turbines and Power*, 123(3):487–494, Jul 2001.

J. Hourmouziadis and G. Albrecht. An integrated aero/mechanical performance approach to high technology turbine design. In *AGARD Conference Proceedings No. 421—Advanced Technology for Aero Gas Turbine Components*, pages 11-1–11-12, 1987. ISBN 92-835-0433-X. Propulsion and Energetics Panel 69$^{\text{th}}$ Symposium, 4$^{\text{th}}$–8$^{\text{th}}$ May 1987, Paris, France (AGARD-CP-421).

P. T. Ireland. *Internal cooling of turbine blades*. DPhil thesis, Oxford University, 1987.

P. T. Ireland, D. R. H. Gillespie, and Z. Wang. *Heating element*. US Patent US 6181874, Jan 2001.

P. Jin and R. J. Goldstein. Local mass/heat transfer on turbine blade near-tip surfaces. *Journal of Turbomachinery*, 125(3):521–528, Jul 2003. Previously published as GT-2002-30556 in *Proceedings of the ASME Turbo Expo 2002: Power for Land, Sea and Air*.

T. V. Jones. Definition of heat transfer coefficients in the turbine situation. In *Proceedings of the Institution of Mechanical Engineers: Turbomachinery—Latest Developments in a Changing Scene*, 1991. ISBN 0-85298-761-7, 19$^{\text{th}}$–20$^{\text{th}}$ Mar 1991, London, UK (C423/046).

L. Kavurmacioglu, D. Dey, and C. Camci. Aerodynamic character of partial squealer tip arrangements in an axial flow turbine: Part I—Detailed aerodynamic field modifications via three dimensional viscous flow simulations around baseline tip. *Progress in Computational Fluid Dynamics*, 7(7):363–373, Jul 2007a.

L. Kavurmacioglu, D. Dey, and C. Camci. Aerodynamic character of partial squealer tip arrangements in an axial flow turbine: Part II—Detailed aerodynamic field modifications via three dimensional viscous flow simulations around a partial squealer tip. *Progress in Computational Fluid Dynamics*, 7(7):374–386, Jul 2007b.

N. L. Key and T. Arts. Comparison of turbine tip leakage flow for flat tip and squealer geometries at high-speed conditions. *Journal of Turbomachinery*, 128(2):213–220, Apr 2006. Previously published as GT2004-53979 in *Proceedings of the ASME Turbo Expo 2004: Power for Land, Sea and Air*.

Y. W. Kim and D. E. Metzger. Heat transfer and effectiveness on film cooled turbine blade tip models. *Journal of Turbomachinery*, 117(1):12–21, Jan 1995.

Y. W. Kim, J. P. Downs, F. O. Soechting, W. Abdel-Messeh, G. D. Steuber, and S. Tanrikut. A summary of the cooled turbine blade tip heat transfer and film effectiveness investigations performed by Dr. D. E. Metzger. *Journal of Turbomachinery*, 117(1):1–11, Jan 1995.

R. C. Kingcombe and R. V. Steeden. The design and test of a turbine rotor blade for reduced overtip loss. In *Proceedings of the Institution of Mechanical Engineers: Turbomachinery—Latest Developments in a Changing Scene*, 1991. ISBN 0-85298-761-7, 19$^{\text{th}}$–20$^{\text{th}}$ Mar 1991, London, UK (C423/046).

S. K. Krishnababu, W. N. Dawes, H. P. Hodson, G. D. Lock, J. Hannis, and C. Whitney. Aero-thermal investigation of tip leakage flows in axial flow turbines. Part II—Effect of relative casing motion. In *Proceedings of the ASME Turbo Expo 2007: Power for Land, Sea and Air*, 2007a. 14^{th}–17^{th} May 2007, Montreal, Canada (GT2007-27957).

S. K. Krishnababu, P. J. Newton, W. N. Dawes, G. D. Lock, H. P. Hodson, J. Hannis, and C. Whitney. Aero-thermal investigation of tip leakage flows in axial flow turbines. Part I—Effect of tip geometry and tip clearance gap. In *Proceedings of the ASME Turbo Expo 2007: Power for Land, Sea and Air*, 2007b. 14^{th}–17^{th} May 2007, Montreal, Canada (GT2007-27954).

S. K. Krishnababu, H. P. Hodson, W. N. Dawes, P. J. Newton, and G. D. Lock. Numerical and experimental investigation of tip leakage flow and heat transfer using idealised rotor-tip models at transonic conditions. *The Aeronautical Journal*, 113 (1141):165–175, Mar 2009.

S. K. Krishnababu, H. P. Hodson, G. D. Booth, G. D. Lock, and W. N. Dawes. Aerothermal investigation of tip leakage flow in a film cooled industrial turbine rotor. *Journal of Turbomachinery*, 132(2):021016, Apr 2010.

M. Kumada, S. Iwata, M. Obata, and O. Watanabe. Tip clearance effect on heat transfer and leakage flows on the shroud-wall surface in an axial flow turbine. *Journal of Turbomachinery*, 116(1):39–45, Jan 1994.

K. Kusterer, N. Moritz, D. Bohn, T. Sugimoto, and R. Tanaka. Reduction of tip clearance losses in an axial turbine by shaped design of the blade tip region. In *Proceedings of the ASME Turbo Expo 2007: Power for Land, Sea and Air*, 2007. 14^{th}–17^{th} May 2007, Montreal, Canada (GT2007-27303).

M. Kuwabara, K. Tsukagoshi, and T. Arts. High coverage blade tip film cooling. In *Proceedings of the ASME Turbo Expo 2004: Power for Land, Sea and Air*, 2004. 14^{th}–17^{th} June 2004, Vienna, Austria (GT2004-53226).

J. S. Kwak and J. C. Han. Heat transfer coefficients and film-cooling effectiveness on a gas turbine blade tip. *Journal of Heat Transfer*, 125(3):494–502, Jun 2003a. Previously published as GT-2002-30194 in *Proceedings of the ASME Turbo Expo 2002: Power for Land, Sea and Air*.

J. S. Kwak and J. C. Han. Heat transfer coefficients and film cooling effectiveness on the squealer tip of a gas turbine blade. *Journal of Turbomachinery*, 125(4):648–657, Oct 2003b. Previously published as GT-2002-30555 in *Proceedings of the ASME Turbo Expo 2002: Power for Land, Sea and Air*.

J. S. Kwak, J. Ahn, J. C. Han, C. P. Lee, R. S. Bunker, R. Boyle, and R. Gaugler. Heat transfer coefficients on the squealer tip and near-tip regions of a gas turbine blade with single or double squealer. In *Proceedings of the ASME Turbo Expo 2003: Power for Land, Sea and Air*, 2003. 16^{th}–19^{th} June 2003, Atlanta, Georgia, USA (GT-2003-38907).

L. S. Langston. Fahrenheit 3,600. *Mechanical Engineering Magazine*, Apr 2007.

J. Li, H. Sun, J. Wang, and Z. Feng. Numerical investigations on the steady and unsteady leakage flow and heat transfer characteristics of rotor blade squealer tip. *Journal of Thermal Science*, 20(4):304–311, Aug 2011.

T. Matsunuma. Effects of Reynolds number and freestream turbulence on turbine tip clearance flow. *Journal of Turbomachinery*, 128(1):166–177, Jan 2006.

R. E. Mayle and D. E. Metzger. Heat transfer at the tip of an unshrouded turbine blade. In U. Grigull, E. Hahne, K. Stephan, and J. Straub, editors, *Heat Transfer 1982—Proceedings of the Seventh International Heat Transfer Conference, Volume 3*, pages 87–92, 1982. ISBN 0-89116-299-2/0-89116-342-5. 6^{th}–10^{th} September 1982, Munich, Fed. Rep. Of Germany.

A. A. McCarter, X. Xiao, and B. Lakshminarayana. Tip clearance effects in a turbine rotor: Part II—Velocity field and flow physics. *Journal of Turbomachinery*, 123(2): 296–304, Apr 2001.

D. E. Metzger and K. Rued. The influence of turbine clearance gap leakage on passage velocity and heat transfer: Part I—Sink flow effects on blade pressure side. *Journal of Turbomachinery*, 111(3):284–292, Jul 1989.

D. E. Metzger, R. S. Bunker, and M. K. Chyu. Cavity heat transfer on a transverse grooved wall in a narrow flow channel. *Journal of Heat Transfer*, 111(1):73–79, Feb 1989.

D. E. Metzger, M. G. Dunn, and C. Hah. Turbine tip and shroud heat transfer. *Journal of Turbomachinery*, 117(1):502–507, Jan 1995.

S. Mhetras, H. Yang, Z. Gao, and J. C. Han. Film-cooling effectiveness on squealer rim walls and squealer cavity floor of a gas turbine blade tip using pressure sensitive paint. In *Proceedings of the ASME Turbo Expo 2005: Power for Land, Sea and Air*, 2005. 6^{th}–9^{th} June 2005, Reno-Tahoe, Nevada, USA (GT2005-68387).

S. Mhetras, D. Narzary, Z. Gao, and J. C. Han. Effect of a cutback squealer and cavity depth on film-cooling effectiveness on a gas turbine blade tip. *Journal of Turbomachinery*, 130(2):021002, Apr 2008.

B. Mischo, A. Burdet, T. Behr, and R. S. Abhari. Control of rotor tip leakage through cooling injection from casing in a high-work turbine: Computational investigation using a feature-based jet model. In *Proceedings of the ASME Turbo Expo 2007: Power for Land, Sea and Air*, 2007. 14th–17th May 2007, Montreal, Canada (GT2007-27669).

B. Mischo, T. Behr, and R. S. Abhari. Flow physics and profiling of recessed blade tips: Impact on performance and heat load. *Journal of Turbomachinery*, 130(2): 021008, Apr 2008. Previously published as GT2006-91074 in *Proceedings of the ASME Turbo Expo 2006: Power for Land, Sea and Air*.

B. Mischo, R. S. Abhari, and T. Behr. *Turbine blade with recessed tip*. US Patent US 0180887, Jul 2009.

J. Moore and K. M. Elward. Shock formation in overexpanded tip leakage flow. *Journal of Turbomachinery*, 115(3):392–399, Jul 1993.

J. Moore and J. S. Tilton. Tip leakage flow in a linear turbine cascade. *Journal of Turbomachinery*, 110(2):18–26, Jan 1988.

J. Moore, J. G. Moore, G. S. Henry, and U. Chaudhry. Flow and heat transfer in turbine tip gaps. *Journal of Turbomachinery*, 111(3):301–309, Jul 1989.

H. Nasir. *Turbine blade tip cooling and heat transfer*. PhD thesis, Louisiana State University and Agricultural and Mechanical College, 2004.

H. Nasir, S. V. Ekkad, R. S. Bunker, and C. Prakash. Effects of tip gap film injection from plain and squealer blade tips. In *Proceedings of the ASME Turbo Expo 2004: Power for Land, Sea and Air*, 2004a. 14th–17th June 2004, Vienna, Austria (GT2004-53455).

H. Nasir, S. V. Ekkad, D. M. Kontrovitz, R. S. Bunker, and C. Prakash. Effect of tip gap and squealer geometry on detailed heat transfer measurements over a high pressure turbine rotor blade tip. *Journal of Turbomachinery*, 126(2):221–228, Apr 2004b.

H. Nasir, S. V. Ekkad, and R. S. Bunker. Effect of tip and pressure side coolant injection on heat transfer distributions for a plane and recessed tip. *Journal of Turbomachinery*, 129(1):151–163, Jan 2007.

P. J. Newton. *Aerodynamic and heat transfer measurements in turbine tip leakage flow models*. PhD thesis, University of Bath, 2005.

P. J. Newton, G. D. Lock, S. K. Krishnababu, H. P. Hodson, W. N. Dawes, J. Hannis, and C. Whitney. Heat transfer and aerodynamics of turbine blade tips in a linear cascade. *Journal of Turbomachinery*, 128(2):300–309, Apr 2006.

P. J. Newton, G. D. Lock, S. K. Krishnababu, H. P. Hodson, W. N. Dawes, J. Hannis, and C. Whitney. Aero-thermal investigation of tip leakage flows in axial flow turbines. Part III: Tip cooling. In *Proceedings of the ASME Turbo Expo 2007: Power for Land, Sea and Air*, 2007. 14^{th}–17^{th} May 2007, Montreal, Canada (GT2007-27368).

D. O. O'Dowd. *Aero-thermal performance of transonic high-pressure turbine blade tips*. DPhil thesis, Oxford University, 2010.

D. O. O'Dowd, Q. Zhang, I. Usandizaga, L. He, and P. M. Ligrani. Transonic turbine blade tip aero-thermal performance with different tip gaps: Part II—Tip aerodynamic loss. In *Proceedings of the ASME Turbo Expo 2010: Power for Land, Sea and Air*, 2010. 14^{th}–18^{th} June 2010, Glasgow, UK (GT2010-22780).

D. O. O'Dowd, Q. Zhang, L. He, P. M. Ligrani, and S. Friedrichs. Comparison of heat transfer measurement techniques on a transonic turbine blade tip. *Journal of Turbomachinery*, 133(2):021028, Apr 2011a.

D. O. O'Dowd, Q. Zhang, L. He, M. L. G. Oldfield, P. M. Ligrani, B. C. Y. Cheong, and I. Tibbott. Aerothermal performance of a winglet at engine representative Mach and Reynolds numbers. *Journal of Turbomachinery*, 130(4):041026, Oct 2011b. Previously published as GT2010-22794 in *Proceedings of the ASME Turbo Expo 2010: Power for Land, Sea and Air*.

M. L. G. Oldfield. Impulse response processing of transient heat transfer gauge signals. *Journal of Turbomachinery*, 130(2):021023, Apr 2008.

P. Palafox. *Gas turbine tip leakage flow and heat transfer*. DPhil thesis, Oxford University, 2006.

P. Palafox, M. L. G. Oldfield, J. E. LaGraff, and T. V. Jones. PIV maps of tip leakage and secondary flow fields on a low speed turbine blade cascade with moving endwall. *Journal of Turbomachinery*, 130(1):011001, Jan 2008. Previously published as GT2005-68189 in *Proceedings of the ASME Turbo Expo 2005: Power for Land, Sea and Air*.

P. Palafox, M. L. G. Oldfield, P. T. Ireland, T. V. Jones, and J. E. LaGraff. Blade tip heat transfer and aerodynamics in a large scale turbine cascade with moving endwall. *Journal of Turbomachinery*, 134(2):021020, Mar 2012. Previously published as GT2006-90425 in *Proceedings of the ASME Turbo Expo 2006: Power for Land, Sea and Air*.

M. Papa, R. J. Goldstein, and F. Gori. Effects of tip geometry and tip clearance on the mass/heat transfer from a large-scale gas turbine blade. *Journal of Turbomachinery*, 125(1):90–96, Jan 2003.

J. S. Park, D. H. Lee, H. H. Cho, and D. H. Rhee. Heat transfer and effectiveness on the film cooled tip and inner rim surfaces of a turbine blade. In *Proceedings of the ASME Turbo Expo 2010: Power for Land, Sea and Air*, 2010. 14th–18th June 2010, Glasgow, UK (GT2010-23203).

P. Phutthavong, I. Hassan, and T. Lucas. Unsteady numerical investigation of blade tip leakage, Part 1: Time-averaged results. *Journal of Thermophysics and Heat Transfer*, 22(3):464–473, Jul–Sep 2008a.

P. Phutthavong, I. Hassan, and T. Lucas. Unsteady numerical investigation of blade tip leakage, Part 2: Time-dependent parametric study. *Journal of Thermophysics and Heat Transfer*, 22(3):474–484, Jul–Sep 2008b.

M. D. Polanka, D. A. Hoying, M. Meininger, and C. D. MacArthur. Turbine tip and shroud heat transfer and loading part A: Parameter effects including Reynolds number, pressure ratio and gas to metal temperature ratio. In *Proceedings of the ASME Turbo Expo 2002: Power for Land, Sea and Air*, 2002. 3rd–6th June 2002, Amsterdam, The Netherlands (GT-2002-30186).

M. D. Polanka, J. P. Clark, A. L. White, M. Meininger, and T. J. Praisner. Turbine tip and shroud heat transfer and loading part B: Comparisons between prediction and experiment including unsteady effects. In *Proceedings of the ASME Turbo Expo 2003: Power for Land, Sea and Air*, 2003. 16th–19th June 2003, Atlanta, Georgia, USA (GT-2003-38916).

T. M. Pollock and S. Tin. Nickel-based superalloys for advanced turbine engines: Chemistry, microstructure and properties. *Journal of Propulsion and Power*, 22(2): 361–374, Mar–Apr 2006.

C. Prakash, C. P. Lee, D. G. Cherry, R. Doughty, and A. R. Wadia. Analysis of some improved blade tip concepts. *Journal of Turbomachinery*, 128(4):639–642, Oct 2006.

D. A. Rains. *Tip clearance flows in axial compressors and pumps*. PhD thesis, California Institute of Technology, 1954.

N. M. Rao and C. Camci. Axial turbine tip desensitization by injection from a tip trench—Part 1: Effect of injection mass flow rate. In *Proceedings of the ASME Turbo Expo 2004: Power for Land, Sea and Air*, 2004a. 14th–17th June 2004, Vienna, Austria (GT2004-53256).

N. M. Rao and C. Camci. Axial turbine tip desensitization by injection from a tip trench—Part 2: Leakage flow sensitivity to injection location. In *Proceedings of the ASME Turbo Expo 2004: Power for Land, Sea and Air*, 2004b. 14th–17th June 2004, Vienna, Austria (GT2004-53258).

N. M. Rao and C. Camci. A flow visualization study of axial turbine tip desensitization by coolant injection from a tip trench. In *Proceedings of ASME International Mechanical Engineering Congress and RD&D Expo 2004*, 2004c. 13th–19th November 2004, Anaheim, California, USA (IMECE2004-60943).

Rolls-Royce plc. *The Jet Engine*. Rolls-Royce plc., London, UK, 6th edition, 2005. ISBN 0-902121-2-35.

A. Rubin de Cervin and J. C. Djelalian. Environmentally Friendly Engine: the Commission authorises aid for a British project led by Rolls-Royce. *European Commission Competition Policy Newsletter*, 3:80–81, 2006.

K. Rued and D. E. Metzger. The influence of turbine clearance gap leakage on passage velocity and heat transfer: Part II—Source flow effects on blade pressure side. *Journal of Turbomachinery*, 111(3):293–300, Jul 1989.

A. K. Saha, S. Acharya, C. Prakash, and R. Bunker. Blade tip leakage flow and heat transfer with pressure side winglet. In *Proceedings of the ASME Turbo Expo 2003: Power for Land, Sea and Air*, 2003. 16th–19th June 2003, Atlanta, Georgia, USA (GT-2003-38620).

A. K. Saha, S. Acharya, R. Bunker, and C. Prakash. Blade tip leakage flow and heat transfer with pressure-side winglet. *International Journal of Rotating Machinery*, 2006(1):1–15, Feb 2006.

H. I. H. Saravanamuttoo, G. F. C. Rogers, H. Cohen, and P. V. Straznicky. *Gas Turbine Theory*. Pearson Education Ltd., Harlow, UK, 6th edition, 2009. ISBN 978-0-13-222437-6.

V. Saxena and S. V. Ekkad. Effect of squealer geometry on tip flow and heat transfer for a turbine blade in a low speed cascade. *Journal of Heat Transfer*, 126(4):546–553, Aug 2004.

V. Saxena, H. Nasir, and S. V. Ekkad. Effect of blade tip geometry on tip flow and heat transfer for a blade in a low-speed cascade. *Journal of Turbomachinery*, 126 (1):130–138, Jan 2004.

Z. Schabowski and H. Hodson. The reduction of over tip leakage loss in unshrouded axial turbines using winglets and squealers. In *Proceedings of the ASME Turbo Expo 2007: Power for Land, Sea and Air*, 2007. 14th–17th May 2007, Montreal, Canada (GT2007-27623).

Z. Schabowski, H. Hodson, D. Giacche, B. Power, and M. R. Stokes. Aeromechanical optimisation of a winglet-squealer tip for an axial turbine. In *Proceedings of the ASME Turbo Expo 2010: Power for Land, Sea and Air*, 2010. 14th–18th June 2010, Glasgow, UK (GT2010-23542).

P. J. Schneider. *Conduction heat transfer*. Addison-Wesley, Cambridge, Massachusetts, USA, 1st edition, 1955.

D. L. Schultz and T. V. Jones. *Heat-transfer measurements in short-duration hypersonic facilities*. AGARDograph AGARD-AG-165, North Atlantic Treaty Organisation Advisory Group for Aerospace Research and Development, Feb 1973.

B. Sen, D. L. Schmidt, and D. G. Bogard. Film cooling with compound angle holes: Heat transfer. *Journal of Turbomachinery*, 118(4):800–806, Oct 1996.

A. Shavalikul and C. Camci. A comparative analysis of pressure side extensions for tip leakage control in axial turbines. In *Proceedings of the ASME Turbo Expo 2008: Power for Land, Sea and Air*, 2008. 9th–13th June 2008, Berlin, Germany (GT2008-50782).

V. Shyam and A. Ameri. Comparison of various supersonic turbine tip designs to minimize aerodynamic loss and tip heating. In *Proceedings of the ASME Turbo Expo 2011: Power for Land, Sea and Air*, 2011. 6th–10th June 2011, Vancouver, Canada (GT2011-46390).

V. Shyam, A. Ameri, and J. P. Chen. Analysis of unsteady tip and endwall heat transfer in a highly loaded transonic turbine stage. *Journal of Turbomachinery*, 134 (4):041022, Oct 2012. Previously published as GT2010-23694 in *Proceedings of the ASME Turbo Expo 2010: Power for Land, Sea and Air*.

S. A. Sjolander and D. Cao. Measurements of the flow in an idealized turbine tip gap. *Journal of Turbomachinery*, 117(4):578–584, Oct 1995.

V. Srinivasan and R. J. Goldstein. Effect of endwall motion on blade tip heat transfer. *Journal of Turbomachinery*, 125(2):267–273, Apr 2003.

J. B. Staubach, O. P. Sharma, and G. M. Stetson. Reduction of tip clearance losses through 3-D airfoil designs. In *Proceedings of the ASME Turbo Asia Conference 1996*, 1996. 5th–7th November 1996, Jakarta, Indonesia (96-TA-13).

B. Sunden and G. Xie. Gas turbine blade tip heat transfer and cooling: A literature survey. *Heat Transfer Engineering*, 31(7):527–554, 2010.

J. Tallman and B. Lakshminarayana. Numerical simulation of tip leakage flows in axial flow turbines, with emphasis on flow physics: Part I—Effect of tip clearance height. *Journal of Turbomachinery*, 123(2):314–323, Apr 2001a.

J. Tallman and B. Lakshminarayana. Numerical simulation of tip leakage flows in axial flow turbines, with emphasis on flow physics: Part II—Effect of outer casing relative motion. *Journal of Turbomachinery*, 123(2):324–333, Apr 2001b.

B. M. T. Tang, P. Palafox, B. C. Y Cheong, M. L. G. Oldfield, and D. R. H. Gillespie. Computational modeling of tip heat transfer to a superscale model of an unshrouded gas turbine blade. *Journal of Turbomachinery*, 132(3):031023, Jul 2010. Previously published as GT2008-51212 in *Proceedings of the ASME Turbo Expo 2008: Power for Land, Sea and Air*.

S. Teng, J. C. Han, and G. M. S. Azad. Detailed heat transfer coefficient distributions on a large-scale gas turbine blade tip. *Journal of Heat Transfer*, 123(4):803–809, Aug 2001. Previously published in *Proceedings of the 8th International Symposium on Transport Phenomena and Dynamics of Rotating Machinery (ISROMAC–8), Volume 1*.

S. J. Thorpe, S. Yoshino, R. W. Ainsworth, and N. W. Harvey. An investigation of the heat transfer and static pressure on the over-tip casing wall of an axial turbine operating at engine representative flow conditions. (I). Time-mean results. *International Journal of Heat and Fluid Flow*, 25(6):933–944, Dec 2004a.

S. J. Thorpe, S. Yoshino, R. W. Ainsworth, and N. W. Harvey. An investigation of the heat transfer and static pressure on the over-tip casing wall of an axial turbine operating at engine representative flow conditions. (II). Time-resolved results. *International Journal of Heat and Fluid Flow*, 25(6):945–960, Dec 2004b.

S. J. Thorpe, S. Yoshino, G. A. Thomas, R. W. Ainsworth, and N. W. Harvey. Blade-tip heat transfer in a transonic turbine. *Proceedings of the Institution of Mechanical Engineers, Part A: Journal of Power and Energy*, 219(6):421–430, Sep 2005.

S. J. Thorpe, R. J. Miller, S. Yoshino, R. W. Ainsworth, and N. W. Harvey. The effect of work processes on the casing heat transfer of a transonic turbine. *Journal of Turbomachinery*, 129(1):84–91, Jan 2007. Previously published as GT2005-68437 in *Proceedings of the ASME Turbo Expo 2005: Power for Land, Sea and Air*.

M. F. Urban and N. Vortmeyer. Experimental investigations on the thermal load and leakage flow of a turbine blade tip section with different tip section geometries. In *Proceedings of the ASME Turbo Expo 2000: Power for Land, Sea and Air*, 2000. 8$^{\text{th}}$–11$^{\text{th}}$ May 2000, Munich, Germany (2000-GT-0196).

D. K. Van Ness II, T. C. Corke, and S. C. Morris. Turbine tip clearance flow control using plasma actuators. In *Proceedings of the 44$^{\text{th}}$ AIAA Aerospace Sciences Meeting*, 2006. 9$^{\text{th}}$–12$^{\text{th}}$ June 2006, Reno, Nevada, USA (AIAA-2006-0021).

D. K. Van Ness II, T. C. Corke, and S. C. Morris. Tip clearance flow visualization of a turbine blade cascade with active and passive flow control. In *Proceedings of the ASME Turbo Expo 2008: Power for Land, Sea and Air*, 2008. 9$^{\text{th}}$–13$^{\text{th}}$ June 2008, Berlin, Germany (GT2008-50703).

G. Vogel, A. Agrawal, and P. Nannapaneni. Turbine blade tip cooling modelling and optimization. In *Proceedings of the ASME Turbo Expo 2009: Power for Land, Sea and Air*, 2009. 8th–12th June 2009, Orlando, Florida, USA (GT2009-59244).

A. R. Wadia and T. C. Booth. Rotor-tip leakage: Part II—Design optimization through viscous analysis and experiment. *Journal of Engineering for Power*, 104(1): 162–169, Jan 1982.

J. Wang, Y. Liu, X. Wang, Z. Du, and S. Yang. Characteristics of tip leakage flow of the turbine blade with cutback squealer and coolant injection. In *Proceedings of the ASME Turbo Expo 2010: Power for Land, Sea and Air*, 2010. 14th–18th June 2010, Glasgow, UK (GT2010-22566).

A. P. S. Wheeler, N. R. Atkins, and L. He. Turbine blade tip heat transfer in low speed and high speed flows. *Journal of Turbomachinery*, 133(4):041025, Oct 2011a. Previously published as GT2009-59404 in *Proceedings of the ASME Turbo Expo 2009: Power for Land, Sea and Air*.

A. P. S. Wheeler, T. Korakianitis, and S. Banneheke. Tip leakage losses in subsonic and transonic blade-rows. In *Proceedings of the ASME Turbo Expo 2011: Power for Land, Sea and Air*, 2011b. 6th–10th June 2011, Vancouver, Canada (GT2011-45798).

F. Whittle. *Improvements relating to the propulsion of aircraft and other vehicles*. British Patent GB 347206, Apr 1931.

L. Willer, F. Haselbach, D. A. Newman, and N. W. Harvey. An investigation into a novel turbine rotor winglet: Part 2—Numerical simulation and experimental results. In *Proceedings of the ASME Turbo Expo 2006: Power for Land, Sea and Air*, 2006. 8th–11th May 2006, Barcelona, Spain (GT2006-90459).

X. Xiao, A. A. McCarter, and B. Lakshminarayana. Tip clearance effects in a turbine rotor: Part I—Pressure field and loss. *Journal of Turbomachinery*, 123(2):296–304, Apr 2001.

A. Yamamoto. Endwall flow/loss mechanisms in a linear turbine cascade with blade tip clearance. *Journal of Turbomachinery*, 111(3):264–275, Jul 1989.

A. Yamamoto, T. Matsunuma, K. Ikeuchi, and E. Outa. Unsteady endwall/tip-clearance flows and losses due to turbine rotor-stator interaction. In *Proceedings of the ASME Turbo Expo 1994: Land, Sea and Air*, 1994a. 13th–16th June 1994, The Hague, Netherlands (94-GT-461).

A. Yamamoto, J. Tominaga, T. Matsunuma, and E. Outa. Detailed measurements of three-dimensional flows and losses inside an axial flow turbine rotor. In *Proceedings of the ASME Turbo Expo 1994: Land, Sea and Air*, 1994b. 13th–16th June 1994, The Hague, Netherlands (94-GT-348).

D. Yang, Z. Feng, and X. Yu. Investigation of film cooling effectiveness on squealer tip of a gas turbine blade. In *Proceedings of the ASME Turbo Expo 2009: Power for Land, Sea and Air*, 2009. 8th–12th June 2009, Orlando, Florida, USA (GT2009-60280).

D. Yang, X. Yu, and Z. Feng. Investigation of leakage flow and heat transfer in a gas turbine blade tip with emphasis on the effect of rotation. *Journal of Turbomachinery*, 132(4):041010, Oct 2010.

H. Yang, S. Acharya, S. V. Ekkad, C. Prakash, and R. Bunker. Flow and heat transfer predictions for a flat-tip turbine blade. In *Proceedings of the ASME Turbo Expo 2002: Power for Land, Sea and Air*, 2002a. 3rd–6th June 2002, Amsterdam, The Netherlands (GT-2002-30190).

H. Yang, S. Acharya, S. V. Ekkad, C. Prakash, and R. Bunker. Numerical simulation of flow and heat transfer past a turbine blade with a squealer-tip. In *Proceedings of the ASME Turbo Expo 2002: Power for Land, Sea and Air*, 2002b. 3rd–6th June 2002, Amsterdam, The Netherlands (GT-2002-30193).

H. Yang, H. C. Chen, and J. C. Han. Numerical prediction of film cooling and heat transfer with different film-hole arrangements on the plane and squealer tip of a gas turbine blade. In *Proceedings of the ASME Turbo Expo 2004: Power for Land, Sea and Air*, 2004. 14th–17th June 2004, Vienna, Austria (GT2004-53199).

H. Yang, H. C. Chen, and J. C. Han. Turbine rotor with various tip configurations flow and heat transfer predictions. *Journal of Thermophysics and Heat Transfer*, 20 (1):80–91, Jan-Mar 2006.

M. Yaras, Z. Yingkang, and S. A. Sjolander. Flow field in the tip gap of a planar cascade of turbine blades. *Journal of Turbomachinery*, 111(3):276–283, Jul 1989.

M. I. Yaras and S. A. Sjolander. Measurements of the effects of winglets on tip-leakage losses in a linear turbine cascade. In F. S. Billig, editor, *Tenth International Symposium on Air Breathing Engines*, pages 127–135, 1991. ISBN 1-56347-006-3. 1st–6th September 1991, Nottingham, UK.

M. I. Yaras and S. A. Sjolander. Effects of simulated rotation on tip leakage in a planar cascade of turbine blades: Part I—Tip gap flow. *Journal of Turbomachinery*, 114(3):652–659, Jul 1992a.

M. I. Yaras and S. A. Sjolander. Prediction of tip-leakage losses in axial turbines. *Journal of Turbomachinery*, 114(1):204–210, Jan 1992b.

M. I. Yaras, S. A. Sjolander, and R. J. Kind. Effects of simulated rotation on tip leakage in a planar cascade of turbine blades: Part II—Downstream flow field and blade loading. *Journal of Turbomachinery*, 114(3):660–667, Jul 1992.

J. H. Yoon and R. F. Martinez-Botas. Film cooling performance in a simulated blade tip geometry. In *Proceedings of the ASME Turbo Expo 2005: Power for Land, Sea and Air*, 2005. 6th–9th June 2005, Reno-Tahoe, Nevada, USA (GT2005-68863).

J. B. Young and J. H. Horlock. Defining the efficiency of a cooled turbine. *Journal of Turbomachinery*, 128(4):658–667, Oct 2006.

D. H. Zhang, M. Zeng, and Q. W. Wang. The influence of rotating speed on film cooling characteristics on GE-E3 blade tip with different tip configurations. In *Proceedings of the ASME Turbo Expo 2009: Power for Land, Sea and Air*, 2009. 8th–12th June 2009, Orlando, Florida, USA (GT2009-60295).

Q. Zhang and L. He. Over-tip choking and its implications on turbine blade-tip aerodynamic performance. *Journal of Propulsion and Power*, 27(5):1008–1014, Sep–Oct 2011.

Q. Zhang, D. O. O'Dowd, L. He, M. L. G. Oldfield, and P. M. Ligrani. Transonic turbine blade tip aero-thermal performance with different tip gaps: Part I—Tip heat transfer. *Journal of Turbomachinery*, 133(4):041027, Oct 2011a. Previously published as GT2010-22779 in *Proceedings of the ASME Turbo Expo 2010: Power for Land, Sea and Air*.

Q. Zhang, D. O. O'Dowd, L. He, A. P. S. Wheeler, P. M. Ligrani, and B. C. Y. Cheong. Overtip shock wave structure and its impact on turbine blade tip heat transfer. *Journal of Turbomachinery*, 133(4):041001, Oct 2011b.

C. Zhou and H. Hodson. The aerodynamic performance of the tip leakage flow with different tip geometries. In F. Heitmeir, F. Martelli, and M. Manna, editors, *Proceedings of the 8th European Conference on Turbomachinery Fluid Dynamics and Thermodynamics*, pages 1469–1481, 2009. ISBN 978-3-85125-036-7, 23rd–27th Mar 2009, Graz, Austria.

C. Zhou and H. Hodson. The tip leakage flow of an unshrouded high pressure turbine blade with tip cooling. *Journal of Turbomachinery*, 133(4):041028, Oct 2011. Previously published as GT2009-59637 in *Proceedings of the ASME Turbo Expo 2009: Power for Land, Sea and Air*.

C. Zhou, H. Hodson, I. Tibbott, and M. Stokes. The aero-thermal performance of a cooled winglet tip in a high pressure turbine cascade. In *Proceedings of the ASME Turbo Expo 2011: Power for Land, Sea and Air*, 2011a. 6th–10th June 2011, Vancouver, Canada (GT2011-46369).

C. Zhou, H. Hodson, I. Tibbott, and M. Stokes. Effects of endwall motion on the aero-thermal performance of a winglet tip in a HP turbine. In *Proceedings of the ASME Turbo Expo 2011: Power for Land, Sea and Air*, 2011b. 6th–10th June 2011, Vancouver, Canada (GT2011-46373).